Design and Testing of a Permanent Magnet Synchronous Motor Drive System with a Novel Power Electronics Converter

Tamanwè Payarou

A Thesis

In the Department

of

Electrical and Computer Engineering

Presented in Partial Fulfillment of the Requirements

For the Degree of

Doctor of Philosophy (Electrical and Computer Engineering) at

Concordia University

Montreal, Quebec, Canada

December 2022

© Tamanwè Payarou, 2022

CONCORDIA UNIVERSITY
SCHOOL OF GRADUATE STUDIES

This is to certify that the thesis prepared

By: Tamanwè Payarou

Entitled: Design and Testing of a Permanent Magnet Synchronous Motor Drive System

with a Novel Power Electronics Converter

and submitted in partial fulfillment of the requirements for the degree of

Doctor of Philosophy (Electrical & Computer Engineering)

complies with the regulations of the university and meets the accepted standards with respect to

originality and quality.

Signed by the final examining committee:

        _____Chair
        Dr. Bruno Lee

        _____External Examiner
        Dr. Kodjo Agbossou

        _____External to Program
        Dr. Radu Grigore Zmeureanu

        _____Examiner
        Dr. Chunyan Lai

        _____Examiner
        Dr. Luiz A.C. Lopes

        _____Thesis Supervisor
        Dr. Pragasen Pillay

Approved by: _____
              Dr. Jun Cai, Graduate Program Director

December 06, 2022 _____
              Dr. Mourad Debbabi, Dean,
       Gina Cody School of Engineering and Computer Science

Abstract

Design and Testing of a Permanent Magnet Synchronous Motor Drive System with a Novel Power Electronics Converter

Tamanwè Payarou, Ph.D.

Concordia University, 2022

Several technologies have been applied to electric vehicles (EVs) to achieve high performance in terms of mileage, speed, and efficiency. However, technological advances and customer demand are constantly revolutionizing the transportation sector. From the conventional internal combustion engine (ICE) vehicles, transportation has reached the area of hybrid electric vehicles (HEVs) and has moved towards fuel cell electric vehicles (FCEVs). Throughout this revolution, electric machines (EMs) made considerable progress. While the ICEs are phasing out because of their efficiency limitations and negative environmental impact, the EMs will remain the fundamental component of EVs. Hybrid topologies have been adopted and optimized by the industry to address several challenges related to efficiency, mileage, and ecology. However, the green transportation trend will undoubtedly lead to dominance of battery and fuel cell electric vehicles. Efficient high-speed EMs and their associated power electronics and control are therefore needed to replace and transcend ICEs.

The requirement of high-speed EMs that can replace and surpass the ICE in terms of efficiency versus speed range requires associated power electronic converters that can drive the EMs through their operating envelopes. The new generation of EVs will be more demanding in terms of power, integration to the grid, efficiency, mileage; ruggedness and size reduction of power electronics interfaces and machines. The aim is to reduce the overall cost/weight of EVs and optimize energy efficiency across the entire drivetrain.

This research proposes and validates a new step-by-step design method for EV drivetrain design and testing. The proposed method is based on analytically obtaining feasible drivetrain parameters from the torque-speed curve and battery nominal voltage specifications. A case study based on a 2010 Toyota Prius motor is used to validate the proposed approach for its ability to estimate feasible parameters that can be matched using finite element analysis (FEA) software. The proposed method's ability to estimate IPMSM parameters from a given SPMSM is validated

experimentally. This method allows machines and drive specialists to work in parallel on the drivetrain component design and speed up the whole drivetrain design process.

A novel integrated multipurpose power electronics interface (IMPEI) designed for PHEVs and EVs is proposed to provide a solution to the increasing need for integration and grid support of EVs. The IMPEI is analyzed, designed, prototyped, tested, and compared with several other integrated power electronics interfaces (IPEIs) and with conventional power electronics interfaces (CPEI) in this work. The proposed IMPEI and different other topologies are compared in terms of configuration, device count, cost, and efficiency, using the BMW i3 as the benchmark application. The design requirements of the IMPEI are presented and discussed, including modes of operation, switch and passive element sizing, and ratings. The results of experiments in propulsion, regenerative braking, and single-phase and three-phase V2G and G2V are presented. The experimental efficiency analysis and comparison are carried out in the propulsion, V2G, and G2V modes.

The proposed analytical drivetrain design approach is used to size the drivetrain of a Renault Twizy. In this design, the IMPEI is used as a drive inverter. The potential fuel economy of the IMPEI-based Renault Twizy drivetrain is investigated based on experimental and simulation data. The IMPEI is sized and simulated in PSIM software to obtain its efficiency map throughout the operating envelope. The designed PMSM efficiency map is obtained from JMAG software. However, the mechanical system efficiency map is obtained practically throughout a drive cycle in Aachen city in Germany. A fuel economy analysis is also carried out in this work.

A comparison of commonly used test benches is provided, followed by the details on the test bench used to obtain the experimental results throughout the thesis. The main components of the test bench are described. Also, a regenerative braking analysis of high-speed permanent magnet synchronous motors (PMSMs) during emergency conditions is presented. Overloading the electric machine during regenerative braking in emergency conditions using field-oriented control (FOC) is investigated.

Acknowledgements

All the praise and thanks be to Allah, The lord of the Universe, the most beneficent and most merciful. May peace and blessing of Allah be upon his messenger Mohamed (s.a.w).

I would like to express deep gratitude to my supervisor Professor Pragasan Pillay for being a source of inspiration, kind support, a professional guide, a boss, and a leader. Thanks for the ultimate opportunity you granted me to achieve my goal, which was a pure dream at some point.

My sincere thanks go to my committee members, Professor Chunyan Lai, Professor Radu Grigore Zmeureanu, Professor Luiz A.C. Lopes, and Professor Kodjo Agbossou, for being committee members even in hardship and for the valuable comments, suggestions, and valuable time.

A special thanks to my family back home for their prayers and continuous support, especially to my father, Mr. Abalo Payarou, and my Mother, Ms. Atèfeimbou Papali. Many thanks for all the sacrifices, prayers, and blessings that opened doors for me by the will of Allah.

I would also like to thank my beloved wife, Ms. Maria Matondo Nkossi. She patiently supported me morally during my research and gave me two lovely daughters Nayla Payarou et Moubaraka Payarou.

Many thanks to my colleagues in the Concordia University Power Electronics and Energy Research (PEER) group for maintaining an excellent research environment. A special thanks to my coauthors, Mr. Mohanraj Muthusamy and Dr. Sumeet Singh, for providing FEA data and to Dr. Mathews Boby and Dr. Akrem Ajaheimi for their suggestions and assistance.

Table of Contents

List of Figures

List of Tables

List of Symbols

Symbol	Unit	Definition
$A, B, C_{1,2\ldots}$	-	Estimation parameters
A_c	1/A	Attenuation constant
B_{max}	T	Maximum flux density
B	Nms/rad	Friction coefficient
C_{eff}	%	Charge efficiency of the battery
C_f	F	LCL filter capacitance
C_φ	-	Flux concentration factor
E_{eff}	%	Energy efficiency of the battery
E_{off}	J	Transistor turn-off energy losses
E_{on}	J	Transistor turn-on energy losses
E_{rr}	J	Reverse recovery energy loss
f_g	Hz	Grid frequency
f_{res}	Hz	Resonance frequency
f_s	Hz	Switching frequency
$FE_{Drivetrain}$	kWh/100 km	Drivetrain fuel economy
FE_{mech}	kWh/100 km	Mechanical system fuel economy
FE_{mech-P}	kWh/100 km	Mechanical system fuel economy during propulsion
$FE_{mech-RB}$	kWh/100 km	Mechanical system fuel economy during braking
g	m	Air gap length
$I_{batt_{char}}$	A	Battery current during the battery charge
$I_{batt_{dis}}$	A	Battery current during the battery discharge
I_c	A	Collector current
i_{ch}	A	Characteristic current
I_{cst}	-	Current constant
i_d	A	D-axis stator current
I_{diode}	A	Diode forward current
i_g	A	Grid current

I_{gs}	A	RMS grid current ripple
I_{PES}	A	Rated current of the power electronics switch
i_q	A	Q-axis stator current
I_{rms}	A	Phase RMS current
I_s	A	Peak rated current of the machine
i_s	A	Stator current
J	kg. m^2	Inertia
k_{st}	-	Lamination stacking factor
l	m	Flux path length
L	H	Total LCL filter inductance
$L_{d_{SPMSM}}$	H	D-axis inductance of the optimized SPMSM
$L_{q_{SPMSM}}$	H	Q-axis inductance of the optimized SPMSM
$L_{d_{IPMSM}}$	H	D-axis inductance of the optimized IPMSM
$L_{q_{IPMSM}}$	H	Q-axis inductance of the optimized IPMSM
L_1	H	Inverter side filter inductance
L_2	H	Grid side filter inductance
L_d	H	D-axis inductance
L_{eq}	H	Equivalent LCL filter inductance
l_m	m	Magnet length
L_{max}	H	Maximum value of the total inductances in the LCL filter
L_{min}	H	Minimum value of the total inductances in the LCL filter
L_q	H	D-axis inductance
L_s	H	Stator inductance
m_a	-	Modulation index
m_{max}	-	Desired maximum modulation index
N	-	Number of winding turns
$n_{b_{Sr}}$	r/min	Calculated speed at $S_{r \neq 1}$
n_{sb}	r/min	Base speed of the motor (elec.)
P	-	Pole pair number
p	-	Derivative operator

pf	-	Power factor
$P_{m,out}$	W	Mechanical output power
$P_{T_{Sn}}$	W	Total power loss of the nth switch
P_c	-	Permeance coefficient
$P_{cond(Diode)}$	W	Diode conduction losses
$P_{cond(Switch)}$	W	Transistor conduction losses
P_d	W	Developed power
P_{in}	W	Input power of the drive inverter
P_{losses}	W	Total losses of the drive inverter
P_{out}	W	Output power of the active front end converter
$P_{sw(Diode)}$	W	Diode switching losses
$P_{sw(Switch)}$	W	Transistor switching losses
pf	-	Power factor
Q	W	Power dissipated by the device
R	H^(-1)	Reluctance
R_d	Ω	Damping resistance
R_s	Ω	Rotor resistance
S	VA	Apparent power
S_r	-	Saliency ratio
T_a	°C	Maximum ambient temperature
T_{char}	s	Charge time
T_{dis}	s	Discharge time
T_e	Nm	Electromagnetic torque
T_{er}	Nm	Rated torque of the machine
$T_{e_{Sr}}$	Nm	Calculated torque at $S_{r \neq 1}$
T_j	°C	Maximum junction temperature
$V_{b,nom}$	V	Nominal battery voltage
$V_{batt_{char}}$	V	Battery voltage during the battery charge
$V_{batt_{dis}}$	V	Battery voltage during the battery discharge

$V_{DC_{Charge}}$	V	DC bus voltage during the charging operation
$V_{DC_{Charge}}$	V	DC bus voltage of the active front end during charging mode
$V_{DC_{max}}$	V	Fully charged battery voltage
$V_{DC_{max}}$	V	Fully charged battery voltage
v_{IMPEI}	V	Inverter phase voltage
$V_{ll,rms}$	V	Line to line RMS voltage
$V_{ph,rms}$	V	Phase to neutral RMS voltage
V_{cc}	V	DC bus voltage
$V_{ce(sat)}$	V	Transistor saturation voltage
v_d	V	D-axis stator voltage
V_{dc}	V	Source dc link inverter input voltage
V_{diode}	V	Diode voltage drop
V_g	V	Grid phase voltage
V_{IMPEIs}	V	RMS inverter voltage ripple
V_o	V	Maximum available per-phase peak fundamental voltage
V_{PES}	V	Rated voltage of the power electronics switch
v_q	V	Q-axis stator voltage
V_R	V	Reverse blocking voltage
w_{bi}	m	Back iron width
w_{tb}	m	Stator tooth width
X_d	Ω	D-axis stator reactance
X_q	Ω	Q-axis stator reactance
η_{IMPEI}	%	Efficiency of the IMPEI
η_m	%	Machine efficiency
η_{PMSM}	%	PMSM efficiency
Θ_{cs}	°C/W	Case to sink thermal resistance
Θ_{jc}	°C/W	Junction to case thermal resistance
Θ_{sa}	°C/W	Sink to ambient temperature thermal resistance
$\lambda_{af_{IPMSM}}$	Wb-turns	Per-phase magnet flux-linkage of the IPMSM to be designed

$\lambda_{af_{SPMSM}}$	Wb-turns	Per-phase magnet flux-linkage of the optimized SPMSM
λ_{af}	Wb-turns	Per-phase magnet flux-linkage
λ_d	Wb-turns	D-axis flux-linkage
λ_q	Wb-turns	Q-axis flux-linkage
μ	H/m	Permeability of the material
φ_g	Wb	Air gap flux
ω_r	rad/s	Electrical speed of the rotor (mech)
ω_{rb}	rad/s	Bases speed of the motor (mech.)
ω_{res}	rad/s	Resonance frequency
ω_{rmax}	rad/s	Maximum speed of the motor (mech.)
ω_{smax}	rad/s	Maximum speed of the motor (elec.)
ω_s	rad/s	Synchronous speed of the motor (elec.)
ω_{sb}	rad/s	Base speed of the motor (elec.)
ω_{scri}	rad/s	Critical speed of the motor (elec.)

List of Abbreviations

AFEC	Active front end converter
APEI	Advanced power electronics interface
BEV	Battery electric vehicles
CPEI	Conventional power electronics interface
DOE	US Department of Energy
DTC	Direct torque control
EV	Electric vehicles
EM	Electric machine
EPA	Environmental protection agency
FCEV	Fuel cell electric vehicles
FHV	Full hybrid vehicle
FOC	Field-oriented control
G2V	Grid-to-vehicle
HEV	Hybrid electric vehicles
ICE	Internal combustion engine
ICEV	Internal combustion engine vehicles
KE	Kinetic energy
IM	Induction motor
IMPEI	Integrated multipurpose power electronics interface
IPEI	Integrated power electronics interface
IPMSM	Interior or inset permanent magnet synchronous motor
ISG	Integrated starter generator
MHV	Mild hybrid vehicle
MPEI	Multipurpose power electronics interface
NEDC	New European driving cycle
NSI	Nine-switch inverter
PE	Power electronics
PEI	Power electronics interface
PES	Power electronics switches

PEVs	Plug-in electric vehicles
PHEV	Plug-in hybrid electric vehicles
PM	Permanent magnet
PMSM	permanent magnet synchronous motor
RE	Renewable energies
SoC	States of charge
SPIC	Single-phase integrated charger
SPMSM	Surface permanent magnet synchronous motor
SVPWM	Space Vector PWM
V2G	Vehicle-to-grid
WLTP	Worldwide harmonized light vehicle test procedure
WTT	Well-to-tank
μHV	Micro-hybrid vehicle
AFEC	Active front end converter

Chapter 1. Introduction

This chapter presents an overview of electric vehicles (EVs) and a state-of-the-art in the electrical transportation area. The type of electric vehicles and their drivetrain elements are discussed. Electric machine testing facilities are also discussed. This chapter is organized as follows: Section 1.1 presents a brief introduction to electrical transportation. In section 1.2, types of EVs are introduced. Section 1.3 discusses the available power electronics interfaces in EVs followed by a discussion on integrated power electronics interfaces (IPEIs) in section 1.4. The research problem statement and motivation are presented in sections 1.5 and 1.6, respectively. The research objectives are in section 1.7, and thesis organization is presented in section 1.8. Contributions of this study are presented in section 1.9.

1.1. Transportation Electrification

The issues of sustainability and emission reduction, on the one hand [1] - [4], and the availability of cleaner energy sources and advancements in battery technologies, on the other hand [5] - [7], are revolutionizing the field of transportation. Traditional internal combustion engine vehicles (ICEVs) have been found to be inefficient and polluting when compared to hybrid electric vehicles (HEVs), battery electric vehicles (BEVs), and fuel cell electric vehicles (FCEVs) [8] - [10]. According to the US Department of Energy (DOE), electric motors in EVs convert over 75% of electrical power from the grid into usable power at the wheels. In comparison, about 12% - 30% is achieved by ICEVs when converting the energy stored in the gasoline into motion [11]. The electrification stages of the transportation are summarized in Fig. 1-1 based on the electrical power in the drivetrain. The ICEV has only an alternator for charging the battery after starting the engine. By replacing the alternator with an integrated starter generator (ISG), the conventional ICEV becomes a micro-hybrid vehicle (μHV) where the ICE is the only power source. The ISG is used to help start the engine and charge the battery when the vehicle is running. The efficiency gain is about 5 to 15%. For mild hybrid vehicles (MHVs), the ICE is the dominant power source. As motor's electrical power is increased, a 30 to 50% increase in efficiency can be achieved. Some practical examples of MHVs are Honda Civic Hybrid and Hyundai Sonata Hybrid. For full hybrid vehicles (FHVs) such as Toyota Prius, Chevrolet Volt, and Ford Escape, the efficiency increase can reach 50 to 100% compared to ICEVs. Plug-in hybrid electric vehicles (PHEVs) differ from FHVs in their increased battery capacity, driving range, and external charging capability [12].
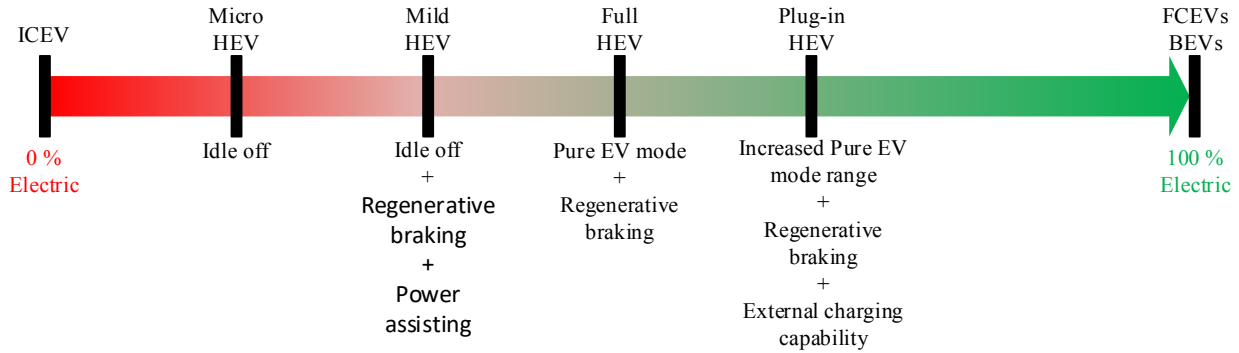
Fig. 1-1. Electrification stages of the transportation.

Nowadays, BEVs and plug-in HEVs (PHEVs) are widely used because of their energy efficiency and environmental friendliness, and they are regarded as promising solutions for sustainable transportation [13]. Gas, coal, oil, solar, wind, biomass, and nuclear energy can be used to reduce PHEVs' reliance on oil [12]. The advancements of battery technology and the vehicle-to-grid (V2G) approach, aimed at transforming BEVs and PHEVs into "virtual power plants" [14], make them the automotive industry's future. The same conclusion was reached in [8] and [15] despite the authors emphasizing that fuel cell electric vehicles (FCEVs) are excellent competitors to PHEVs due to their cleanliness and refill time, comparable to ICEVs. However, FCEVs are not widely used due to issues with the availability of FCEV infrastructure [14]. In addition, when well-to-tank (WTT) emissions are considered, FCEVs have the highest emissions due to hydrogen production [16].

1.2. Type of Electric Vehicles

Several types of EVs are encountered in the literature. Fig. 1-2 summarizes the available EV types in terms of energy source and cleanliness. EVs can be categorized into two main groups; power and energy sources-based. The basic EV is the BEV, where the only energy source is the battery. The combination of elements from the two main groups results in HEVs. This is done by taking advantage of each of the sources. The fundamental definition of HEV is presented as an EV with at least two onboard energy/power sources [17]. The energy sources are listed as batteries, flywheels, etc. The power sources are internal combustion engines (ICEs), fuel cells, batteries, and ultracapacitors. As a result of the combination, some HEVs are cleaner than others because of the nature of their dominant source of energy/power. The predominant type of HEVs combines the ICE and the battery storage system. The battery is used for starting the vehicle and
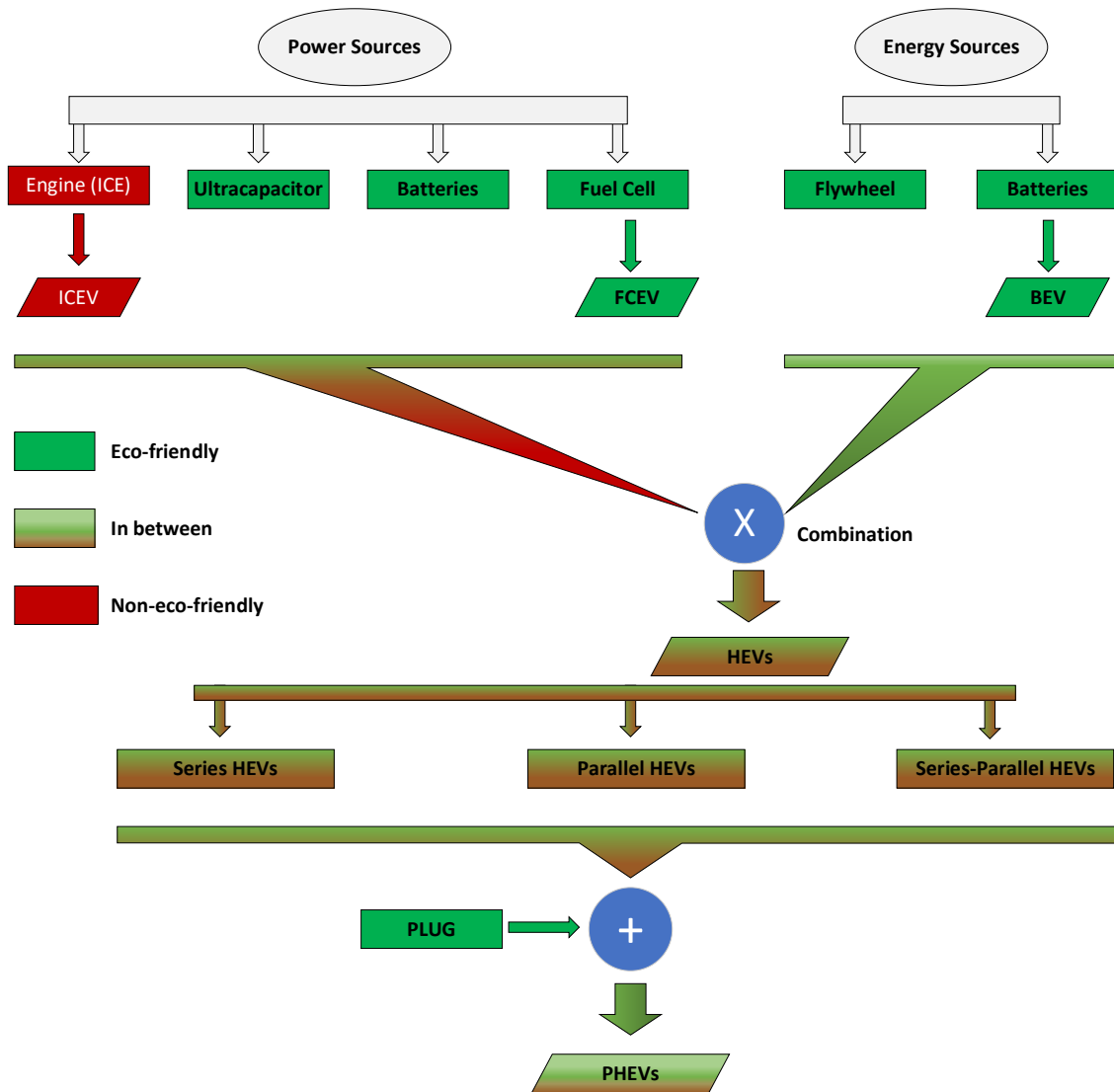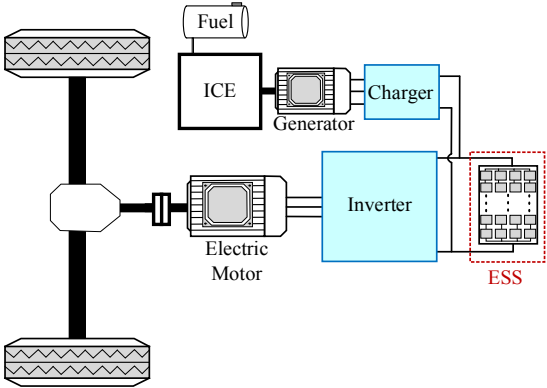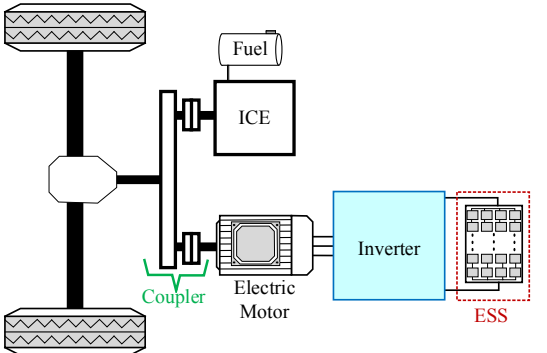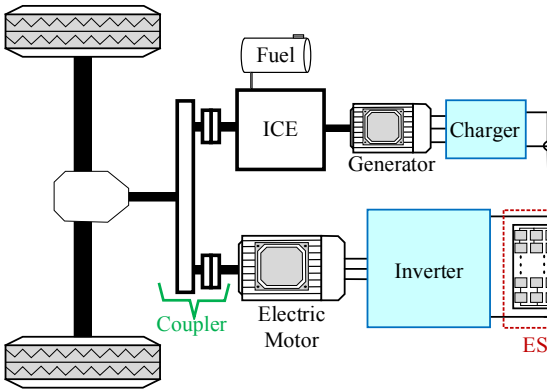
Fig. 1-2. EV architecture.

for the regenerative braking. The battery is charged through a generator coupled to the ICE. This method of recharging the battery is not efficient.

To increase the performance of HEVs, PHEVs were introduced as a modified form of HEVs with external charging capability, higher fuel economy, higher efficiency, and longer range in pure electric propulsion mode. Therefore, they have a higher energy density battery pack that can be charged internally and externally. However, they are not as clean as FCEVs, which use fuel cells as an alternative power source to the ICE. Some of the advantages of FCEVs are direct energy conversion without combustion, quietness, robustness (no moving parts), fuel flexibility, and low air pollution [17]. From a user point of view, the advantages and limitations of each EV type are listed in Table 1-1 [12], [17].

Table 1-1. Drivetrains of HEVs and FCEVs.

	Description	Advantages	Limitations
Series HEVs	The ICE is used to charge and assist the battery.	• Low fuel consumption in city driving. • Smaller engine.	• Poor efficiency due to the cascaded structure. • Relatively Heavy, bulky and, expensive power unit.
Parallel HEVs	The ICE is used for cruising. The battery is recharged via the ICE during cruising mode	• More efficient in urban stop-and-go drive cycles. • Low fuel consumption in highway driving.	• Complex control and coordination strategy. • Complex gearbox.
Series-Parallel HEVs	The ICE is used for cruising, battery assist, and charging. This configuration takes advantage of the series and parallel configurations.	• Low fuel consumption and high mileage capability compared to series and parallel HEVs	• Complex control strategy. • Complex hardware and gearbox.

4
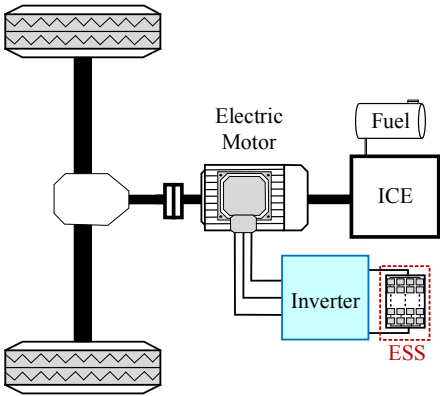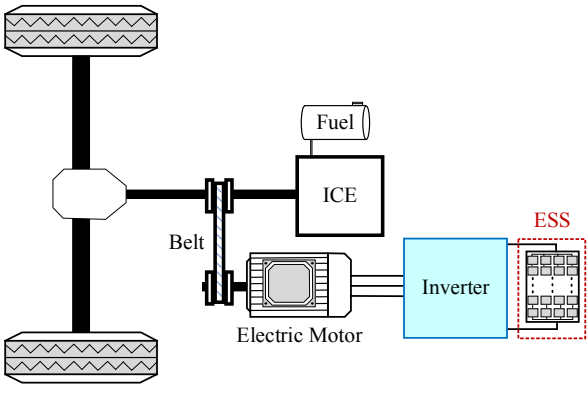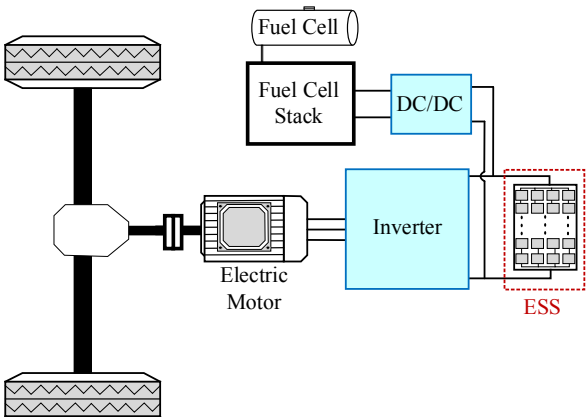
Crankshaft assisted ISG system	 It is a variant of parallel HEVs. The electric motor and ICE can be operated separately or simultaneously.	• Low fuel consumption. • More power generation capability. • Simpler gearbox compared to parallel HEVs.	• Complex control and coordination strategy. • Complex mechanical design and alignment for high speed operations.
Side mounted ISG	 It is a variant of parallel HEVs and Crankshaft assisted ISG system.	• Low cost and simple implementation. • Minimal modification in the hardware. • Low fuel consumption, and more power generation capability.	• Complex control and coordination strategy. • Simpler mechanical design and alignment for high speed operations.
FCEVs		• Fuel flexibility. • Low air pollution. • Almost constant efficiency. • Direct energy conversion without combustion. • Quiet and robust (no moving parts).	• Charging infrastructure not available and costly. • Requires batteries for transient operation. • They are limited by the current electric machine's technology.

Table 1-1 shows that while the ICE is phasing out from the electrical transportation area, the electric machines (EMs) are establishing their unavoidable presence. The current and future

challenge is to improve the performance of EMs for efficiency and operating range. The power electronics interfaces required to drive the higher performance electric machines should be developed and tested.

1.3. Power Electronics Interfaces

Power electronics interface (PEI) in electric vehicles is used to name any power electronics circuitry used in an EV drivetrain to interface the battery to the EM or the grid to the battery. PEIs are one of the most important components of EV systems. Topologies presented in [18] - [21] and control strategies discussed in [22] - [24] that can provide better interfaces and improve EVs' performance are being investigated in areas of power electronics and control. Fig. 1-3(a) shows that the most common PEIs in BEVs and PHEVs are three-phase inverters, DC-DC converters, and onboard chargers (AC-DC converters). The three-phase inverter is used for propulsion and regenerative braking. The bidirectional DC-DC converters regulate the DC voltage, and the plug-in onboard charger is used to charge the car while parked. It can be seen that the system is cascaded. In terms of efficiency, an ideal electric vehicle's drivetrain should have a single-stage interface between the battery and the inverter. In a cascaded system, efficiencies are multiplied, resulting in a lower overall efficiency of the drivetrain [25]. One of the conventional EV drivetrains is depicted in Fig. 1-3(a). As can be seen, charging the battery necessitates an AC-DC conversion stage first, followed by a DC-DC stage. A two-stage conversion is required for propulsion and regenerative braking as well. The battery is sized for drive operation in the single-stage configuration shown in Fig. 1-3(b), and its voltage can be as high as 400 V in most modern EVs [26], and [27]. 800 V EV drivetrains are now available [28], and their fast charging capabilities are being investigated [29], and [30]. The weight and control complexity of the PEI can be reduced by sizing the battery for the drive operation. A study in [31] compared a battery-powered inverter (T1) to a battery cascaded to the inverter via a bidirectional DC-DC converter (T2) and found that T1 is less complex, has a lower cost, and is smaller than T2. However, T2 topology can provide lower voltage distortion and improved power factor performance by properly controlling its variable DC bus voltage. T1 has higher efficiencies at high speeds, while T2 has higher efficiencies at low speeds while partially loaded. Based on the discussion above, the DC-DC interface between the battery and the propulsion inverter can be removed to improve the drivetrain efficiency, particularly at high speeds and full loads.
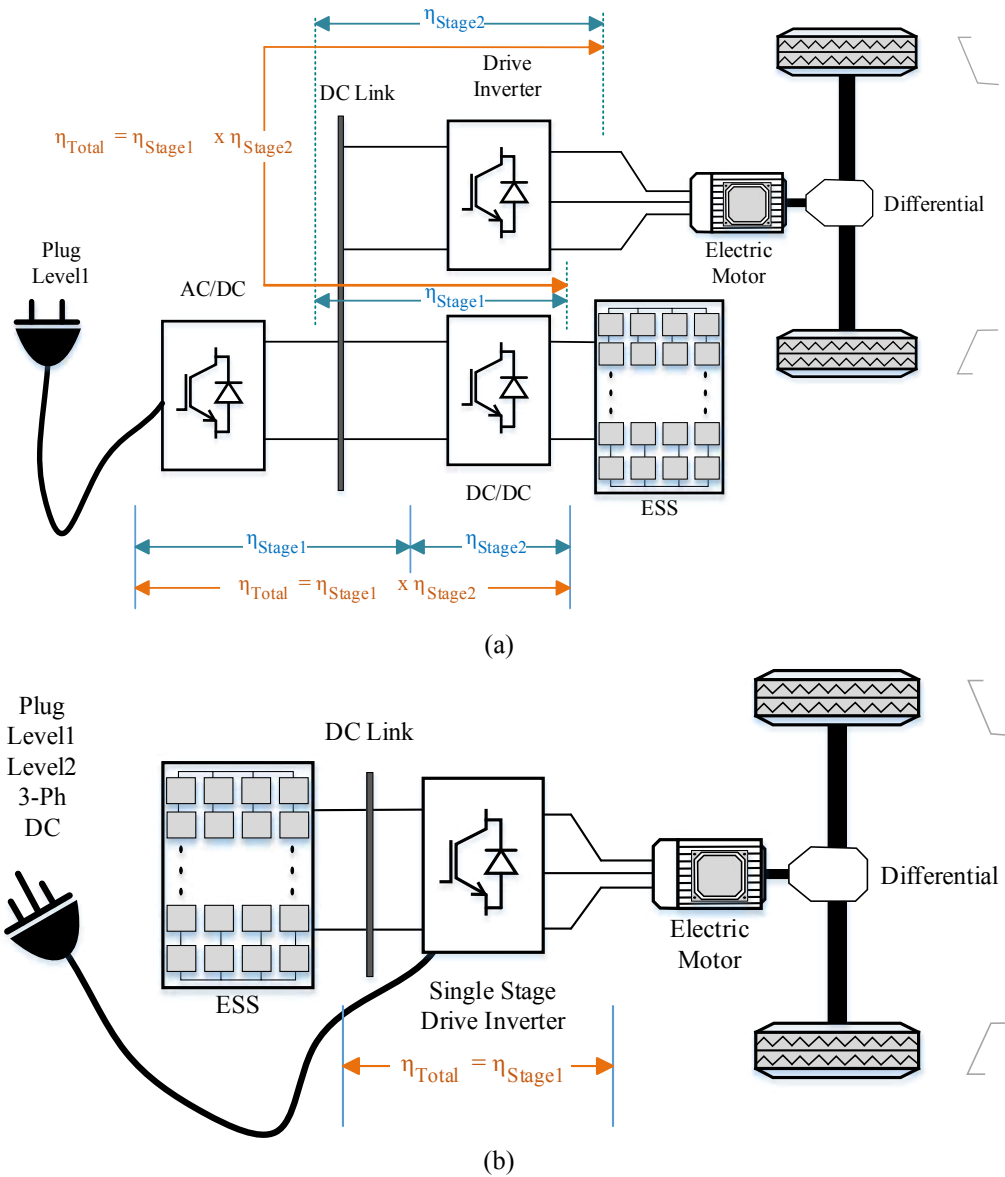
Fig. 1-3. BEV drivetrain architectures: (a) conventional, (b) single-stage BEV drivetrain.

The main disadvantages of the conventional BEV drivetrain configurations are the limited charging capability of the onboard charger, the amount of space it occupies, as well as its weight during propulsion. To minimize the weight and size of the additional components, onboard chargers in conventional EVs are designed with limited charging capability [32]. This limits the charging rate of the EV. Also, the plug-in onboard charger acts as a "free traveling passenger" during propulsion. The same is true for the three-phase inverter during charging while the car is parked. The charger and inverter can be integrated to reduce the number of components and the amount of space occupied by PEIs in EVs. Furthermore, some PEI components can be reused in other modes of operation, resulting in an integrated PEI (IPEI).

1.4. Integrated Power Electronics Interfaces

Integrated onboard chargers are being adopted as a solution for compact, small-scale, and low-volume EV drivetrains. They provide high-power onboard charging by reusing some drivetrain components [32]. The feasibility of integrating EV chargers and the propulsion inverter as integrated (bidirectional) battery chargers has been investigated in the literature [33] - [40]. On the one hand, some of the proposed solutions only support single-phase charging [33], [41], while others support three-phase charging [42] and [43]. Furthermore, some of them only provide vehicle-to-grid (V2G) operation [34], [44], and [45], while others provide both V2G and grid-to-vehicle (G2V) operations [46] and [47]. The work in [32], and [48] - [51] provides an overview on onboard chargers and integrated chargers. The available integrated topologies can be grouped into two categories: those that aim to reduce the number of power electronics switches (PESs) and those that aim to reduce the number of passive elements (mostly inductors by using the winding of the propulsion motor). The available integrated topologies offer a trade-off solution between desired modes of operation (propulsion, regenerative braking, V2G, and G2V), cost, component stress, switch count, and active and passive element count.

1.5. Problem Statements

The summary in Table 1-1 shows that the ICE is phasing out from the transportation area while the EMs are establishing their unavoidable presence. The new generation EMs should provide the same or better performance as ICE in terms of torque-speed ranges and efficiency. The current and future challenges will be to improve the performance of EMs in terms of efficiency and operating range. EVs' drivetrain components should be designed and tested. Also, the designed PEIs should be matched with EMs for better efficiency.

Designing and testing EVs is time-consuming because of the iterations involved in the electric machines (EMs) and their power electronics (PEs) designs. Most of the time, both designs are done sequentially by using the output of the machine design step for proper sizing of its PEIs. This makes the whole EV drivetrain design and testing time-consuming and iterative.

For the new generation of EVs, the available PEIs required to drive the EMs don't have operational flexibility. They are mainly designed for a few tasks: propulsion, regenerative braking, charging, and sometimes grid support. New generation EVs should be able to turn into "virtual power plants" as needed. This translates to an EV's ability to perform V2G and G2V

operations in urban and rural areas while using various energy sources, both with and without a charging station. Hence, the whole EV drivetrain should be developed and tested to validate the EMs' operating ranges and capabilities.

1.6. Motivation

Electrical transportation is going through an irreversible transformation and focuses on integrating renewable energies (REs) and eco-friendly alternative fuel sources into the EV drivetrain. Vehicles are evolving from non-eco-friendly to mild eco-friendly to eco-friendly by adopting different strategies to improve performance. The EM is one of the main elements of EVs. Hence, while the EMs evolve to meet the market requirement, compatible PEIs should be developed to run them. Also, assumingly, IPEIs will be required to allow V2G and G2V operations to support the grid in times of high load or stress.

Designing EMs to meet certain requirements is sometimes more challenging than coming up with ideas to improve their performance, especially in EVs applications where volume and weight are the most significant constraints. Available design steps that enable both the drive and machine design engineers to be on the same page during the whole process are not available in the literature.

In addition, EM test facilities are not always available and cannot always thoroughly test the EMs. In fact, for high-speed EM test facilities, the requirements are many, very challenging, and require a higher level of technology for the test bench design, EMs alignment, and testing. Having a reference high-speed test bench will not only allow machine testing but also decrease the risks related to unexpected issues during acceleration, field weakening, and regenerative braking.

1.7. Objectives

This research aims to:
- Investigate the parameters requirement of a PMSM given the torque-speed envelope and the battery voltage. It will focus on estimating the key parameters of the PMSM that will serve as a reference for machine design engineers as well as drive engineers in their design process. It will speed up the overall design and testing processes. This includes

9

- o developing the EV drivetrain design criteria that provide equations for estimating the required parameters for a given EV drivetrain specification, and
  - o validating the proposed EV design criteria for surface and interior PMSMs.
- Propose an IPEI that will provide current EV drivetrains with onboard grid flexibility and expanded modes of operation while maintaining an acceptable trade-off between operation modes, component count, cost, grid flexibility, and efficiency. This includes
  - o proposing a novel integrated multipurpose PEI (IMPEI) for EVs and PHEVs, and
  - o designing, comparing, prototyping, and validating the modes of operation of a novel IMPEI.
- Validate and test the proposed PMSM-based EV drivetrain design by testing and characterizing the designed PMSM and the associated IPEI. This includes
  - o developing a high-speed test bench with its associated control and coordination, and
  - o characterizing the prototyped high-speed PMSM and its associated IMPEI.

1.8. Thesis Organization

This thesis is organized as follows.

Chapter 1 presents an introduction to electrical transportation and the type of EVs. Different power electronics interfaces available in EVs are discussed. The research problem statement, the motivation, and the objectives are listed, and followed by the research and the thesis organization.

Chapter 2 proposes a novel, fast, and systematic process which provides valuable insight into the EV drivetrain component parameters (EMs and PEs) before finalizing the design. It allows EM design and drives engineers to work in parallel and speed up the EV drivetrain development process. The proposed method estimates the key parameters such as magnet flux linkage, the d-q axes inductances, and motor terminal voltages and currents based on the drive requirements in terms of torque-speed envelope and battery terminal voltage. New equations have been developed for determining IPMSM parameters from a feasible SPMSM design. A case study based on a 2010 Toyota Prius motor has been performed to show the feasibility of the proposed approach. Design steps and performance characteristics are discussed using simulation and finite element analysis (FEA) software. Practical validation has been performed on a SPMSM and a IPMSM motor.

Chapter 3 proposes, describes, designs, compares, and validates the modes of operation of a novel IMPEI designed for the new generation of BEVs and PHEVs. The IMPEI is a reconfigurable PEI that integrates the onboard charger with the drive inverter allowing the same interface to be used for various modes of operation such as propulsion, regenerative braking, V2G, and G2V with grid flexibility. For each mode of operation, the IMPEI is reconfigured into a previously existing topology. The operating principle and coordination of the IMPEI in its various modes are explained. Based on component count, operating modes, and control complexity, a comparison between the proposed IMPEI and recently proposed IPEIs is provided. The specifications of the BMW i3 drivetrain components are used as the benchmark for comparing sizing, cost, and efficiency.

Chapter 4 investigates the drive cycle analysis of the Renault Twizy's drivetrain using the proposed IMPEI. Sizing the drivetrain components using the design criteria proposed in Chapter 2 has been discussed. The efficiency maps of the main drivetrain components have been discussed, followed by the estimation of the Renault Twizy drivetrain fuel economy.

Chapter 5 discusses the commissioned dynamometer used to test machines with varying power ratings and speed ranges throughout this thesis. The main components of the test bench are described. This chapter also studies current handling during regenerative braking operation of high-speed PMSMs in emergency conditions.

Chapter 6 presents the conclusion and future works.

1.9. Contribution of Authors

1.9.1. Journal papers

- T. Payarou, P. Pillay, "Integrated Multipurpose Power Electronics Interface for Electric Vehicles," *IEEE Transactions on Transportation electrification.* Sep. 2022, DOI: 10.1109/TTE.2022.3209098.

- T. Payarou, S. Singh, M. Muthusamy, P. Pillay, "A Methodology for Electric Vehicle Drivetrain Design," *IEEE Transactions on Industrial Electrification.* [Submitted: Sep 2022].

- S. Singh, T. Payarou, M. Boby, M. Ibrahim, F. Bernier, J. M. Lamarre, S. Grenier, P. Pillay, "Cold Spray Additive Manufacturing of a Petal Shaped Surface Permanent Magnet Traction Motor," *IEEE Transactions on Transportation electrification.* [Accepted: Dec. 2022].

   Not related topic:

- T. Payarou, S. Rahimi, K. Kuruvinashetti, P. Pillay and M. Packirisamy, "Detailed Electrochemical Model of Microphotosynthetic Power Cells," *IEEE Transactions on Industry Applications*, vol. 57, no. 2, pp. 1703-1714, March - April 2021, DOI: 10.1109/TIA.2020.3044032.

1.9.2. Conference papers

- T. Payarou, P. Pillay, "A Novel Integrated Multipurpose Power Electronics Interface for Electric Vehicles," *Dep. of Electrical and Computer Engineering*, *Concordia University 6th Annual ECE Graduate Student Research Conference 2022,* Montreal, Canada, 2022.

- T. Payarou, S. Singh, M. Muthusamy, P. Pillay, "Design Criteria for EV Drivetrain," *IECON 2021 - 47th Annual Conference of the IEEE Industrial Electronics Society,* Toronto, Canada Oct. 13 - 16,2021.

- T. Payarou, P. Pillay, "A Novel Multipurpose V2G & G2V Power Electronics Interface for Electric Vehicles," *IEEE Energy Conversion Congress and Exposition (ECCE*), Detroit, Michigan, USA, *2020.*

   Not related topic:

- C. S. Cyusa, T. Payarou, D. Barman, T. Bertenyi, P. Raphals, C. Lai, P. Pillay, " Modeling and Design of a Tubular Linear Generator for Direct-Drive Free-Piston Engine," *IECON 2021 - 47th Annual Conference of the IEEE Industrial Electronics Society,* Toronto, Canada Oct. 13 - 16,2021.

- T. Payarou, P. Pillay, and M. Packirisamy, "Updated Electrochemical Model of Micro Photosynthetic Power Cells," *IEEE Energy Conversion Congress and Exposition (ECCE),* Baltimore, MD, USA, USA, *2019.*

1.9.3. Awards and Achievements

- First place award, *6th Annual ECE Graduate Student Research Conference.* Concordia University   2022

- Concordia University Conference and Exposition Award   2019

- Bourse d'études Réseau Québécois sur l'Énergie intelligente (scholarship)   2020-2021

- Concordia University Conference and Exposition Award   2019

- Concordia International Tuition Award of Excellence   2018-2021

Chapter 2. A Methodology for Electric Vehicle Drivetrain Design

2.1. Introduction

The electrification of transportation made permanent magnet (PM) motors more popular than induction motors [52] and [53]. Also, the requirement of high-speed EMs that can replace and surpass the ICE in terms of efficiency versus speed range requires associated PE converters that can drive the EM through its operating envelope. Designing EMs to meet some requirements is challenging, especially in EV application where volume and weight are the biggest constraints [54] and [55]. For the drive specialists, the focus is on the input and output behaviors in terms of voltage, current, torque, and speed. Internal characteristics of EMs are used for the design of the controller [56]. However, for PMSM design specialists, many aspects are considered before coming up with a final design based on given specifications. Fig. 2-1 shows different design aspects of PMSMs based on their electromagnetic, structural, and thermal considerations. It is a summary of the design steps mentioned in [52], [57] - [62].

As can be seen from Fig. 2-1, determining the final design based on given specifications is a time-consuming process. This results in delaying the other processes that depend on the EM's design process, e.g., designing PEIs. However, designing the PEs without the machine parameters in hand leads to improper sizing of PE devices. Available design steps that enable both the drive and the machine design engineers to be synchronized during the whole drivetrain design process are the subject of this chapter. For given specifications in terms of torque and speed requirements and the available battery voltage, the equations for evaluating the torque-speed envelope of a PMSM as well as its current and speed-voltage limits can be summarized using the equations below.

$$v_q = R_s i_q + p\lambda_q + \omega_s \lambda_d \, , \tag{2.1}$$

$$v_d = R_s i_d + p\lambda_d - \omega_s \lambda_q \, , \tag{2.2}$$

$$\lambda_d = L_d i_d + \lambda_{af} \, , \tag{2.3}$$

$$\lambda_q = L_q i_q \, , \tag{2.4}$$

$$T_e = \frac{3}{2} P\big[\lambda_{af} i_q + (Ld - Lq) i_d i_q\big] \, , \tag{2.5}$$

$$p = \frac{d}{dt} \, , \tag{2.6}$$

14

where v_q and v_d are respectively the q- and d-axes stator voltages, R_s is the stator resistance, λ_q and λ_d are respectively the q- and d-axes flux-linkages, i_q and i_d are respectively the q- and d-axes currents, L_q and L_d are the q- and d-axes inductances, P is the number of pole pairs, p is the derivative operator. λ_{af} is the per-phase magnet flux-linkage and T_e is the electromagnetic torque. By neglecting R_s from equations (2.1) and (2.2) at steady state, we have,

$$v_d = -X_q i_q \,, \tag{2.7}$$

$$v_q = X_d i_d + \omega_s \lambda_{af} \,, \tag{2.8}$$

$$v_d^2 + v_q^2 \leq V_o^2 \,, \tag{2.9}$$

$$i_q^2 + \left[\frac{X_d}{X_q}\right]^2 \left[i_d + \frac{\omega_s \lambda_{af}}{X_d}\right]^2 \leq \left[\frac{V_o}{X_q}\right]^2 \,, \tag{2.10}$$

$$i_d^2 + i_q^2 \leq I_s^2 \,, \tag{2.11}$$

$$X_d = \omega_s L_d \,, \tag{2.12}$$

$$X_q = \omega_s L_q \,, \tag{2.13}$$

$$\omega_s = P\omega_r \,, \tag{2.14}$$

$$V_o = 0.577 m_a V_{dc} \text{ (SVPWM)}, \tag{2.15}$$

$$\lambda_{af} = L_d i_{ch} \,, \tag{2.16}$$

$$\frac{i_q^2}{V_o^2/(\omega_s L_q)^2} + \frac{(i_d + i_{ch})^2}{V_o^2/(\omega_s L_d)^2} \leq 1 \,, \tag{2.17}$$

where X_q, and X_d are respectively the q-axis and d-axis reactances, I_s is the peak rated current of the machine, ω_s is the electrical synchronous speed of the motor, V_o is the maximum available per-phase peak of the voltage fundamental component from the DC link, V_{dc} is the inverter input voltage, m_a is the modulation index, and i_{ch} is the characteristic current. It is the equivalent armature current required to generate λ_{af}. Equations (2.10) and (2.11) represent the voltage and current limits for various speeds in the $i_d - i_q$ plane. The voltage limit equation can be rewritten as in (2.17). From (2.17), since the terminal voltage and machine parameters are assumed constant, it is evident that as ω_s increases to the limit, T_e goes to zero to keep the constraints of current limit, i.e., $T_e \rightarrow 0$, $i_q \rightarrow 0$, (2.18). Therefore, producing power at infinite speed is possible if $i_d \rightarrow -i_{ch}$, and $I_s = i_{ch}$. This leads to the infinite speed criteria at constant power in (2.19).
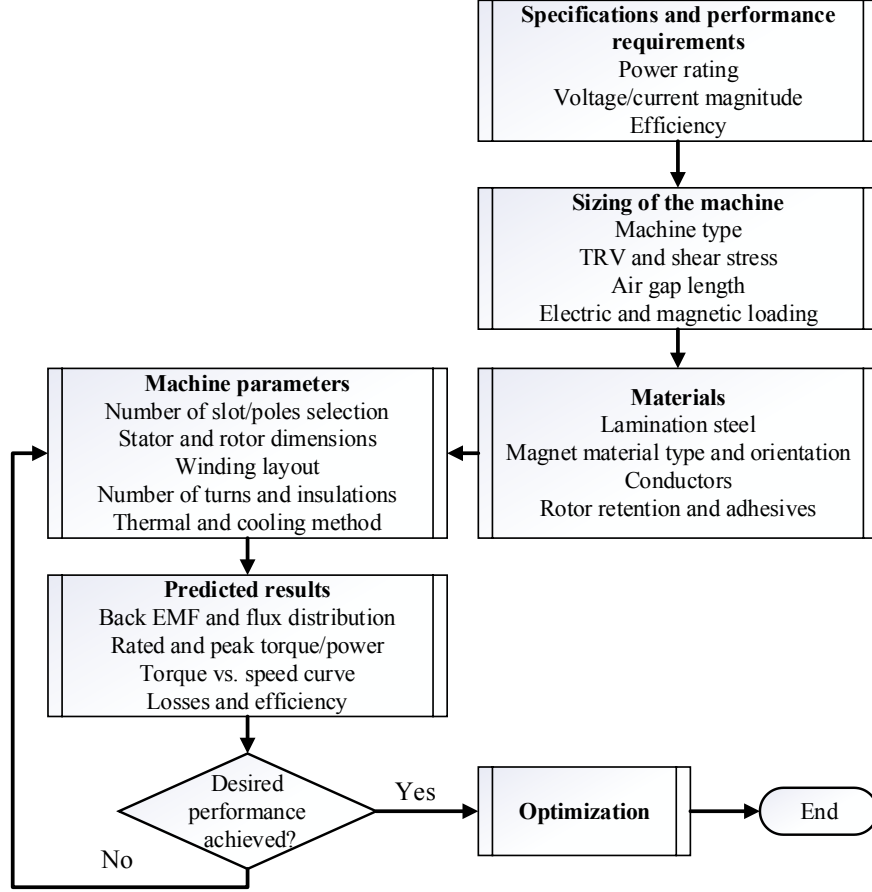
Fig. 2-1. Typical electric machine design approach.

$$(i_d + i_{ch})^2 \leq \frac{V_o^2}{(\omega_s L_d)^2}, \tag{2.18}$$

$$\lambda_{af} = L_d I_s . \tag{2.19}$$

Therefore, to meet some given specifications, the key parameters $V_o, I_s, L_q, L_d,$ and λ_{af} have to be found for solving the above equations. These parameters have to remain unchanged or within acceptable tolerances after all the electromagnetic, thermal, mechanical analyses, and optimizations. Also, these key parameters are the same parameters required by drive engineers for sizing the PEs as well as for the control algorithm design. This approach, therefore, sets the common ground which both groups can work on in parallel to speed up the design and testing processes of the EV drivetrain.

This novel drivetrain design approach sets the design steps based on the drivetrain specifications and investigates the parameter requirements for PMSMs and their associated

power electronic interfaces (PEIs), given the torque-speed envelope and battery specifications. The obtained parameters such as of inductances, magnet flux, number of poles, and topology serve as a reference for machine design engineers as well as drive engineers in their switching frequency selection and devices' rating process. It will enable the estimation of the PEI requirements and speed up the overall drivetrain design, emulation, and testing processes. This chapter is organized as follows; the PMSM model is presented in this section. The proposed analytical process for design parameter requirements of the PMSMs and their associated PEI are investigated in section 2.2. FEA-based verification of designed parameters and their results are shown in sections 2.3 and 2.4. Experimental results and practical validation are discussed in section 2.5. The conclusions are drawn in section 2.6.

2.2. Proposed Analytical Process for the Drivetrain Design

The proposed analytical design process is discussed using the specifications for the 2010 Toyota Prius, which are summarized in Table 2-1 as a benchmark. All calculations and estimations performed by the proposed method are based on these inputs.

Table 2-1. Technical Specifications of 2010 Toyota Prius.

Symbol	Parameter	Value
	Rated output power	60 kW
Motor	Rated torque	207 Nm
(PMSM)	Maximum speed	13500 r/min
	Number of poles	8
DC Bus	Nominal voltage	650 V

Based on the data in Table 2-1, the base speed (ω_{rb}) of the motor is 289.85 rad/s (n_{sb} = 2768 r/min). The corresponding electrical speed (ω_{sb}) is 1159.42 rad/s. The maximum speed (ω_{rmax}) is 1413.72 rad/s.

The proposed synchronized drivetrain design process provides SPMSM and IPMSM data. Since solving equations related to IPMSM is complex, the proposed process is organized so that the IPMSM design steps come after determining feasible SPMSM drivetrain parameters.

2.2.1. Design equations for the SPMSM

SPMSMs are not good candidates for high-speed operations due to mechanical constraints and power factor limitation. However, for the proposed approach, calculating the SPMSM parameters is crucial and facilitates the estimation of the corresponding IMPSM parameters. The following equations provide the input data and are initial parameter estimation steps for designing an

SPMSM associated with its drive inverter that meets the design requirements. It is assumed that a space vector PWM (SVPWM) scheme is used to generate the drive inverter's terminal voltage.

$$V_o = 0.577 \, V_{b,nom} \, m_{max} , \tag{2.20}$$

$$V_{ph,rms} = \frac{V_o}{\sqrt{2}} , \tag{2.21}$$

$$V_{ll,rms} = V_{ph,rms} \, \sqrt{3} , \tag{2.22}$$

$$P_{m,out} = \sqrt{3} V_{ll,rms} \, I_{rms} \, \eta_m \, pf , \tag{2.23}$$

$$I_{rms} = \frac{P_{m,out}}{\sqrt{3} \, V_{ll,rms} \, \eta_m \, pf} , \tag{2.24}$$

where V_o is the peak-phase-fundamental output voltage from the drive, $V_{b,nom}$ is the nominal voltage of the battery, m_{max} is the maximum modulation index, $V_{ph,rms}$ is the phase to neutral RMS voltage available from the drive, $V_{ll,rms}$ is the line to line RMS voltage available from the drive, $P_{m,out}$ is the machine's rated output power, pf is the machine's power factor, η_m is the machine's efficiency, and I_{rms} is the phase RMS current in the machine. The battery nominal voltage is given as $V_{b,nom} = 650 \, V$. The modulation index is limited to the linear region with $m_{max} = 0.95$ to compensate for the deadtime associated loss, voltage drop across the PESs, parasitic impedance, voltage drop across R_s, and filter (if any) voltage drops. The remaining parameters to be determined are, therefore λ_{af}, L_d and L_q. With the assumption that the machine is a SPMSM $L_d = L_q = L_s$, $I_s = \sqrt{2} I_{rms}$, and $I_d = 0$ at rated condition.

$$T_{er} = 1.5 \, P \, I_s \lambda_{af} , \tag{2.25}$$

$$\lambda_{af} = \frac{T_{er}}{1.5 \, P \, I_s} , \tag{2.26}$$

$$L_s = \frac{\lambda_{af}}{I_{ch}} , \tag{2.27}$$

where T_{er} is the rated torque. For the SPMSM, equation (2.17) becomes (2.28), and the base speed can be calculated using (2.29).

$$i_{qmax}^2 + i_{ch}^2 \leq \frac{V_o^2}{(\omega_{sb} L_s)^2} , \tag{2.28}$$

$$\omega_{sb} = \frac{V_o}{L_s} \frac{1}{\sqrt{I_s^2 + I_{ch}^2}} . \tag{2.29}$$

Let $I_{ch} = AI_s$, where A is a constant. A = 1 for $I_{ch} = I_s$, A > 1 for $I_{ch} > I_s$, and A < 1 for $I_{ch} < I_s$. Equation (2.29) becomes,

$$\omega_{sb} = \frac{V_o}{L_s I_s \sqrt{1 + A^2}} = \frac{V_o}{L_s I_s B} \frac{1}{B}, \tag{2.30}$$

where $B = \sqrt{1 + A^2}$. Including (2.25) and (2.26) in (2.27), L_s can be calculate as follows,

$$L_s = \frac{T_{er}}{1.5PI_s I_{ch}}. \tag{2.31}$$

Then, (2.30) becomes,

$$\omega_{sb} = \frac{1.5PV_o}{T_{er}} \frac{1}{B} I_{ch} = \frac{1.5PV_o}{T_{er}} \frac{A}{B} I_s. \tag{2.32}$$

Equation (2.32) can be expanded by adding the equation for I_s as follows,

$$\omega_{sb} = \frac{1.5PV_o}{T_{er}} \frac{A}{B} \left(\frac{\sqrt{2} P_{m,out}}{\sqrt{3} V_{ll,rms} \eta_m} \right) \frac{1}{pf}. \tag{2.33}$$

Equation (2.33) can be simplified as follows,

$$\omega_{sb} = \frac{1.5PV_o}{T_{er}} \frac{A}{B} \frac{C}{pf}. \tag{2.34}$$

where C is a constant. Solving (2.34) for pf, gives

$$pf = \frac{1.5PV_o}{T_{er}} \frac{C}{\omega_{sb}} \frac{A}{B}. \tag{2.35}$$

Equation (2.35) embeds much information. Assuming that the power rating of the machine (speed and torque) and the battery voltage are fixed, as is the case in many designs, then A and B are the only parameters that can be modified to improve the power factor at the rated speed. The selection of the pole numbers does not affect the power factor since there is a torque term in the denominator which is directly proportional to the pole number.

For the special case where $I_{ch} = I_s$, $\omega_{rmax} = \infty$, A = 1, and $B = \sqrt{2}$. The achievable power factor can be calculated using (2.36). At the rated operation, the obtained pf is 72.90%.

$$pf_{(I_{ch}=I_s)} = \frac{1.5pV_o}{\sqrt{2} T_{er}} \frac{C}{\omega_{sb}}. \tag{2.36}$$

For the case where $I_{ch} \neq I_s$ and $\omega_{rmax} \neq \infty$, the achievable power factor can be calculated using (2.37).

$$pf = k\frac{A}{B},$$
(2.37)

where k is the parameter representing all the constant terms in (2.35). In this case, $k = 1.0309$. The calculated drive specifications are summarized in Table 2-2.

Table 2-2. Drive Specifications with SVPWM Technique.

Symbol	Parameter	Unit
η_m (assumed)	97.00	%
V_o	356.30	V
$V_{ph,rms}$	251.14	V
$V_{ll,rms}$	436.37	V
C	81.84	A
$pf_{(I_{ch}=I_s)}$	72.90	%

The effect of the A parameter on the power factor of the machine is illustrated in Fig. 2-2. It can be seen that in terms of pf, the best option is to select I_{ch} to be greater than I_s ($A > 1$). This reduces the drivetrain current requirement and, therefore, the ohmic losses. For this case, having a greater A factor helps achieve higher power factors. In the following discussions, the case A < 1 is ignored.

From equation (2.26), the magnet flux linkage λ_{af} is related to the I_s which is directly proportional to pf. Therefore, improving the pf increases λ_{af}, which in turn increases v_q. Fig. 2-3 illustrates the vector diagram of a SPMSM for two pf conditions. It can be seen that for achieving the exact base speed specifications at a higher pf, $I_{s2} > I_{s1}$. As a result, the $pf = \cos(\phi)$ is improved.

The effect of the A parameter on the constant power speed range (CPSR) is illustrated in Fig. 2-4. The torque-speed and power-speed envelopes at different A factors show that the A factor affects the pf of the machine and the CPSR. As the A parameter increases, the power factor increases, and the CPSR ratio decreases. In the considered case, the CPSR ratio is selected to be at least 4.88. This translates to an A factor of 1.24 and a power factor of about 0.80. The speed at which the power is zero is known as the critical speed (ω_{scri}), which can be calculated from (2.17) by setting $i_q = 0$ and $i_d = i_s$.
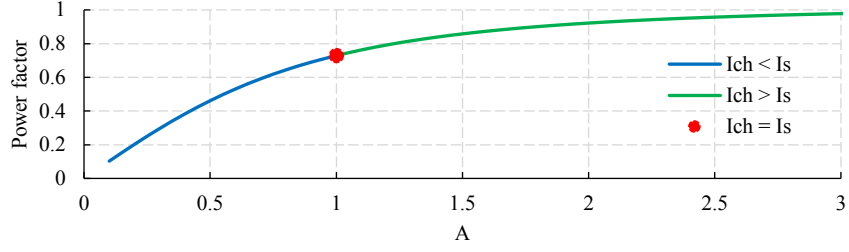
Fig. 2-2. The relationship between A and the power factor
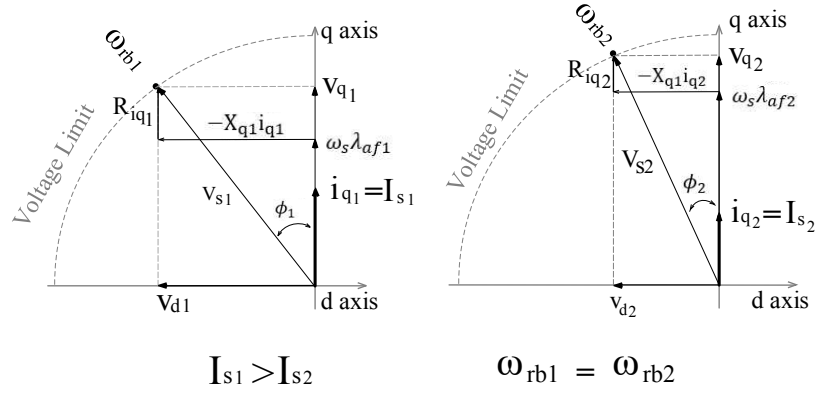
$$I_{s1} > I_{s2} \qquad \omega_{rb1} = \omega_{rb2}$$

Fig. 2-3. Vector diagram of the SPMSM motor
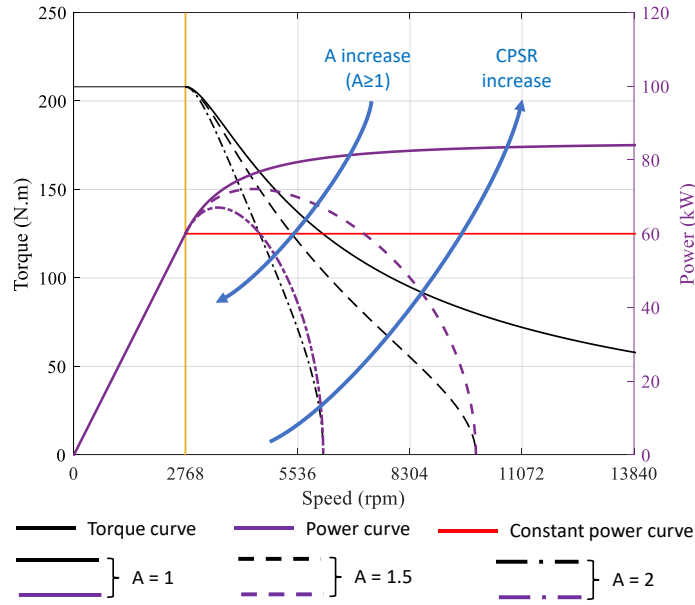
Fig. 2-4. Required power factor for base speed operation

$$i_s + i_{ch} \leq \frac{V_o}{\omega_s L_s}. \tag{2.38}$$

The relationship between ω_{scri} and ω_{sb} is therefore as follows.

$$\frac{\omega_{scri}}{\omega_{sb}} = \frac{B}{A-1}. \tag{2.39}$$

To find the developed power (P_d) at any speed greater than ω_{sb}, the following power equation is derived.

$$P_d = T_e \omega_r = 1.5 \, P \, I_s \lambda_{af} \omega_r = 1.5 \, I_s \lambda_{af} \omega_s \, . \tag{2.40}$$

By deriving I_d from (2.17) and substituting it into (2.11), equation (2.40) can be rewritten as follows,

$$P_d = 1.5 \, \lambda_{af} \sqrt{C_1 \omega_s^2 + \frac{C_2}{\omega_s^2} + C_3} \, , \tag{2.41}$$

where

$$C_1 = \left(1 - \left(\frac{B^2}{2A}\right)^2\right) I_s^2, \; C_2 = -\left(\frac{V_o^2}{2AI_sL_s^2}\right)^2, \; \text{and} \; C_3 = \frac{2B^2 V_o^2}{4A^2 L_s^2} \, .$$

Equation (2.41) can be used to plot the power-speed curve. It can also be used to find ω_{smax} by solving equation (2.42).

$$C_1 \omega_s^4 + C_4 \omega_s^2 + C_2 = 0 \, , \tag{2.42}$$

where $C_4 = C_3 - \left(\frac{P_r}{1.5\lambda_{af}}\right)^2$ and P_r is the rated power of the machine. Solving equation (2.42) provides $\pm \omega_{sb}$ and $\pm \omega_{smax}$.

$$\omega_{sb}^2 = \frac{-C_4 + \sqrt{C_4^2 - 4C_1 C_2}}{2C_1} \, , \tag{2.43}$$

$$\omega_{smax}^2 = \frac{-C_4 - \sqrt{C_4^2 - 4C_1 C_2}}{2C_1} \, . \tag{2.44}$$

2.2.2. Design Equations for the IPMSM

In SPMSM design calculations, the steps were simplified with $L_d = L_q$. However, in IPMSMs, the saliency ratio is not unity, $L_d < L_q$. Solving equations (2.13) and (2.14) for L_d, L_q, and λ_{af} by keeping equation (2.22) in mind for the constant power operation during flux weakening is more complex. The IPMSM's designs that meet the design specifications are derived from the obtained SPMSM parameters using the following equations.

$$S_r = \frac{L_q}{L_d} \, , \tag{2.45}$$

$$I_{cst} = \frac{n_{sb}T_e}{n_{sb_{Sr}}T_{e_{Sr}}}, \tag{2.46}$$

$$A_c = \frac{n_{sb_{Sr}}}{n_{sb}I_{cst}}, \tag{2.47}$$

$$\lambda_{af_{IPMSM}} = \lambda_{af_{SPMSM}}A_cI_{cst}, \tag{2.48}$$

$$L_{d_{IPMSM}} = L_{d_{SPMSN}}A_c, \tag{2.49}$$

$$L_{q_{IPMSM}} = L_{d_{SPMSN}}S_r, \tag{2.50}$$

$$I_{S_{IPMSM}} = I_{S_{SPMSM}}I_{cst}, \tag{2.51}$$

where $\lambda_{af_{IPMSM}}$ is the per-phase magnet flux linkage of the IPMSM to be designed, $\lambda_{af_{SPMSM}}$ is the per-phase magnet flux linkage for the optimized SPMSM, S_r is the saliency ratio, A_c is the attenuation constant, which is $0 < A_c < 1$, I_{cst} is the factor that takes care of the change in the power factor, $I_{cst} > 1$, and $n_{b_{Sr}}$ and $T_{e_{Sr}}$ are respectively the calculated speed and torque values at $S_r \neq 1$. The steps for getting the IPMSM parameters are summarized by the flowchart shown in Fig. 2-6.

2.2.3. Design Flowchart

The flowchart in Fig. 2-6 summarizes the essential steps for determining the SPMSM and IPMSM drivetrain parameters. The algorithm starts with the mechanical and electrical requirements. In this step, the required torque, rated and maximum speed, and available DC bus voltage are obtained (Table 2-1). The pole number of the PMSM is selected at this stage. Table 2-3 shows valuable information on PMSMs used in commercial EVs. It can be a reference for choosing the pole number and the maximum speed.

Table 2-3. Overview of EV motors [63].

Electric vehicles	Year	Number of slots/poles	Maximum speed (r/min)
Jaguar I-Pace	2019	48/8	13000
Tesla Model 3	2017	54/6	18100
Chevy Bolt	2016	72/8	8810
BMW i3	2013	72/12	11400
Nissan Leaf	2010	48/8	10400
Toyota Prius IV	2017	48/8	17000
BMW 225xe	2016	48/8	14000
Audi A3 e-tron	2014	24/16	6000
Chevy Volt Gen 1	2010	72/12	9000
Toyota Prius III	2010	48/8	13500

The desired efficiency at the rated power is then selected, and the A parameter is defined. For the A parameter, an initial value of 1.1 is preferred since the speed in EV motors is limited. A = 1 results in an infinite speed with a low power factor. A loop function that increments the A value at each iteration can be used to obtain the maximum speed. The increment value needs to be selected for the accuracy of the results. An increment value of 0.000001 has been used in this study. The output of this step is summarized in Table 2-4. It can be seen that the required base and maximum speeds are obtained. The power factor at the rated condition has been improved from 0.73 to 0.8. The torque-speed and power-speed envelopes are shown in Fig. 2-5. For the stop condition, the base speed can also be used in the algorithm instead of the maximum speed.

The proposed algorithm provides insight into high power factor PMSM requirements by exploiting equation (2.37). Hence, one can select a power factor and calculate the A parameter from the following equation,

$$A = \sqrt{\frac{pf^2}{k^2 - pf^2}}. \tag{2.52}$$

Using (2.52) to find A based on the specified pf will remove the iteration process. Hence, for a power factor of 0.9, $A = 1.79$. Then, the maximum achievable speed is 2211.50 rad/s instead of 5654.90 rad/s at $pf = 0.8$. Choosing the power factor is, therefore, a tradeoff.

Table 2-4. SPMSM Drive Specifications for ω_{smax}.

Symbol	Desired	Calculated	Unit
A	-	1.23	-
B	-	1.59	-
C	-	115.74	A
k	-	1.03	-
pf	-	80.02	%
$I_s = I_{s_{SPMSM}}$	-	144.69	A
I_{ch}	-	177.96	A
$\lambda_{af} = \lambda_{af_{SPMSM}}$	-	0.24	Wb-turn
$L_s = L_{d_{SPMSN}}$	-	1.34	mH
C_1	-	-917.95	-
C_2	-	$-3.95x10^{16}$	-
C_3	-	$5.87x10^{10}$	-
C_4	-	$3.06x10^{10}$	-
ω_{sb}	1159.40	1159.40	rad/s
ω_{smax}	5654.90	5654.90	rad/s
ω_{scri}	-	7954.60	rad/s
T_{er}	207.00	207.00	Nm
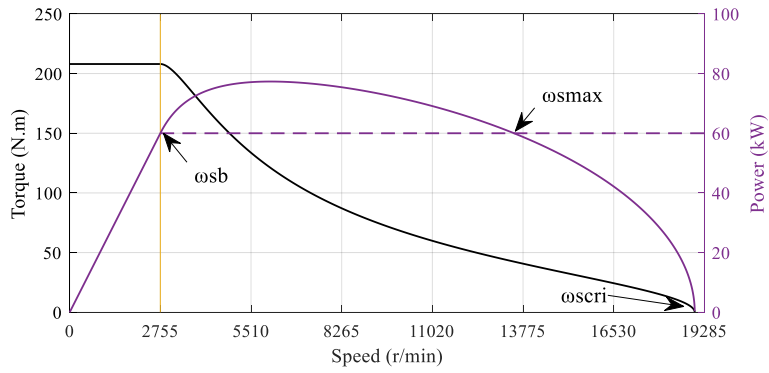
Fig. 2-5. Estimated toque-speed and power speed operating envelopes of 2010 Toyota Prius drivetrain SPMSM.
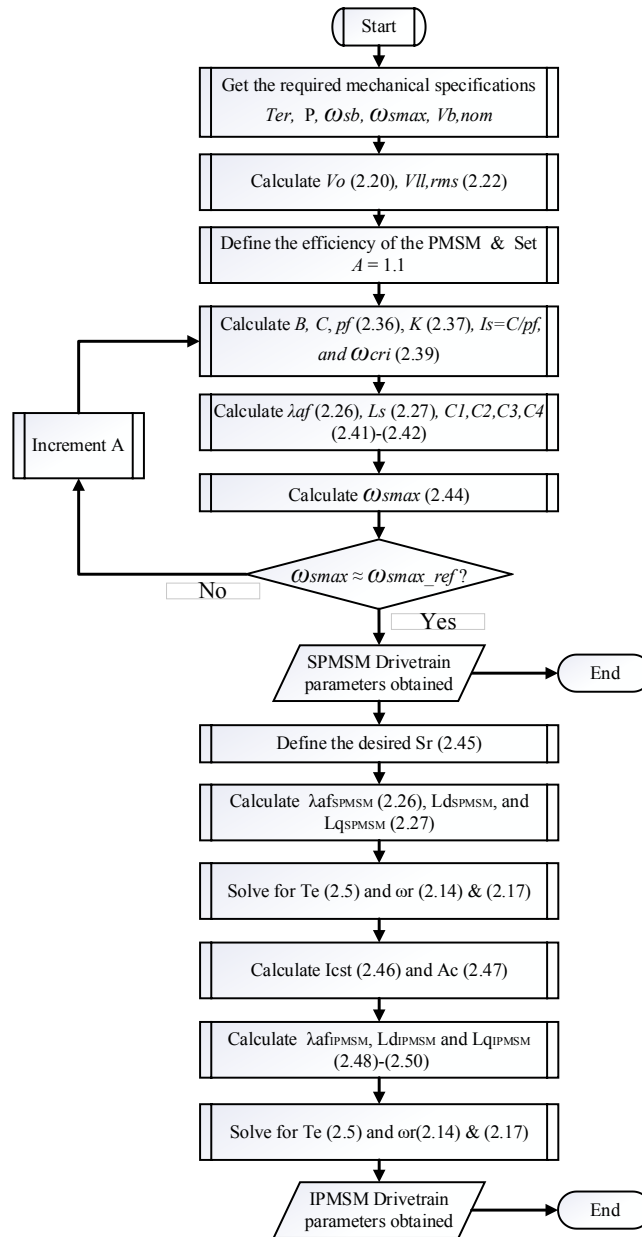
Fig. 2-6. Parameter calculation flowchart for SPMSM and IPMSM (Step I).

The equivalent IPMSM parameters for the rated power operation are obtained directly from the SPMSM parameters, as illustrated by the flowchart in Fig. 2-6. These steps, as proposed, don't require iterations. It starts by selecting S_r and calculating the resultant torque and base speed. The currents I_{ch} and I_s are taken from the SPMSM data (Table 2-4). The base speed in r/min (n_{sb}) is obtained from ω_{sb}. The possible parameters for the 2010 Toyota Prius motor are summarized in Table 2-5. It can be seen that the base speed and the torque values match the design requirements. Same torque and base speed values have been obtained for both SPMSM and IPMSM designs. The maximum speed of the SPMSM has been increased by $1/A_c$. Therefore, the CPSR ratio of the IPMSM compared with the one of the SPMSM has increased from 4.88 to 7. The current limit circle and voltage limit ellipses are illustrated in Fig. 2-7. Also, the power-speed and torque-speed curves are given in Fig. 2-8. This provides valuable insight about the control design and testing. The drive inverter can be designed and sized using the information in Table 2-2. The motor's basic design can be obtained by matching the data in Table 2-5. Optimization can be performed afterward. In addition, the emulation as proposed in [64] can be used to test the drive inverter and the controller prior to prototyping the motor. Hence, this way of systematically estimating the drivetrain parameters enables the EV drivetrain components to be designed and tested in parallel.

Table 2-5. IPMSM Drive Specifications.

Symbol	Desired	Calculated	Unit
S_r	2.37	2.37	-
$n_{sb_{Sr}}$	-	1955.1	r/min
$T_{e_{Sr}}$	-	277.75	Nm
I_{cst}	-	1.05	-
A_c	-	0.70	-
$\lambda_{af_{IPMSM}}$	-	0.17	Wb-turn
$L_{d_{IPMSM}}$	-	897.13	µH
$L_{q_{IPMSM}}$	-	2126.20	µH
$T_{er_{IPMSM}}$	207	206.97	Nm
$n_{sb_{Sr_{IPMSM}}}$	2767.86	2768.00	r/min
$I_{s_{IPMSM}}$	-	152.65	A

2.3. IPMSM Base Design Through FEA and Parameters Validation

In this section, an IPMSM is designed using the parameters obtained in section II. Instead of running several trial and error cases to obtain the required torque-speed envelope as done conventionally, here, the process is to match the required characteristic current, d-axis inductance, q-axis inductance, and magnet flux linkage. Fig. 2-9 shows a flowchart that can be
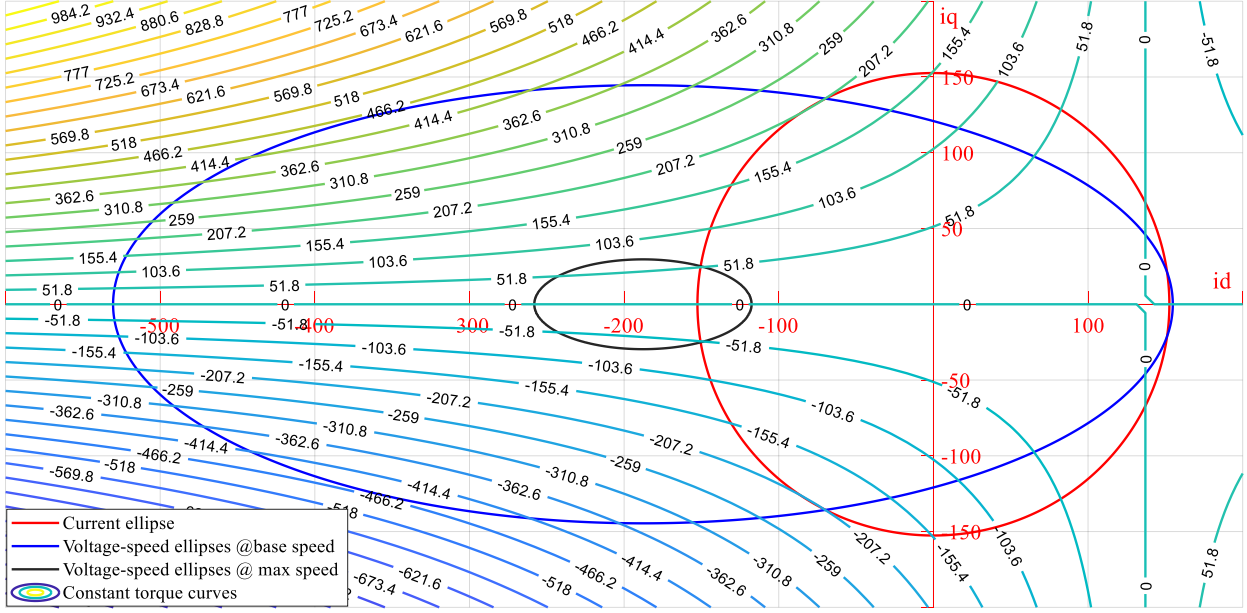
Fig. 2-7. Voltage-speed ellipses for nb and $nmax$, current limit ellipse, and constant torque curves for the designed IPMSM.
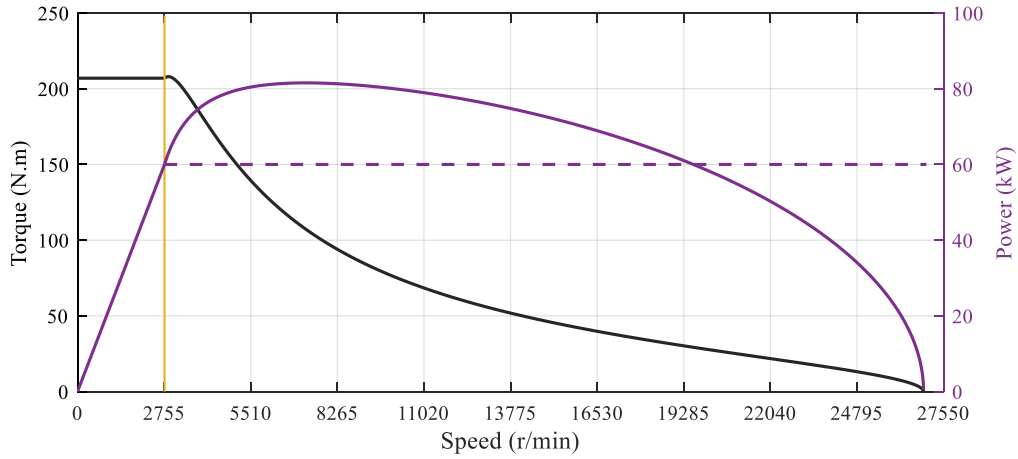
Fig. 2-8. Analytical toque-speed and power speed operating envelopes of 2010 Toyota Prius drivetrain IPMSM.

used to match the parameters via a machine design software. The flowchart uses information embedded in equations (2.34) - (2.39) to match the parameters obtained from step I.

$$P_c = \frac{l_m}{g C_\varphi}, \tag{2.53}$$

$$\lambda_{af} = \frac{N^2}{\Re} I, \tag{2.54}$$

$$L = \frac{\lambda}{I} = \frac{N^2}{\Re}, \tag{2.55}$$

$$\Re = \frac{l}{\mu A}, \tag{2.56}$$
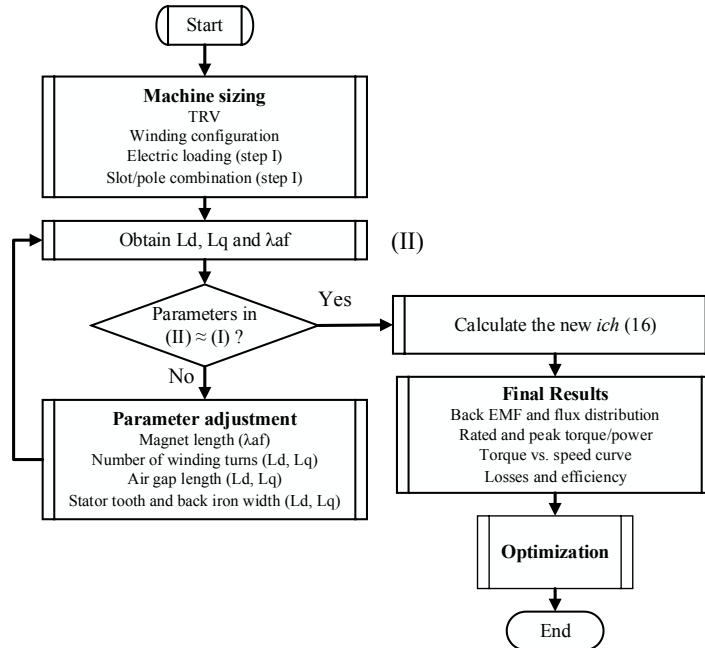
Fig. 2-9. Typical flowchart to match the parameters obtained in step I (Step II).

| (a) | (b) |
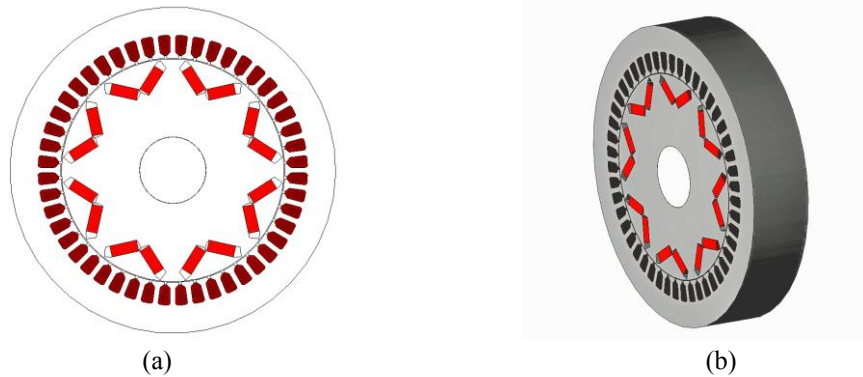
Fig. 2-10. Designed 2010 Toyota Prius motor: (a) 2-D view, (b) Isometric view.
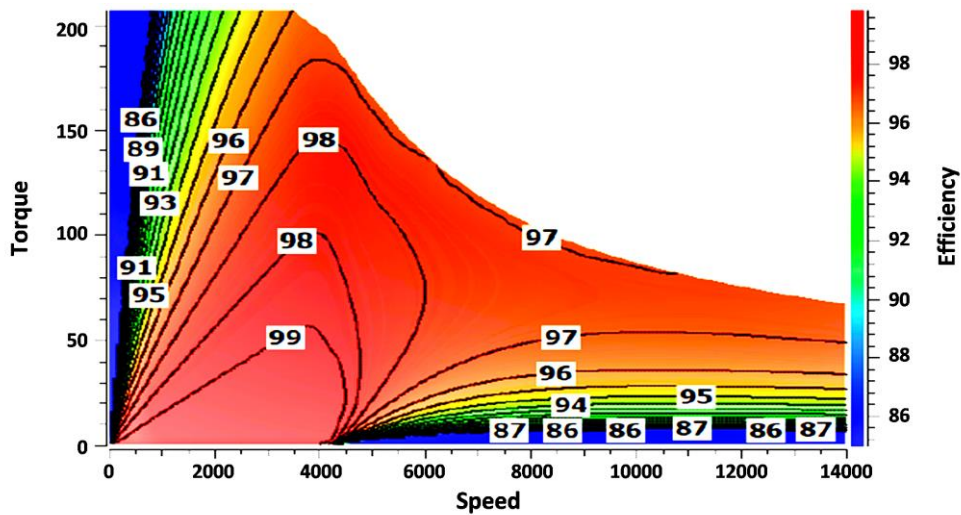
Fig. 2-11. Torque-speed and efficiency maps.

$$w_{tb} = \frac{\varphi_g}{N_{sm}B_{max}k_{st}L}, \tag{2.57}$$

$$w_{bi} = \frac{\varphi_g}{2B_{max}k_{st}L}, \tag{2.58}$$

where P_c is the permeance coefficient, l_m is the magnet length, g is the air gap length, C_φ is the flux concentration factor, $\mathfrak{R}$ is the reluctance, N is the number of turns, φ_g is the air gap flux, B_{max} is the maximum flux density, k_{st} is the lamination stacking factor, w_{tb} is the stator tooth width, w_{bi} is the back iron width, l is the flux path length, and μ is the permeability of the material.

A 2010 Toyota Prius motor is simulated using an FEA software [65]. Fig. 2-10 shows the isometric view of the designed IPMSM. The information obtained from step 1 (current, voltage, and pole number) is used as a drive input to JMAG, and the flowchart in Fig. 2-9 is used to tune the machine parameters to match the precalculated values of λ_{af}, L_d, and L_q. The obtained parameters from JMAG and the estimated parameters are compared in Table 2-6. It can be seen that the parameters match closely, and the required rated torque and base speed are obtained. Perfect matching of all parameters is not required since terms in (2.53) - (2.58) are interrelated. The torque-speed and efficiency maps of the designed motor are illustrated in Fig. 2-11. As can be seen, the designed PMSMs can deliver the rated torque of 207 Nm at 2800 r/min during motoring operation and can reach 13400 r/min as per the requirements. These results are obtained by simply matching the analytically calculated parameters without any optimization. Therefore, the design can be optimized afterward based on specific requirements. However, the optimized parameters should not deviate too much from the ones obtained in Table 2-5.

Table 2-6. Parameter Comparison.

Symbol	Calculated	Designed	Unit
$\lambda_{af_{IPMSM}}$	0.17	0.17	Wb-turn
$L_{d_{IPMSM}}$	0.897	0.898	mH
$L_{q_{IPMSM}}$	2.126	2.227	mH
$T_{er_{IPMSM}}$	206.97	206.82	Nm
$n_{sb_{Sr_{IPMSM}}}$	2768	3080	r/min
$I_{S_{IPMSM}}$	152.65	159.81	A

2.4. A Parameter Validation through a Design Case A = 1 using JMAG

2.4.1. Validation using Analytical and FEA Designs

A case study for A = 1 has been investigated in this section to validate the drivetrain design process. The base speed (n_b) is $3400 \ r/min$, the rated torque is (T_e) is $20 \ Nm$, and the maximum speed is (n_{max}) is $10000 \ r/min$. The nominal battery voltage of the car is 96 V. The design steps of the proposed approach as illustrated in the previous sections have been used. Table 2-7 summarizes the drive specifications. The outputs from design step I (analytical calculations) and design step II (parameter matching using FEA) for SPMSM and IPMSM are summarized in Table 2-8 and Table 2-9, respectively. The later tables show that the parameters are feasible and can be closely matched using JMAG FEA software. The voltage and current limit circles for the SPMSM are shown in Fig. 2-12(a). The corresponding torque-speed and power-speed curves are shown in Fig. 2-12(b). For the IPMSM, the voltage limit ellipse and the current limit circle are shown in Fig. 2-13(a), and the corresponding torque-speed and power-speed curves are shown in Fig. 2-13(b).

Table 2-7. Drive Specifications with SPWM Technique.

Parameter	Value	Unit
η_m (assumed)	0.95	
V_o	43.20	V
$V_{ph,rms}$	30.55	V
$V_{ll,rms}$	52.91	V
$P_{m,out}$	7.12	kW
pf	0.74	
I_{rms}	110.52	A
T_e	20.1	Nm
n_b	3402	r/min

Table 2-8. Comparison for SPMSM.

	Analytical (Step I)	Designed (Step II)
I_{ch} [A]	156.30	156.27
λ_{af} [Wb-turn]	0.0214	0.0207
L_d [mH]	0.137	0.132
L_q [mH]	0.137	0.132

Table 2-9. TABLE Design parameters Comparison for IPMSM (Sr = 1.83).

	Analytical (Step I)	Designed (Step II)
I_{ch} [A]	161.13	162.49
λ_{af} [Wb-turn]	0.017	0.019
L_d [mH]	0.106	0.114
L_q [mH]	0.193	0.191
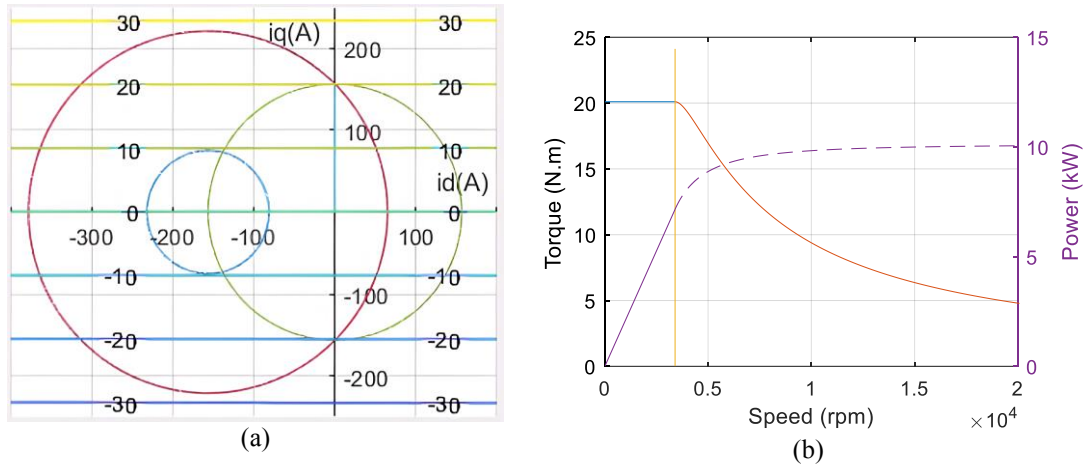
Fig. 2-12. SPMSM, (a) voltage-speed circles for n_b and n_{max} and current limit circle, (b) torque-speed and power-speed curves.
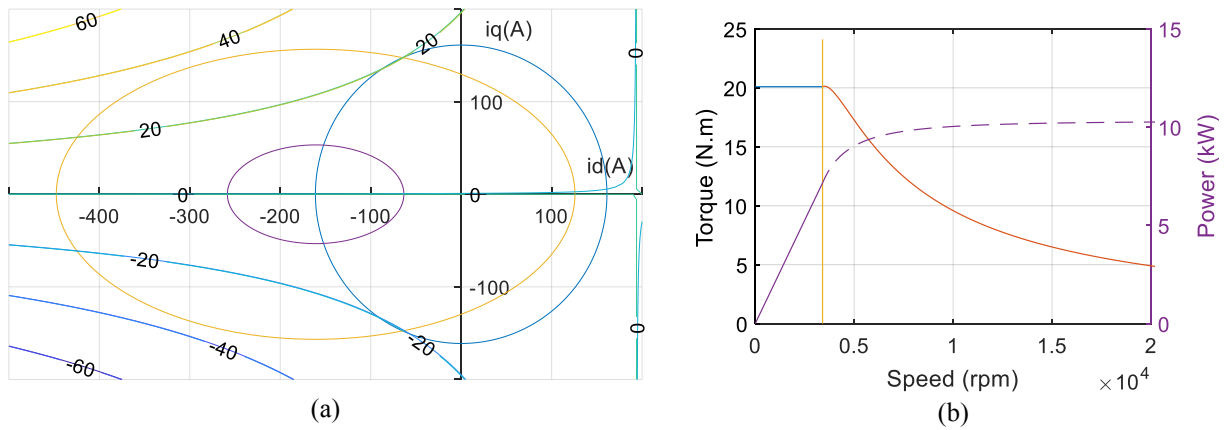
Fig. 2-13. IPMSM, (a) voltage-speed ellipses for n_b and n_{max} and current limit circle, (b) torque-speed and power-speed curves (S_r=1.83).

Designed SPMSM and IPMSM motors using JMAG software are shown in Fig. 2-14 and Fig. 2-15, respectively. The obtained characteristics meet the requirements in terms of rated torque and base speed. It can be seen that the toque-speed and power-speed curves obtained analytically and via the FEA software are perfectly matching. Fig. 2-14(c) and Fig. 2-15(c) show that the power after the base speed is not dropping. In fact, it increases because of the increased power factor.

2.4.2. Drive Cycle Validation

The IPMSM parameters obtained from JMAG and summarized in Table IV are used in MATLAB Simulink to simulate the whole drivetrain (designed IPMSM and its associated drive inverter) and its operating modes. For control purposes, the decoupled speed and torque control method proposed in [66] for IPMSM drives is used. The remaining parameters are summarized
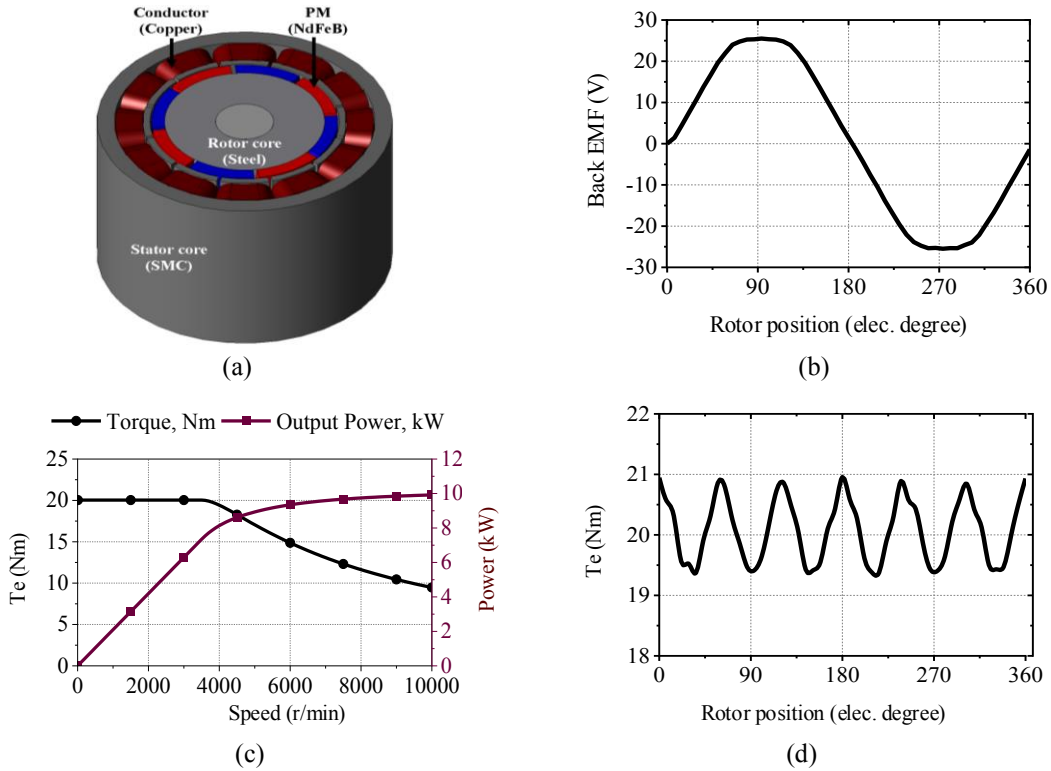
Fig. 2-14. SPMSM, (a) Isometric view, (b) back EMF, (c) torque-speed, and power-speed curves, (d) electromagnetic torque.
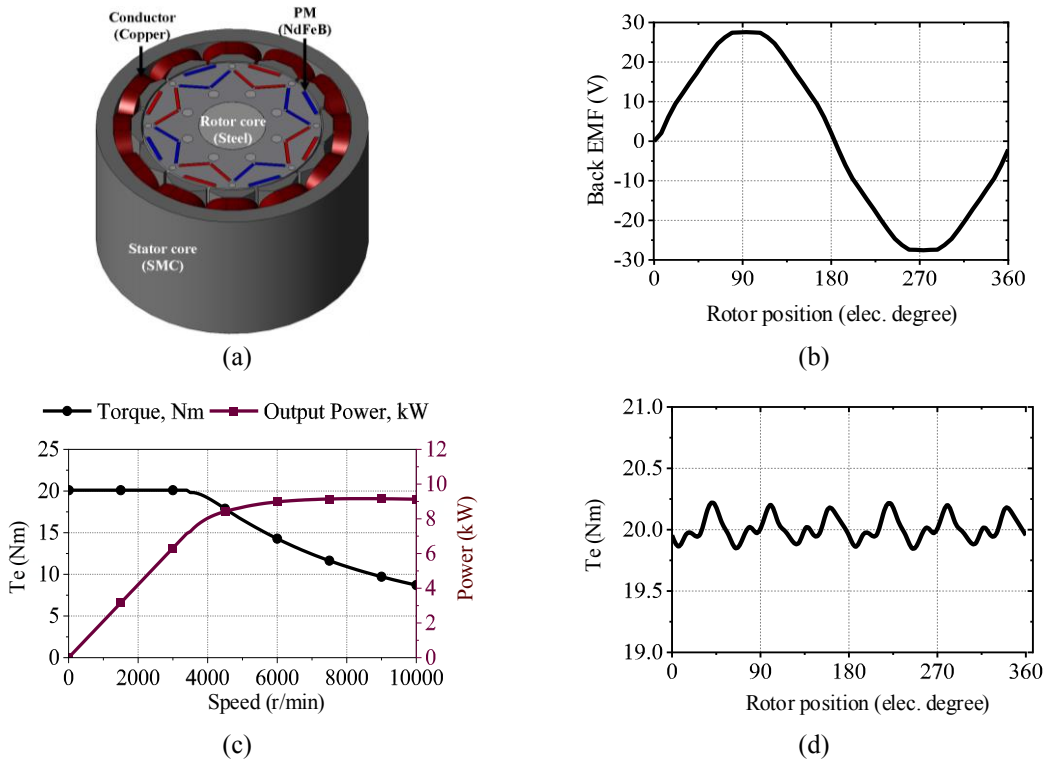
Fig. 2-15. IPMSM, (a) Isometric view, (b) back EMF, (c) torque-speed, power-speed curves, and (d) electromagnetic torque.

32
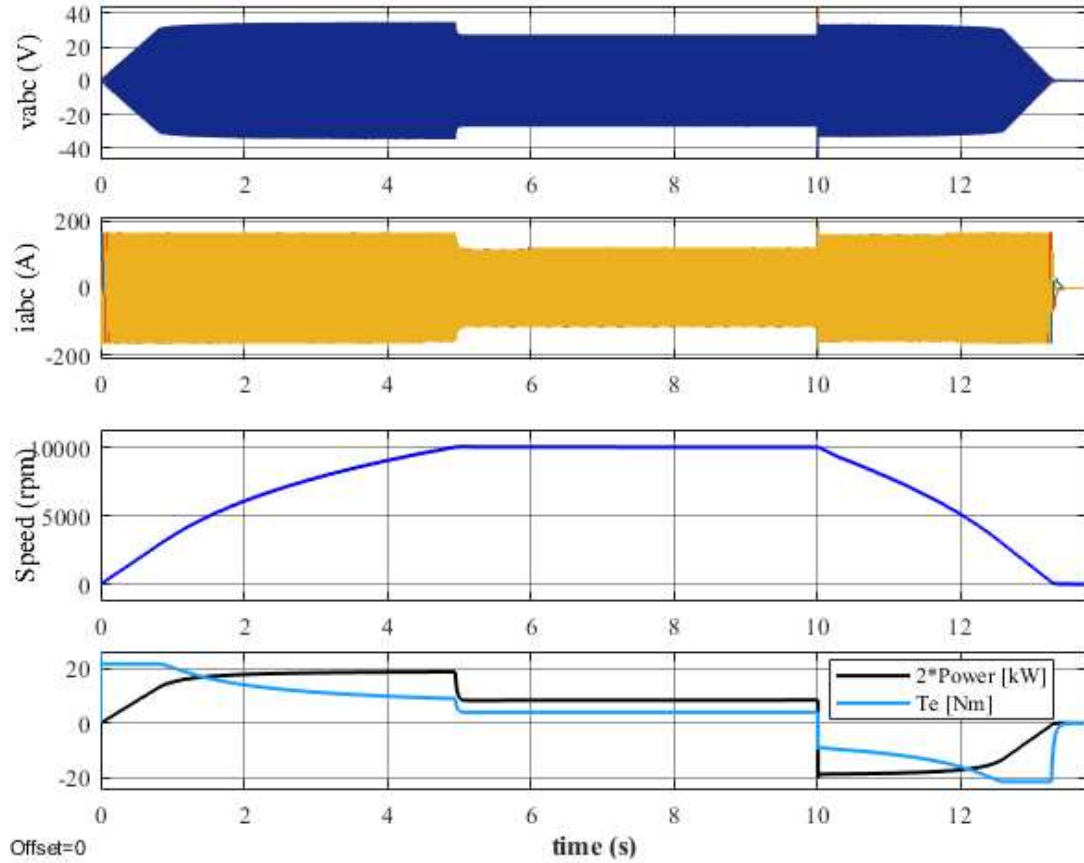
Fig. 2-16. Designed EV drive cycle.

in Table 2-10. Simulation results are shown in Fig. 2-16. It can be seen that the designed IPMSM can be accelerated up to 10000 r/min within the torque-speed envelope with the well-known field-oriented control (FOC) algorithm in the constant torque and power regions. The regenerative braking results show that the designed machine has the same torque-speed characteristics in the generating mode. These results validate once more the parameters obtained analytically (Step I) and through JMAG (Step II).

Table 2-10. Other Parameters Used in the Simulation.

Parameters	Description	Designed (Step II)
R_s [Ω]	Stator resistance	0.004
J [$\mathbf{kg.\,m^2}$]	Inertia	0.05
B [Nms/rad]	Friction coefficient	0.001

2.5. Practical Validation of the Proposed Method

In this section, the proposed methodology is applied to calculate the parameters of an 8 hp SPMSM and an IPMSM designed to have identical characteristics. Fig. 2-17(a) and Fig. 2-17(c) show the rotors of the SPMSM and IPMSM, respectively. Fig. 2-17(b) shows the stator used for both rotors. The specifications of the PMSMs are summarized in Table 2-11.

Table 2-11. Technical Specifications of the SPMSM and IPMSM.

	Parameter	Value
Motor (PMSM)	Rated output power	6 kW
	Rated speed	1300 r/min
	Rated torque	44 Nm
	Number of poles	4
DC Bus	Nominal voltage	300 V

To validate the applicability of the proposed method for estimating the IPMSM parameters from the corresponding SPMSM, the SPMSM has been tested to obtain its parameters; L_d, L_q, R_s, and λ_{af} (Table VIII). The obtained line-to-line back electromotive force (Emf) is 192.5 V and the stator resistance (R_s) is 0.37 Ω. Based on [67], the $V_{ll,rms}$ should be close to the Emf for unity power factor operation. Hence, the parameters $V_o = 157.87\,V$, $V_{ll,rms} = 193.34\,V$, $C = 25.34$ A, and $k = 1$ are obtained using SVPWM technique with a modulation index of 0.91. Since the calculations are based on an ideal SPMSM without losses, the efficiency is assumed 100% at the rated condition. The A parameter is calculated using (2.52). The remaining parameters are calculated using the chart in Fig. 2-6. and listed in Table VIII. The experimental results have been taken, using the setup in Fig. 2-18, at zero speed (locked rotor) and at several other points by controlling the speed of the dynamometer and varying I_d and I_q of the PMSM to operate on the current and voltage limit using [68]. It can be seen from Table 2-12 and Fig. 2-19 that the calculations and the experimental data obtained from the SPMSM match.

Parameters for the equivalent IPMSM have been calculated by following the proposed flowchart in Fig. 2-6. A saliency ratio $S_r = 3.78$, obtained experimentally, has been used. The calculated and experimental parameters are summarized in Table 2-13. Here, a mismatch between the estimated and the practical parameters L_d, L_q, and λ_{af} has been observed. Since the stator is kept the same, this mismatch is due to the IPMSM rotor manufacturing constraints and tolerances. The obtained torque-speed curves are shown in Fig. 2-20. The rated torque was practically obtained at speed current values however, a voltage boost is required to match the

(a)   (b)   (c)
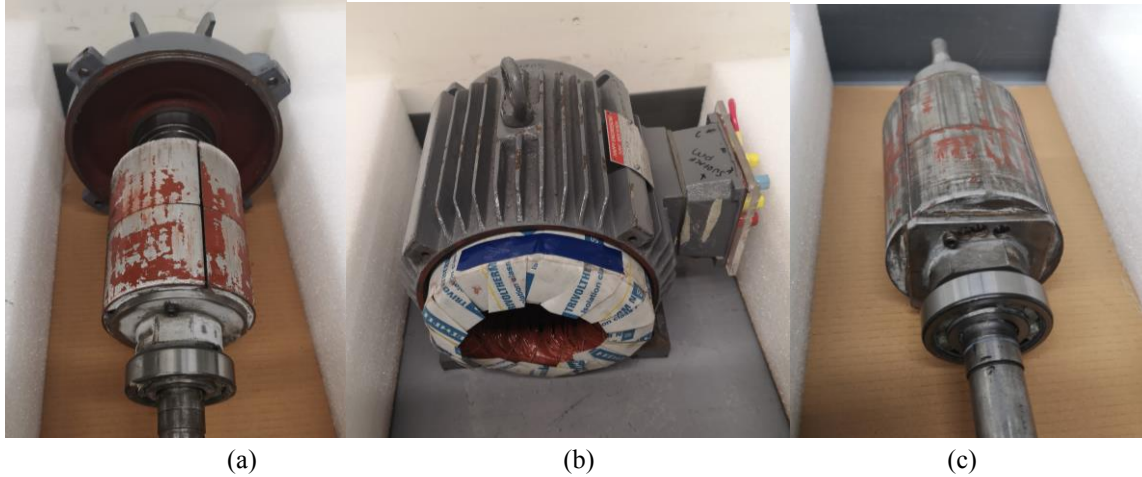
Fig. 2-17. Tested PMSM motors: (a) SPMSM rotor, (b) IPMSM rotor, and (c) common stator.
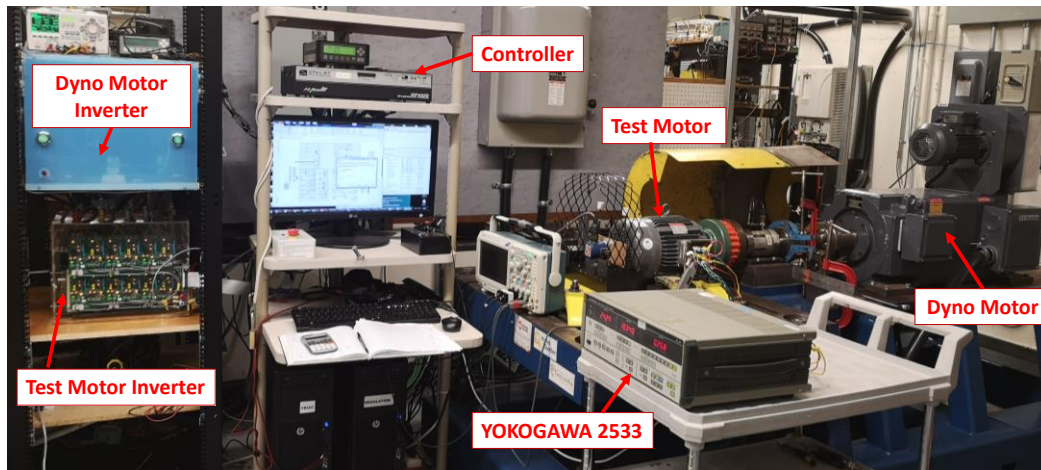
Fig. 2-18. Experimental setup.

base speed. These practical constraints should be considered by adding some margins around the desired base speed and rated torque.

Table 2-12. SPMSM Drivetrain Parameters.

Symbol	Desired	Calculated	Measured	Unit
A	-	15.80	-	-
B	-	15.83	-	-
$I_{s_{SPMSM}}$	-	25.38	25.17	A
$\lambda_{af_{SPMSM}}$	-	0.58	0.58	Wb-turn
$L_{d_{SPMSN}}$	-	1.4	1.54	mH
C_1	-	$-3.99x10^4$	-	-
C_2	-	$-2.22x10^{14}$	-	-
C_3	-	$6.01x10^9$	-	-
C_4	-	$5.96x10^9$	-	-
ω_{sb}	272.13	272.13	272.27	rad/s
ω_{scri}	-	291.10	-	rad/s
T_{er}	44.00	44.10	44.0	Nm

35
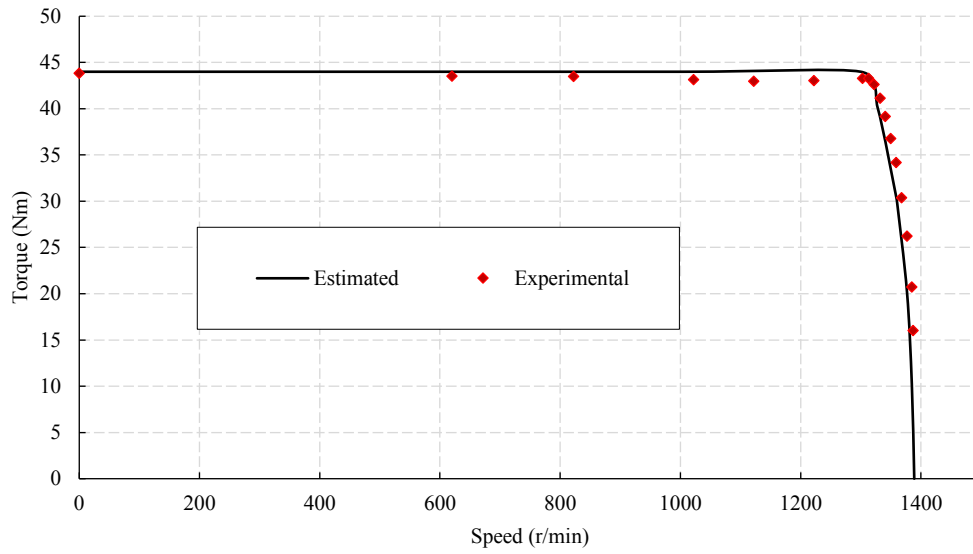
Fig. 2-19. Results comparison for the SPMSM.
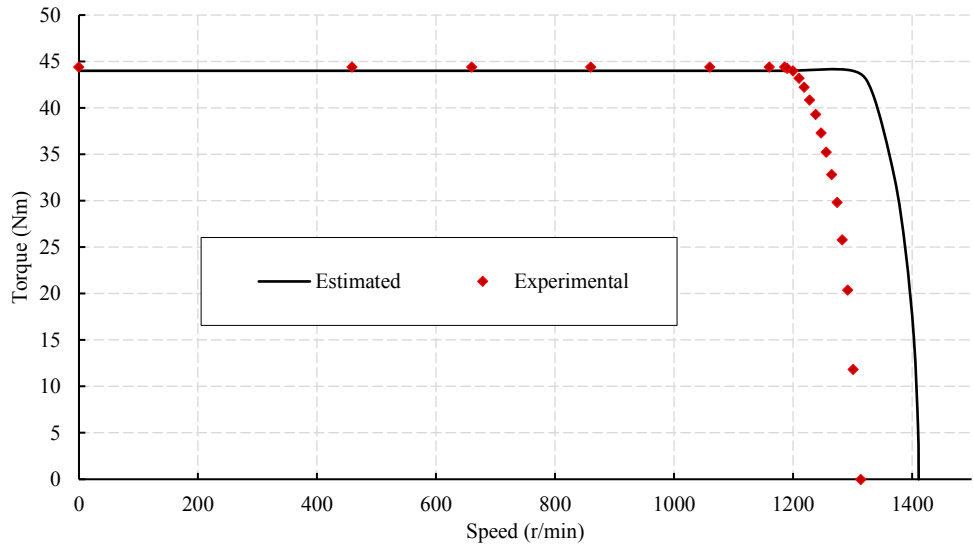
Fig. 2-20. Results comparison for the IPMSM.

Table 2-13. IPMSM Drive Specifications.

Symbol	Desired	Calculated	Measured	Unit
$n_{sb_{Sr}}$	-	1276.8	-	r/min
$T_{e_{Sr}}$	-	44.68	-	Nm
I_{cst}	-	1.002	-	-
A_c	-	0.98	-	-
$\lambda_{af_{IPMSM}}$	-	0.57	0.62	Wb-turn
$L_{d_{IPMSM}}$	-	1.4	2.02	mH
$L_{q_{IPMSM}}$	-	5.2	7.56	mH
$T_{er_{IPMSM}}$	44	44.0	44.4	Nm
$n_{sb_{Sr_{IPMSM}}}$	1300	1300.1	1186	r/min
$I_{s_{IPMSM}}$	-	25.42	23.5	A

2.6. Summary

This chapter has proposed a new step-by-step design method for EV drivetrain design and testing, considering the PMSM and its drive inverter specifications. From the torque-speed curve and battery nominal voltage information, feasible parameters were obtained analytically. A new set of equations have been developed in this chapter for calculating IPMSM parameters from feasible SPMSM parameters. Estimating the parameters beforehand was found to be crucial since it provides both drive and machine designers the ability to foresee the feasibility of the specifications and their effects on the rating of the drive system. Also, this step provides feasible machine parameters; voltage and current which are the input to FEA software and emulating setups. A case study based on a 2010 Toyota Prius motor validated this method for its ability to estimate feasible parameters that can be matched using FEA software. The obtained experimental results validated the ability of the proposed method to estimate IPMSM parameters from a given SPMSM. Therefore, for design, using the FEA software, and practical testing of the drivetrain point of view, it can be concluded that the proposed method has the ability to speed up the EV drivetrain design, emulation, and testing by providing initial guidelines allowing machines and drive specialists to work in parallel on the drivetrain components design.

Chapter 3. A Novel Integrated Multipurpose Power Electronics Interface for EVs

3.1. Introduction

A novel integrated multipurpose power electronics interface (IMPEI) for the new generation of plug-in electric vehicles (PEVs) and plug-in hybrid electric vehicles (PHEVs) is proposed in this chapter. The design of the IMPEI, comparison of the IMPEI with existing topologies, and validation of the modes of operation is provided. The IMPEI is a reconfigurable power electronics interface (PEI) that integrates the onboard charger with the drive inverter allowing the same interface to be used for various modes of operation such as propulsion and regenerative braking as well as vehicle-to-grid (V2G) and grid-to-vehicle (G2V) operations with grid flexibility. For each mode of operation, the IMPEI is reconfigured into a previously existing power converter topology. The principles of operation and coordination of various modes of operation of the IMPEI are explained in this chapter. Based on component count, operating modes, and control complexity, a comparison of the IMPEI and recently proposed integrated PEIs (IPEIs) is provided. Specifications of BMW i3 are used as the benchmark for comparing size, cost, and efficiency. This chapter discusses and validates experimental results.

3.2. The novel Integrated Multipurpose Power Electronics Interface

The detailed circuit of the proposed IMPEI is shown in Fig. 3-1(a). The originality of the proposed topology is its ability to use only one integrated interface to perform all tasks (V2G, G2V, propulsion, and regenerative braking). The IMPEI is an interface consisting of the multipurpose PEI (MPEI) and the filter. The IMPEI consists of nine power electronic switches (switches $s1 - s6$ and $s1' - s3'$), and the filter consists of three capacitors ($C1$, $C2$, and Co), two contactors ($K1$ and $K2$), and an inductor (Lo). The IMPEI can be used in BEV drivetrains, Fig. 3-1(b) as well as in PHEV drivetrains, Fig. 3-1(c). It is also a reconfigurable interface that can be modularized. For instance, the IMPEI's nine switches can be easily packed and used as a single power module to implement the IMPEI.

3.3. Operating Modes

3.3.1. BEV Operation of the IMPEI

The equivalent PEIs for each mode of operation, as illustrated in Table 3-1, are shown in Fig. 3-2. To simplify the equivalent PEIs, continuously ON switches are represented by a short,
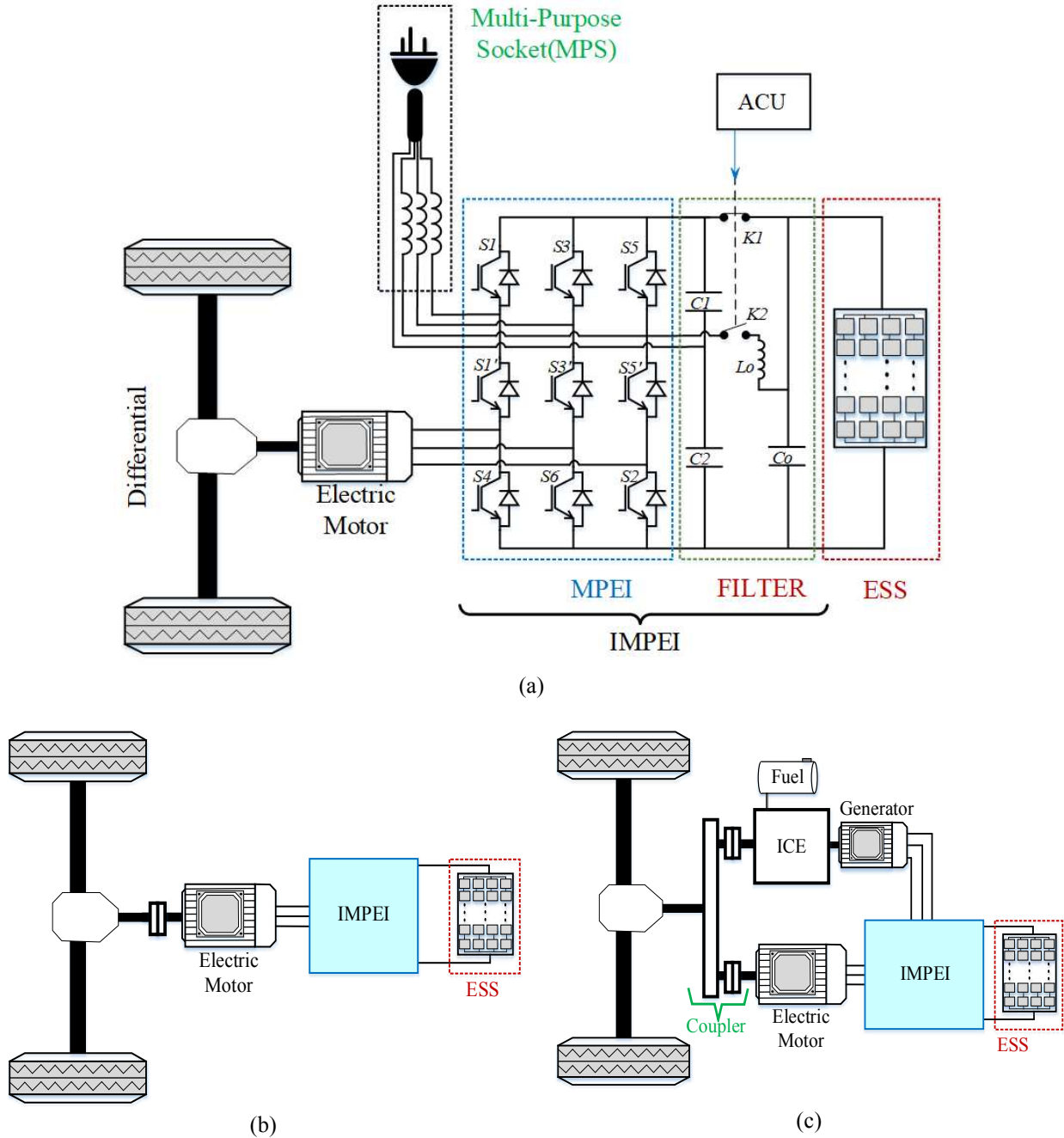
Fig. 3-1: (a) Proposed integrated multipurpose power electronics interface (IMPEI), (b) IMPEI-based BEV, (c) IMPEI-based PHEV.

and the ones that are continuously OFF are omitted. Fig. 3-2(a) illustrates the equivalent PEI during the propulsion and regenerative braking modes. This well-known equivalent PEI is obtained by keeping S1, S3, and S5 continuously ON and controlling the remaining switches. Field-oriented control (FOC) as presented in [69] and [12] can be used to generate the PWM signals.

Table 3-1: State of Switches during each operation mode.

Switches	Operating Modes				
	Single-Phase			DC	Three-Phase
	Propulsion and Regenerative Braking	*V2G-G2V*	*V2G-G2V*	*V2G-G2V*	*V2G-G2V*
S1	ON	PWM	PWM	PWM	PWM
S3	ON	PWM	OFF	PWM	PWM
S5	ON	PWM	PWM	PWM	PWM
S1'	PWM	PWM	PWM	PWM	PWM
S3'	PWM	PWM	OFF	PWM	PWM
S5'	PWM	PWM	PWM	PWM	PWM
S2	PWM	ON	ON	ON	ON
S6	PWM	ON	OFF	ON	ON
S4	PWM	ON	ON	ON	ON
K1	ON	OFF	OFF	ON	ON
K2	ON/OFF	ON	ON	OFF	OFF
Figure	Fig. 3-2(a)	Fig. 3-2(b)		Fig. 3-2(c)	Fig. 3-2(d)

Fig. 3-2(b) shows two equivalent configurations of the MPEI during single-phase G2V and V2G: the full-bridge active front end converter (AFEC) based bi-directional AC-DC converter on the left (Fig. 3-2(b1)) and the half-bridge AFEC based bi-directional AC-DC converter on the right (Fig. 3-2(b2)). Both of them can also be configured to operate as single-stage or two-stage AC-DC converters. The equivalent configurations obtained with IMPEI during single-phase V2G and G2V are well-known in terms of their applications and their control, [70] and [71]. The
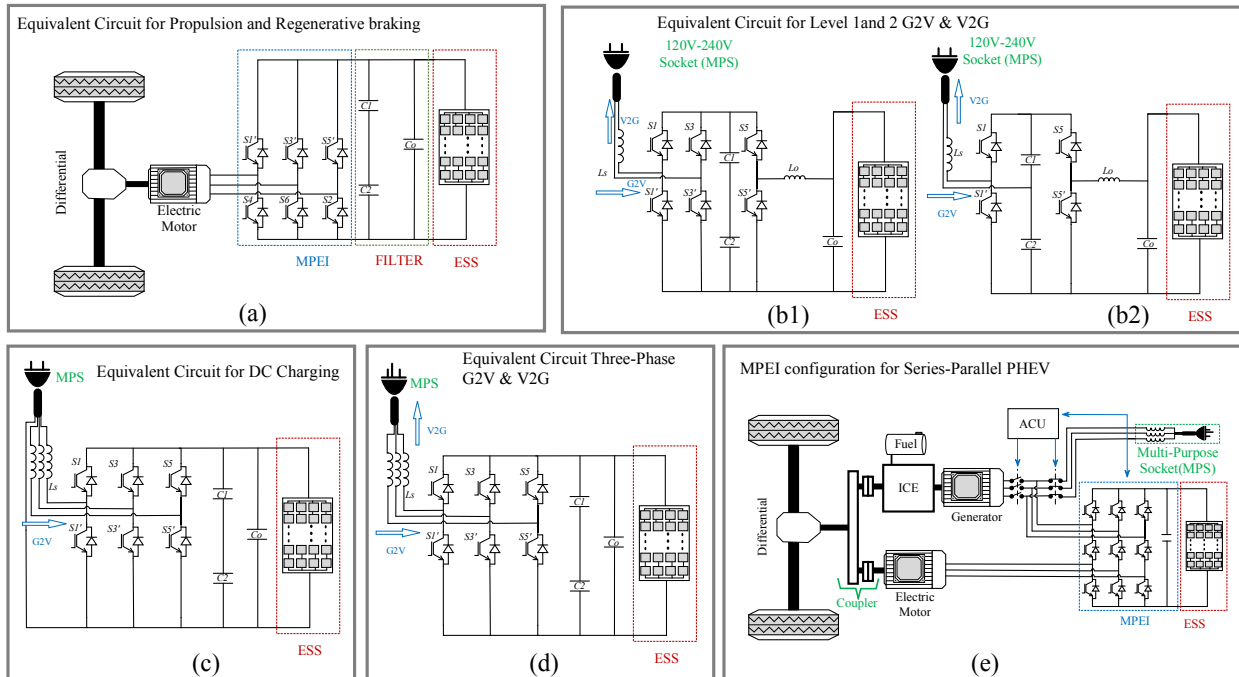
Fig. 3-2. Proposed integrated multipurpose power electronics interface (IMPEI). (a) equivalent PEI for propulsion and regenerative braking, (b) equivalent PEI for level 1 and 2 V2G and G2V, (c) equivalent PEI for DC charging, (d) equivalent PEI for three-phase V2G and G2V, and (e) IMPEI configuration for series-parallel PHEV.

choice between single-stage and two-stage along the advantages and disadvantages are discussed in [72]. The IMPEI allows its user to switch between all these configurations only by swapping the control scheme. The IMPEI can be controlled for Level-1 and Level-2 V2G and G2V operations. For Level-1 V2G and G2V modes, configurations shown in Fig. 3-2(b) can be used. Both of them offer two-stage conversion allowing both DC and AC side regulations. Depending on the power demand, the AC side of the full-bridge configuration (Fig. 3-2(b)) can be reconfigured into an interleaved or a paralleled half-bridge AC-DC converter. The DC-DC side will ensure that DC currents are pushed or pulled from the battery. During this mode of operation, switches s2, s4, and s6 are turned continuously ON, bypassing the driving motor. Level 2 chargers are offboard because of their relatively larger size compared to level 1 onboard chargers. In the proposed IMPEI, since the current requirement in EVs during the propulsion mode is most of the time higher than its requirement during the onboard charging mode, the ratings of the devices in terms of current capability are mainly selected for propulsion operation. Therefore, they can be used for higher power V2G and G2V operations. Hence, the configuration and the control strategy used in level 1 V2G and G2V operations can be reused without modification for the level 2 V2G and G2V operations. This feature makes the IMPEI-based EV/PHEVs more integrated and flexible in voltage levels and charging requirements. More discussion regarding the device sizing is provided in section III as a case study.

Fig. 3-2(c) shows the equivalent configuration (Interleaved DC-DC Converter) of the MPEI for DC charging. The DC source can be PV panels. DC fast charging nowadays is commercial. High power rated DC chargers are offboard, and most of them use three-phase inputs to generate a high DC link voltage [73]. Applications from renewable energy such as solar EV chargers are not thoroughly considered in most EVs/PHEVs designs. The proposed IMPEI can be turned into multiphase boost/buck converters to obtain higher efficiency, lower ripple output voltage, and better transient performance. This ability of the IMPEI allows both onboard DC fast charging and the use of renewable energy as a charging source. This results in a more sustainable transportation and enables the use of the EV battery as storage. This configuration can be controlled as an interleaved DC-DC converter. More details on interleaved DC-DC converters regarding the control and design can be found in [74] and [75].

Fig. 3-2(d) illustrates the IMPEI equivalent configuration during three-phase G2V and V2G. The switches S2, S4, and S6 are OFF, and the remaining are controlled for AC to DC power

conversion. The control strategies for three-phase AFECs are well-known in the literature [70]. This operation mode is found in heavy-duty HEVs and some fast-charging stations. It is not commonly seen in personal and passengers' PHEVs because most households run on a single-phase, and the additional weight three-phase onboard chargers may add to the EV weight. The IMPEI offers the possibility of a single-phase onboard charger and three-phase operation, allowing flexibility on power sources.

Therefore, the proposed topology is a reconfigurable PEI, which makes it possible to use the same interface for different operating modes by reconfiguring the IMPEI in an already existing topology for this mode. These equivalent configurations with IMPEI are possible since the G2V/V2G and the propulsion operation cannot happen simultaneously in PEVs and PHEVs. The equivalent PEIs obtained are well-known, [72] and [76]. Hence, any control strategy developed or available in the literature can be implemented. Therefore, this chapter will not focus on control strategies; however, it will use the existing control strategies along with the IMPEI switch states in Table 3-1 to validate the concept theoretically and experimentally.

3.3.2. PHEV Operation of the IMPEI

The proposed MPEI has a unique feature enabling it to be used in a PHEV configuration without any modification in its architecture. Fig. 3-2(e) shows the series-parallel PHEV using the IMPEI. The ICE and the electric motor can be operated simultaneously or independently depending on the driving regime for efficient energy utilization. For parallel operation, the power flow during each operation mode is illustrated in Fig. 3-3. The lower six switches are used for start-up (Fig. 3-3(a)), acceleration (Fig. 3-3(b)), regenerative braking (Fig. 3-3(d)), and parking (Fig. 3-3(e)). During these operating modes, the equivalent circuit is similar to the one depicted in Fig. 3-2(a). However, the upper six switches are used for recharging the battery with the ICE during the high-speed cruising operation of the PHEV Fig. 3-3(c)). In this mode, the equivalent circuit is similar to the three-phase G2V (Fig. 3-2(d) and Fig. 3-3(f)). Here, the generator is used instead of the grid. The principle of the series PHEV operation using the IMPEI is based on generating two groups of three-phase waveforms from the single common DC bus. Available control strategies for controlling both motors simultaneously in this configuration are discussed and validated practically in [77] - [79].
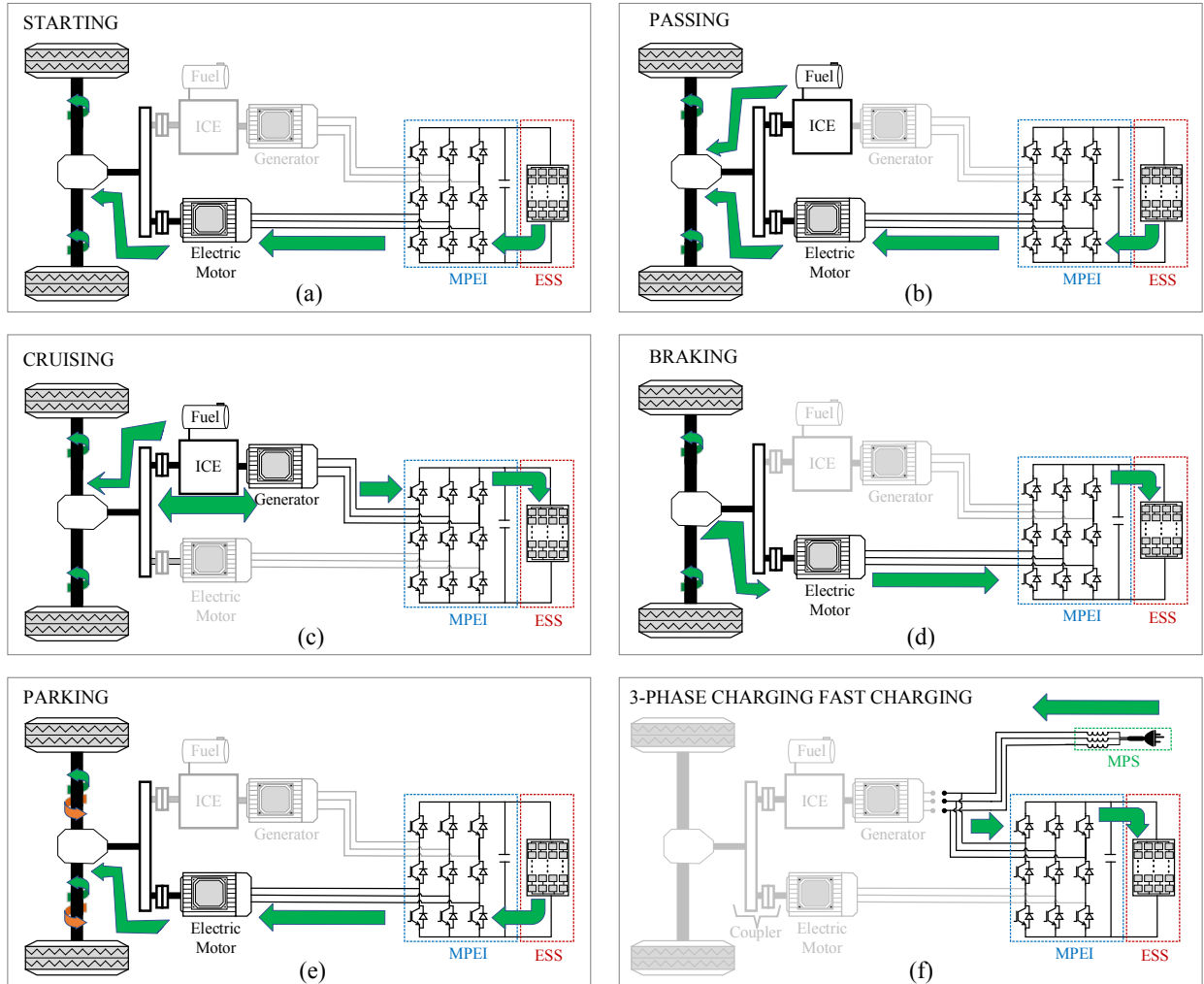
Fig. 3-3. Power flow in IMPEI based PHEV. (a) starting, (b) passing, (c) cruising, (d) braking, (e) parking, and (f) three-phase charging.

3.3.3. Comparison Between the IMPEI and the Nine-Switch Inverter (NSI)

The proposed topology has nine switches; however, configuration, control, and operating modes are not similar to the existing nine-switch topology ([77] - [79]). The reasons why the proposed IMPEI topology is not equivalent to the nine-switch inverter (NSI) are given below.

3.3.3.1. Topology

The fundamental difference between the two topologies is that there are two additional capacitors, two contactors, and one inductor in the proposed IMPEI topology (Fig. 3-4(a)) when compared to the NSI (Fig. 3-4(b)). These additional components provide a substantial increase in in the number of possible operating modes, grid connection flexibility, and power capability.
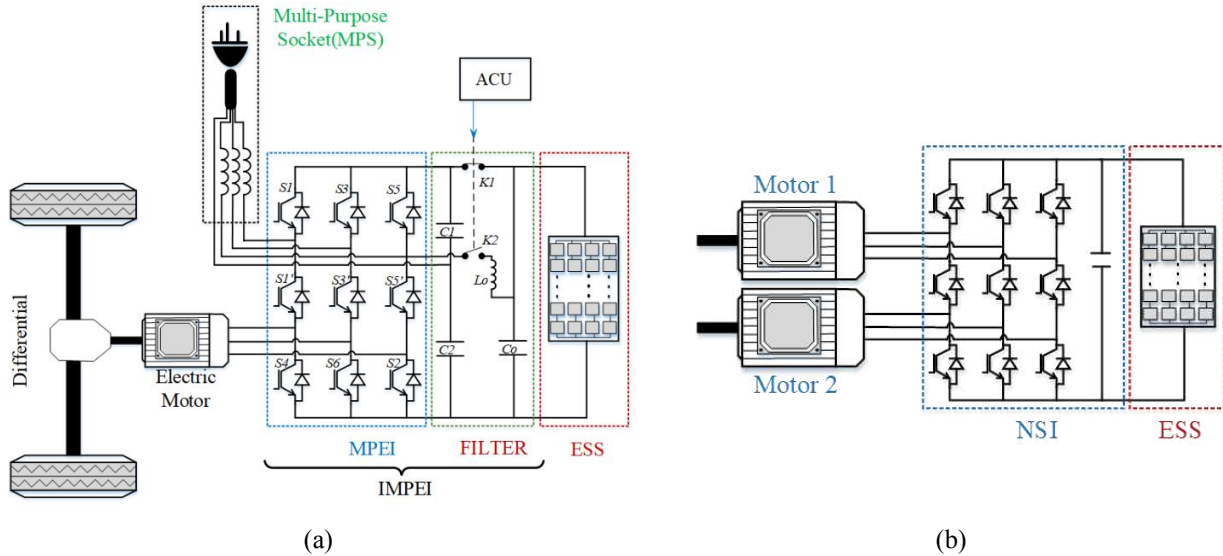
Fig. 3-4. Layout comparison between the IMPEI and the NSI. (a) IMPEI (9 switches + 2 Contactors+ 3 Capacitors+ 1 inductor) and (b) NSI (9 switches + 1 Capacitor)

3.3.3.2. Operating modes

The operating modes of the NSI as reported in the literature are summarized below from Fig. 3-5(a) to Fig. 3-5(d). In Fig. 3-5(a), two motors are connected to the NSI and can be controlled simultaneously at different speeds and torques. In Fig. 3-5(b), a multiphase motor/open winding motor is connected to the NSI. The motor can be also controlled by applying the proper control strategy. In Fig. 3-5(c), the NSI is connected to a motor and to a grid. This is a microgrid configuration. In Fig. 3-5(d), two grids are connected to the NSI. This configuration is used as a frequency converter.

The IMPEI apart from being able to operate in the modes depicted in Fig. 3-5 without any modification can also operate in the modes shown in Fig. 3-2. By using the IMPEI, several important additional modes of operations that cannot be achieved by the NSI are made possible. To do so, a new switching configuration is proposed. Fig. 3-2(a) shows the equivalent circuit for propulsion and regenerative braking. The lower six switches are used. The upper 3 switches are kept turned ON always. Fig. 3-2(b1) adds two additional modes which are single-phase G2V and V2G using a two-stage conversion: the AC-DC stage using the full-bridge configuration and the DC-DC stage. Here, the contactors are used to provide the hardware reconfiguration allowing the IMPEI to connect to 120 V and 240 V grids. The upper six switches are used in this mode as well to control the power flow while the lower three switches are kept ON continuously. Fig. 3-2(b2)
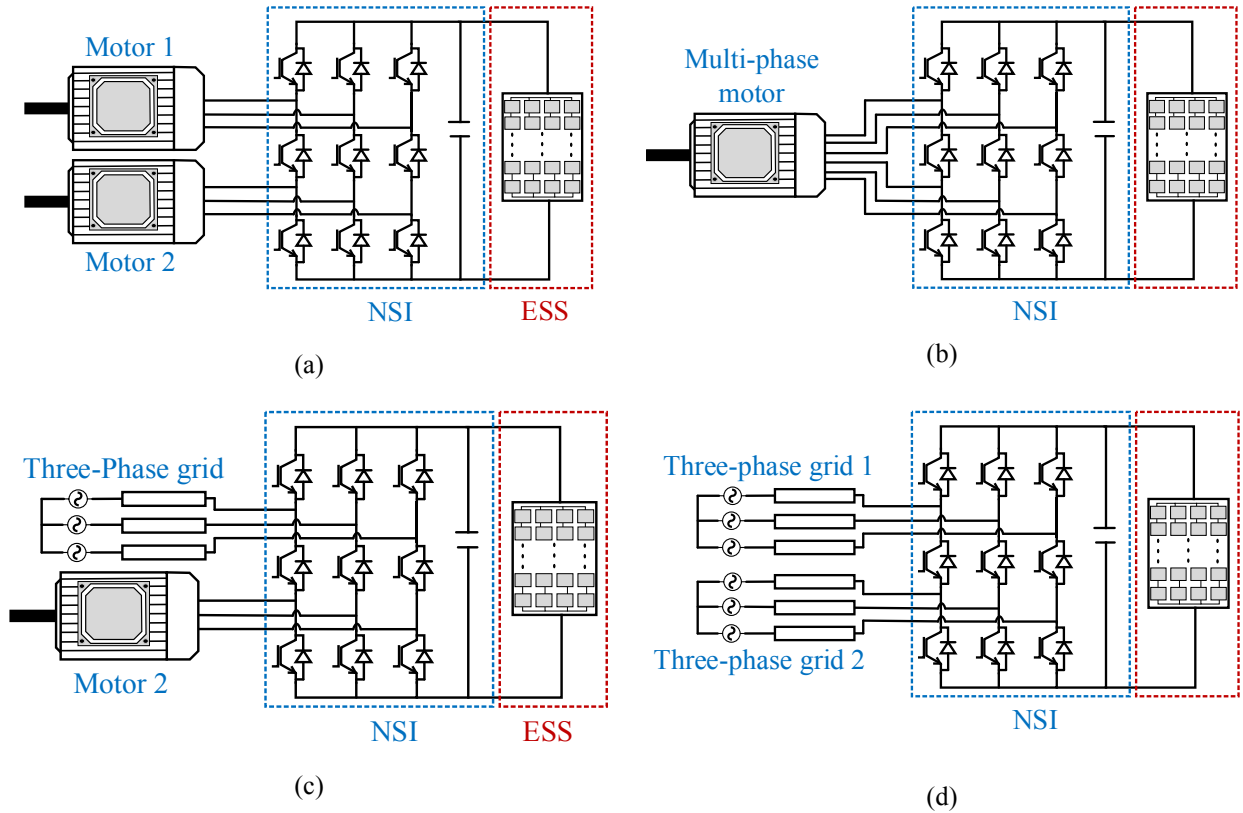
Fig. 3-5. Operating modes of the NSI: (a) parallel operation of two motors, (b) multi-phase motor operation, (c) micro-grid configuration, (d) grids interfacing.

adds two additional modes of operation by using the half-bridge configuration in the AC-DC conversion stage. The DC-DC part is similar to Fig. 3-2(b1). The configuration in Fig. 3-2(b2) uses a lesser number of switches as compared to the one in Fig. 3-2(b1) and has a higher voltage boosting capability. Fig. 3-2(c) is the equivalent configuration for DC interleaved charging from a DC source which can be a DC power supply or photovoltaic system having a different voltage rating. Here the upper six switches are used while the lower three switches are kept ON. The same configuration is used for the three-phase grid-to-vehicle (G2V) and vehicle-to-grid (V2G), which are two additional modes, Fig. 3-2(d). Therefore, an additional ten (10) operating modes have been added by the IMPEI thanks to its reconfiguration ability.

It can also be seen that the longer commutation paths involved in NSI modes of operation due to the generation of two sets of three-phase voltage and current waveforms are avoided in the proposed IMPEI. This is done by adopting a new switching configuration where the IMPEI operates like the conventional 6-pack inverter (CPEI). Table 3-1 summarizes the states of switches in the IMPEI modes as discussed above. It can be seen that although the IMPEI has a

layout similar to nine switch inverters but with different load voltages, it is still controlled as a regular 6-pack voltage source converter. In terms of configuration (device count), application, modes of operation, and control, the IMPEI and the NSI are different.

3.3.4. Other BEV Configurations Using the IMPEI

Several other BEV configurations using the IMPEI are still possible using the proposed IMPEI and control. Moreover, all control strategies used for NSI can be used when needed without a change in the hardware. Fig. 3-6 shows a few possible configurations of the BEV drivetrains using the IMPEI. Fig. 3-6(a) depicts the situation when two motors are coupled in series. Motor 2 is of open windings type, which can be used for V2G applications. It can also be used as the launch assist to motor 1 during starting and acceleration. It can also be dedicated to the regenerative braking application. Fig. 3-6(b) illustrates a four-wheel drive using the IMPEI. In this configuration, motor 1 is the main drive motor, and motor 2 can be used for the same functions as in Fig. 3-6(a). Finally, Fig. 3-6(c) depicts an interesting configuration that uses a six-phase machine or an open winding machine. The flexibility in the IMPEI allows controlling the coupled motor using the proper control strategies or as a regular three-phase machine by shorting the rotor terminals (turning s1, s3, and s5 continuously ON). The realizations of the depicted operation may require additional components.

3.4. Coordination

This IMPEI offers easy coordination and switching between the operating modes mentioned in the previous section. The change in the mode of operation is done only by swapping the control strategies after the design is completed, as shown in Fig. 3-7. Hence, the driver can charge the EV using the available power source. Moreover, an automatic swapping algorithm can be developed for selecting the operating mode based on the charging connector type.

3.5. IMPEI Design Chart

Here, the focus is on selecting the type and rating of PESs, considering the battery voltage level and the operating modes. On the one hand, it is reported in the literature that the practical EV battery voltage is from 100 V - 800 V. Voltages in the range of 100 V – 200 V is commonly used in Hybrid Electric Vehicles (HEVs) and Plug-in HEVs (PHEVs). However, 400 V – 800 V voltage range is used in Battery EVs (BEVs) [30]. There are also BEVs with battery voltages less
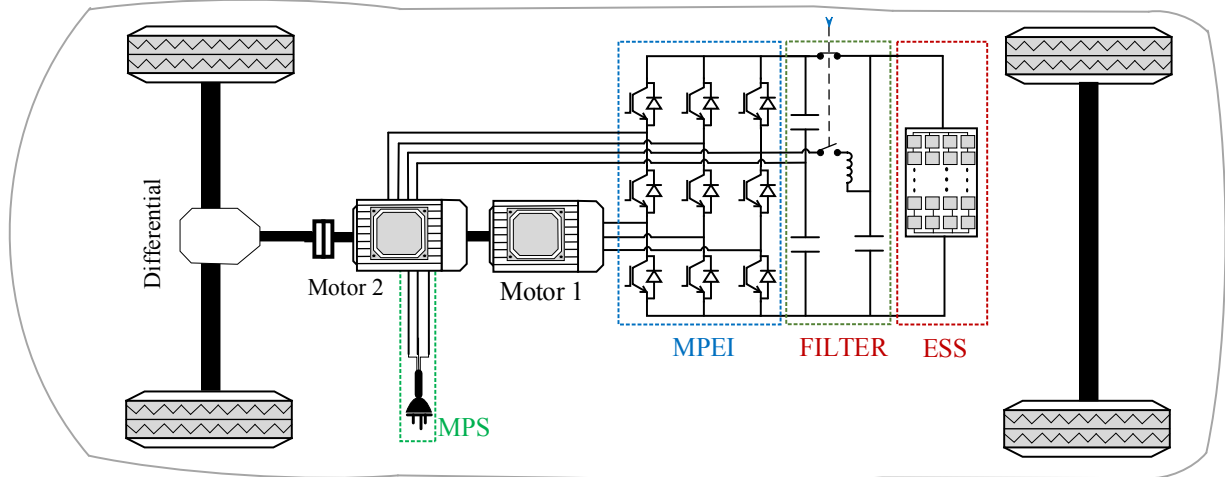
(a)
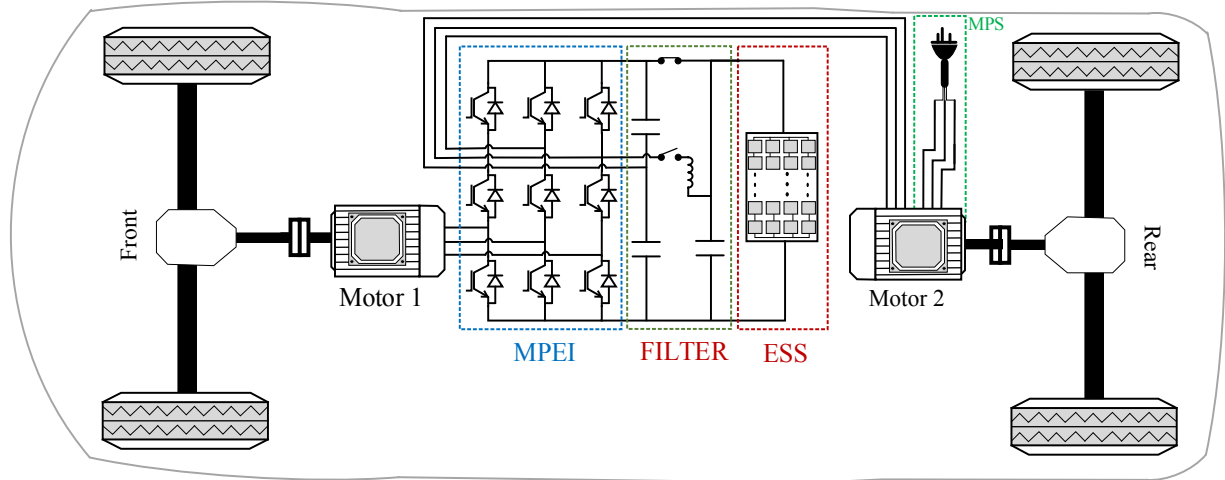
(b)
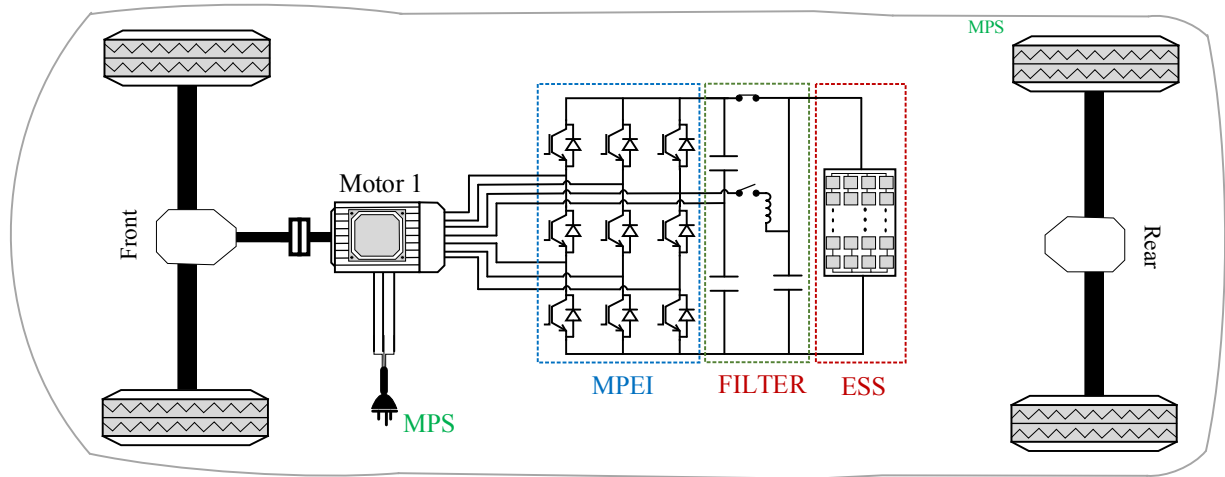
(c)

Fig. 3-6. Possible Applications of the IMPEI in EVs: (a) crankshaft integrated motor, (b) all wheels drive configuration, (c) EV with open winding motor or six-phase motor.
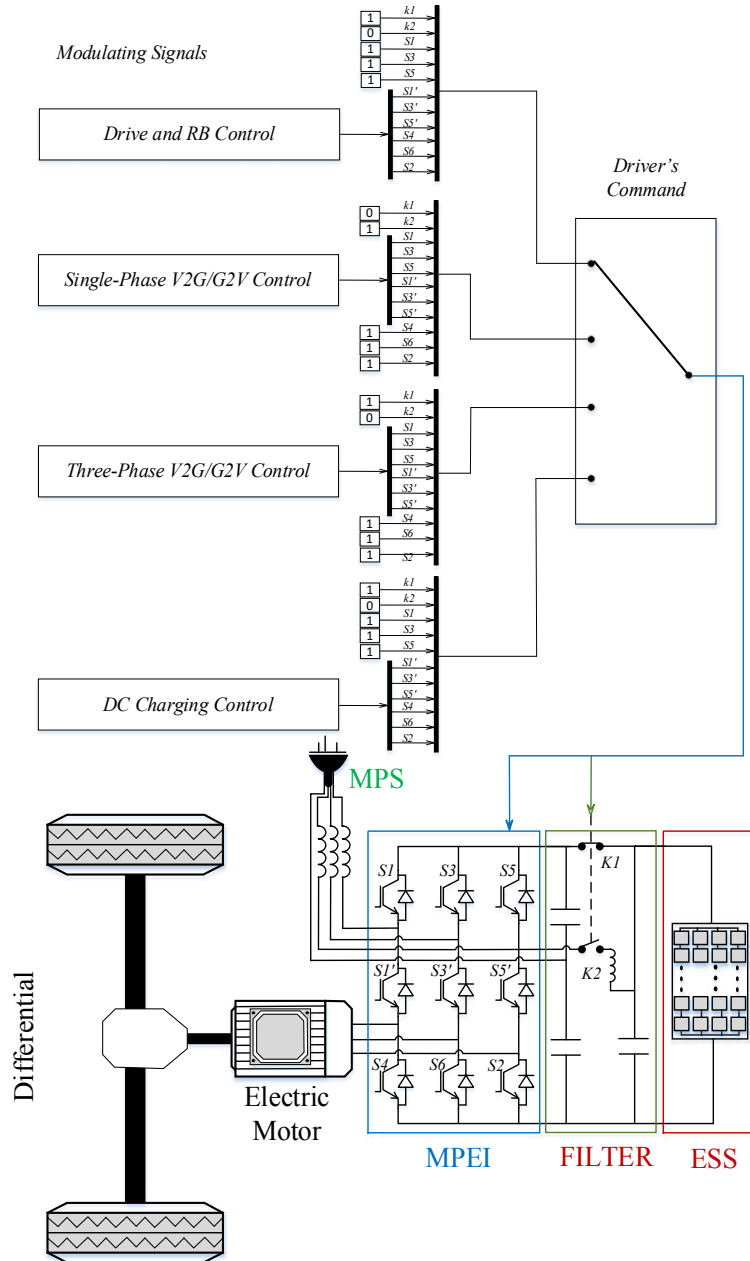
Fig. 3-7. Coordination diagram of the IMPEI.

than 100 V, 100 V, e.g., Renault Twizy-80, and BEVs with battery voltages in the range of 200 V - 400 V, e.g., Tesla Model 3 and Audi e-Tron. For EV chargers, depending on the source voltage level, there are DC, level 1 (120 V), level 2 (240 V), and three-phase (208 V - 600 V) chargers.

Depending on the operating modes desired to be included in the IMPEI, the design considerations are illustrated in Fig. 3-8. The practical limits consider the linear duty ratio range

(0.25 to 0.9 for AC-DC conversion stage and 0.25 to 0.8 for DC-DC conversion stage during V2G and G2V), power level, and experimental BEVs data in [80]. The minimum requirement for V2G and G2V operation is expressed by (3. 1).

$$V_{DC} > \sqrt{2}V_{grid} \, , \tag{3. 1}$$

where V_{DC} is the DC bus voltage of the active front-end converter and V_{grid} is the phase rms or line rms voltages for single-phase and three-phase grids respectively. For proper controllability, $V_{DC} > 1.15\sqrt{2}V_{grid}$ is used [81].

The equivalent PEIs are designed and simulated in MATLAB Simulink to verify the voltage ranges. Here, only MOSFET and IGBTs are considered because they are widely used in EV drives. New PESs with wide bandgap (WBG) semiconductor materials, such as silicon carbide (SiC) and gallium nitride (GaN), can be used as well. The ranges I to VI are defined based on the number of feasible equivalent PEIs and the battery voltage range. For instance, IMPEI can only offer level 1 charging using the full-bridge AFEC converter for any design specifications in the range I. However, for design specifications in region II, IMPEI can offer level 1 and level 2 charging using the best between the half-bridge and the full-bridge AFECs. In this region, a proper decision between the MOSFET and IGBT is required for better efficiency. All equivalent PEIs for level 1 and level 2 can be used in region III. The selection between PEIs will depend on the performance and power level.

Region IV unveils all the abilities of the IMPEI; level 1, level 2, and three-phase charging are possible. This range is well suited for current BEVs in the market. In region V, charging in level 1 using the full-bridge AFEC-based charger is not feasible based on the selected modulation ranges.
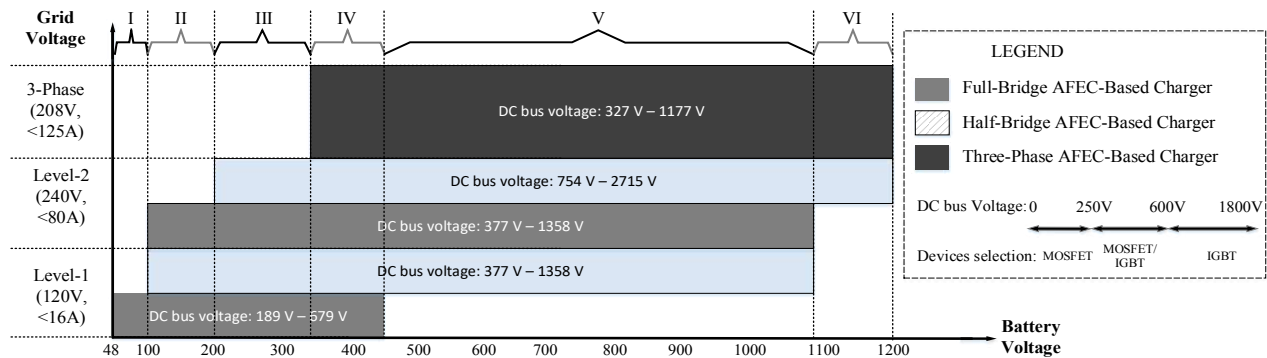
Fig. 3-8. IMPEI design chart.

However, level 2 and three-phase charging remain practical. Region V is the ideal range for 800 V battery EVs and heavy-duty EVs. Here, the advantage of fast charging can be exploited, [29] and [30]. In region VI, three-phase and level 2 charging (using half-bridge AFEC) are still feasible; however, three-phase charging may be preferable based on the power level. IGBTs are the preferred PESs in this region.

Regarding the PESs selection for the IMPEI, the graph in Fig. 3-8. provides guidance based on DC bus voltage requirements. For IMPEI design, device current and voltage ratings are decided based on the highest current and voltage required for operation in the selected modes. Choosing between the MOSFET and IGBT or WBG semiconductor materials is a "gray area" specific to the application [82]. Optimization is required in rating, cost, size, speed, and thermal requirements to select the PES type properly. IGBTs are most commonly used for propulsion inverters having less than 20 kHz switching frequencies, while MOSFETs are used for the charging circuitry. The WBG semiconductors have higher power density and efficiency and can operate at higher voltages and frequencies [16].

3.6. Comparative Study
3.6.1. PEI Comparison: Configuration and Devices Count

A component count comparison is provided in Table 3-2, where the IMPEI is compared with three other PEIs. The first PEI is a conventional PEIs for BEVs with its onboard charger (Fig. 3-9). This PEI can be easily implemented and controlled. It has separate PEIs for propulsion and grid interface. The second PEI is the advanced power electronics interface (APEI) proposed in [83] and illustrated in Fig. 3-10. It has an integrated BEV drivetrain consisting of a DC-DC converter, an onboard battery charger, and an inverter. The third PEI is the single-phase integrated charger (SPIC) using a quasi-Z-source network proposed in [51] (Fig. 3-11). The latter has the three-phase motor used for propulsion integrated into it. Table 3-2 shows the comparison data between the four PEIs.

The capacitor across the battery has been neglected in the four configurations for comparison purposes. The required components for a minimal realization of each PEI are considered resulting in a device count range. For instance, depending on the power level under consideration, four PESs can be used for the DC-DC section of the APEI instead of eight PESs, even though eight PESs are preferred. The advantage of using eight PESs instated of four is discussed in [83]. It can

50
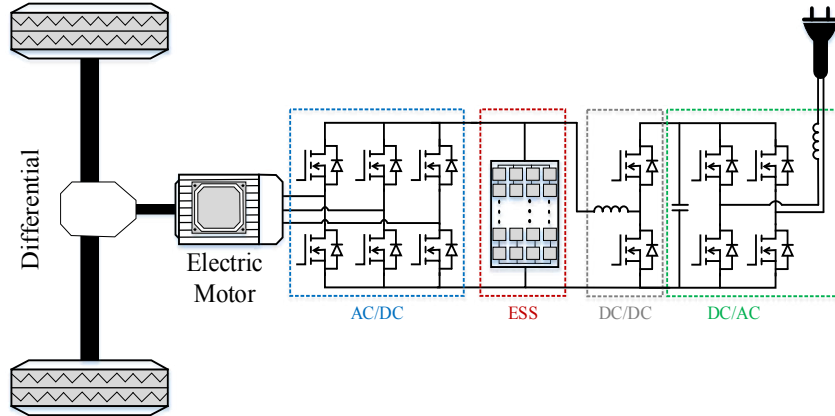
Fig. 3-9. Conventional BEV drivetrain with bidirectional onboard charger (CPEI).
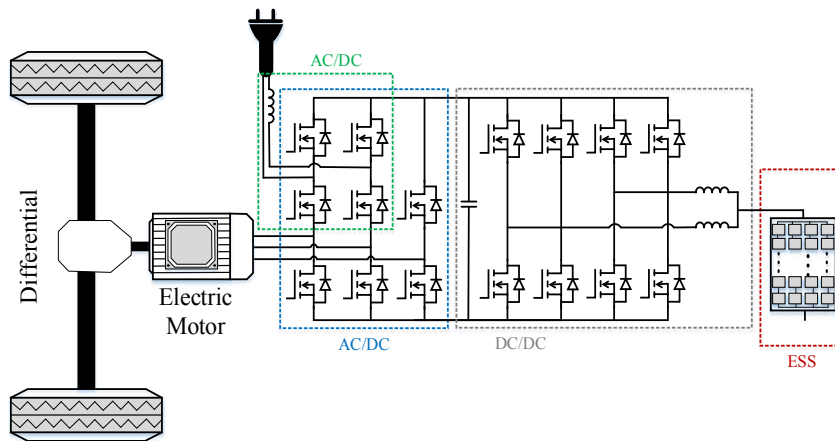
Fig. 3-10. Advanced power electronics interface (APEI). Updated from [83].
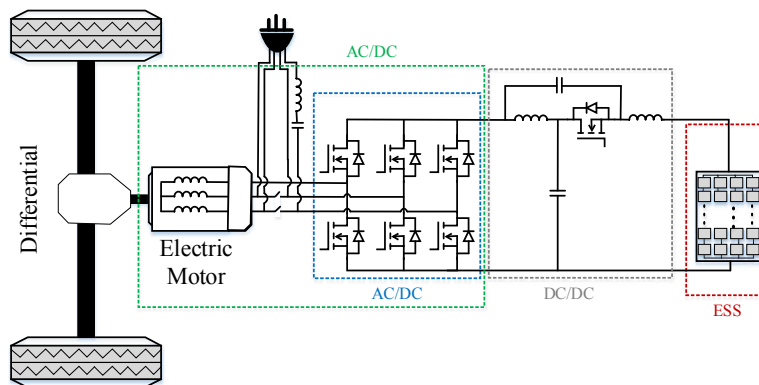
Fig. 3-11. Single-phase integrated charger using quasi-Z-source network (SPIC). Updated from [51].

be seen that the SPIC has an overall lower switch count (PESs and contactors) followed by the IMPEI. These two configurations use additional two contactors for operating mode change. These contactors are not hard switched. The change of mode occurs at zero current. They are designed to carry the full current during the selected mode of operation. The CPEI, APEI, and IMPEI have a comparable number of capacitors. The SPIC, however, has the largest number of inductors and

capacitors. The PEIs that have the lower total number of components are the CPEI and the IMPEI. The APEI has the largest component count.

In terms of operation, the IMPEI and CPEI have the battery directly connected to the inverter, making them the PEIs that use fewer components during propulsion, regenerative braking, V2G, and G2V modes. The other two have the DC-DC bidirectional converter between the battery and the inverter. This makes them more efficient at low speed and light load. However, the CPEI and the IMPEI types of PEIs are the preferred choices for high speed and full load operations [31].

Table 3-2: Device Count Comparison for Various PEIs.

		CPEI	APEI	SPIC	IMPEI
Total number of PESs		12	12-16	7	9
Total number of capacitors		1	1	3	1-2
Total number of inductors		2	3	4	3-4
Total number of contactors		0	0	2	2
Total number of components		15	16-20	16	15-17
Number of components in propulsion and regenerative braking modes	PESs	6	12-16	7	9
	Capacitors	0	1	2	0
	Inductors	0	2	2	0
	Stages	1	2	2	1
Number of components in single-phase V2G and G2V	PESs	6	10-14	7	6-9
	Capacitors	1	1	3	1
	Inductors	2	3	3-4	2
	Stages	2	2	2	2
Three-phase V2G and G2V	PESs	NA	NA	NA	9
	Capacitors	NA	NA	NA	0
	Inductors	NA	NA	NA	3
NA= Not Applicable					

In terms of control, the CPEI offers the most straightforward control architecture. It has a separate PEI and control for propulsion and regenerative braking and another separate PEI and control for V2G and G2V. The IMPEI and the CPEI have a single conversion stage for the propulsion and regenerative braking and two conversion stages for V2G and G2V. However, the SPIC and APEI have two conversion stages for all the modes, which makes them the ones with a more complex control structure. Although the IMPEI has a layout similar to nine switch inverters, it is controlled as the CPEI. It uses the same control algorithms as the CPEI, except that some switches have to be kept ON, as illustrated in Table 3-1. This makes the IMPEI less efficient compared to CPEI.

On the other hand, the IMPEI has grid flexibility and is reconfigurable. This allows it to interface with different sources: single-phase, three-phase, and DC without change in the

hardware. It can also be used in a PHEV as shown in Fig. 3-3. The IMPEI offers more compact designs and operating modes than the APEI and SPIC drivetrains.

Regarding reliability and safety, IPEIs such as APEI, SPIC, and IMPEI are less reliable compared to CPEI because a fault during charging mode may impact the propulsion mode. The integration of power electronics interfaces is therefore a trade-off. IMPEI offers more flexibility during fault conditions compared to APEI and SPIC. For instance, a short circuit on the DC bus can be eliminated by opening the continuously conducting switch in the IMPEI. Moreover, in a case where the middle leg is defective, the configuration in Fig. 3-2(b2) can be used for V2G and G2V operations, while the two healthy legs can be used to drive the EV to the repair shop. To solve this reliability issue, the switches in the IPEIs should be designed to allow modularity. If packaged in module form, IMPEI's nine switches can be easily replaced in the event of a fault without labor-intensive work and reduced down time.

3.6.2. Device Sizing and Cost

a- Design Specifications

Sizing of the PEIs to meet the propulsion and grid interface requirements of the BMW i3 2016 is described in this section. The specifications of BWM i3 2016 as per the FY2016 annual progress report [84] are summarized in Table 3-3.

Table 3-3: Technical specifications. BMW i3 2016 (120 Ah).

		Specifications
Motor	Rated output power	125 kW
	Rated torque	250 Nm
	Rated speed	4000 r/min
	Max speed	11400 r/min
Battery	Voltage	360 V
	Energy	22 kWh
	DC current	530 A for full torque
Charger	On-board	3.7 kW / 16 A / 240 V
DC bus Capacitor		475 uF, 450 V
IGBT Module (Infineon FS800R07A2E3)		650 VDC, 800 A/1600 A peak
Current sensors LEM HC5F700		700 A

The battery in the BMW i3 is selected to match the operating voltage of the motor. This configuration is similar to the CPEI and the IMPEI. The APEI and the SPIC require a DC-DC conversion stage. On the other hand, based on the battery nominal voltage, it can be seen that the IMPEI is in region IV (Fig. 3-8). The included modes consist of single-phase, split-phase, and

three-phase V2G and G2V. For the CPEI, APEI, and SPIC, V2G and G2V operations at 240 V is considered for the charger sizing. The parameter design for the SPIC and APEI can be found in [51] and [83], respectively. It has been assumed that the DC bus in the SPIC and APEI has a voltage level compared to that of the battery. Hence, the devices used for the DC-DC conversion stage in the SPIC and APEI are rated for 600 A. This current rating could increase if there is a significant mismatch between the battery and the DC bus voltages.

b- Passive Elements Sizing

The LCL filter, which is shown in Fig. 3-12(a), is selected for the grid interface. Most assumptions and calculations are based on [85] and IEEE-519 standard. To keep the comparison simple, a maximum grid current of 30 A is assumed in V2G and G2V modes for the IMPEI, APEI, SPIC, and CPEI. This provides the IMPEI with 10 kW charging capability in three-phase V2G and G2V. From the transfer function obtained in Fig. 3-12(b), the following equation can be derived.

$$\frac{i_g}{v_{IMPEI}} = \frac{1}{sL(1 + s^2 CL_{eq})}, \tag{3.2}$$

where $L = L_1 + L_2$ and $L_{eq} = \frac{L_1 L_2}{L_1 + L_2}$. The resonance frequency f_{res} is selected to obey (3. 3). f_g and f_s are the grid frequency and the switching frequency, respectively.

$$\omega_{res} = \frac{1}{\sqrt{CL_{eq}}} = 2\pi f_{res}; \quad f_g \ll f_{res} \ll f_s. \tag{3.3}$$

For this application, the switching frequency is kept at 10 kHz for the single-phase and the three-phase operating modes. f_{res} is selected to be at least ten times higher than f_g and two times less than f_s. The reactive power capability of the filter capacitor is limited to 5% of the rated apparent power of the charger. The value of the LCL capacitor is obtained as follows.

$$C_f = \frac{0.05\, S}{V_g^2 (2\pi f_g)}, \tag{3.4}$$

where V_g is the RMS phase voltage and S is the apparent power.

The maximum value of the inductances in the LCL filter is calculated using (3. 5) to ensure that the voltage drop on the filter is less than 20% of the grid voltage.
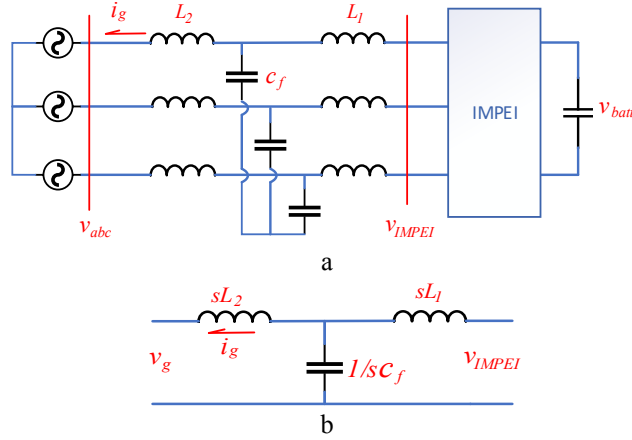
Fig. 3-12. LCL filter: a-grid interface, b-Per phase equivalent circuit in phase domain.
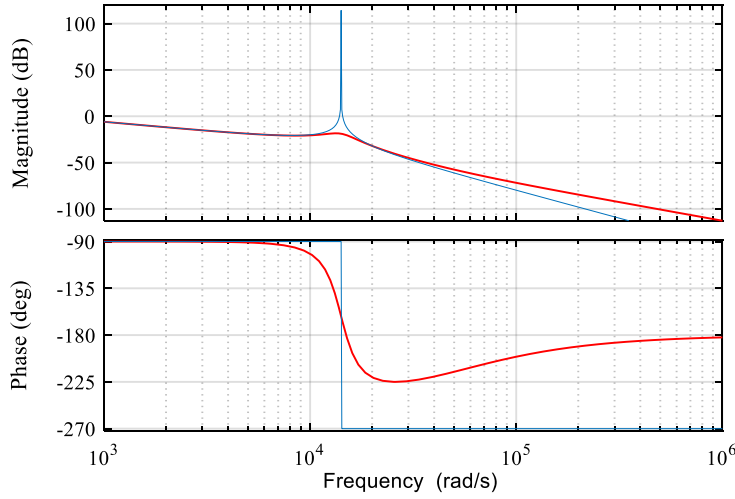
Fig. 3-13. LCL filter: Bode plot with R_d (red) and without R_d (blue).

$$L_{max} \leq \frac{0.2V_g}{2\pi f_g I_g}. \tag{3.5}$$

The minimum value of the inductance is obtained by evaluating the transfer function (3. 2) at the switching frequency as follows.

$$\left| \frac{1}{\omega_s \frac{I_{gs}}{V_{IMPEIs}} \left(1 - \frac{\omega_s^2}{\omega_{res}^2}\right)} \right| \leq L_{min}, \tag{3.6}$$

where $\omega_s = 2\pi f_s$, $\omega_{res} = 2\pi f_{res}$, $I_g = 30\ A$. I_g is the RMS grid current, I_{gs} is the RMS grid current ripple, V_{IMPEIs} is the RMS IMPEI voltage, and $L = L_1 + L_2$. For practical implementation, $I_{gs} = 0.003I_g$ and $V_{IMPEIs} = 0.9V_g$ have been used. For the IMPEI, the value of

55

the LCL components should be selected to meet the requirements for all the modes of operation under consideration. For this study, single-phase (120 V and 240 V) and three-phase (208 V) G2V and V2G modes are considered. The value of $L = 2\,mH$ has been selected. L_1 and L_2 are kept equal. A capacitor of 10 µF is selected to satisfy (3. 3) and (3. 4) under the considered modes of operation. The series passive damping resistance (R_d) of the capacitor is calculated using (3. 7) to be 2.3Ω. The Bode plot of the designed LCL filter with and without R_d is shown in Fig. 3-13.

$$R_d = \frac{1}{3C\omega_{res}}.$$

(3. 7)

For the DC link capacitor size, (3. 8) has been used. P_{out} is the output power, $V_{DCripple}$ is the allowable ripple voltage on the DC bus, and V_{DCmin} is the minimum DC link voltage.

$$C_f \geq \frac{P_{out}}{2\pi f_g V_{DCmin} V_{DCripple}}.$$

(3. 8)

For the propulsion mode, the DC capacitor across the battery terminals is sized to limit the ripple voltage on the DC bus and provide a low impedance paths for ripple current caused by output inductance of the load as well as the PWM frequency of the inverter and the DC bus voltage. The capacitor in Table 3-3 is used as a reference. The high-frequency inductor of the buck converter in level 1 and level 2 V2G and G2V modes is sized to operate in continuous conduction mode (CCM) mode. The components sizing is provided in Table 3-4.

c- Cost Analysis

The rating of individual components and their cost are given as a reference in Table 3-4. The calculations have been performed to obtain the size of the passive elements that meets the requirements. For verification purposes, MATLAB Simulink simulations have been performed to ensure the validity of the device rating for all the modes; propulsion and charging modes (single-phase, split-phase, and three-phase). The selection of components is based on the drive and charger specifications and the required modes of operation.

The cost is provided in per unit based on the North American market and on companies which offer customized products. The modules have been preferred over the discrete components, when available, to lower the cost and reduce the footprint. This is the case for the CPEI and the SPIC drive inverters, where a single device is used. Whereas for the IMPEI and APEI, discrete single-leg IGBTs have been selected. The device manufacturers can easily overcome this limitation since

56

three-level three-phase inverter modules, which are more complex, are now available for commercial use. Inductor model 195C30 from Hammond Manufacturing are selected for the LCL filter. For the IMPEI, the filter is the only additional component required to perform V2G and G2V. One can state that part of the IMPEI filter components can use the space that the CPEI charging circuitry would have used for its heatsink and PESs.

The chart in Fig. 3-14 shows a comparison where it can be seen on the one hand that the total cost of developing the IMPEI is about 58% higher than the CPEI. This is due to the unavailability of modular semiconductor components to implement the 9-switch configuration and the line filter components to include three-phase charging in the operating modes of the IMPEI.

Table 3-4: Sizing and Cost Comparison.

			CPEI	IMPEI	APEI	SPIC
	Device and Specifications	Unit Price (Scaled)	Extended Cost (Scaled)	Extended Cost (Scaled)	Extended Cost (Scaled)	Extended Cost (Scaled)
Drive	IGBT 6-pack module: 650 V, 800 A	4.63	4.63	-	-	4.63
	IGBT single-leg module: 1200 V, 800 A	1.03	-	6.15	5.13	0.51
	IGBT single-leg module: 650 V, 200 A	0.75	-	-	3.00	-
	Current sensors: 700 A	0.70	2.10	2.10	2.10	2.10
	Capacitor: 470 uF, 630 V	0.10	0.10	0.10	0.10	0.19
	Capacitor: 3300 μF, 630 V	0.76	-	0.76	0.76	0.76
	DC-DC inductors: 1 mH, 400 A	3.00	-	-	6.00	-
	DC-DC inductors: 1 mH, 800 A	6.00	-	-	-	12.00
	AC contactor: 800 A	5.00	-	-	-	5.00
	DC contactor: 600 A	0.93	-	0.93	-	-
Charger	IGBT 6-pack module: 600 V, 30 A	0.21	0.21	-	-	-
	Custom high frequency inductor: 10 mH, 30 A	0.13	0.13	0.13	-	-
	Capacitor: 3300 μF, 630 V	0.76	0.76	-	-	-
	LCL filter capacitor: 10 μF, 450 V	0.05	0.05	0.15	0.05	0.10
	LCL filter inductor: 1 mH, 30 A	0.64	1.28	3.83	1.28	1.28
	Voltage sensor: 500 V	0.23	0.68	1.13	0.68	0.68
	Current sensor: 30 A	0.03	0.06	0.12	0.09	0.09
	Contactor: 30 A	0.44	-	0.44	-	-
	Total		10.00	15.84	19.19	27.34
	Safe charging modes	Single-phase	120 V 30 A	120 V 30 A	120 V 30 A	120 V 30 A
		Split-phase	240 V 30 A	240 V 30 A	240 V 30 A	240 V 30 A
		Three-phase	NA	208 V 30 A	NA	NA

On the other hand, the APEI and the SPIC are more expensive by 92% and 173%, respectively. This is due to the high current requirement of inductors used in their DC-DC
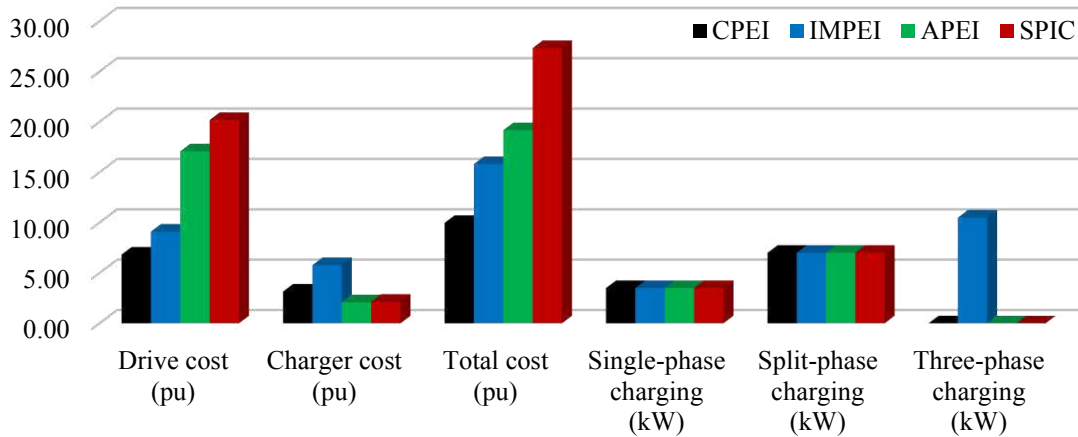
Fig. 3-14. Comparison chart between the CPEI, APEI, SPIC, and IMPEI.
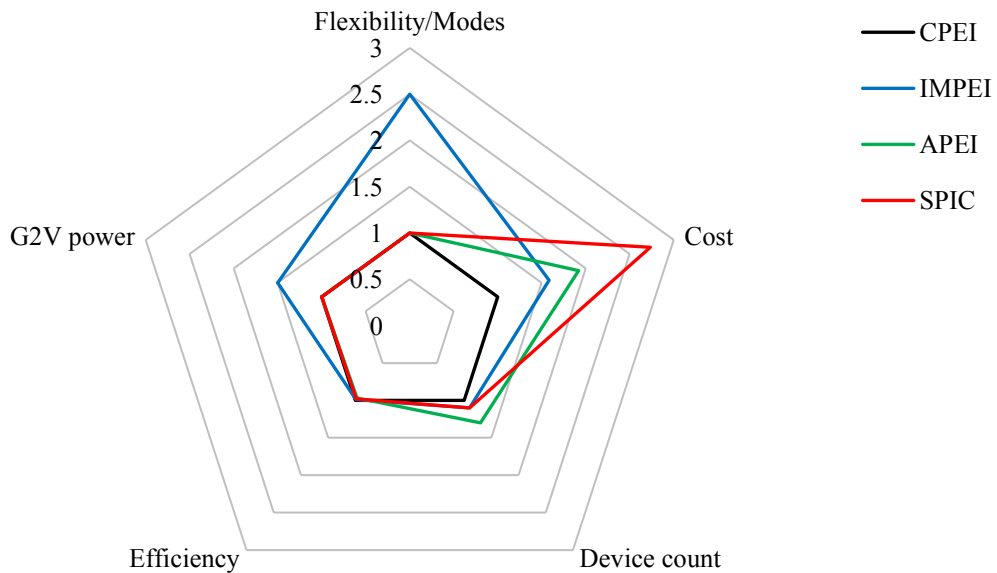
Fig. 3-15. Spider chart for the CPEI, APEI, SPIC, and IMPEI.

converters, and due to the AC contactors for the SPIC. From the V2G and G2V points of view, the IMPEI has a 50% increase in power capability. It can offer single-phase and three-phase V2G and G2V onboard. The CPEI, APEI, and SPIC do not feature three-phase charging. For instance, adding three-phase charging to the CPEI will require additional heatsinks (space and weight), switches, and passive elements (LCL filters) that will bring the overall cost comparable to the IMPEI. Even with this, the CPEI will not be able to offer the same modes of operation as the IMPEI. Therefore, sizing the IMPEI for 30 A V2G and G2V operations is cost-effective. For heavy-duty electric vehicles where space is not a limitation, the onboard charging capability can be increased up to the current handling capability of the PESs by selecting proper filter devices.

The IMPEI, apart from its gain in the charging capability, has everything onboard without requiring dedicated circuitry for V2G and G2V modes. This makes the IMPEI-based EV able to charge from many sources with or without a charging station.

The chart in Fig. 3-15 compares the IMPEI to other IPEIs, with the CPEI serving as the baseline. Table 3-3 and Table 3-4 have been used to estimate the size and cost of the components. Advantages of MIPEI over other IPEIs are emphasized. As can be seen, the IMPEI is the most flexible of the IPEIs, with up to ten modes of operation (propulsion, regenerative braking, single-phase V2G, single-phase G2V, split-phase V2G, split-phase G2V, three-phase V2G, three-phase G2V, DC V2G, and DC G2V). In spite of this this flexibility, IMPEI has a 50% increase in V2G and G2V capabilities compared to CPEI, APEI, and SPIC. In terms of component count, the IMPEI is comparable to the SPIC. All IPEIs have comparable efficiencies. Depending on the mode of operation, the IMPEI has the highest efficiency among the IPEIs and is 1 to 2 percent less efficient than the CPEI. Detailed efficiency comparison is provided in the following sections.

3.6.3. Drive Cycle Efficiency Comparison

To quantify the losses due to additional conducting switches, theoretical efficiencies of the designed IMPEI and CPEI are compared in propulsion mode at different power levels. An analytical study of a drive cycle is performed using the thermal model of the selected PESs in PSIM simulation software. As per Table 3-4, the selected IGBT for the IMPEI is 2MBI800XNF120-50. For the CPEI, 2MBI800XNF120-50 and FS800R07A2E3 IGBTs have been used. The CPEI simulated with 2MBI800XNF120-50 is indexed as CPEI, and the one simulated with FS800R07A2E3 is named i3 since the same IGBT model is used in the BMW-i3 2016. The developed models of the IMPEI and the CPEI included the selected PESs datasheet specifications and the thermal circuit. The conduction and switching losses across each IGBT and its internal diode are measured and used to compute the PEIs losses (P_{losses}). The efficiency is calculated as per (3.9), where P_{in} is the power delivered by the battery, and the losses are as denoted by equations (3. 10) - (3. 14).

$$Efficiency = \frac{P_{in} - P_{losses}}{P_{in}}, \tag{3.9}$$

$$P_{losses} = P_{cond(Diode)} + P_{cond(Switch)} + P_{sw(Diode)} + P_{sw(Switch)}, \tag{3. 10}$$

$$P_{cond(Switch)} = V_{ce(sat)} I_c, \tag{3. 11}$$
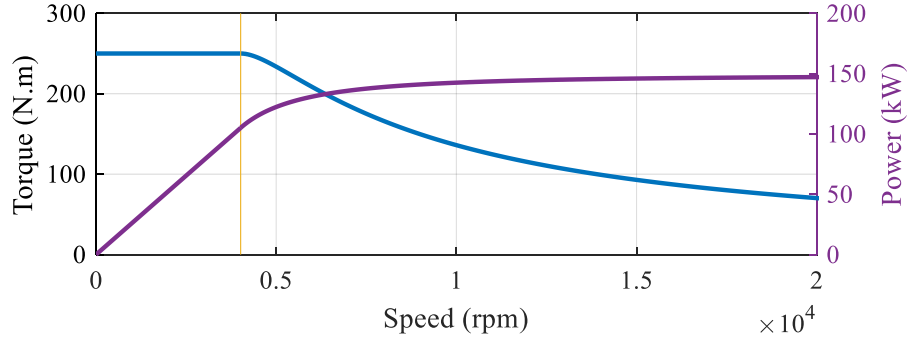
Fig. 3-16. Selected motor characteristics.

$$P_{sw(Switch)} = \frac{(E_{on} + E_{on})V_{cc}}{V_{cc(datasheet)}} f_{sw} , \qquad (3.12)$$

$$P_{cond(Diode)} = V_{diode} I_{diode} , \qquad (3.13)$$

$$P_{sw(Diode)} = \frac{E_{rr} V_R}{V_{R(datasheet)}} f_{sw} , \qquad (3.14)$$

where $P_{cond(Switch)}$ is the transistor conduction losses, $P_{sw(Switch)}$ is the transistor switching losses, $P_{cond(Diode)}$ is the diode conduction losses, and $P_{sw(Diode)}$ is the diode switching losses. The diode turn-on losses are neglected. $V_{ce(sat)}$ is the transistor saturation voltage, I_c is the collector current, and E_{rr} is the reverse recovery energy loss. E_{off} and E_{on} are the transistor turn-off and on energy losses, respectively. V_{diode} is the diode voltage drop, I_{diode} is the diode forward current, V_{cc} is the DC bus voltage, V_R is the reverse blocking voltage, and f_{sw} is the switching frequency. The values of parameters are constantly updated from the device database in PSIM software by monitoring the device temperature and the collector current.

A surface PMSM (SPMSM) is considered for simulation. The parameters of a 125 kW motor are estimated based on [86]. Obtained parameters are summarized in Table 3-5, and the torque-speed envelope is shown in Fig. 3-16. The drive is controlled using FOC technique.

Table 3-5: Estimated Machine Parameters.

Parameters	Value
Number of Poles	12
Magnet Flux Linkage	0.0454 Wb-turns
D-axis Inductance	74.27 μH
Q-axis Inductance	74.27 μH

The ECE drive cycle, which is shown in Fig. 3-17, has been used to investigate the efficiencies at different power levels. The analysis of the losses in each device showed that
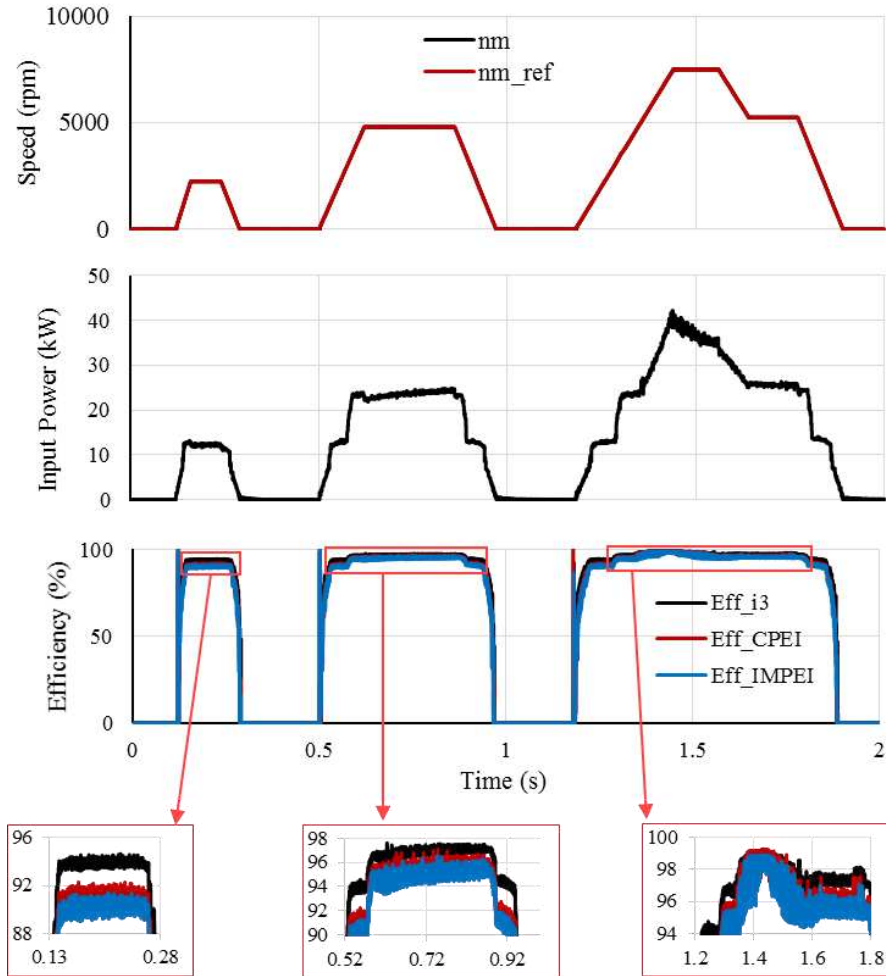
Fig. 3-17. Drive cycle efficiency comparison chart (simulation results).

switches S1, S3, and S5 (continuously turned ON) have only conduction losses. These losses were equal to the conduction losses in the corresponding switches S1', S3', and S5'. On average, it has been observed that PES losses in the IMPEI are 10%s higher than the losses in the CPEI. At different power levels, this ratio may change due to the change in the conduction losses. This ratio has been practically investigated in section 3.7 of this chapter. In terms of efficiency, Fig. 3-17 shows that the highest efficiency is obtained with the i3 module. The efficiency difference between the IMPEI and the CPEI using the same module ranges from 0.3% to 1% on average for the entire drive cycle.

3.7. Experimental Validation

3.7.1. Experimental Setup

The experimental setup in this work is designed to allow the usage of the same control algorithms and devices to test and compare the IMPEI and the CPEI. Hence, a 48 kVA IMPEI in

Fig. 3-18 is developed for the proof of concept. The prototyped IMPEI is 60 A for propulsion mode and 30 A maximum grid current for G2V and V2G operations at 120 V, 240 V, and 208 V. This prototype is built using a total of six SKM75GB12V PESs. Passive components with similar specifications to Table 3-4 are taken from the laboratory. The CPEI of the exact specifications as the MPEI is obtained by bypassing the three upper switches of the IMPEI. To emulate the battery, a bidirectional programable power supply (California Instruments, model MX30-3PI) terminal voltage is set to 360 V and connected to a series resistance of 0.5 Ω. The developed experimental setup is shown in Fig. 3-19. A digital power meter, YOKOGAWA 2533, is used to measure the AC single-phase and three-phase powers, while the DC power is calculated using the DC voltage and current readings from FLUKE-289 and FLUKE-376 FC, respectively. More details on the prototyped IMPEI is provided in Appendix A.

3.7.2. Propulsion and Regenerative Braking Modes

a- Propulsion and Regenerative Braking

For this mode of operation, FOC is used to control a 5 hp PMSM in propulsion and regenerative braking modes. The motor was first brought up to 1200 r/min and then to zero r/min by applying the regenerative braking. The current limit for the controllers is set to 16 A ($i_{d\,max}^* = 0\,A, i_{q\,max}^* = 16\,A$). The experimental results (motor current, motor speed, battery voltage, and battery current) are shown in Fig. 3-20. It can be seen that expected results of 1200 r/min, 16 A limits, positive battery current during propulsion, and negative battery current during regenerative braking are obtained with the FOC technique. This validates the operation of the IMPEI in propulsion and regenerative braking modes using the same control as the CPEI. The real-time implementation of this control is provided in Appendix B and C.

b- Efficiency Comparison

For experimental efficiency comparison, the 5 hp SPMSM is brought to 1350 r/min by using a 150 hp dynamometer set in speed control mode. The SPMSM is controlled in torque mode. With this configuration, several torque values were applied to the dynamometer. Results for IMPEI and CPEI are obtained from the hardware setup, however, experimental results for the APEI of a similar power rating are taken from [83]. Here, the comparison is based on the power level. Fig. 3-21 shows the efficiency of the IMPEI and CPEI at several states of charges (SoCs). The assumed nominal and fully-charged voltages of the battery are 360 V and 390 V respectively. It
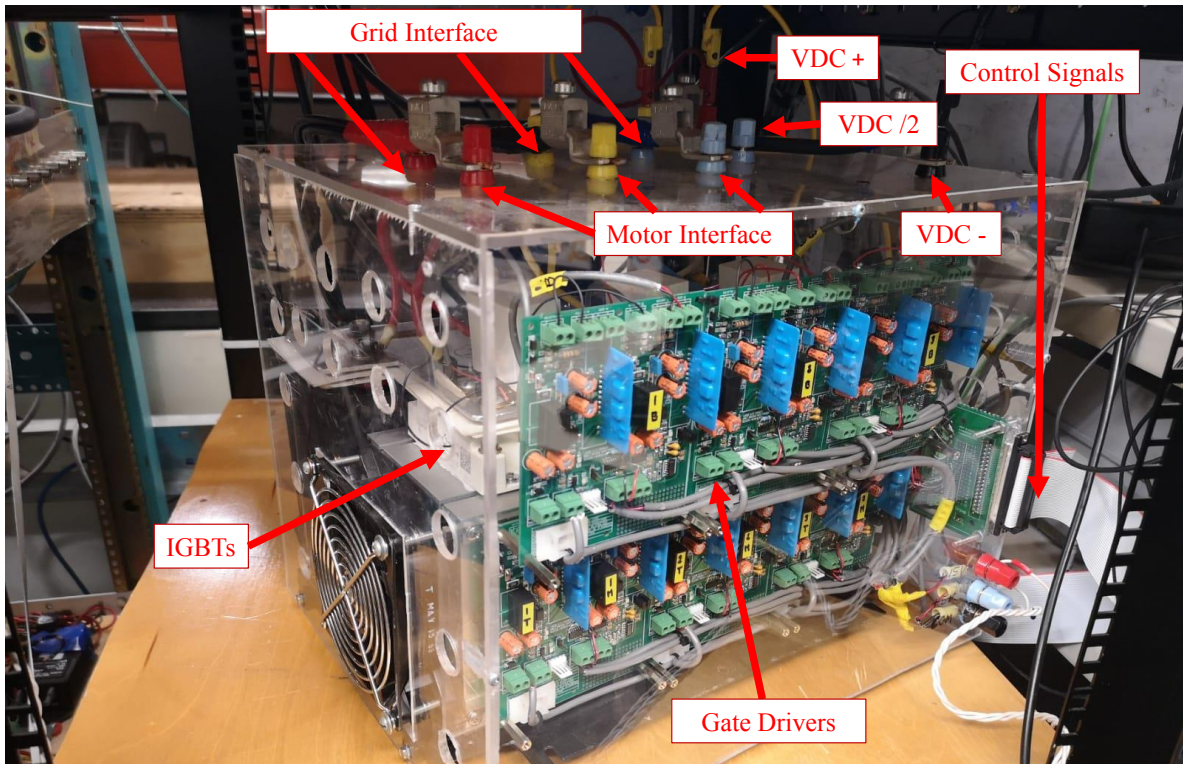
Fig. 3-18. Prototyped IMPEI.
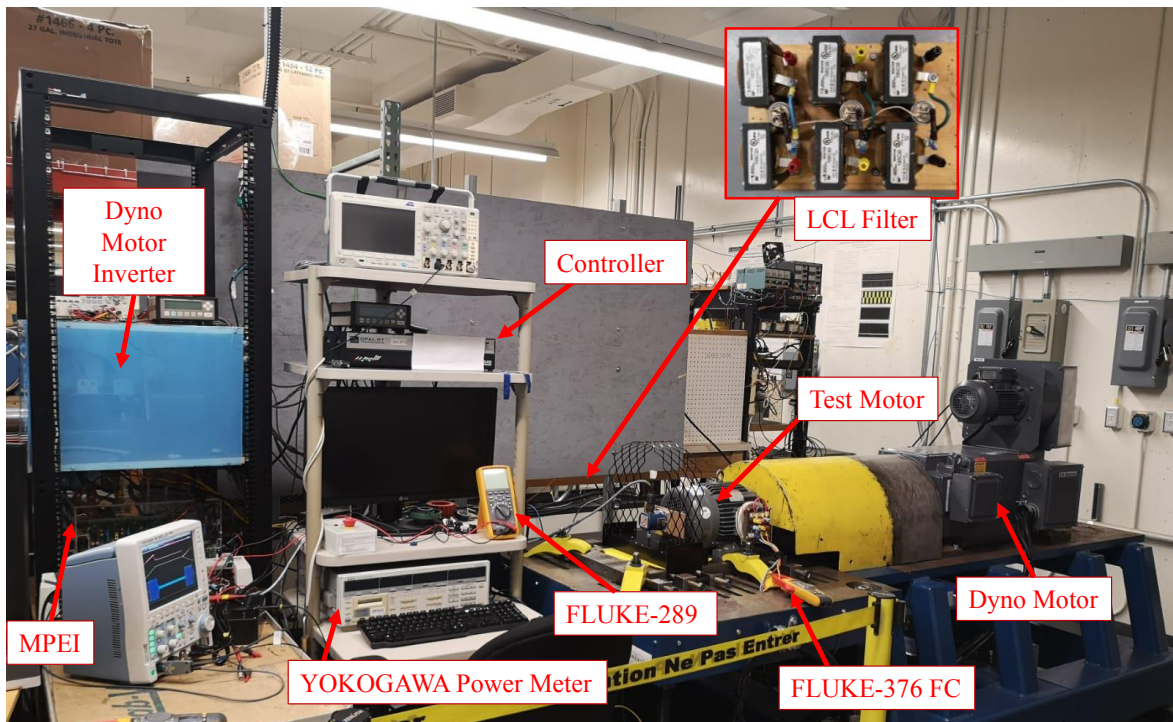
Fig. 3-19. Experimental setup.

can be seen in Fig. 3-21 that there is an efficiency drop between the CPEI and the IMPEI. This efficiency drop is in the range of 1% under the considered SoCs and power levels. The observed
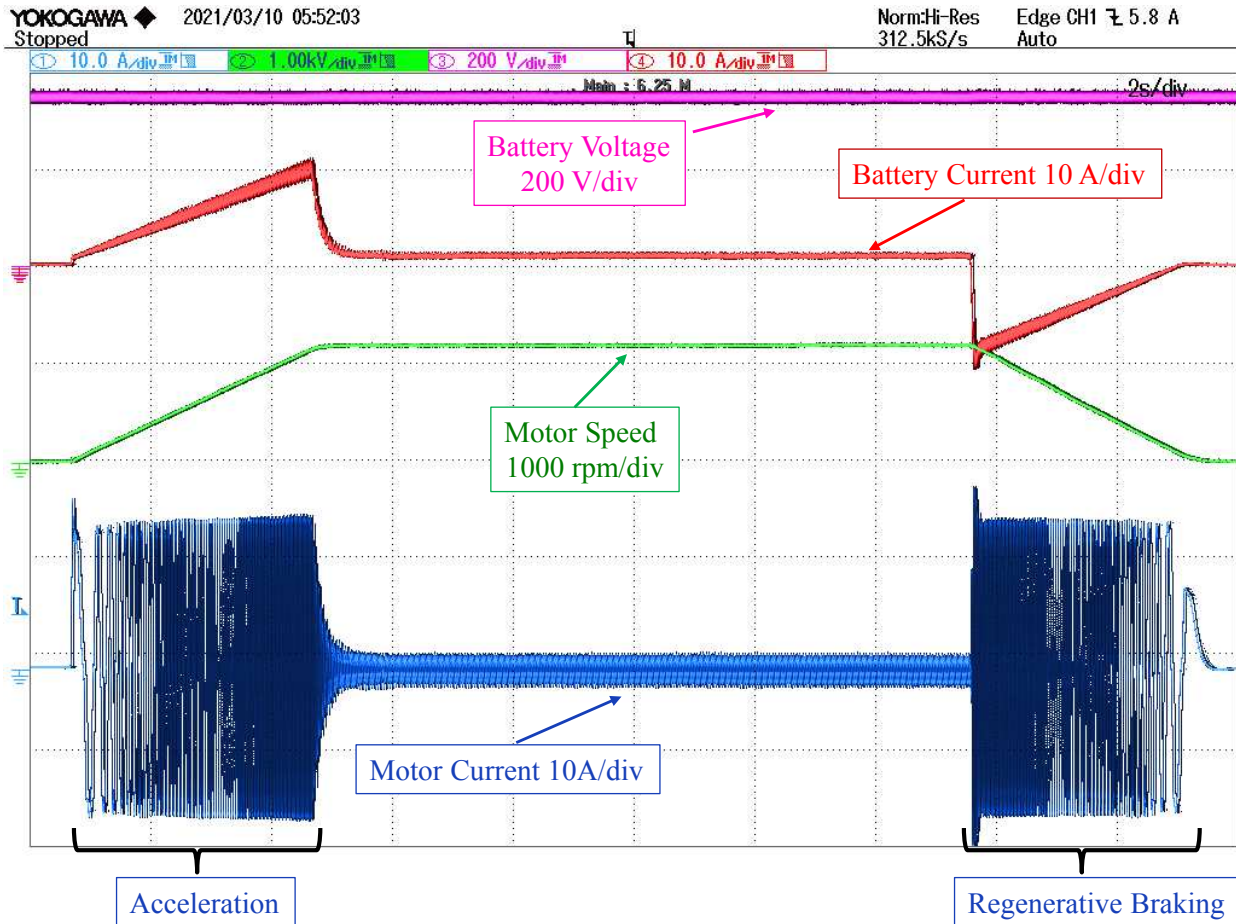
Fig. 3-20. Practical battery voltage and current, motor speed and phase current.

efficiency difference between the IMPEI and the CPEI is because the upper three PESs in the IMPEI are kept continuously ON. The APEI's battery voltage is 200 V, and the DC link voltage is 400 V [83]. Hence, comparing the efficiencies of the APEI, the CPEI, and the IMPEI at several power points in Fig. 3-21(a), it can be seen that the APEI has the lowest efficiency because of its cascaded nature and its higher number of PESs.

3.7.3. Three-phase V2G and G2V Modes

The IMPEI is controlled using FOC. The real-time implementation of this controller is provided in Appendix D. The equivalent circuit of this mode and the PESs status are illustrated in Fig. 3-2(d) and Table 3-1, respectively. Fig. 3-22 and Fig. 3-23 show the experimental results for G2V and V2G, respectively at 208 V. The obtained efficiencies in G2V and V2G modes are summarized in Table 3-6 along with the input powers at the measured efficiencies. The CPEI cannot provide this mode of operation as per Fig. 3-9. However, for efficiency studies, CPEI results are provided to evaluate the losses due to additional PESs in the IMPEI.
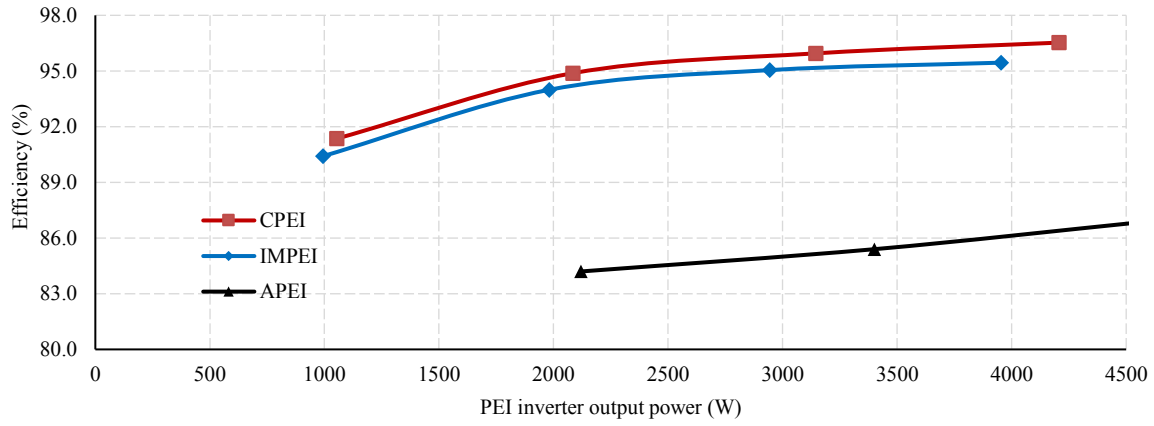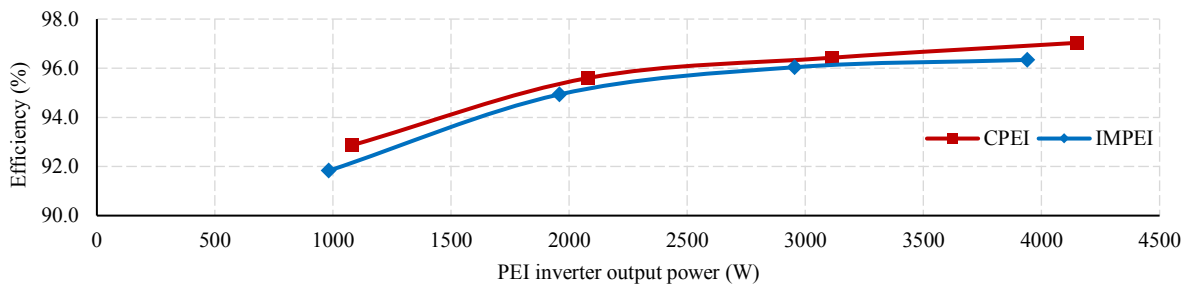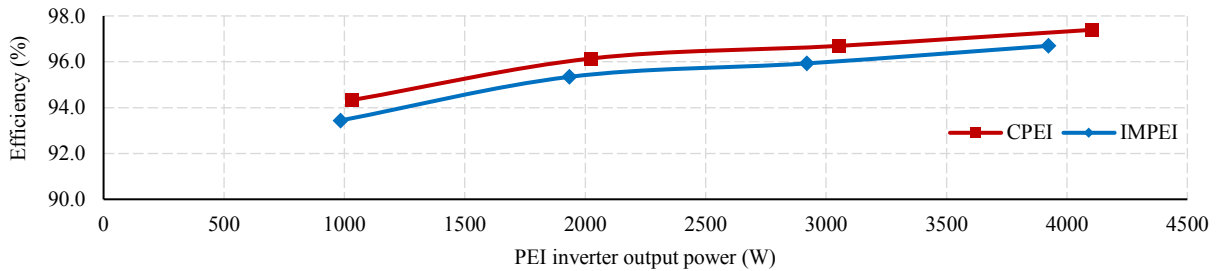
Fig. 3-21. Experimental PEIs efficiency comparison at different battery voltages (SoC): (a) rated voltage (360 V), (b) partially discharged (375 V), and (c) fully charged (390 V).

Table 3-6: Efficiency in Three-Phase G2V and V2G Modes.

	G2V (9.1 kW)	V2G (9.7 kW)
IMPEI	94.6%	96.1%
CPEI	95.2%	97.0%
Drop	0.6%	0.8%
Loss ratio	1.12	1.30

Table 3-6 shows that continuously conducting PESs in the IMPEI result in a less than 1% efficiency drop at full G2V and V2G capability of the IMPEI.

3.7.4. Single-phase V2G and G2V Modes

The two configurations in Fig. 3-2(b) have been used to evaluate and validate these modes of operation. Due to the limitation in the available grid capability in terms of protection (circuit breaker rating), the current drawn from or fed to the grid is limited to 12 A in this experiment.
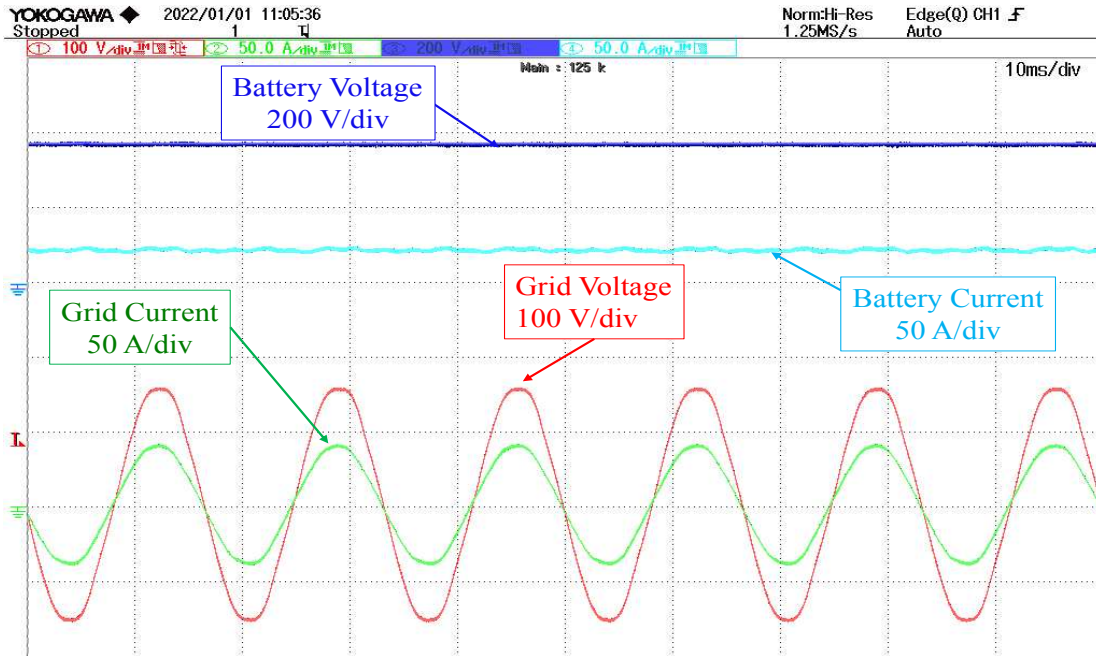
Fig. 3-22. Experimental three-phase G2V results: battery voltage and current, grid voltage and current (phase a).
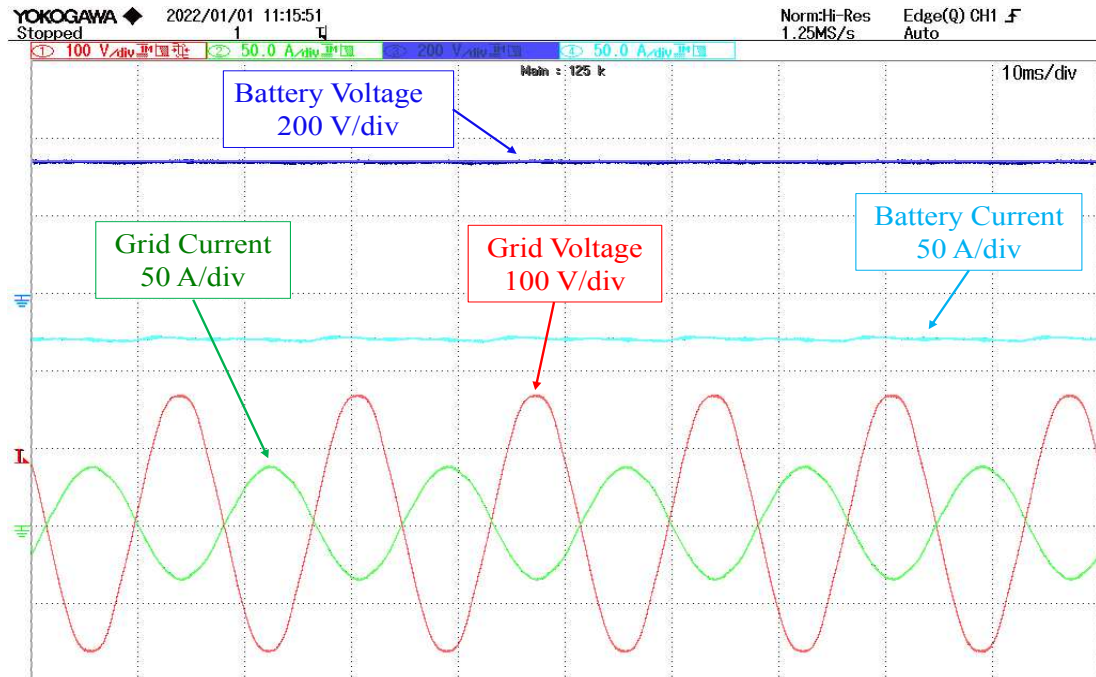
Fig. 3-23. Experimental three-phase V2G results: battery voltage and current, grid voltage and current (phase a).

a- Full-bridge configuration at 120 V

Results for G2V and V2G operations are shown in Fig. 3-24 and Fig. 3-25, respectively. DC bus voltage, battery current, and grid voltage and current of the IMPEI in both modes are shown. Efficiencies are summarized in Table 3-7. The input power levels are indicated as well. Power factors of 0.99 and 0.98 are obtained in G2V and V2G modes, respectively. The modeling and
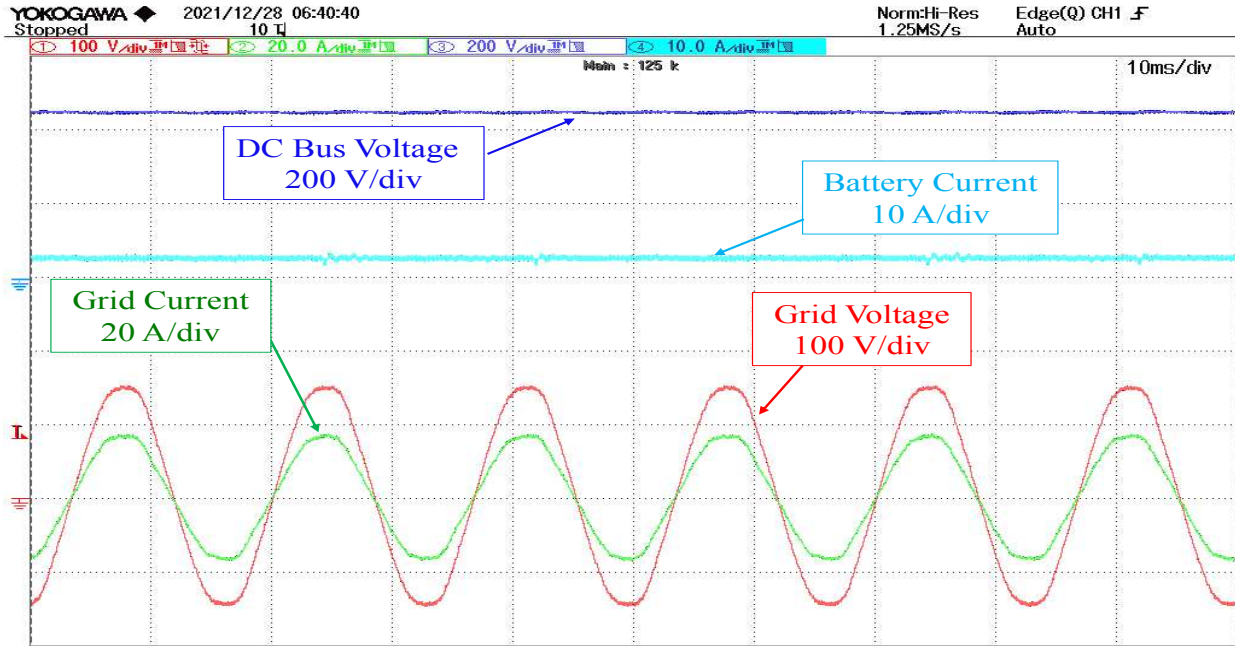
Fig. 3-24. Experimental G2V results with single-phase full-bridge AFEC at 120 V: battery voltage and current, and grid voltage and current.
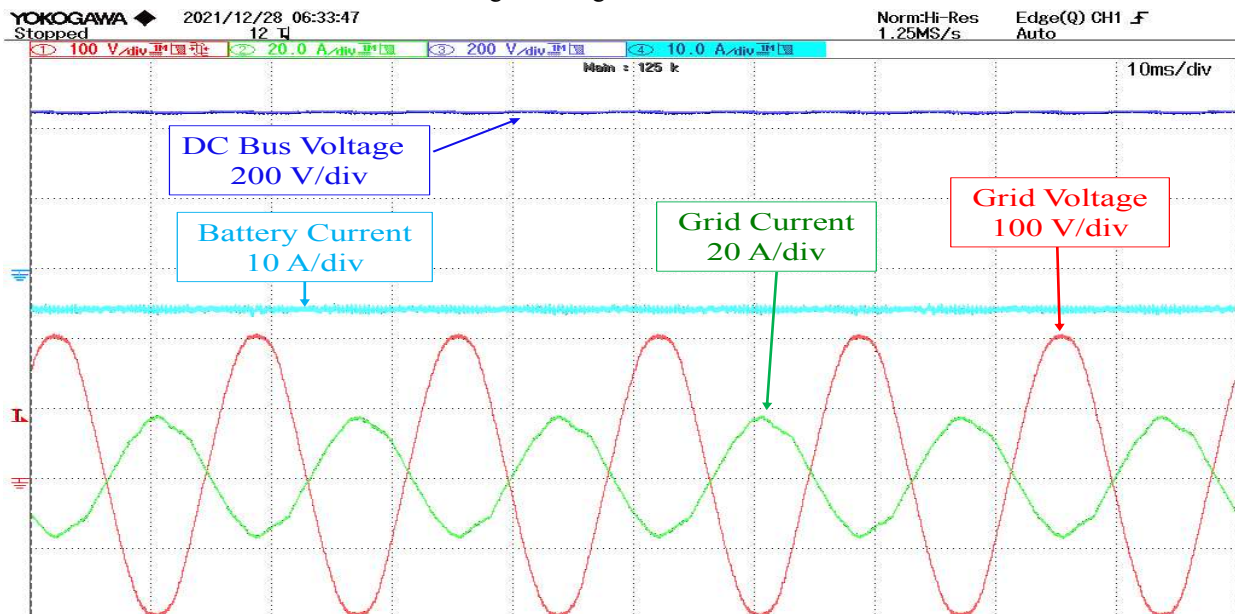
Fig. 3-25. Experimental V2G results with single-phase full-bridge AFEC at 120 V: battery voltage and current, and grid voltage and current.

control of the IMPEI in Level-1 and Level-2 V2G and G2V based on [70] is presented in Appendix E. The real-time implementation of this controller is provided in Appendix F.

Table 3-7: Efficiency in Single-Phase 120 V G2V and V2G Modes using Full-Bridge Configuration.

	G2V (1.3 kW)	V2G (2.0 kW)
IMPEI	82.3%	85.7%
CPEI	83.7%	86.5%
Drop	1.4%	0.8%
Loss ratio	1.08	1.06

As shown in Table 3-7, the difference in efficiency between the IMPEI and the CPEI is negligible and decreases as the power increases.

b- Half-bridge configuration at 120 V

Results for G2V and V2G operations of the IMPEI are shown in Fig. 3-26 and Fig. 3-27, respectively. Obtained efficiencies in G2V and V2G modes are summarized in Table 3-8. The input power at the measured efficiencies is also provided. The real-time implementation of this controller is provided in Appendix E.

Table 3-8: Efficiency in Single-Phase 120V G2V and V2G Modes using Half-Bridge Configuration.

	G2V (1.3 kW)	V2G (2.0 kW)
IMPEI	85.1%	92.7%
CPEI	85.6%	93.0%
Drop	0.5%	0.3%
Loss ratio	1.03	1.04

Table 3-8 shows that the half-bridge configuration is more efficient than the full-bridge configuration. The power factors are 0.99 and 0.98 in G2V and V2G modes, respectively.

c- Full-bridge configuration at 240 V

To realize this mode, a transformer is used to generate 240 V from 120 V. The current drawn from or fed to the grid is limited to 7.5 A. Results for G2V and V2G operations of the IMPEI are shown in Fig. 3-28 and Fig. 3-29, respectively. The real-time implementation of this controller is provided in Appendix E. Obtained efficiency in G2V and V2G modes are summarized in Table 3-9. The input power at the measured efficiencies is also provided. The power factor is 0.98 in G2V mode and 0.92 in V2G mode. The efficiency difference between the CPEI and the IMPEI is similar to that obtained in Table 3-7. The distortion observed on the grid current is caused by the added transformer and the variable autotransformer to generate 240 V from a 120 V grid.
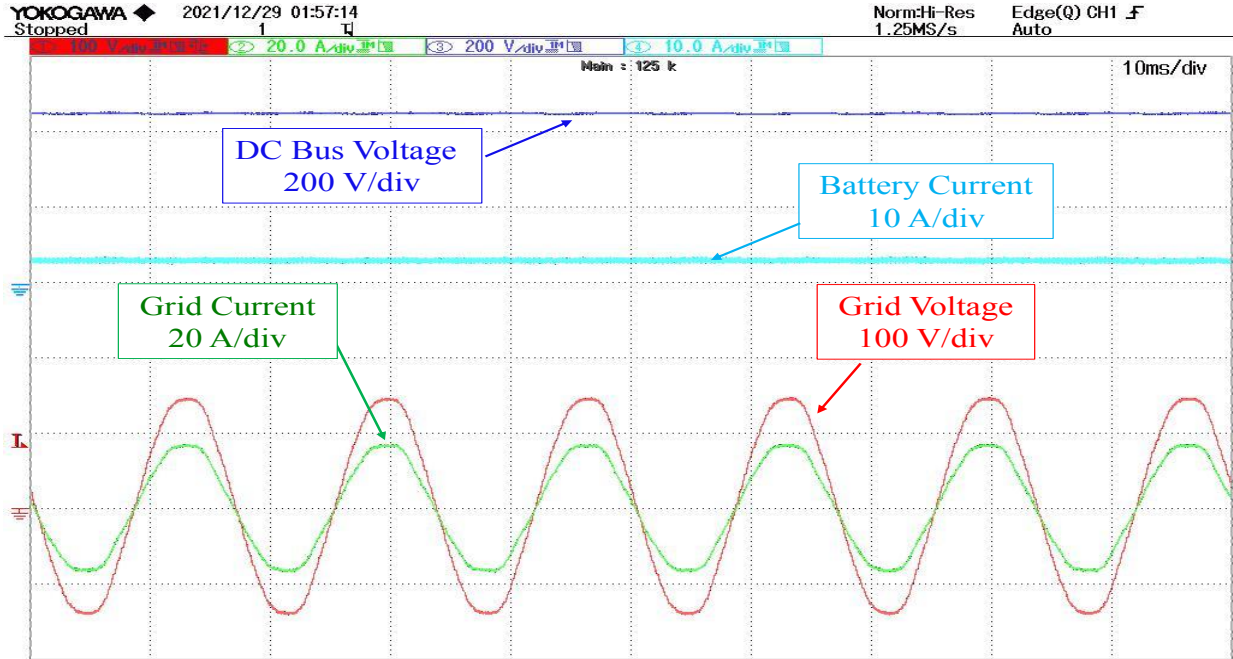
Fig. 3-26. Experimental G2V results with single-phase half-bridge AFEC at 120 V: battery voltage and current, and grid voltage and current
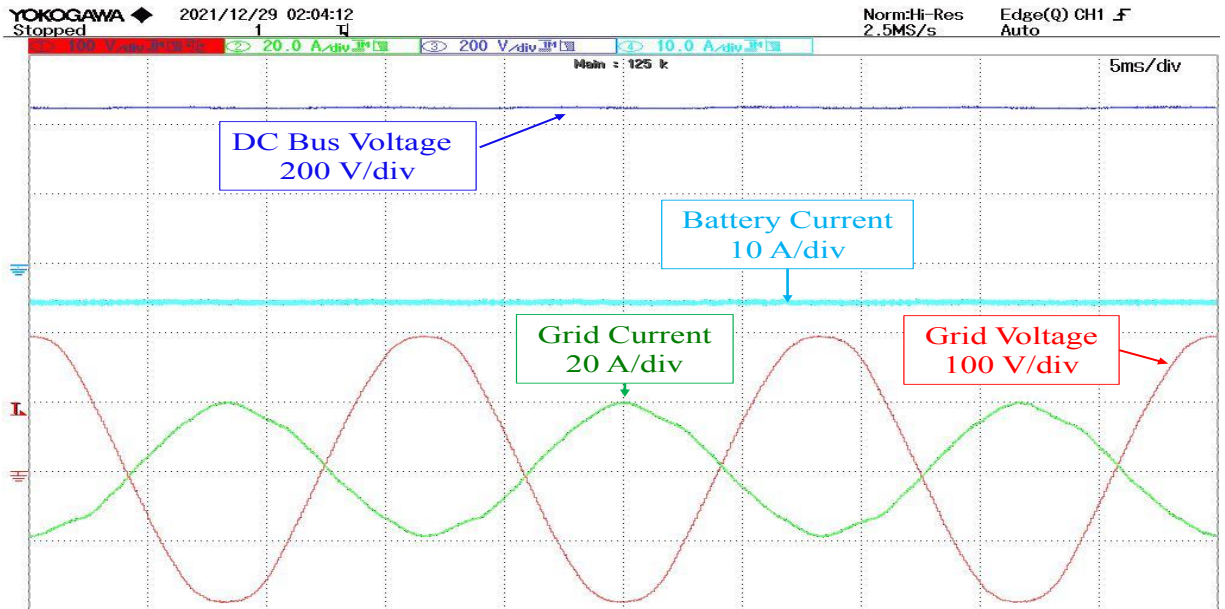
Fig. 3-27. Experimental V2G results with single-phase half-bridge AFEC at 120 V: battery voltage and current, and grid voltage and current

Table 3-9: Efficiency in Single-Phase 240 V G2V and V2G Modes using Full-Bridge Configuration.

	G2V (1.5 kW)	V2G (2.2 kW)
IMPEI	87.2%	90.3%
CPEI	88.8%	91.0%
Drop	1.6%	0.7%
Loss ratio	1.14	1.08
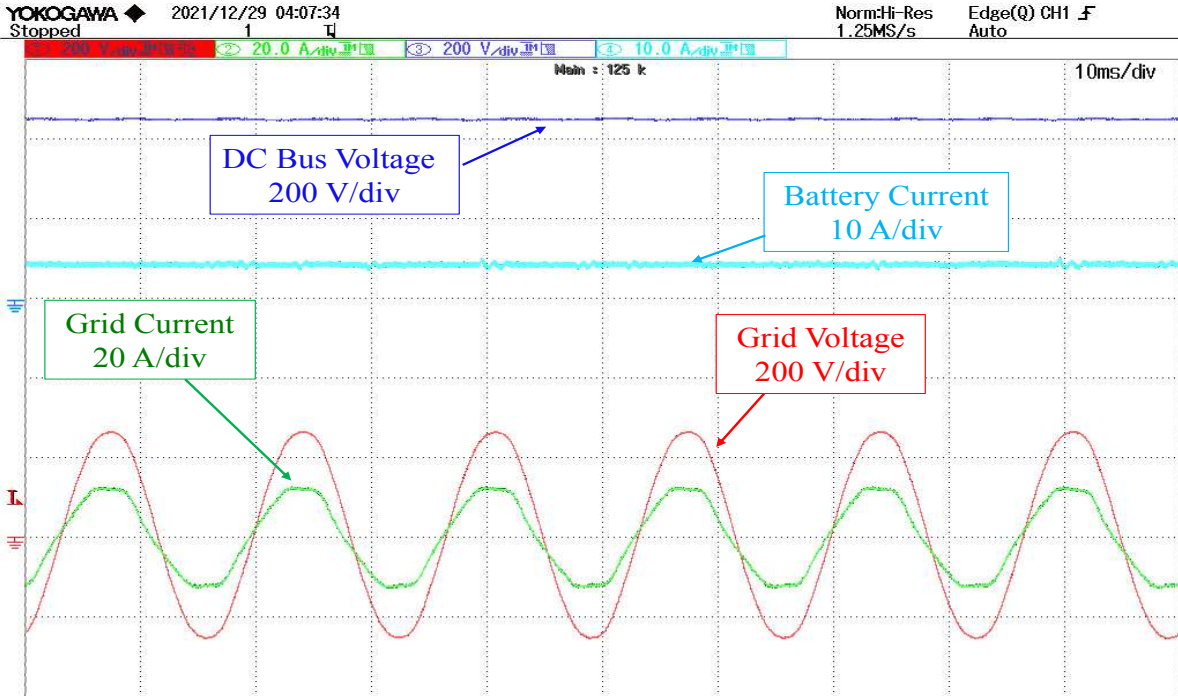
Fig. 3-28. Experimental G2V results with single-phase full-bridge AFEC at 240 V: battery voltage and current, and grid voltage and current
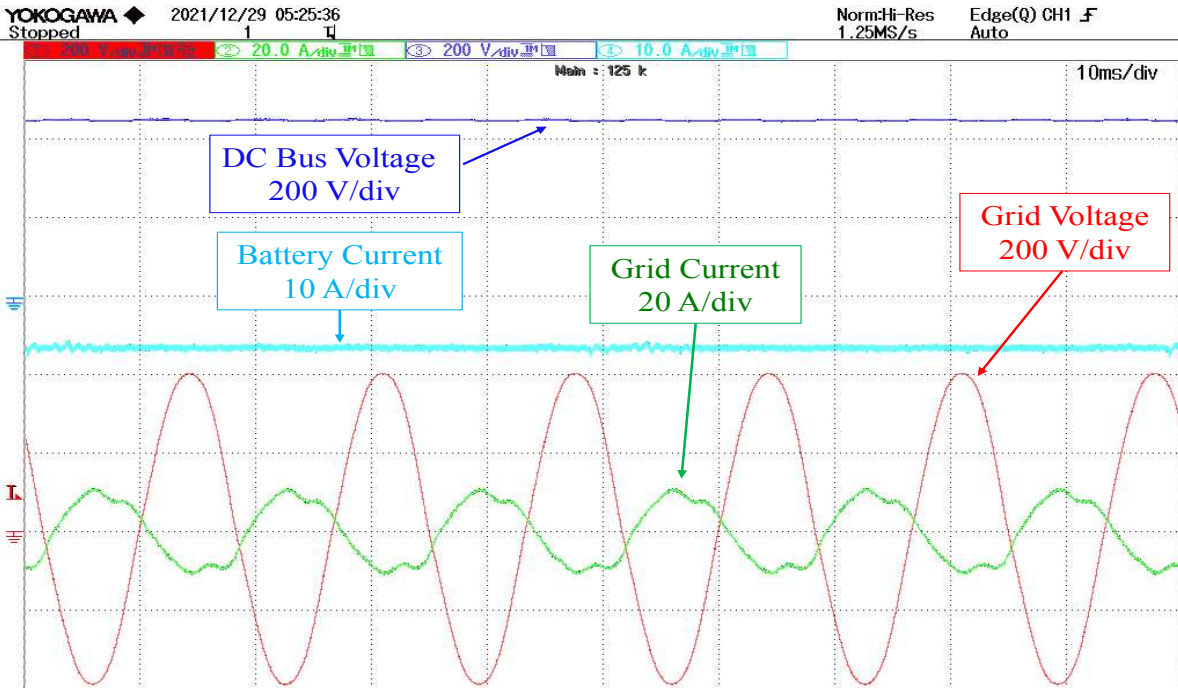
Fig. 3-29. Experimental V2G results with single-phase full-bridge AFEC at 240 V: battery voltage and current, and grid voltage and current

3.8. Summary

The integrated multipurpose power electronics interface (IMPEI) designed for PHEVs and EVs was analyzed and compared to several other integrated power electronics interfaces (IPEIs) and the conventional power electronics interface (CPEI) in this chapter. Analyses and measurements have revealed that the IMPEI has the highest flexibility in modes of operation and can be reconfigured to interface with various grid systems in both vehicle-to-grid (V2G) and grid-to-vehicle (G2V) modes. This is accomplished by using the flexible IPEI topology and its associated control strategies. The IMPEI and other topologies were compared in terms of configuration, device count, cost, and efficiency, using BMW i3 as the benchmark application. The design requirements are presented and discussed including modes of operation, switch and passive element sizing, and ratings. According to the findings of this study, the IMPEI, among other IPEIs, has a low switch count, more flexibility in operating modes (propulsion, regenerative braking, single-phase and three-phase V2G and G2V), and high efficiencies. It has also been demonstrated that the IMPEI is cost-effective and easy to implement. The results of experiments in propulsion, regenerative braking, and single-phase and three-phase V2G and G2V were presented. The experimental efficiency analysis was also carried out in the propulsion, V2G, and G2V modes. The difference in efficiency between the IMPEI and the CPEI was quantified. This chapter validates the IMPEI concept and demonstrates that the IMPEI's reconfigurability offers an acceptable trade-off in terms of charging capability, grid flexibility, efficiency, and cost.

Chapter 4. Drive Cycle Analysis of Renault Twizy

4.1. Introduction

This chapter investigates the drive cycle efficiency and fuel economy of the Renault Twizy drivetrain using a new motor and the IMPEI inverter proposed in Chapter 3. Pictures of the Renault Twizy are shown in Fig. 4-1. The load requirement of the drivetrain is illustrated in Fig. 4-2. The base speed is (n_b) is $3400\ r/min$, the rated torque is (T_e) is $20\ Nm$, and the max speed is (n_{max}) is $10000\ rpm$. The machine is required to operate at a constant power in the field weakening region. The nominal battery voltage of the car is 96 V. For this EV, the main drivetrain components are shown in Fig. 4-3. As shown in Fig. 4-3, there are four main components of the Twizy electric drive namely; the battery, the inverter (power electronics), the electric motor, and the mechanical system. To evaluate the potential fuel economy of the Twizy measured in kWh/100 km or liter/100 km, two methods can be used: a direct method and an indirect method.

The direct method consists of running the EV and measuring the net battery energy used and the traveled distance. Since the fuel economy of the EV depends on the type of drive cycle (city, highway, mountain, etc.), this method requires driving the EV over long distances and under various terrain and weather conditions (temperatures). This method is, therefore, expensive and time-consuming. For proper fuel economy analysis, EV Dynamometers can be used by applying standardized test procedures that combine different drive cycles, terrain, and weather conditions such as the new European driving cycle (NEDC), the worldwide harmonized light vehicle test procedure (WLTP), and the environmental protection agency (EPA) test.

The second method is based on the efficiencies of the aforementioned main drivetrain components at each operating point. This leads to battery, inverter, electric motor, and mechanical system efficiency maps. This method is mainly used for estimation. The efficiency data is primarily available from design software and can also be obtained experimentally. This method also provides more information on the drivetrain.

This chapter analyses the Twizy EV drivetrain using the IMPEI and a new IPMSM. The newly designed drivetrain is investigated for potential fuel economy and drive cycle efficiency using direct and indirect methods. It is assumed that the mechanical system remains unchanged and the battery pack is already selected. Therefore, the motor and its inverter have to be designed. For this, the motor and its power electronics have been designed using the proposed approach and

(a)   (b)
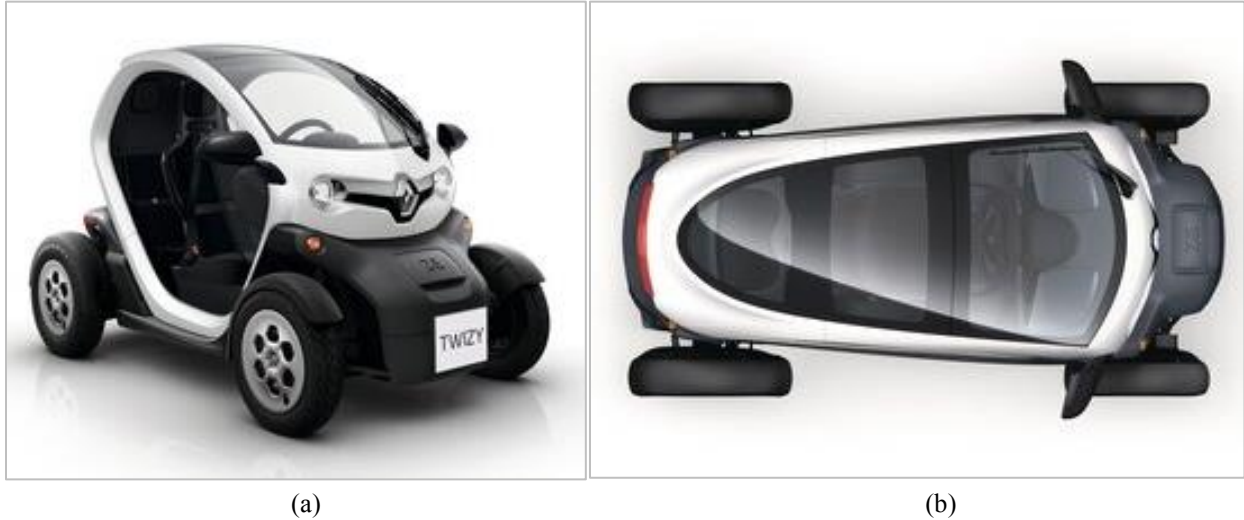
Fig. 4-1. Renault Twizy: (a) diagonal view, (b) top view [107].
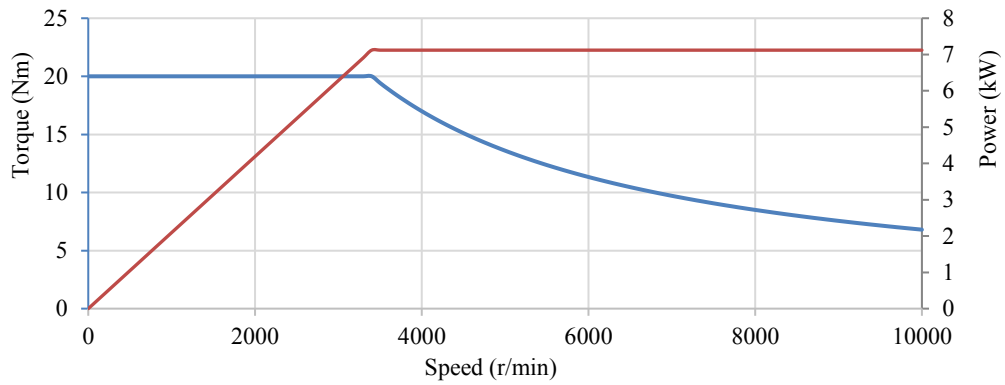
Fig. 4-2. Torque/power-speed requirement of Renault Twizy.
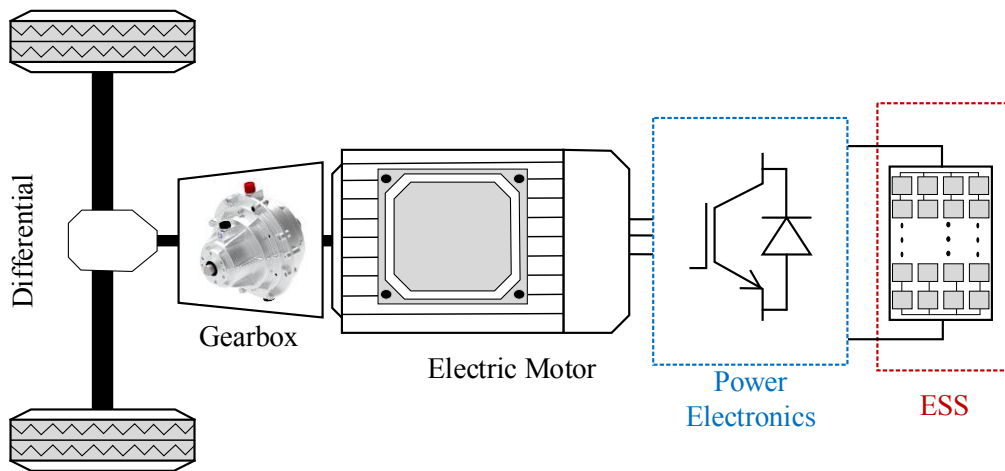
Fig. 4-3. Main drivetrain components of Renault Twizy.

PEI in Chapter 2 and Chapter 3, respectively. The IMPEI proposed in Chapter 3 serves as the drive inverter and the charger for the Twizy.

To be on the safe side, the m_{max} is selected to be 0.9. The rated conditions are chosen as 3500 r/min and 21 Nm. 10100 r/min has been selected to be the maximum speed at the rated power. The obtained feasible parameters for a ten pole SPMSM are listed in Table 4-1. The estimated torque-speed and power-speed operating envelopes are shown in Fig. 4-4. The voltage-speed circles for the base and maximum speeds, the current limit circles, and the constant torque curves for the designed SPMSM are shown in Fig. 4-5. As discussed in Chapter 2, the SPMSM parameters serve as the base for calculating the equivalent IPMSM parameters.

Table 4-1: SPMSM Drive Specifications.

Parameters	Desired	Calculated	Unit
V_o	-	49.85	V
V_{phrms}	-	35.25	V
V_{llrms}	-	61.06	V
A	-	1.43	-
B	-	1.75	-
C	-	102.97	A
k	-	1.00	-
pf	-	82.05	%
$I_s = I_{s_{SPMSM}}$	-	125.49	A
I_{ch}	-	180.14	A
$\lambda_{af} = \lambda_{af_{SPMSM}}$	-	0.0223	Wb-turn
$L_s = L_{d_{SPMSN}}$	-	123.91	μH
C_1	-	-2149.30	-
C_2	-	$-2.02x10^{17}$	-
C_3	-	$1.20x10^{11}$	-
C_4	-	$6.73x10^{10}$	-
ω_{sb}	1832.6	1832.60	rad/s
ω_{smax}	5288.3	5288.30	rad/s
ω_{scri}	-	7362.10	rad/s
T_{er}	21	21.01	Nm

For the IPMSM design, concentrated windings have been chosen over distributed windings because of the advantages listed in Table 4-2. To reduce the effect of the significant harmonic content, which usually results in increased eddy current losses, present in the magnetomotive force (MMF), soft magnetic composite (SMC) materials have been used in the stator. Since this type of winding leads to a low saliency ratio, using the conventional IPMSM magnet layout is not feasible. Also, laying the magnets on the surface of the rotor is not good for high-speed operations. Therefore, the spoke type IPMSM was selected.
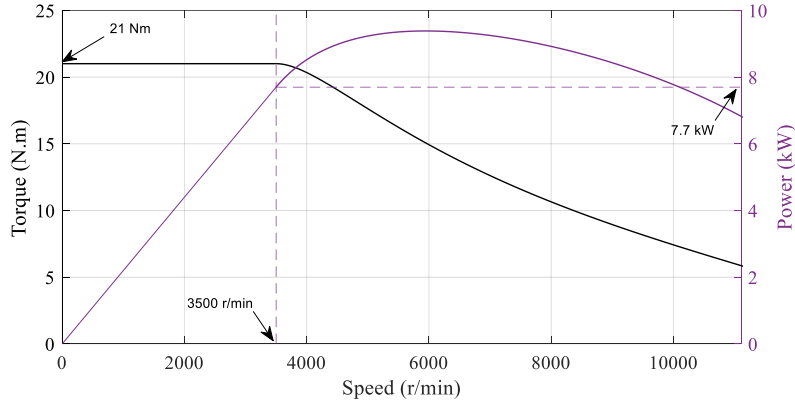
Fig. 4-4. Estimated toque-speed and power speed operating envelopes of Twizy SPMSM.
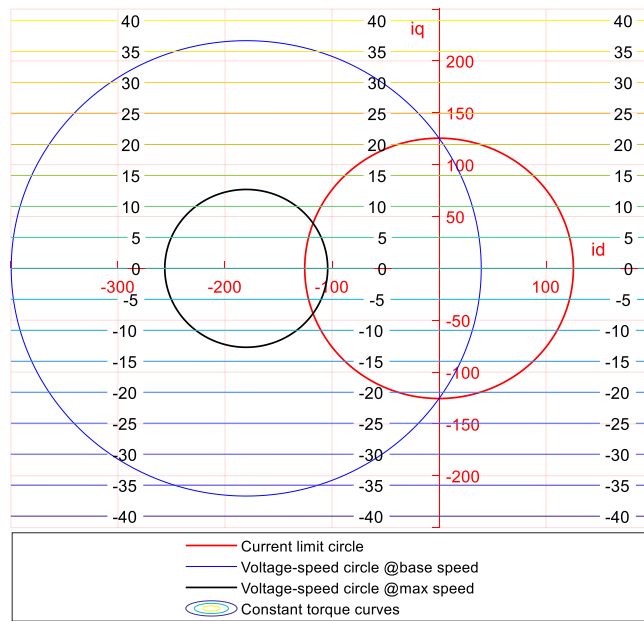
Fig. 4-5. Voltage-speed circles for nb and $nmax$, current limit circle, and constant torque curves of Twizy SPMSM.

Table 4-2: Concentrated versus Distributed Windings [12].

	Concentrated Windings	Distributed Windings
End turn length	short non-overlapping	long overlapping
Slot fill factor	high (0.5 ~ 0.65)	low (0.35 ~ 0.45)
Copper loss	small	large
Working harmonic	higher order	fundamental
MMF harmonics	large	small
Even harmonics	present	absent
Saliency ratio	small	large
Power density	relatively small	large
PM loss	large	small
PM usage	large	small
Suitable PM location	surface or slightly imbedded	surface or interior
Convenience in winding	easy	complex
Mutual inductance	small	large
Fault tolerance	high	low

75

The equivalent parameters for the IPMSM are calculated using a saliency ratio of 1.02. The obtained parameters are summarized in Table 4-3. They meet the design requirement. The estimated torque-speed and power-speed operating envelopes of the spoke type IPMSM with concentrated windings are shown in Fig. 4-6. The corresponding voltage-speed ellipses for the base and maximum speeds, current limit circle, and constant torque curves for the designed IPMSM are shown in Fig. 4-7. The initial steps for the Twizy drivetrain design are therefore completed. The main parameters needed in the design of the specified Twizy motor using the FEA software are obtained. This provide the efficiency map of the motor. Also, the power electronics can be designed and tested from this point onward to obtain the efficiency map.
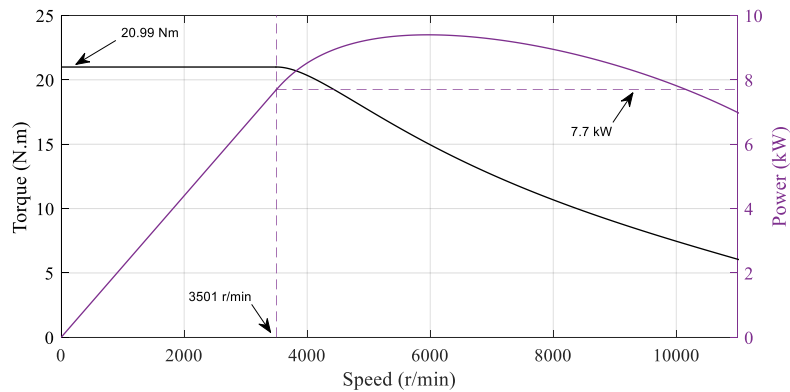
Fig. 4-6. Estimated toque-speed and power speed operating envelopes of Twizy SPMSM.
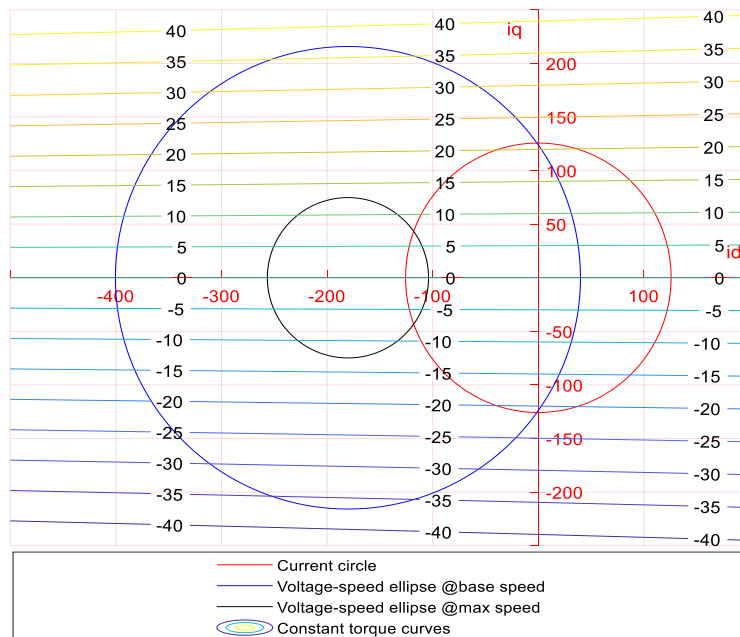
Fig. 4-7. Voltage-speed circles for nb and $nmax$, current limit circle, and constant torque curves of Twizy SPMSM.

Table 4-3: IPMSM Drive Specifications.

Symbol	Desired	Calculated	Unit
S_r	-	1.02	-
$n_{sb_{Sr}}$	-	3496.10	r/min
$T_{e_{Sr}}$	-	20.99	Nm
I_{cst}	-	$100.16x10^{-2}$	-
A_c	-	$99.7x10^{-2}$	-
$\lambda_{af_{IPMSM}}$	-	0.0223	Wb-turn
$L_{d_{IPMSM}}$	-	123.54	μH
$L_{q_{IPMSM}}$	-	126.02	μH
$T_{er_{IPMSM}}$	207	20.99	Nm
$n_{sb_{Sr_{IPMSM}}}$	2767.86	3501.00	r/min
$I_{S_{IPMSM}}$	-	125.69	A

4.2. IMPEI Efficiency Map

This section designs and evaluates the efficiency of the IMPEI drive inverter. Based on the information provided in Table 4-1 and Table 4-3, devices in the IMPEI can be selected. The device current rating is selected so that (4. 1) is matched.

$$I_{PES} \geq 1.5\, I_{S_{IPMSM}}\,.$$
4. 1

MOSFETs are selected for this application because of the voltage level of the drive. For the voltage rating of the PESs, the fully charged battery voltage ($V_{DC_{max}}$) is assumed to be 10% higher than its nominal value. Therefore, the PESs voltage rating is based on (4. 2).

$$V_{PES} \geq 1.5\, V_{DC_{max}}$$
4. 2

Since the IMPEI also serves as a charger, the DC bus voltage during charging should be considered. Based on the IMPEI design chart, which is shown in Fig. 3-8, only level 1 charging can be included in the modes of operation of the IMPEI due to the battery voltage level. Hence, using (3. 1), the DC bus voltage during the charging operation (V_{DC_Charge}) can be estimated. Equation (4. 2) becomes

$$V_{PES} \geq 1.5 MAX\left\{V_{DC_{max}}, V_{DC_{Charge}}\right\}.$$
4. 3

Table 4-4: IMPEI Specifications.

Parameters	Specifications
I_{PES}	≥ 188.53 A
$V_{DC_{max}}$	105.6 V
V_{DC_Charge}	195.15 V
V_{PES}	≥ 292.74 V

For the specifications in Table 4-4, IXFH100N30X3-ND MOSFET has been selected. This MOSFET has a drain to source voltage of 300 V with a current capability of 100 A at $25°\,C$ junction temperature. Based on the datasheet, this PES is able to carry its rated current up to $60°\,C$ junction temperature. The maximum value of its drain to source resistance at $25°\,C$ as per the datasheet is 13.5 mΩ with a typical value of 10.6 mΩ. At $60°\,C$, it is between 14.84 mΩ and 18.90 mΩ.

To meet the design specifications, three IXFH100N30X3-ND MOSFETs have been paralleled to form a switch having a 300 V drain to source voltage withstanding capability and 300 A rating. By doing so, the typical value of the drain to source resistance has been decreased to 3.53 mΩ. The following formula approximates the required heatsink thermal resistance [87].

$$\Theta_{sa} \leq \frac{T_j - T_a}{Q} - \left(\Theta_{jc} + \Theta_{cs}\right),$$

4. 4

where Θ_{sa} is the sink to ambient temperature thermal resistance, Θ_{jc} is the junction to case thermal resistance, and Θ_{cs} is the case to sink thermal resistance. T_j is the maximum junction temperature, and T_a is the maximum ambient temperature. Q is the power dissipated by the device. For simulation, the Wakefield-Vette (127709) heatsink having a value of $\Theta_{sa} = 0.85°\,C/W$ at natural convection is used. Since the practical heatsink will have a blower fan connected to it, Θ_{sa} will reduce. This will increase the heatsink efficiency.

PSIM simulation software has been used to estimate the losses of the designed IMPEI throughout the operating envelope of the Twizy motor. The drivetrain circuit layout as well as the control, are illustrated in Fig. 4-8. PESs in Fig. 4-8.a are constituted by three parallel IXFH100N30X3-ND MOSFETs. The settings of individual IMPEI PESs are shown in Fig. 4-9. Almost all the available information in Fig. 4-8.a is taken from the datasheet. The PMSM parameters are taken from Table 4-3. The control of the drive provided in Fig. 4-8.b is based on [66].
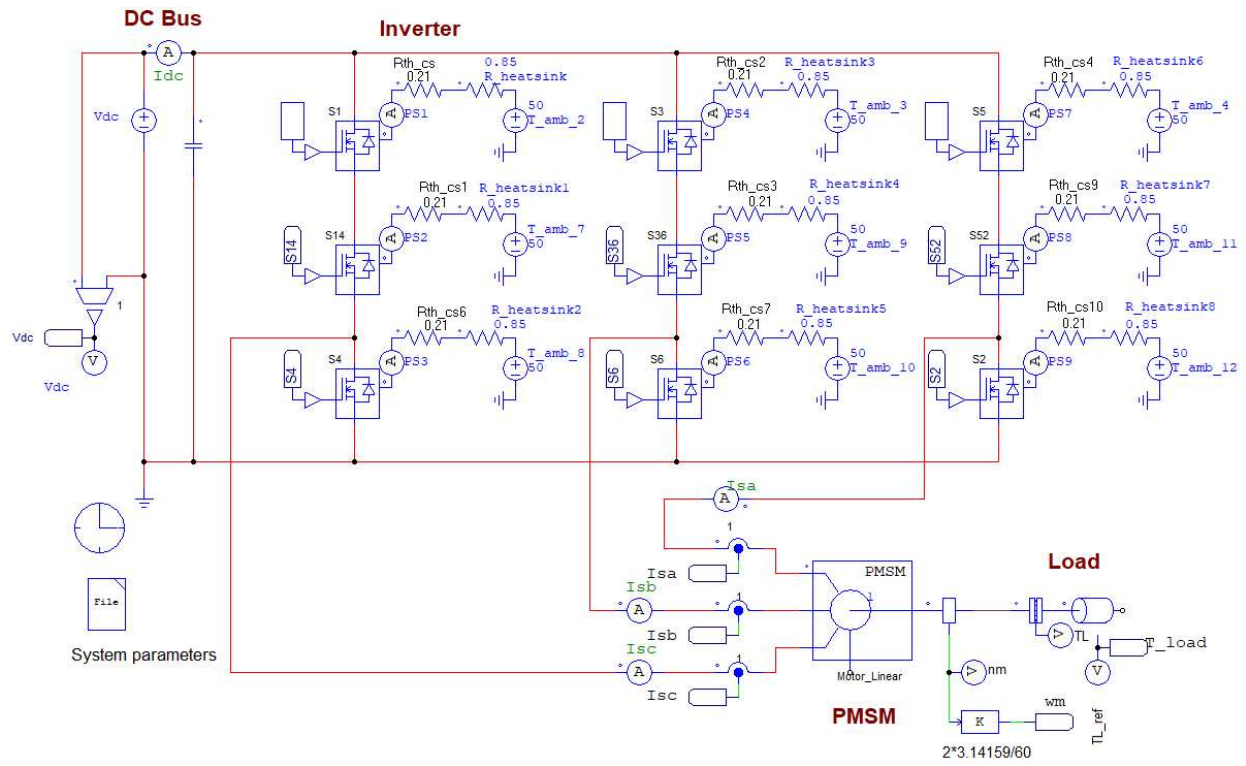
(a)
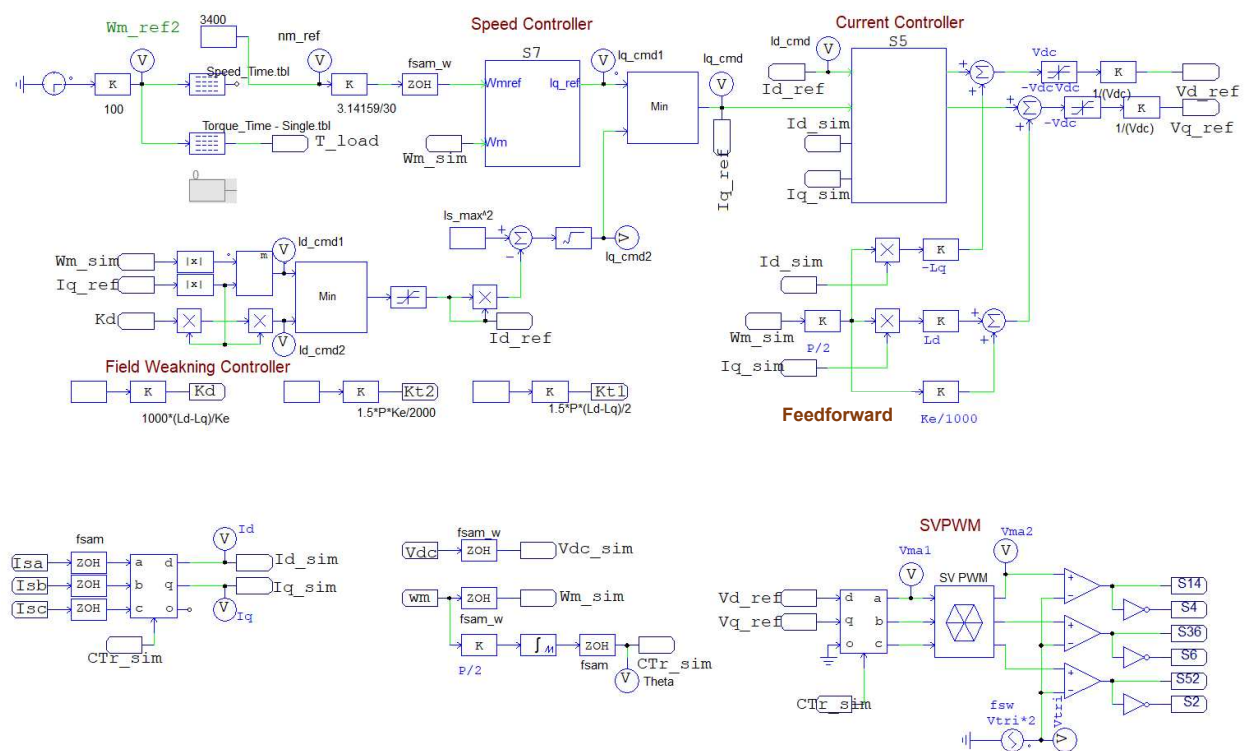
(b)

Fig. 4-8. PSIM schematics of the Twizy drivetrain with the IMPEI: (a) drivetrain circuit, (b) PMSM control diagram including field weakening.
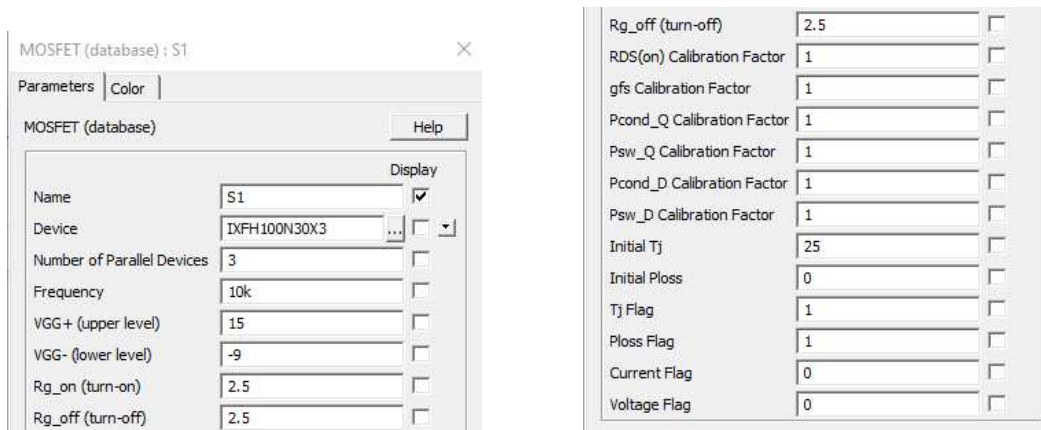
Fig. 4-9. Switch settings.

The operating envelope is obtained by accelerating the motor from zero to its maximum speed. The selected moment of inertia of the drivetrain is $J = 0.00179 \ kg.m^2$. The obtained results are shown in Fig. 4-10. It can be seen that the maximum speed is obtained in Fig. 4-10(a) and that the controller is able to transition from the maximum torque per ampere (MTPA) region into the field weakening region as shown in Fig. 4-10(b) and Fig. 4-10(c). Also, the commanded i_d and i_q are perfectly tracked, as depicted in Fig. 4-10(d). This validates the ability of the controller to help run the drivetrain at the desired operating point for recording the efficiency of the IMPEI.

To plot the efficient map of the IMPEI, efficiencies at serval operating points have to be recorded. For this purpose, at each incremental speed of 500 r/min, the torque is increased from zero to the maximum possible torque. The maximum possible torque is obtained at the point where the speed cannot be held constant by the controller. This usually happens in the field weakening region where the torque developed by the motor is lower than its rated torque.

A case study at the base speed has been performed to investigate the losses of the IMPEI. Fig. 4-11 shows the loss measurement process at the rated speed. The motor has been brought to the desired speed as depicted in Fig. 4-11(a). Then, the load torque is increased linearly from zero to the rated torque, as shown in Fig. 4-11(b). The torque related to the friction and windage has been neglected by setting the friction coefficient to zero. Recorded losses of the PESs in the IMPEI have been summed to obtain the total loss of the PESs, as illustrated in Fig. 4-11(c). The instantaneous current waveforms are plotted in Fig. 4-11(d). The losses of each switch in the A-phase leg (S1, S14, and S4) have been analyzed to validate the accuracy of the model. For S1, results are shown in Fig. 4-12. From Fig. 4-12(a) and Fig. 4-12(c), it can be seen that there is
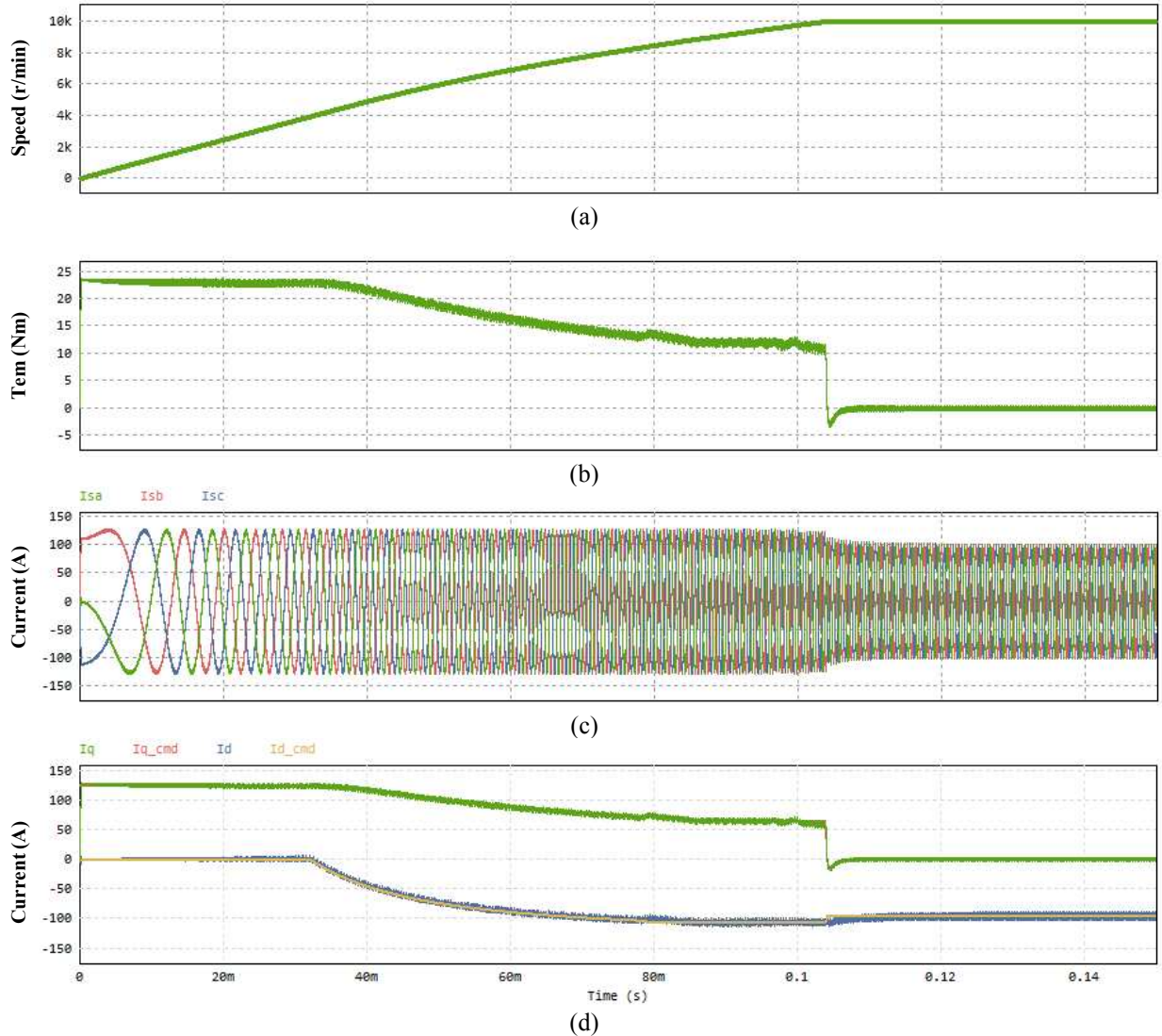
Fig. 4-10. Operating envelope: (a) speed, (b) electromechanical torque, (c) instantaneous phase currents, and (d) control currents using the FOC.

neither diode conduction nor switching losses. This is expected since the MOSFETs are selected to have a forward diode bias voltage higher than the product of the drain current and the ON resistance. Also, the switching losses are absent since S1 is always kept turned ON, as seen in Fig. 4-12(d). The only losses in S1 are the switch conduction loss, as depicted in Fig. 4-12(b) and Fig. 4-12(e).

For S14, which is the middle switch, the losses are depicted in Fig. 4-13. As seen from Fig. 4-13(d), extra switching losses have been observed as compared to S1. Similar results have been observed in Fig. 4-14(d). These losses are negligible due to the selected switching frequency. Therefore, the total losses in S1 and S14 are mainly due to conduction losses.
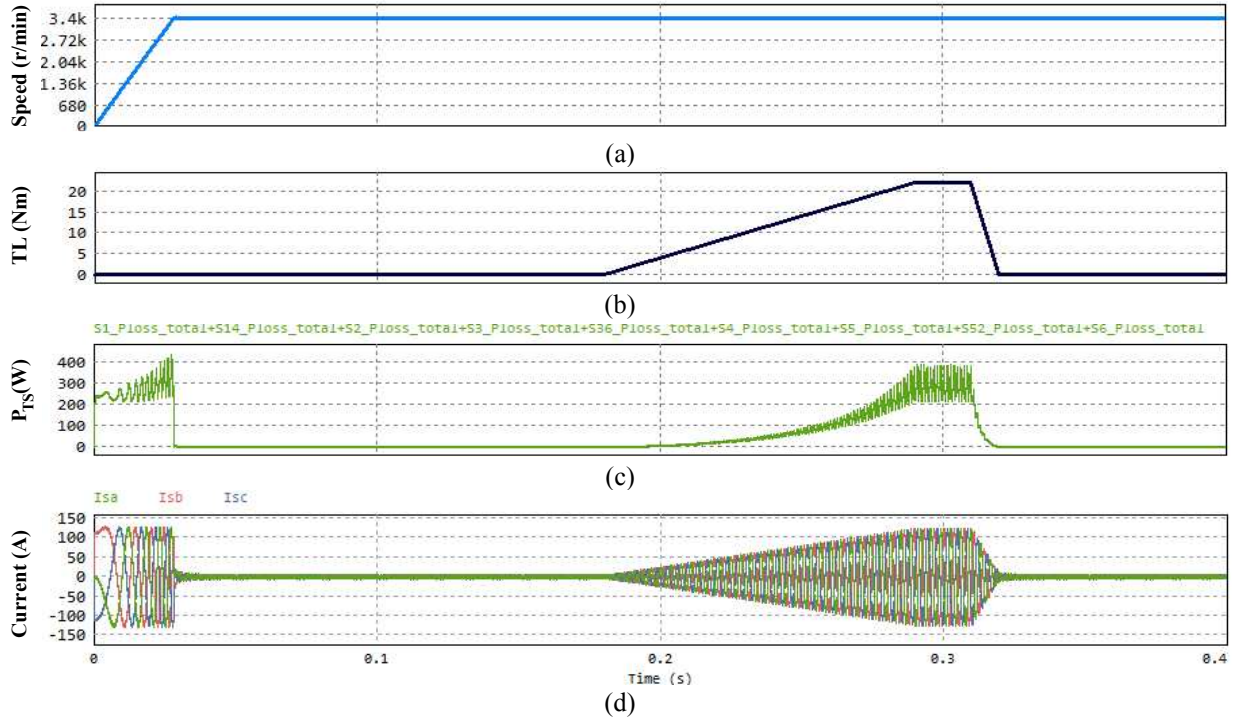
Fig. 4-11. Loss evaluation at the rated condition: (a) motor speed, (b) load torque, (c) total losses of the PESs, and (d) instantaneous phase currents.
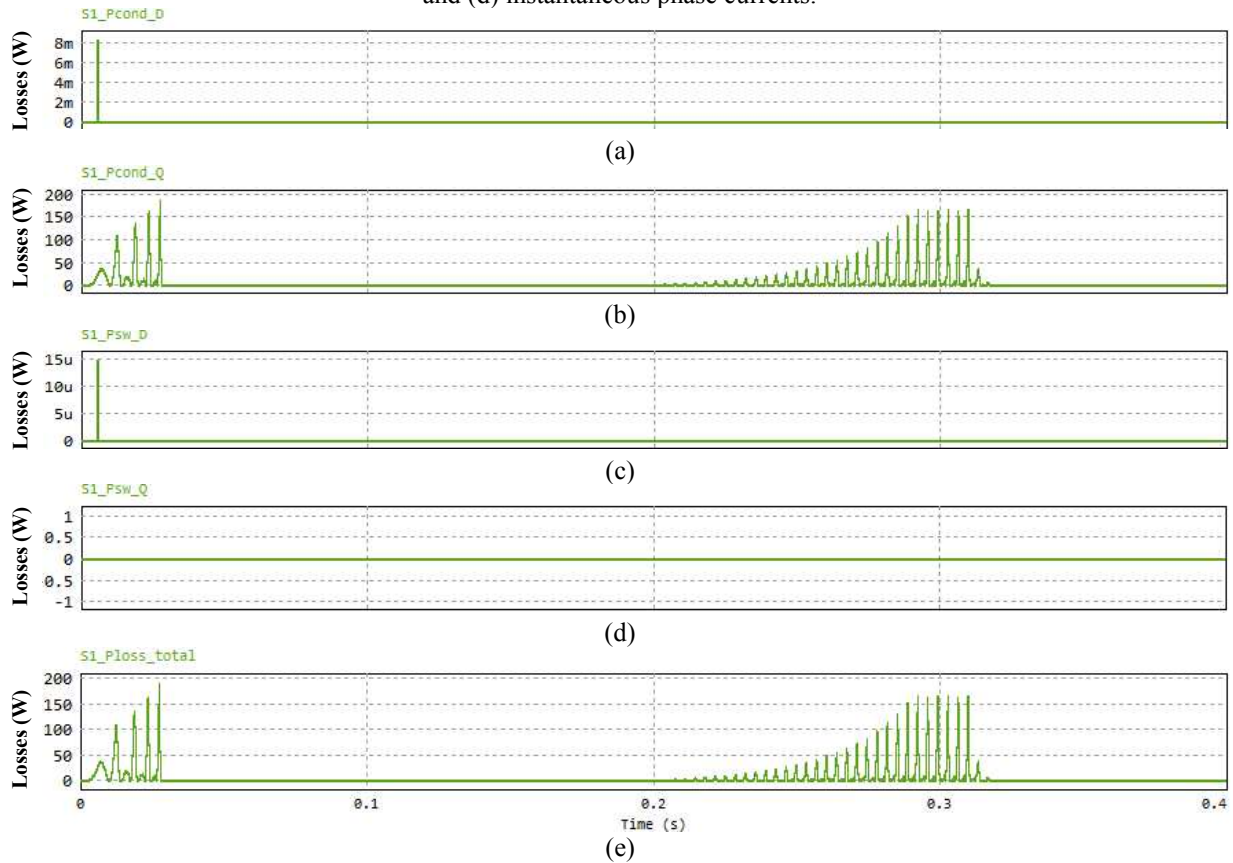
Fig. 4-12. Loss evaluation at the rated condition for switch S1: (a) diode conduction loss, (b) switch conduction loss, (c) diode switching loss, (d) switch switching loss, and (e) total power loss.
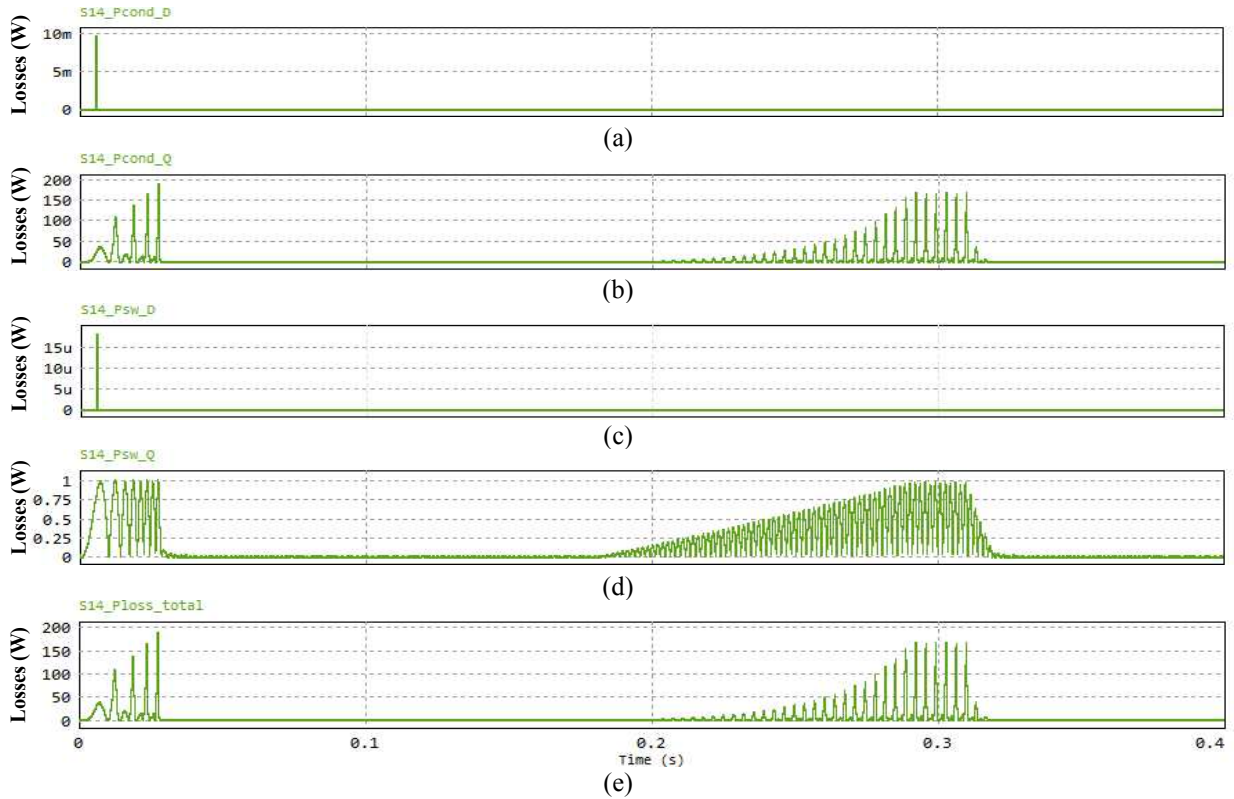
Fig. 4-13. Loss evaluation at the rated condition for switch S14: (a) diode conduction loss, (b) switch conduction loss, (c) diode switching loss, (d) switch switching loss, and (e) total power loss.
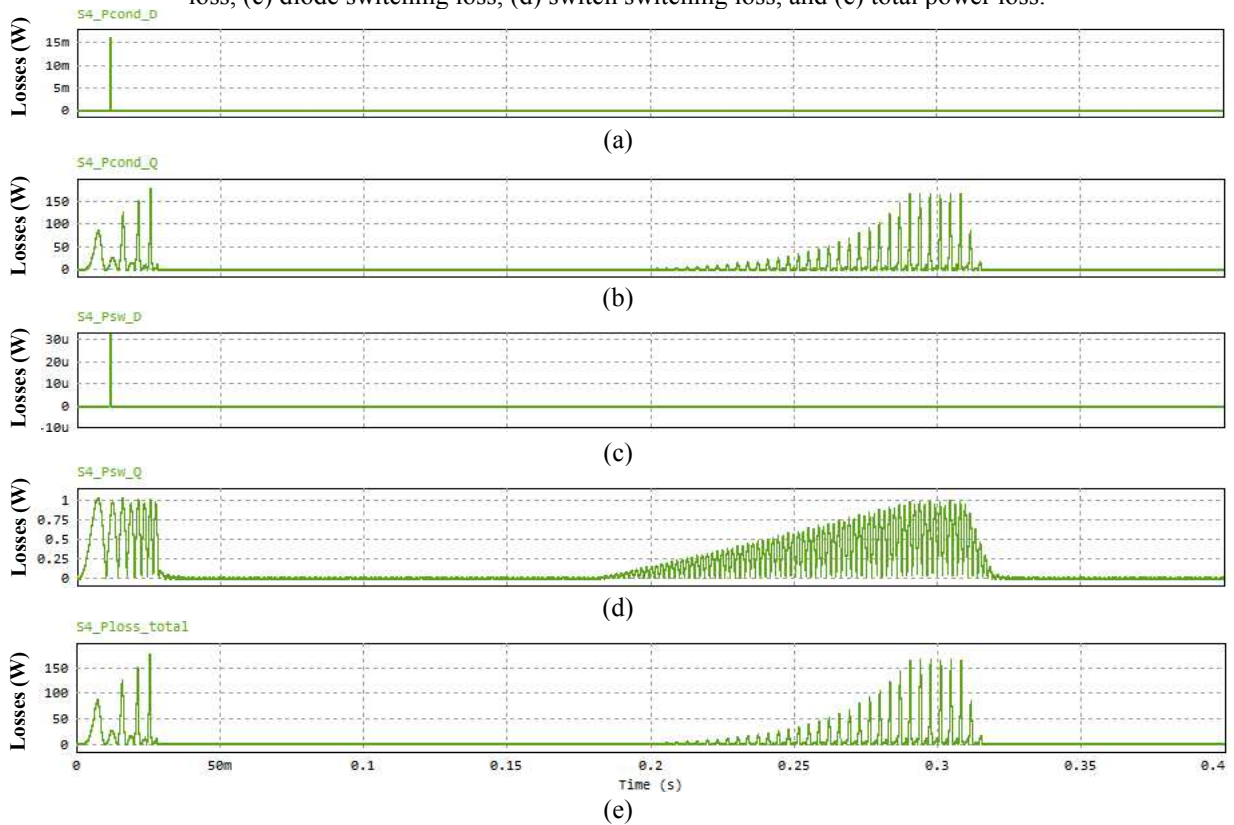
Fig. 4-14. Loss evaluation at the rated condition for switch S4: (a) diode conduction loss, (b) switch conduction loss, (c) diode switching loss, (d) switch switching loss, and (e) total power loss.

To calculate the efficiency of the IMPEI at each operating point, the shaft power of the motor has been used. The developed formula is as follows.

$$\eta_{\text{IMPEI}} = \frac{T_e \omega_m}{T_e \omega_m + \sum_{n=1,2,3,4,5,6,14,36,52}(P_{T_{Sn}})} \; ,$$

4.5

where η_{IMPEI} is the efficiency of the IMPEI, and $P_{T_{Sn}}$ is the total power loss of the nth switch. This equation is possible since the used PMSM model has only negligible ohmic losses. These losses can be assumed as the IMPEI losses due to parasitic elements and system wiring encountered in any practical system. Using the battery power or the inverter output power requires filtering, which can affect the results' accuracy. Hence, using this equation, the efficiency at several operating points has been recorded and plotted as a map, which is depicted in Fig. 4-15. Fig. 4-15(a) shows the entire map with efficiency range from 0 to 100%. Fig. 4-15(b) is the zoomed version of Fig. 4-15(a). These data points will be used for the Twizy drivetrain efficiency estimation.

(a)

(b)
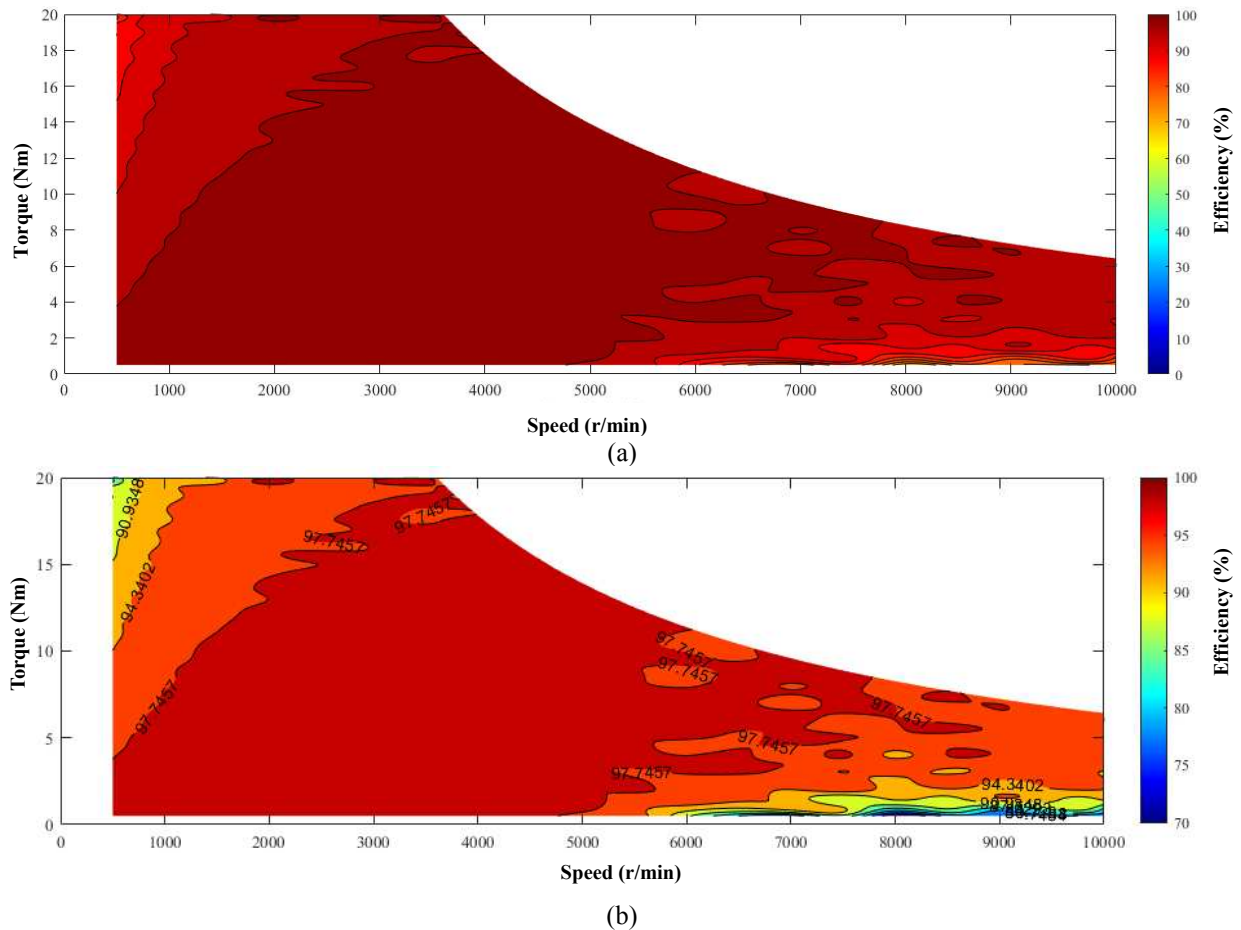
Fig. 4-15. IMPEI efficiency map: (a) full map, and (b) zoomed version.

4.3. Machine Efficiency Map

To validate the drivetrain methodology proposed in Chapter 2, the motor has been designed by a motor design specialist using finite element analysis (FEA) software. The motor parameters obtained from JMAG are compared to the estimated ones in Table 4-5.

Table 4-5: Parameter comparison between the estimated and FEA results.

Parameters	Estimated	FEA	Units
L_d	0.123	0.103	mH
L_q	0.126	0.106	mH
λ_{af}	0.022	0.02	Wb-turn
I_s	125.69	169.70	A

The FEA parameters are obtained after several rounds of modifications that facilitate the prototyping. Hence, there is a bit of a mismatch between the estimated and the FEA results. This was expected, and the IMPEI was sized accordingly. Table 4-5 shows that sizing the IMPEI to have a current rating of at least 1.5 times the calculated current is very useful in this approach. From the provided machine efficiency data, the efficiency map of the designed Twizy motor is obtained as depicted in Fig. 4-16 using MATLAB software. It can be said that the designed motor has higher efficiencies at high-speed high-torque region.
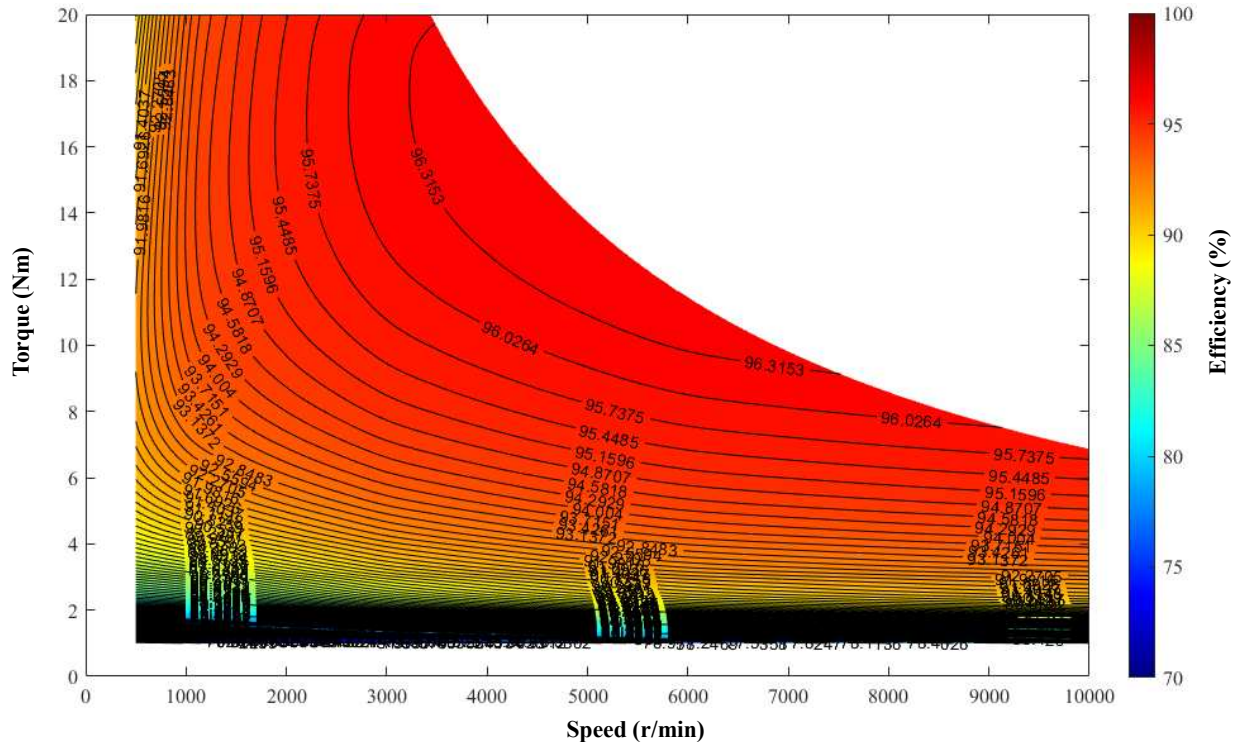
Fig. 4-16. Designed PMSM efficiency map.

85

4.4. Mechanical Efficiency Map

This section evaluates the efficiency of the mechanical system from the electric motor shaft to the EV wheels including the gearbox. For this, Twizy has been tested over a distance of 50 000 km in various weather conditions and drive cycles. Data in several operating points have been recorded during the test. Table 4-6 shows the summary of the data provided by the industry partner (Stackpole International). The energy column has been calculated using (4. 6).

$$Energy \ [kWh] = \frac{\pi}{30} \frac{Torque \ Speed \ Time}{1000}. \hspace{2cm} 4.6$$

Table 4-6: Practical Mechanical System Load spectrum in Aachen Drive Cycle.

Percentage	Torque [Nm]	Distance traveled [km]	Time [h]	Speed [r/min]	Fuel economy kWh/100km	Energy [kWh]
14.40%	-4.98	7200.209	1028.60	956.97	-7.13	-513.34
10.22%	7.68	5109.489	729.93	956.97	10.99	561.78
9.27%	-11.31	4636.774	662.40	956.97	-16.19	-750.77
4.49%	-4.98	2247.132	149.81	956.97	-3.33	-74.76
3.97%	7.68	1982.968	86.22	2050.65	7.17	142.19
3.70%	14.01	1850.886	59.71	3144.33	14.88	275.43
3.65%	7.68	1823.080	121.54	2050.65	10.99	200.45
3.49%	14.01	1743.135	37.09	5331.69	16.64	290.11
3.19%	14.01	1595.412	69.37	2050.65	13.08	208.69
3.15%	-11.31	1572.819	50.74	3144.33	-12.01	-188.95
2.92%	7.68	1461.592	47.15	3144.33	8.16	119.23
2.85%	-4.98	1426.834	62.04	2050.65	-4.65	-66.34
2.55%	20.34	1275.634	27.14	5331.69	24.16	308.23
2.34%	7.68	1169.621	24.89	4238.01	7.25	84.82
2.33%	14.01	1166.145	77.74	2050.65	20.06	233.89
2.08%	-11.31	1037.539	26.60	4238.01	-12.87	-133.53
2.07%	33	1034.063	26.51	4238.01	37.55	388.32
1.88%	33	938.478	19.97	5331.69	39.20	367.90
1.85%	14.01	922.836	23.66	4238.01	15.94	147.13
1.77%	-11.31	886.340	38.54	2050.65	-10.56	-93.60
1.46%	20.34	729.927	31.74	3144.33	29.12	212.55
1.46%	33	729.927	23.55	3144.33	35.05	255.85
1.41%	7.68	707.334	18.14	4238.01	8.74	61.82
1.41%	20.34	707.334	22.82	3144.33	21.60	152.82
1.21%	14.01	603.059	86.15	956.97	20.06	120.96
1.17%	26.67	587.417	12.50	5331.69	31.68	186.11
1.04%	-4.98	517.901	16.71	3144.33	-5.29	-27.39
1.03%	-11.31	514.425	10.95	4238.01	-10.68	-54.94
1.00%	20.34	498.783	12.79	4238.01	23.15	115.45

0.70%	26.67	349.322	11.27	3144.33	28.33	98.96
0.70%	33	347.584	15.11	3144.33	47.24	164.21
0.69%	-4.98	345.846	8.87	4238.01	-5.67	-19.60
0.65%	26.67	323.253	8.29	4238.01	30.35	98.11
0.55%	20.34	276.330	18.42	2050.65	29.12	80.47
0.49%	20.34	245.047	35.01	956.97	29.12	71.36
0.47%	-4.98	232.881	4.95	4238.01	-4.70	-10.95
0.44%	33	222.454	31.78	956.97	47.24	105.10
0.30%	26.67	149.461	6.50	3144.33	38.18	57.07
0.26%	26.67	130.344	18.62	956.97	38.18	49.77
0.25%	7.68	125.130	2.28	5331.69	7.80	9.76
0.24%	-4.98	119.917	2.18	5331.69	-5.06	-6.06
0.22%	26.67	109.489	7.30	2050.65	38.18	41.80
0.21%	-11.31	104.275	1.90	5331.69	-11.48	-11.97
0.12%	33	60.827	4.06	2050.65	47.24	28.74
0.07%	-11.31	34.758	2.32	956.97	-7.56	-2.63
0.00%	33	1.738	0.03	6425.37	40.37	0.70
0.00%	14.01	0.000	0.00	5331.69	0.00	0.00
0.00%	20.34	0.000	0.00	5331.69	0.00	0.00
0.00%	26.67	0.000	0.00	5331.69	0.00	0.00

It can be seen from Table 4-6 that the EV uses regenerative braking to restore the energy back to the battery and increase the mileage. The highest torque value during the regenerative braking operation is 11.31 Nm. However, for propulsion, 33 Nm was possible. In terms of drive cycle regimes, as shown in Fig. 4-17, 58% of this drive cycle was in propulsion mode. This corresponds to 5239.74 kWh energy consumption. The remaining was 42% in regenerative braking mode, which corresponds to 1954.84 kWh energy generation. Therefore, over a distance of 49855.75 km, net energy of 3284.95 kWh was consumed by the mechanical system. This results in 6.59 kWh/100km fuel economy for the mechanical system.

To evaluate the whole Twizy drivetrain fuel economy, the fuel economy map of the mechanical system is required. Hence, data in Table 4-6 was processed by calculating the fuel economy at each operating point. The obtained new data is shown in Table 4-7. The highlighted data in Table 4-7 is obtained by averaging the data of the operating points which have more than one data. The obtained fuel economy map of the mechanical system is shown in Fig. 4-18. It can be seen that at low torque values, the mechanical system of Twizy has excellent fuel economy. The lowest fuel economy is obtained at low speeds and full torque.
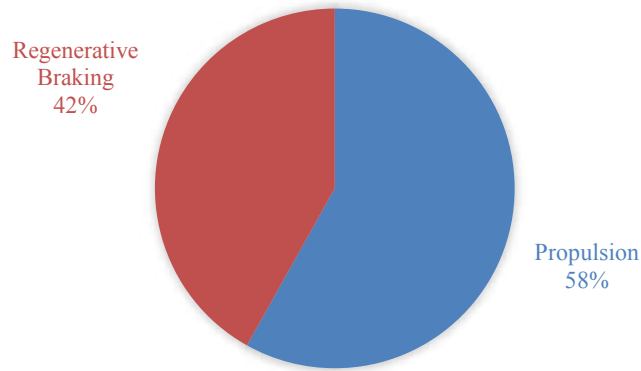
Fig. 4-17. Drive Cycle Regimes
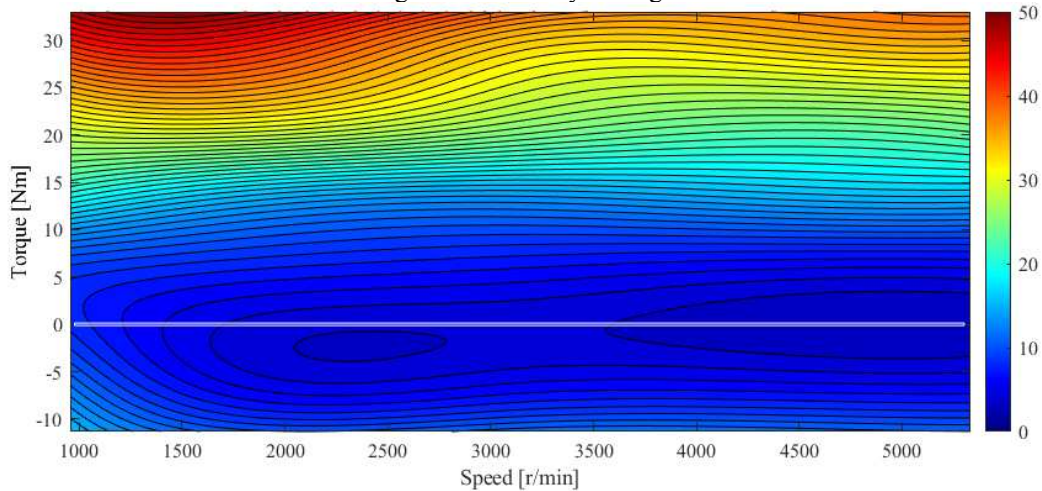
Fig. 4-18. Fuel economy map of the mechanical system.

Table 4-7: Fuel economy data [kWh/100km]

Torque [Nm]	Speed [r/min]				
	5331.69	4238.01	3144.33	2050.65	956.97
33	39.2	37.55	39	47.24	47.24
26.67	31.68	30.35	31.28	38.18	38.18
20.34	24.16	23.15	25.42	29.12	29.12
14.01	16.64	15.94	14.88	16.02	20.6
7.68	7.8	7.81	8.16	9	10.99
-4.98	5.06	5.27	5.29	4.65	11.24
-11.31	-11.48	12.14	12.01	10.56	16.12

4.5. Battery Efficiency

So far, the efficiency of the mechanical system, the electrical motor, and the drive inverter are known. The missing component is the battery efficiency which is complex to evaluate. In fact, two terms are generally used to discuss the efficiency of the battery; energy efficiency and charge efficiency. Energy efficiency refers to the ratio between the energy used during discharge and the

energy used for charging it back to the same state of charge. It can be expressed using the following formula.

$$E_{eff} = 100 \frac{V_{batt_{dis}} I_{batt_{dis}} T_{dis}}{V_{batt_{char}} I_{batt_{char}} T_{char}} ,$$ 4.7

where E_{eff} is the energy efficiency of the battery, $V_{batt_{dis}}$ and $I_{batt_{dis}}$ are, respectively, the battery voltage and current during the battery discharge. $V_{batt_{char}}$ and $I_{batt_{char}}$ are, respectively, the battery voltage and current during the battery charge. T_{dis} and T_{char} are, respectively, the time required to discharge and charge the battery back to its original state. This efficiency is typically about 70% to 80%. This shows that more energy is used to recharge the battery. This is due to the battery voltage level during charging and discharging.

Practically, the charge efficiency, also known as the Ampere-hour (Ah) efficiency, is used for calculations during design steps. It is defined as the ratio between the Ah used during discharge and the Ah used for charging it back to the same state of charge. It can be expressed using the following formula.

$$C_{eff} = 100 \frac{I_{batt_{dis}} T_{dis}}{I_{batt_{char}} T_{char}} ,$$ 4.8

where C_{eff} is the charge efficiency. This efficiency is around 90% to 95%.

For the drive cycle efficiency analysis, the E_{eff} is used since it considers the voltage drop across the battery's internal resistance. To ease the calculation process, 100% E_{eff} is used during propulsion mode, and 70% E_{eff} is used during regenerative braking. Therefore, the drive cycle efficiency is estimated using (4.9). Since the mechanical system fuel economy is known, the drivetrain fuel economy ($FE_{Drivetrain}$) is estimated by multiplying the mechanical system fuel economy with the efficiencies of other components as follows.

$$FE_{Drivetrain} = \frac{FE_{mech-P}}{\eta_{IMPEI} \eta_{PMSM}} - 0.7 FE_{mech-RB} \eta_{IMPEI} \eta_{PMSM} ,$$ 4.9

where FE_{mech} is the mechanical system fuel economy obtained in section 4.3, and η_{PMSM} is the efficiency of the motor obtained in section 4.2. FE_{mech-P} and $FE_{mech-RB}$ are respectively the FE_{mech} during propulsion and regenerative braking. These two modes of operation don't occur simultaneously. When $|FE_{mech-P}| > 0$, $|FE_{mech-RB}| = 0$ and vice versa.

4.6. Twizy Drivetrain Load Spectrum for Aachen Drive Cycle and Fuel Economy

To obtain the load spectrum of the Twizy drivetrain using the Aachen drive cycle, equation (4.9) is applied to Table 4-6. The drivetrain efficiency of the Twizy is estimated as shown in Table 4-8. The operating modes that are not in the range of the designed motor and IMPEI are discarded, i.e., assumed to have zero kilometers and zero energy.

Table 4-8: Estimated Partial Twizy Load spectrum in Aachen Drive Cycle.

Frequency	Torque [Nm]	Speed [r/min]	Distance [km]	Shaft Energy [kWh]	η_{PMSM} [%]	η_{IMPEI} [%]	E_{eff}	Energy at the Battery [kWh]
14.40%	-4.98	956.97	7200.21	-513.34	90.87	98.52	0.7	-321.70
10.22%	7.68	956.97	5109.49	561.78	93.17	97.84	1	616.27
9.27%	-11.31	956.97	4636.77	-750.77	93.90	96.66	0.7	-477.01
4.49%	-4.98	956.97	2247.13	-74.76	90.87	98.52	0.7	-46.85
3.97%	7.68	2050.65	1982.97	142.19	94.29	98.90	1	152.47
3.70%	14.01	3144.33	1850.89	275.43	96.12	98.62	1	290.55
3.65%	7.68	2050.65	1823.08	200.45	94.29	98.90	1	214.95
3.49%	14.01	5331.69	1743.13	290.11	96.62	98.81	1	303.86
3.19%	14.01	2050.65	1595.41	208.69	95.49	97.90	1	223.23
3.15%	-11.31	3144.33	1572.82	-188.95	95.78	98.65	0.7	-124.97
2.92%	7.68	3144.33	1461.59	119.23	94.98	99.18	1	126.58
2.85%	-4.98	2050.65	1426.83	-66.34	92.03	99.29	0.7	-42.43
2.34%	7.68	4238.01	1169.62	84.82	95.36	99.48	1	89.41
2.33%	14.01	2050.65	1166.14	233.89	95.49	97.90	1	250.19
2.08%	-11.31	4238.01	1037.54	-133.53	96.09	99.17	0.7	-89.07
1.85%	14.01	4238.01	922.84	147.13	96.41	98.56	1	154.84
1.77%	-11.31	2050.65	886.34	-93.6	95.16	98.28	0.7	-61.27
1.46%	20.34	3144.33	729.93	212.55	96.13	96.91	1	228.16
1.41%	20.34	3144.33	707.33	61.82	96.13	96.91	1	66.36
1.41%	7.68	4238.01	707.33	152.82	95.36	99.48	1	161.09
1.21%	14.01	956.97	603.06	120.96	94.02	95.76	1	134.34
1.04%	-4.98	3144.33	517.90	-27.39	92.96	99.51	0.7	-17.74
1.03%	-11.31	4238.01	514.42	-54.94	96.09	99.17	0.7	-36.65
0.69%	-4.98	4238.01	345.85	-19.6	93.51	99.68	0.7	-12.79
0.55%	20.34	2050.65	276.33	80.47	95.43	95.83	1	87.99
0.49%	20.34	956.97	245.05	71.36	93.47	92.65	1	82.40
0.47%	-4.98	4238.01	232.88	-10.95	93.51	99.68	0.7	-7.14
0.25%	7.68	5331.69	125.13	9.76	95.66	98.68	1	10.34
0.24%	-4.98	5331.69	119.92	-6.06	93.95	99.50	0.7	-3.97
0.21%	-11.31	5331.69	104.27	-11.97	96.33	99.19	0.7	-8.01
0.07%	-11.31	956.97	34.76	-2.63	93.90	96.66	0.7	-1.67
0.00%	14.01	5331.69	1.74	0.7	96.62	98.81	1	0.73

Throughout this partial drive cycle, the total traveled distance becomes 43098.71 km, and the total energy at the shaft is 1019.33 kWh. The net battery energy is 1942.49 kWh. The fuel economy is therefore obtained to be 4.51 kWh/100 km.

To get the fuel economy that covers the whole Aachen drive cycle, the operating modes that are not in the range of the designed motor and IMPEI and PMSM are obtained by extrapolating the IMPEI and PMSM efficiency map data using Excel.

Table 4-9: Estimated Full Twizy Load Spectrum in Aachen Drive Cycle.

Frequency	Torque [Nm]	Speed [r/min]	Distance [km]	Shaft Energy [kWh]	η_{PMSM} [%]	η_{IMPEI} [%]	E_{eff}	Energy at the Battery [kWh]
14.40%	-4.98	956.97	7200.209	-513.34	90.87	98.52	0.7	-321.70
10.22%	7.68	956.97	5109.489	561.78	93.17	97.84	1	616.27
9.27%	-11.31	956.97	4636.774	-750.77	93.90	96.66	0.7	-477.01
4.49%	-4.98	956.97	2247.132	-74.76	90.87	98.52	0.7	-46.85
3.97%	7.68	2050.65	1982.968	142.19	94.29	98.90	1	152.47
3.70%	14.01	3144.33	1850.886	275.43	96.12	98.62	1	290.55
3.65%	7.68	2050.65	1823.08	200.45	94.29	98.90	1	214.95
3.49%	14.01	5331.69	1743.135	290.11	96.62	98.81	1	303.86
3.19%	14.01	2050.65	1595.412	208.69	95.49	97.90	1	223.23
3.15%	-11.31	3144.33	1572.819	-188.95	95.78	98.65	0.7	-124.97
2.92%	7.68	3144.33	1461.592	119.23	94.98	99.18	1	126.58
2.85%	-4.98	2050.65	1426.834	-66.34	92.03	99.29	0.7	-42.43
2.55%	20.34	5331.69	1275.634	308.23	96.68	96.78	1	329.43
2.34%	7.68	4238.01	1169.621	84.82	95.36	99.48	1	89.41
2.33%	14.01	2050.65	1166.145	233.89	95.49	97.90	1	250.19
2.08%	-11.31	4238.01	1037.539	-133.53	96.09	99.17	0.7	-89.07
2.07%	33.00	4238.01	1034.063	388.32	93.20	96.20	1	433.11
1.88%	33.00	5331.69	938.478	367.9	94.00	92.80	1	421.75
1.85%	14.01	4238.01	922.836	147.13	96.41	98.56	1	154.84
1.77%	-11.31	2050.65	886.34	-93.6	95.16	98.28	0.7	-61.27
1.46%	20.34	3144.33	729.927	212.55	96.13	96.91	1	228.16
1.46%	33.00	3144.33	729.927	255.85	92.80	90.00	1	306.33
1.41%	20.34	3144.33	707.334	61.82	96.13	96.91	1	66.36
1.41%	7.68	4238.01	707.334	152.82	95.36	99.48	1	161.09
1.21%	14.01	956.97	603.059	120.96	94.02	95.76	1	134.34
1.17%	26.67	5331.69	587.417	186.11	95.80	94.80	1	204.93
1.04%	-4.98	3144.33	517.901	-27.39	92.96	99.51	0.7	-17.74
1.03%	-11.31	4238.01	514.425	-54.94	96.09	99.17	0.7	-36.65
1.00%	20.34	4238.01	498.783	115.45	96.39	97.70	1	122.59
0.70%	26.67	3144.33	349.322	98.96	95.10	94.10	1	110.58

0.70%	33.00	3144.33	347.584	164.21	92.80	90.00	1	196.61
0.69%	-4.98	4238.01	345.846	-19.6	93.51	99.68	0.7	-12.79
0.65%	26.67	4238.01	323.253	98.11	95.40	96.90	1	106.13
0.55%	20.34	2050.65	276.33	80.47	95.43	95.83	1	87.99
0.49%	20.34	956.97	245.047	71.36	93.47	92.65	1	82.40
0.47%	-4.98	4238.01	232.881	-10.95	93.51	99.68	0.7	-7.14
0.44%	33.00	956.97	222.454	105.1	88.00	83.20	1	143.55
0.30%	26.67	3144.33	149.461	57.07	95.10	94.10	1	63.77
0.26%	26.67	956.97	130.344	49.77	91.50	88.50	1	61.46
0.25%	7.68	5331.69	125.13	9.76	95.66	98.68	1	10.34
0.24%	-4.98	5331.69	119.917	-6.06	93.95	99.50	0.7	-3.97
0.22%	26.67	2050.65	109.489	41.8	97.80	95.80	1	44.61
0.21%	-11.31	5331.69	104.275	-11.97	96.33	99.19	0.7	-8.01
0.12%	33.00	2050.65	60.827	28.74	99.10	94.90	1	30.56
0.07%	-11.31	956.97	34.758	-2.63	93.90	96.66	0.7	-1.67
0.00%	14.01	5331.69	1.738	0.7	96.62	98.81	1	0.73
0.00%	20.34	5331.69	0	0	96.68	96.78	1	0.00
0.00%	26.67	5331.69	0	0	95.80	94.80	1	0.00
0.00%	33	6425.37	0	0	0.00	0.00	1	0.00

Hence, throughout this full drive cycle, the total traveled distance becomes 49855.75 km, and the total energy at the shaft is 3284.95 kWh. The net battery energy is 4517.90 kWh. The fuel economy is therefore obtained to be 9.06 kWh/100 km.

To get the equivalent fuel economy in terms of fuel (gasoline) consumption in ICEVs, the conversion formula in the equation (4. 10) can be used [88].

$$1 \, l/100 \, km \; = \; 8.9 \, kWh \, /100 \, km \, . \qquad \qquad 4.\,10$$

This results in a $0.6 \, l/100 \, km$ to $1.02 \, l/100 \, km$. This fuel economy range is feasible. The Renault Twizy 2017 data in [89] shows that the fuel economy is $0.7 \, l/100 \, km$.

4.7. Prototyped Drivetrain Components

The prototyped IMPEI is shown in Fig. 4-19. More details are provided in Appendix G. The designed PMSM for Renault Twizy is being prototyped. The frame of the motor being prototyped is illustrated in Fig. 4-20, the rotor drawing in Fig. 4-21 and the motor stator in Fig. 4-22.
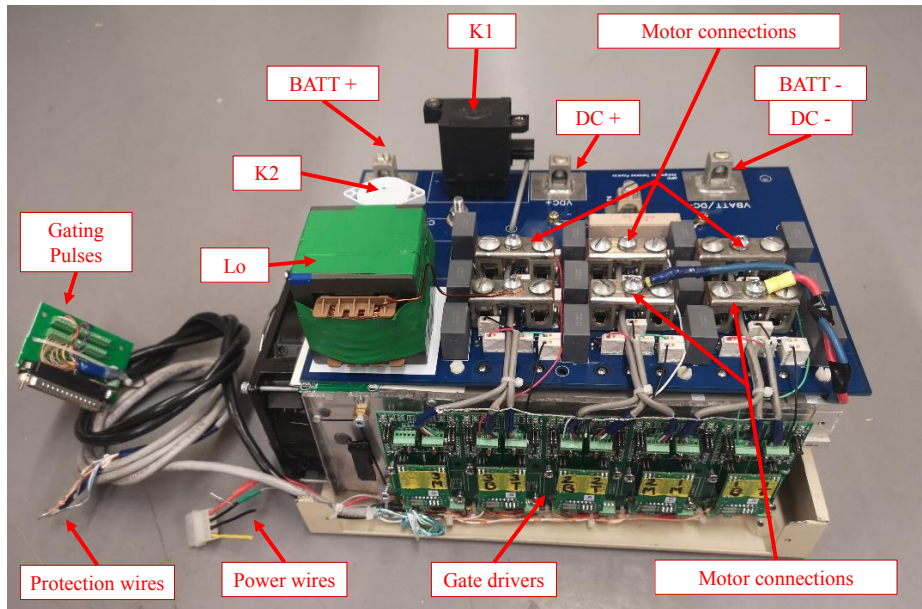
Fig. 4-19. Prototyped MOSFET-based IMPEI.

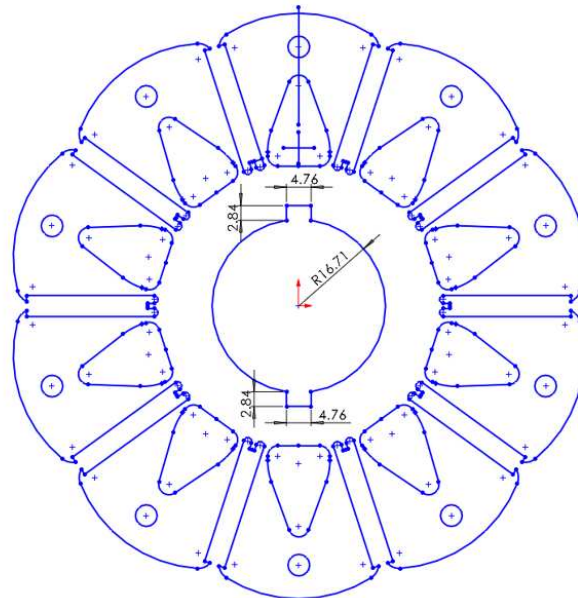Fig. 4-20. Frame of the motor being prototyped.

Fig. 4-21. Rotor drawing of the motor being prototyped (all dimensions in mm).

Fig. 4-22. Stator of the motor being prototyped

4.8. Summary

In this chapter, the potential fuel economy of the drivetrain of the Twizy EV, based on experimental and simulation data, has been investigated. From the drivetrain specifications in terms of battery nominal voltage, base speed, maximum speed, and rated torque, the proposed method in Chapter 2 has been used to estimate the size and parameters of the motor and of the drive inverter. The proposed IMPEI, in Chapter 3, has been sized and simulated in PSIM software to obtain its efficiency map throughout the operating envelope. The designed PMSM efficiency map is obtained from JMAG software. However, the mechanical system efficiency map is obtained practically throughout a drive cycle in Aachen city in Germany. The fuel economy analysis provided results that are close to reality.

Chapter 5. High-Speed Test Bench Development and Regenerative Braking Study of High-Speed PMSMs

5.1. Introduction

This chapter presents a dynamometer for testing machines with various power ratings and speed ranges. The test bench's main components are described. Also, a study on current handling during regenerative braking operation of high-speed PMSMs in emergency conditions is also presented.

5.2. High Speed Machines Test Bench Development

5.2.1. Machine Test Benches

The schematics of the commonly used test benches are shown in Fig. 5-1 to Fig. 5-4. The main components are the dyno motor and its power electronics, the test motor and its power electronics, the power supply, the instrumentation (sensors and transducers), the control, and the protection.

The test bench in Fig. 5-1 is the basic test bench that enables testing motors. When in motoring mode, the dyno motor is powered through the diode rectifier. This configuration doesn't allow power flow in the reverse direction. Hence, to run the test motor in motoring mode, a resistive load is required to dissipate the power generated by the dyno motor. This type of test bench usually employs DC motors as dyno motors. Regenerative braking is not possible with this test bench configuration.

For test benches that use induction machines (IMs) as dyno motors, the configuration shown in Fig. 5-2 is used primarily. This configuration allows the control of the IM in motoring and generating modes and performs regenerative braking when required. The chopper circuitry maintains the DC bus below a threshold by chopping the excess power into a resistive load.

Fig. 5-3 shows a test bench configuration found in modern motor test facilities. It is more efficient than the test benches in Fig. 5-1 and Fig. 5-2. It uses AFECs to regulate the DC bus voltage. With this configuration, the generated power from the dyno or test motor in generating mode is fed back to the grid. This configuration draws losses when the system is operated at steady state. With separated AFECs, this test bench configuration has a DC bus voltage flexibility and can be used with drive inverters having different power ratings.
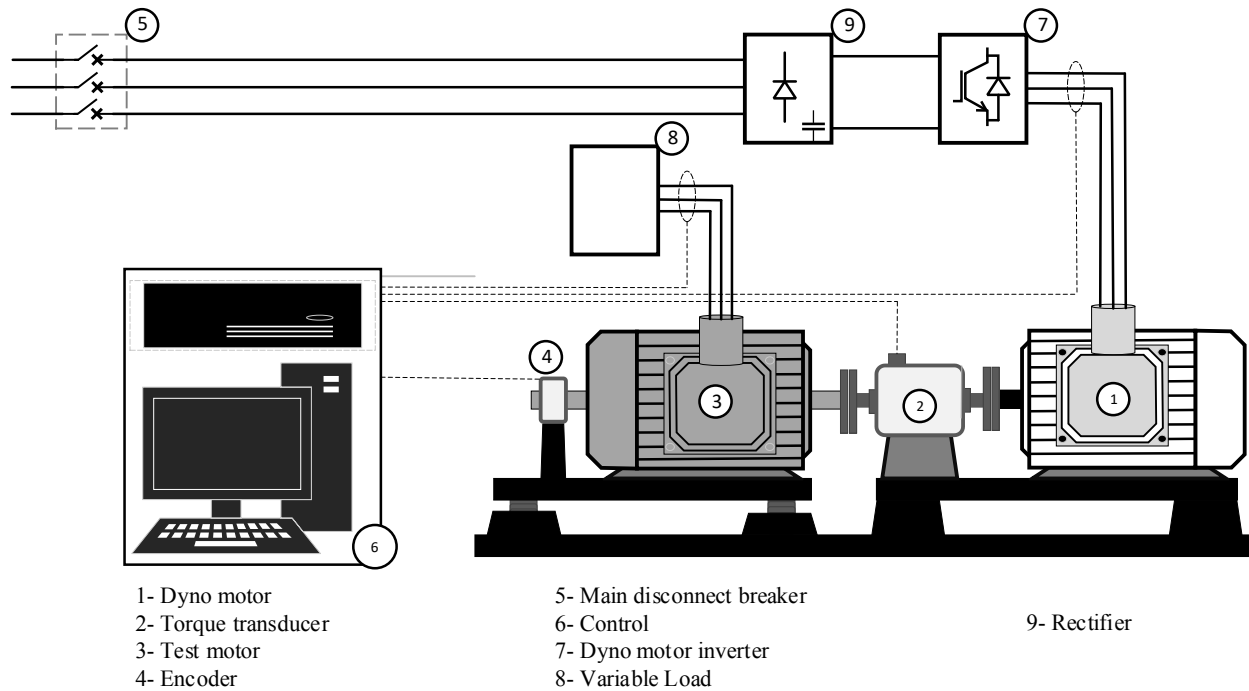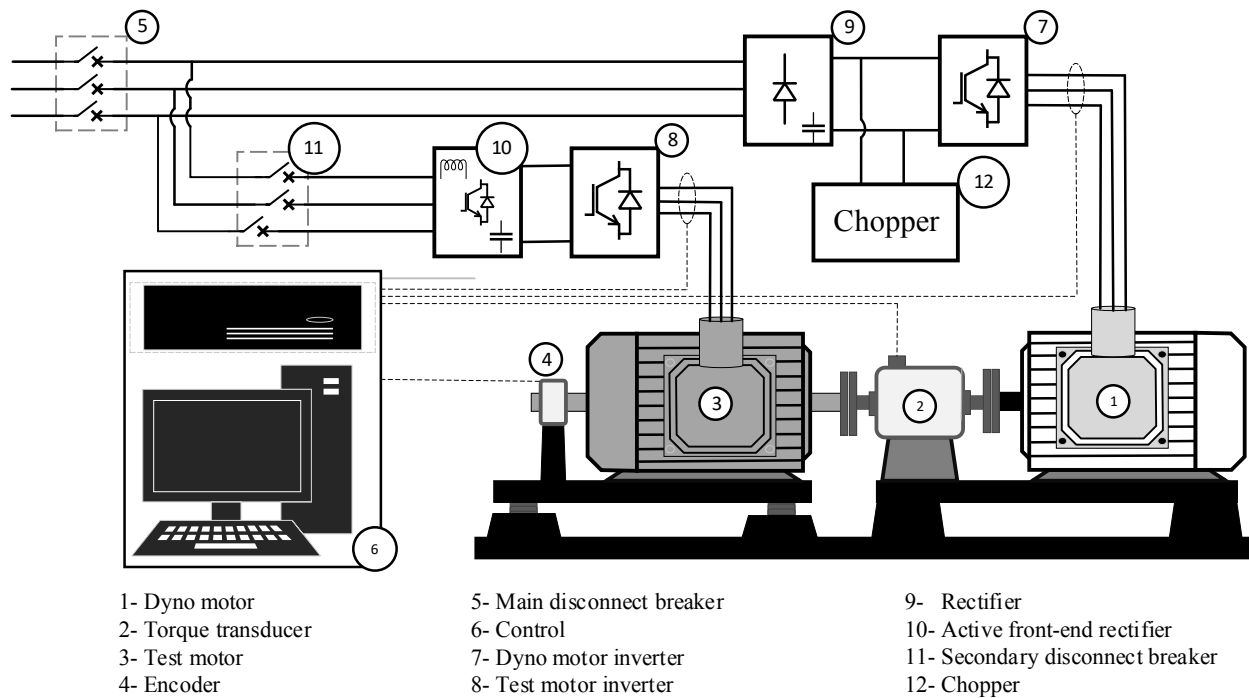
1- Dyno motor
2- Torque transducer
3- Test motor
4- Encoder

5- Main disconnect breaker
6- Control
7- Dyno motor inverter
8- Variable Load

9- Rectifier

Fig. 5-1. Conventional test bench layout: option 1.

1- Dyno motor
2- Torque transducer
3- Test motor
4- Encoder

5- Main disconnect breaker
6- Control
7- Dyno motor inverter
8- Test motor inverter

9- Rectifier
10- Active front-end rectifier
11- Secondary disconnect breaker
12- Chopper

The configuration in Fig. 5-4 is the modified version of the test bench configuration in Fig. 5-3. It has a reduced number of PEIs but doesn't have the DC bus voltage flexibility. In this configuration, only one AFEC is required. This AFEC will supply the losses during the steady
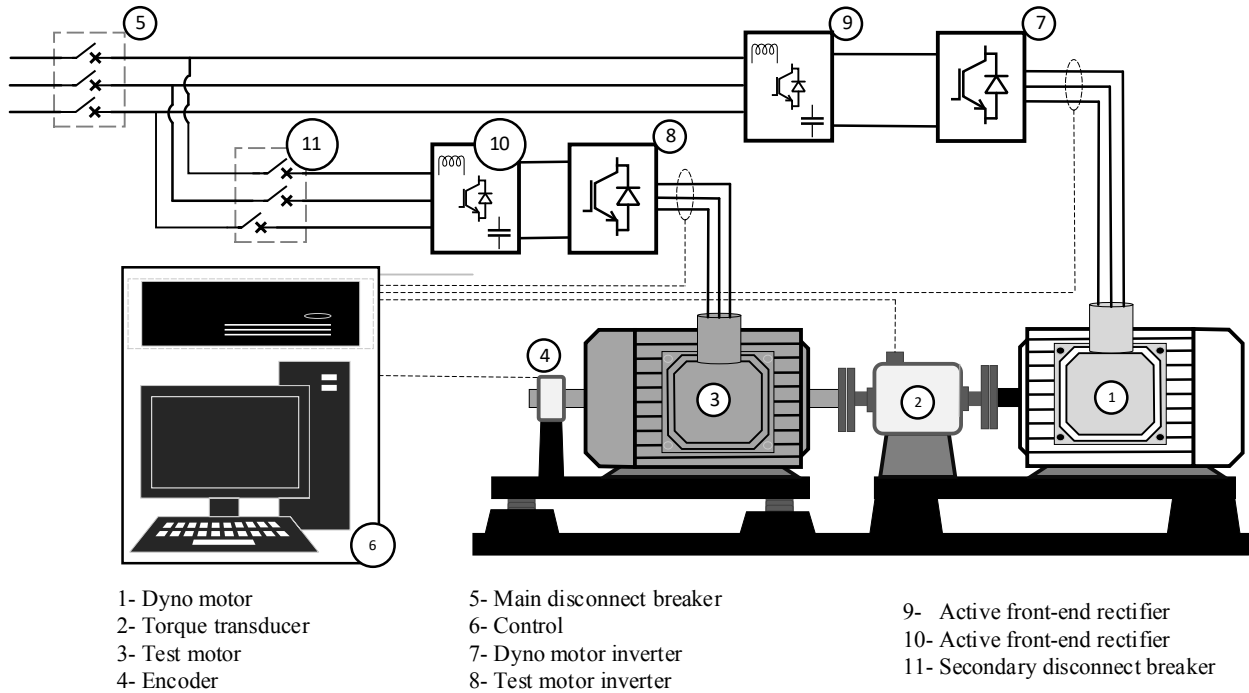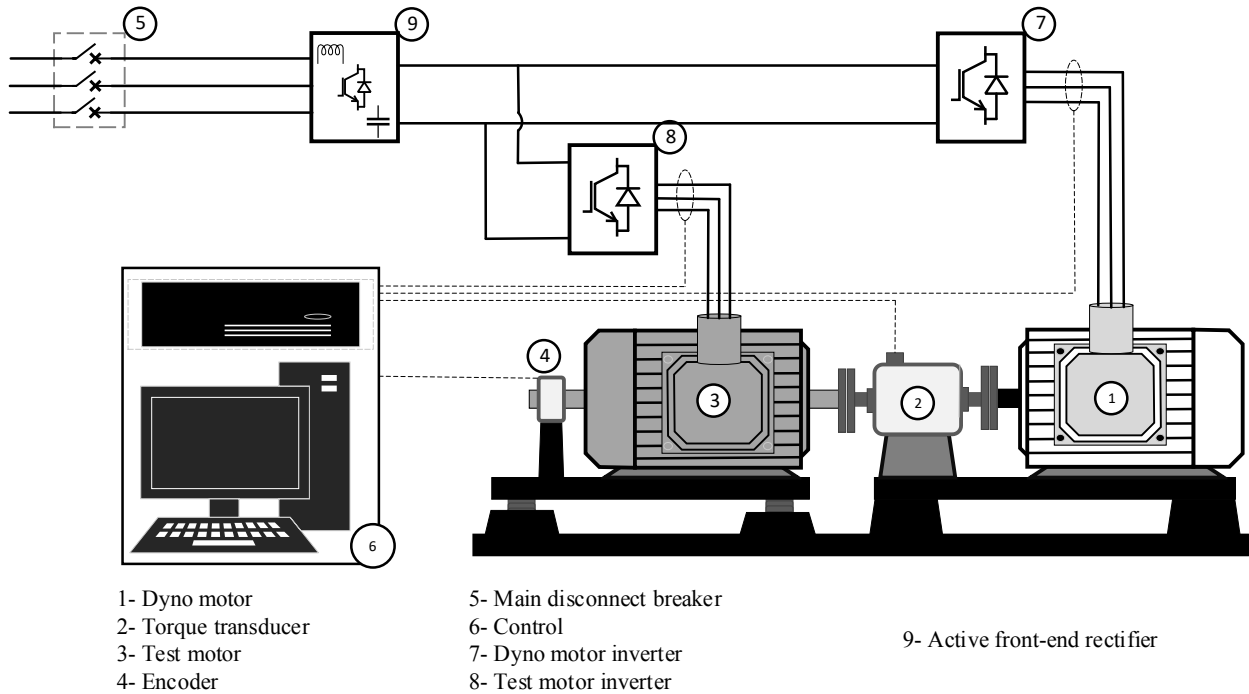
96

1- Dyno motor   5- Main disconnect breaker
2- Torque transducer   6- Control
3- Test motor   7- Dyno motor inverter
4- Encoder   8- Test motor inverter

9- Active front-end rectifier
10- Active front-end rectifier
11- Secondary disconnect breaker

Fig. 5-3. Conventional test bench layout: Option 3.

1- Dyno motor   5- Main disconnect breaker
2- Torque transducer   6- Control
3- Test motor   7- Dyno motor inverter
4- Encoder   8- Test motor inverter

9- Active front-end rectifier

state operation and the required power during transient conditions. This reduces the cost, size, and coordination of the setup. Table 5-1 summarizes the practical machine test benches.

Table 5-1: Motor test bench comparison table.

	Advantages	Limitations
Option 1 (Fig. 5-1)	• Less expensive. It uses fewer components. • Low control complexity. Only the dyno inverter needs to be controlled. • Simple implementation and testing.	• Limited to one quadrant at a time: The dyno motor can only run in motoring mode while the test motor is in generating mode. • Not efficient: The power generated by the test motor is dissipated as heat through the load.
Option 2 (Fig. 5-2)	• Offers four quadrant operation.	• Not efficient: The power from the dyno motor during generating mode is dissipated as heat through the chopper circuitry.
Option 3 (Fig. 5-3)	• Offers four quadrant operation. • Relatively efficient.	• Expensive: AFECs are expensive. • Complex coordination and protection because of the increased number of PEIs in the system. • Bulky: Each PEI should be sized for the full power rating of the motor.
Option 4 (Fig. 5-4)	• Offers four quadrant operation. • Most efficient. • Relatively simple coordination and control.	• Required a DC-DC conversion stage when the drive inverters do not have the same voltage ratings.

## 5.2.2. Commissioned High-Speed Machine Test Bench

The developed test bench is shown in Fig. 5-5. Fig. 5-5(a) shows the schematic layout of the developed dyno system, highlighting the bidirectional power flow. It can be seen that a DC power supply is used to power the inverters of the dyno and the test motors. Fig. 5-5(b) shows the physical system, which is similar to the ones shown in Fig. 2-18, and Fig. 3-19. This test bench has the same layout as the one depicted in Fig. 5-4. It has two main parts; the dyno motor side, which is fixed, and the test motor side, which is flexible. The test motor side can be brought up or down to facilitate the vertical alignment. With the help of the side adjustment screws, as depicted in Fig. 5-6, the test motor can be aligned horizontally. The clamps shown in Fig. 5-6 are used to lock the test motor once aligned. This test bench is commissioned for the following tasks:

- Torque-speed curve measurements. This data is obtained by controlling the torque from the test motor while running the dyno motor at a constant speed. The opposite is also possible.
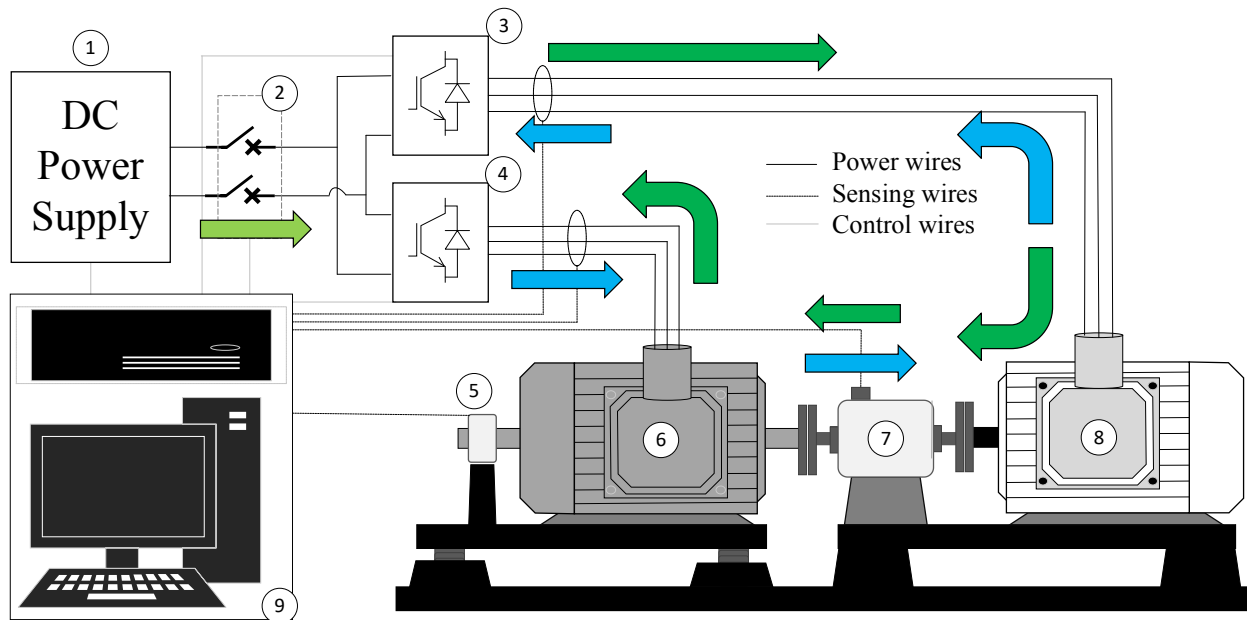
1- Bidirectional programmable dc power supply   4- Test motor inverter   7- Torque transducer
2- DC output breaker   5- Encoder   8- Dyno motor
3- Dyno motor inverter   6- Test Motor   9- Control

(a)
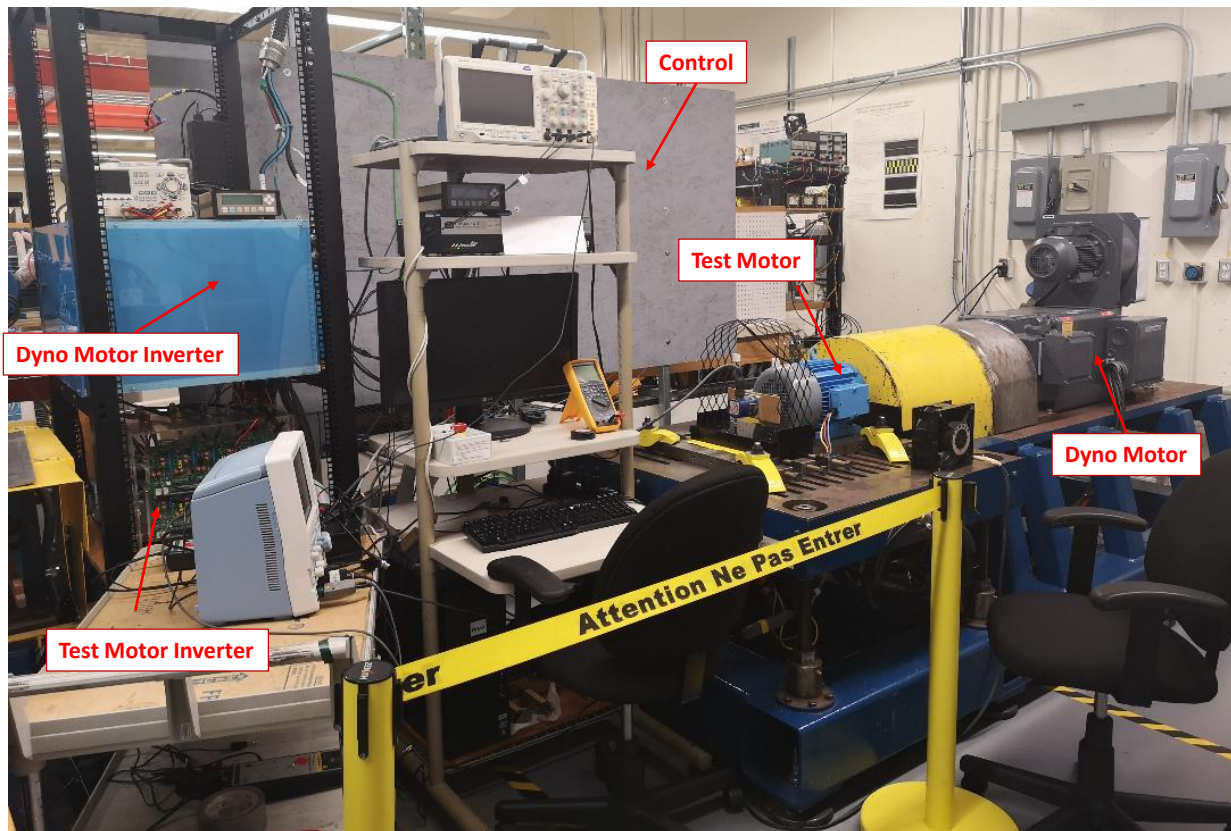
(b)

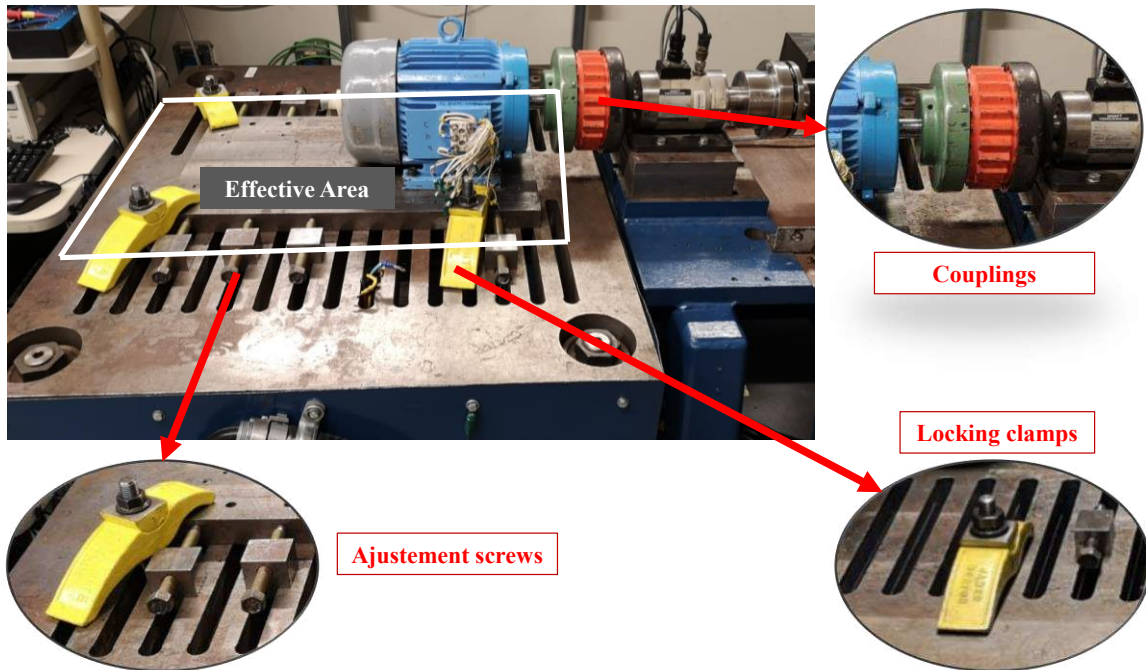Fig. 5-5. Commissioned test bench: (a) schematic layout, and (b) physical system.

Fig. 5-6. Work area of the 150 hp dyno.

- Torque-angle curve measurements. For PMSMs, the data is obtained by locking the rotor at several positions and applying the full current to the motor using a controller. FOC is suitable for this purpose.

- Back-EMF measurements. This data is obtained by spinning the test motor (PMSM) to a predetermined speed (usually its rated speed) and measuring the motor's open terminal voltage.

- Rated operation validation: This test is performed by bringing the test motor to its rated speed and applying the rated torque. This helps validate the efficiency of the motor and the cooling requirement.

- Efficiency measurements. With this test bench, the efficiency of the test motor can be obtained at the desired operating point. The efficiency of its driving inverter as well can be measured. The test allows the generation of motor and inverter efficiency maps. The drivetrain's efficiency can be obtained. It can also perform the fuel economy analysis.

- Driving and regenerative braking tests: This test allows for testing and validating EV drivetrains components and control.

The specifications of the components in the test bench are summarized in Table 5-2.

Table 5-2: Specifications of the components in the developed test bench.

Description		Specification
Dyno motor	T-T Electric Four pole induction motor	Rated torque: 150 hp Rated voltage: 575 V Rated current: 153 A Base speed: 2200 r/min Maximum speed: 6700 r/min
Torque transducer	Himmelstein MCRT Model: 2904T (5-3)	Maximum speed 10 000 r/min Torque: 565 Nm
Dyno motor inverter	Applied Power System INC. IAP100T120 SixPac	Rated DC bus voltage: 850 V Maximum voltage rating: 1200V Rated current: 100A Switching frequency: 20 kHz
AFEC	California Instruments Mx30-3pi programmable power supply	Power rating: 30 kVA Maximum voltage: 400 V DC, AC Current @ 400V DC: 60 A
Test motor inverter	Option 1: IGBT-based IMPEI	Power rating: 48 kVA Maximum DC bus voltage: 800 V Rated current: 60 A
	Option 2: MOSFET-based IMPEI	Power rating: 50 kVA Maximum DC bus voltage: 250 V Rated current: 200 A
Encoder for the dyno motor	Wachendorff WDGI 58B (Optical)	Maximum operating speed: 8000 r/min Power supply: 5 - 30 V DC Maximum pulse per revolution: 25000 Resolution: 1500 PPR
Encoder for the test motor	Model H25Absolute Encoder Gray coded	Maximum operating speed: 12000 r/min Nominal speed: 8000 r/min Power supply: 5 - 28 V DC Resolution: 12 bits
Current sensors	LEM LF 210-S	Nominal current: 200A Supply voltage: 15.75 V Nominal sensitivity: 0.5 mA/A Linearity error: 0.05 % of nominal current Bandwidth: 100 kHz
Controller	APAL-RT OP4510	Sampling frequency 50 kHz Reconfigurable digital and analog input/outputs

From Table 5-2, it can be seen that the dyno inverter has a current rating lower than the rated current of the dyno motor. Also, the used bidirectional power supply has a voltage capability lower than the DC bus voltage required to supply the rated voltage of the dyno motor. These are the main limitations of this testbench. Therefore, this test bench cannot be used at its full power with this configuration. For the coordination during the test, the dyno motor is controlled using

101

direct torque control (DTC) or V/F control strategies. The closed loop V/F control is preferred for tests such as the back-EMF measurement, while the DCT is selected when the dyno motor controls the torque. However, the test motor (PMSM) is controlled using FOC.

5.2.3. Discussion on Increasing the Power and Speed Range of the Test Bench

With the commissioned test bench, the testing capability is reduced to almost 50 hp with a maximum speed of 6700 r/min. A 100 hp ABB ACS800 drive has been commissioned as an alternative drive for motors of higher power ratings. For the speed range over 6700 r/min, however, the test bench has to be modified, and a gearbox is required. The industry partner (Stackpole International) proposed two types of gearboxes. These gearboxes are depicted in Fig. 5-7. Based on the space and mechanical constraints, the gearbox cannot be mounted on the dyno side of the test bench. Hence, the test bench after modification will be similar to the one depicted in Fig. 5-8. It can be seen that the addition of the gearbox to the test bench necessitates another torque transducer. This adds another mechanical constraint related to the alignment of the whole system. Based on the size of the gearboxes and the limited effective area as depicted in Fig. 5-6 and Fig. 5-8, It was concluded that the available test bench with the gearbox would not be able to accommodate the standard 112 motor frame like the one used in prototyping the designed PMSM.

5.3. Regenerative Braking Case Study in High-speed PMSMs.

The use of regenerative braking in EVs is gaining importance nowadays. The market is irreversibly transitioning to EVs. In conventional vehicles, the braking energy is lost in the form of heat due to friction loss. The introduction of EVs opens the door to regenerative braking, which utilizes the kinetic energy generated by the motor during the braking process to recharge the battery of the EV. Therefore, recovering the braking energy has been proved to be a practical approach for improving the driving range of an EV [90] - [93]. In regenerative braking, the motor acts as a generator, and the kinetic energy is recovered by applying the proper switching schemes to the power converter switches. This energy can be used to charge the battery of the EV or stored in an ultracapacitor bank [94] - [96].
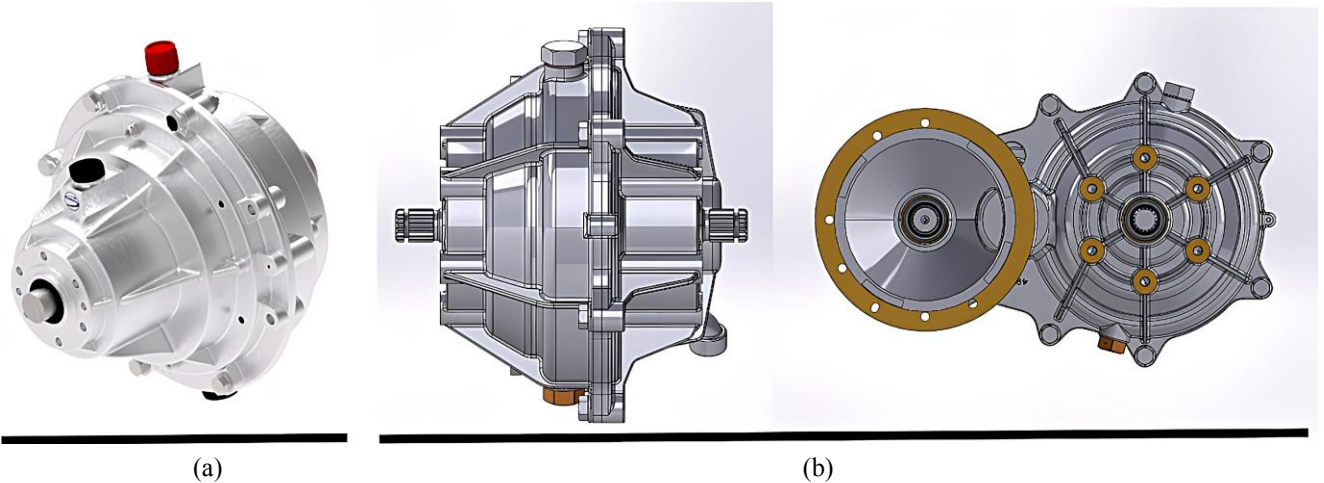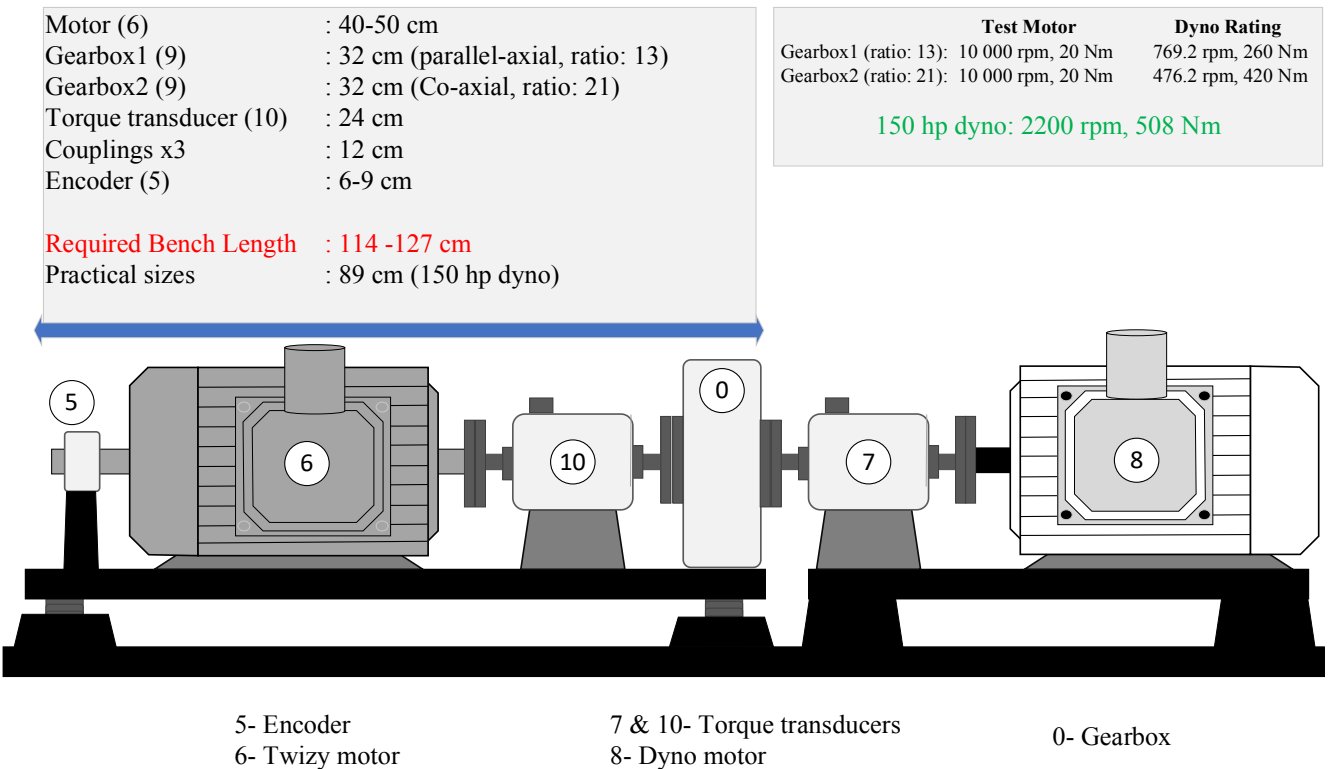
Fig. 5-7. Gearboxes from the industry partner (Stackpole International) (a) parallel axis, and (b) co-axial.

Motor (6)	: 40-50 cm
Gearbox1 (9)	: 32 cm (parallel-axial, ratio: 13)
Gearbox2 (9)	: 32 cm (Co-axial, ratio: 21)
Torque transducer (10)	: 24 cm
Couplings x3	: 12 cm
Encoder (5)	: 6-9 cm
Required Bench Length	: 114 -127 cm
Practical sizes	: 89 cm (150 hp dyno)

	Test Motor	Dyno Rating
Gearbox1 (ratio: 13):	10 000 rpm, 20 Nm	769.2 rpm, 260 Nm
Gearbox2 (ratio: 21):	10 000 rpm, 20 Nm	476.2 rpm, 420 Nm

150 hp dyno: 2200 rpm, 508 Nm

5- Encoder	7 & 10- Torque transducers	0- Gearbox
6- Twizy motor	8- Dyno motor	

Fig. 5-8. Required test bench components for speeds more than 6700 r/min.

The regenerative braking strategies can be slightly different depending on the type of electric machine used in propulsion. Transportation electrification made PM motors more popular than induction motors [97] and [98]. PM machines have a faster response than IMs because of lower inertia due to the absence of a rotor cage. They also have higher efficiency since they have no rotor losses and magnetizing currents. They require a lower kVA rating of the PEI due to their higher power factor. For automotive applications with weight and size constraints, PM machines

103

have smaller physical sizes, offer more accessible heat extraction features, and have a more straightforward operation in field weakening, constant power range, and regenerative braking thanks to FOC. The FOC provides smooth drive transitions into and out of the flux-weakening mode, fast response, and automatic adjustment to changes in the DC source voltage [53] and [99]. PMSMs are used in a vast number of EVs available in the market. The braking strategies in a PMSM-based EV can be divided into two categories, as described in Fig. 5-9. The difference among these categories is the braking technique.

The non-regenerative braking dissipates the kinetic energy in the form of heat. It is used in light vehicles and during low-speed operations of the EMs. Among the non-regenerative braking techniques are mechanical braking, where the friction force is used to stop the EV; dynamic braking using a resistor to dissipate the energy, and FOC braking where the losses are dissipated in the drivetrain components (EM and drive inverter) [100], and [101]. Plugging, also known as reverse voltage braking, is used in extreme conditions. It is also a non-regenerative braking technique. In plugging braking, the motor is halted by changing the phase sequence of the three-phase voltages of the EM [100] - [103]. This braking technique is the source of surge currents in the drivetrain that can damage the whole system.

The regenerative braking, however, stores the energy back into the battery for later use. However, it is not effective in low-speed regions. Several techniques have been developed in the literature to harvest energy during regenerative braking, among which are the speed control-based, torque control-based FOC, and the maximum energy recovery switching scheme (MERSS) [104] - [106]. In terms of energy recovery efficiency, the study in [106] revealed that the MERSS outperforms the FOC in terms of regenerative braking efficiency. However, getting good
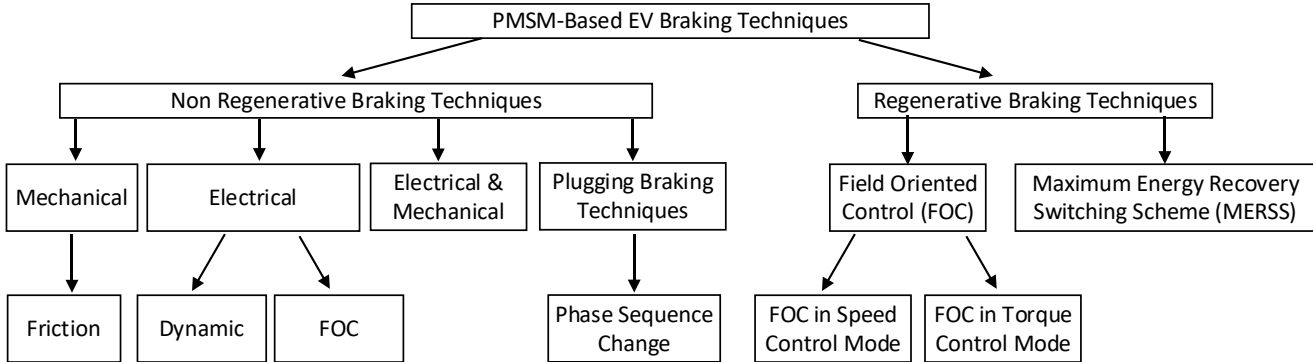

Fig. 5-9. EV braking strategies.

104

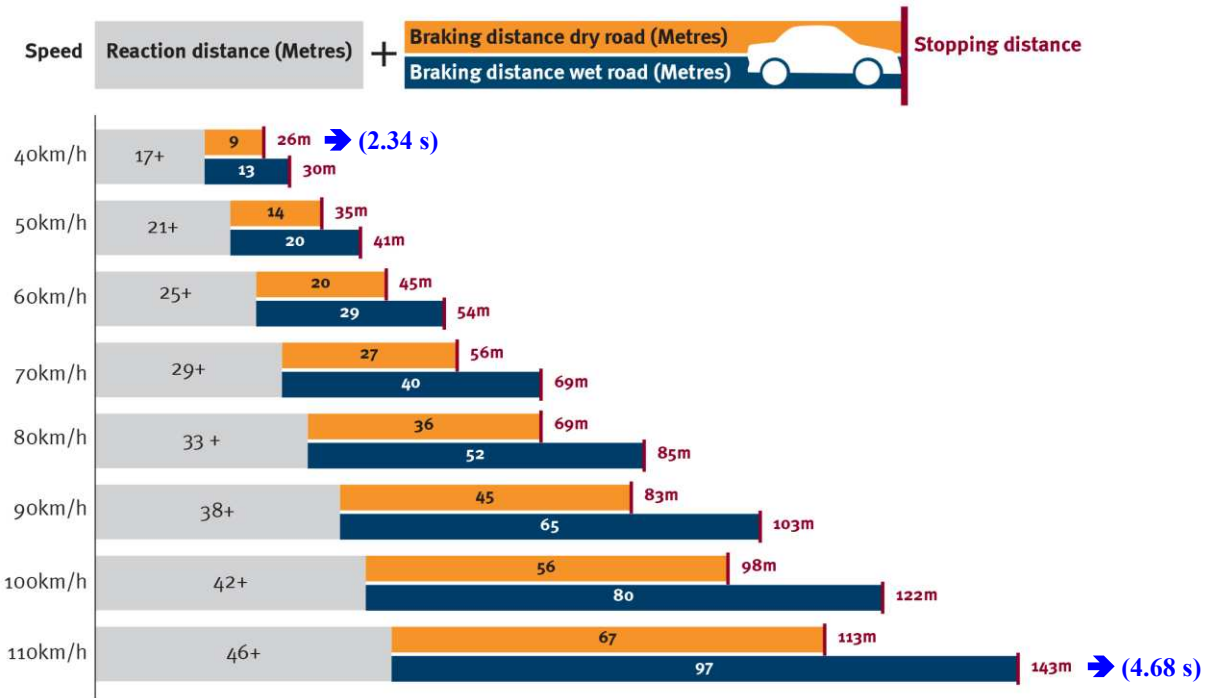## How long it takes to stop (driving an average family car)

| Speed | Reaction distance (Metres) | + | Braking distance dry road (Metres) / Braking distance wet road (Metres) | Stopping distance |

40km/h — 17+ — 9 → 26m → **(2.34 s)** — 13 → 30m

50km/h — 21+ — 14 → 35m — 20 → 41m

60km/h — 25+ — 20 → 45m — 29 → 54m

70km/h — 29+ — 27 → 56m — 40 → 69m

80km/h — 33+ — 36 → 69m — 52 → 85m

90km/h — 38+ — 45 → 83m — 65 → 103m

100km/h — 42+ — 56 → 98m — 80 → 122m

110km/h — 46+ — 67 → 113m — 97 → 143m → **(4.68 s)**

Fig. 5-10. Stopping distances in an emergency situation-updated from [108].

efficiencies with the MERSS depends on the proper duty cycle selection. This conclusion is preliminary and more study is required to compare both regenerative braking strategies. Nevertheless, the FOC and the MERSS-based controllers can effectively control the amount of regenerated energy. Therefore, the current can be handled more safely.

Using regenerative braking techniques in EVs to gain extra miles shouldn't compromise the safety of the driver and the passengers. In fact, during an emergency, an EV has to be able to stop in a few seconds. The chart in Fig. 5-10 shows the braking distance concerning the driving speed. It can be seen that in an emergency situation, the car has to break in less than 5 seconds. Assuming an electrical machine running at 10000 r/min as the one designed in Chapter 4, the kinetic energy generated by regenerative braking can be expressed as,

$$KE = \frac{1}{2}J\omega^2 \, , \qquad (1)$$

where KE is the kinetic energy, J is the inertia of the system in $kg\,m^2$, and ω is the angular velocity in rad/s. It can be seen that the available KE varies with the square of the velocity. Therefore, the question is, how fast can an electric motor absorb this amount of energy more

safely? Here comes the necessity of handling the surge current during regenerative braking. Most manufacturers prefer mechanical braking or hybrid braking for safety reasons and the lower cost associated with the development of such a system.

5.3.1. Simulink Case Study of Regenerative Braking

The Twizy motor designed in Chapter 4 is used for this case study. The obtained results are shown in Fig. 5-11. The first plot shows the terminal voltage of the machine, the second plot depicts the current of the machine. The third one shows the speed, and the last one shows the power and torque of the machine. It can be seen that the acceleration time from 0 to 10000 r/min is around 5s. The toque curve shows that full torque is applied from zero to 3400 r/min, which is the base speed. After the base speed, the constant power control is used to keep the control command within the operating envelope of the selected IPMSM. Therefore, throughout the acceleration process, the maximum available torque within the operating envelope of the selected IPMSM is applied to ensure that the motor accelerates as fast as possible. This prevents overloading the machine and provides good performance of the drive.

After the reference speed is reached, the motor must overcome only the load torque and the losses due to friction and windage. This explains the decrease in torque. During regenerative braking, the maximum available negative torque within the operating envelope of the IPMSM is applied to ensure that the motor brakes as fast as possible with regenerative braking. Effectively, the motor is able to brake in 2.8 seconds. During this period, the product of speed and torque results in a negative power, which means that the motor during the regenerative braking, behaved like a generator and captured the braking energy. This energy can be stored back in the battery.

It can be seen that the transitions from zero speed to maximum speed and back to zero speed are smooth and there is no surge of current. The controlled current over the illustrated drive cycle does not exceed the designed IPMSM current rating. This shows how effective the FOC is in terms of regulating the current applied to the machine. Therefore, a proper FOC control algorithm is the key to avoiding surge currents during regenerative braking. A braking time of 2.8 seconds is acceptable based on the chart in Fig. 5-10, However, this time may be too long in critical situations. Mechanical brakes can assist in emergency cases where the PMSM can only apply the rated torque.
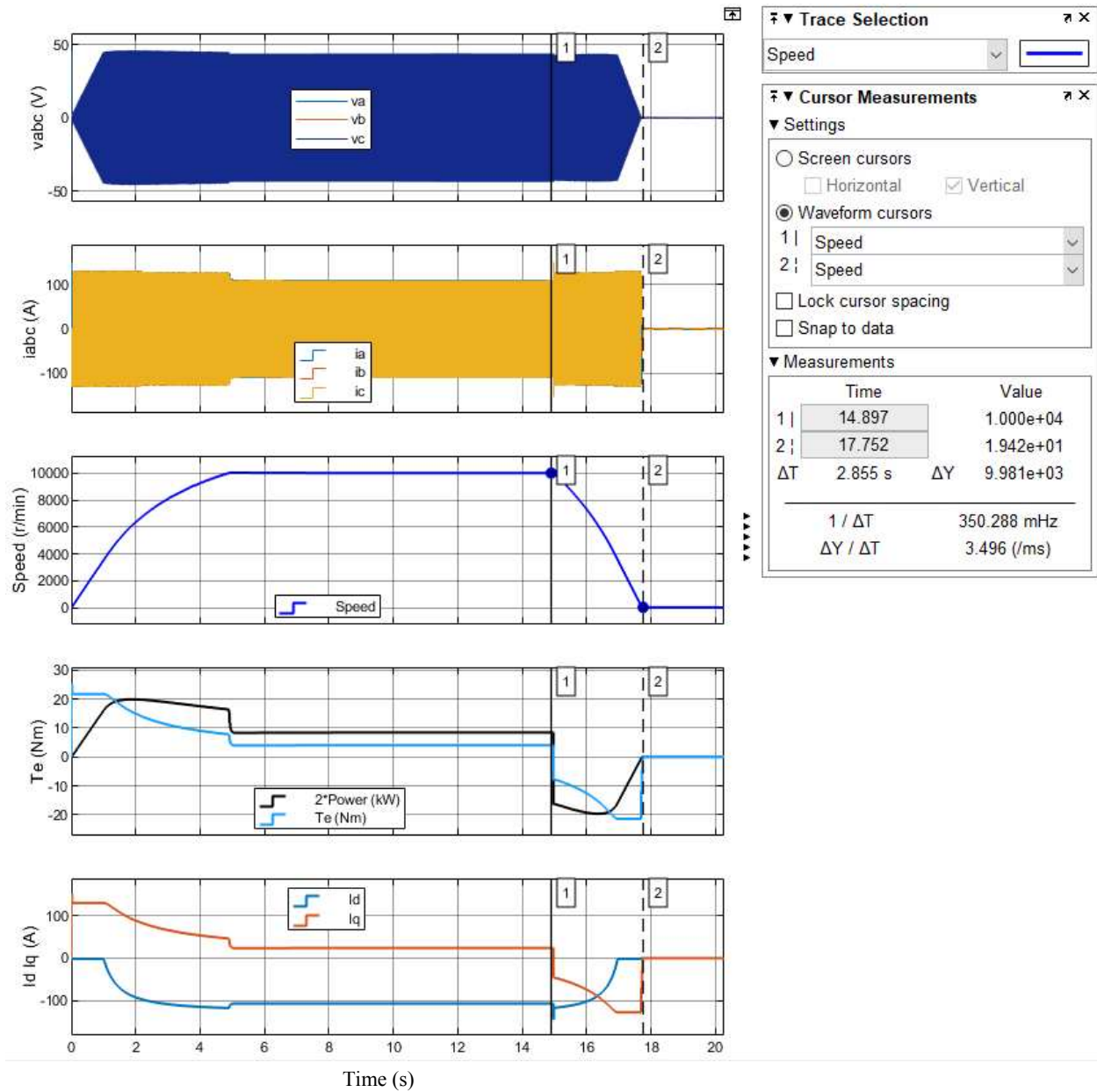
Fig. 5-11. Drive and regenerative braking of the high-speed IPMSM

5.3.2. Overloading the Electrical Machine During the Regenerative Braking

Electric machines can be loaded more than their ratings depending on the thermal time constant. This principle can be used during emergencies. In the case of EVs, electric machines can be overloaded during emergency braking situations. This section investigates this principle using the FOC. In the first result presented in Fig. 5-11 (case1), both the accelerating and braking torques are of the same magnitude, and so are the limits of the current. Recalling equation (2.5), the electromagnetic torque is strongly related to the current magnitude.
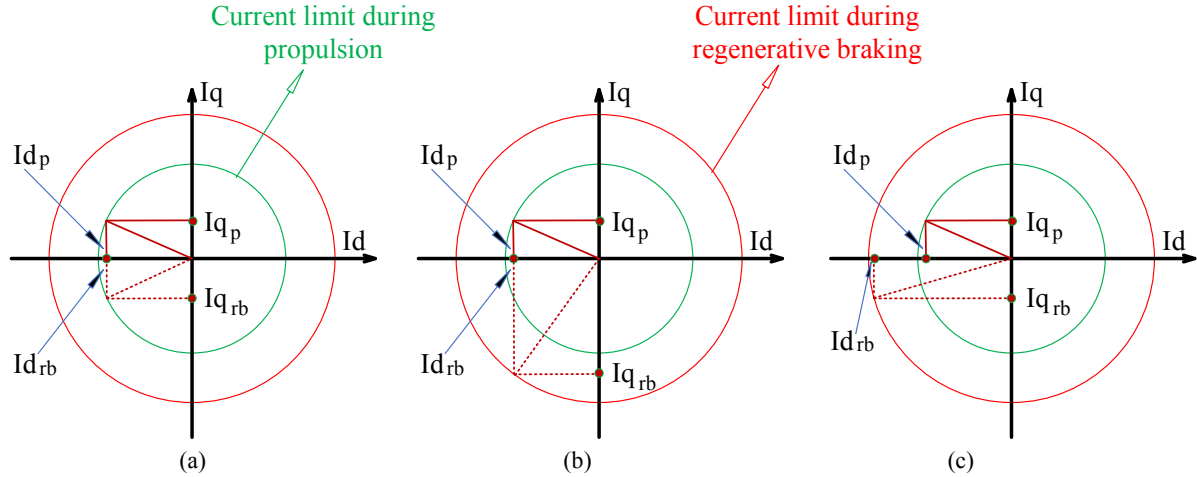
Fig. 5-12. Regenerative braking scenarios in the current plane, (a) conventional regenerative braking using FOC, (b) increasing the current limit (scenario 1), and (c) increasing the current limit (scenario 2).

For high-speed PMSMs where operating in the field weakening region is required, increasing the current limit during regenerative braking and forcing the control to operate inside the current limit circle (2.11) leads to two scenarios:

- Keeping the maximum available d-axis current during the propulsion mode (I_{d_p}) equals the initial d-axis current during regenerative braking ($I_{d_{rb}}$). The resulting q-axis current ($I_{q_{rb}}$) during the transition from the propulsion mode to the regenerative braking mode can be obtained using equation (2.11). This is illustrated in Fig. 5-12(b). Based on equations (2.7) and (2.8), the q-axis voltage (v_q) during the transition remains unchanged, while the d-axis voltage v_d will be proportional to $I_{q_{rb}}$. This violates the voltage limit circle described in equation (2.9). This scenario is, therefore, not feasible.

- Keeping the maximum available q-axis current during the propulsion mode (I_{q_p}) equals the initial q-axis current during regenerative braking ($I_{q_{rb}}$). The resulting d-axis current ($I_{d_{rb}}$) can be obtained following the equation (2.11). Fig. 5-12(c) illustrates this scenario. In this case, the flux is weakened based on equations (2.7) and (2.8). This reduces the q-axis voltage and creates room for increasing $I_{q_{rb}}$ to operate at the intersection of the current limit circle and the voltage limit ellipse (2.10). Increasing $I_{q_{rb}}$ increases the braking torque allowing the EV to stop faster.
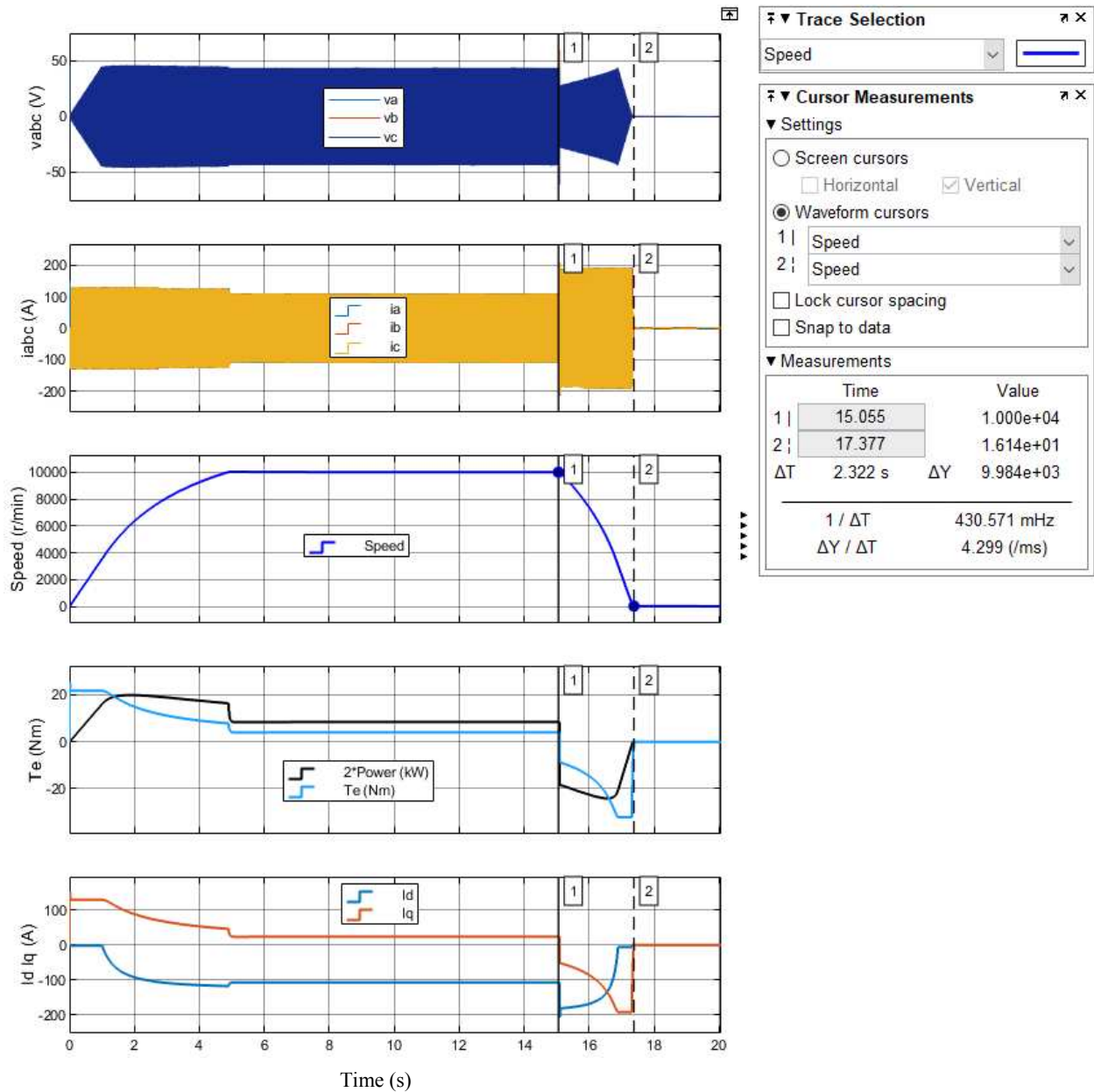
Fig. 5-13. Drive and emergency regenerative braking of the high-speed IPMSM.

The second scenario is implemented in a new case study. The current limit during acceleration is kept unchanged, while the current limit during regenerative braking is 1.5 times the rated current to increase the braking torque. Fig. 5-13 shows the simulation results using the specifications of the designed high-speed PMSM. It can be seen that the braking torque increased by a factor of 1.5. This results in 2.3 seconds braking time, which is less than the braking time observed in case 1 by approximately 18.4%. It can be seen that the control is very smooth and
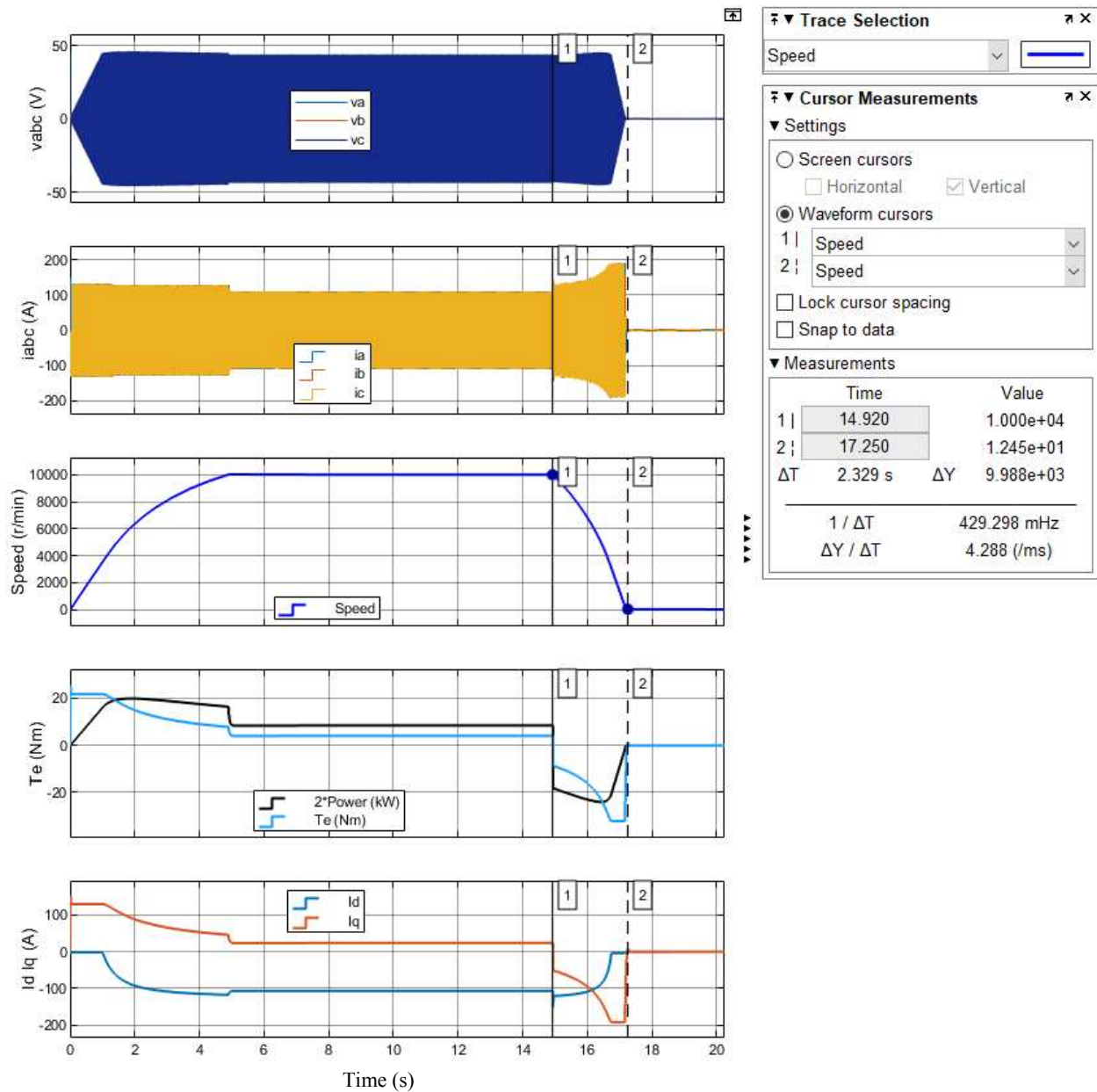
Fig. 5-14. Drive and emergency regenerative braking of the high-speed IPMSM.

does not result in a surge current. The current limit and voltage limits were not violated and the transition from the first current limit circle to the second one is smooth.

A second simulation has been performed to maximize the regenerative braking efficiency by reducing the stator current, Fig. 5-14. This is done by controlling the increase in $I_{d_{rb}}$ since its contribution to the torque production is negligible. The applied $I_{d_{rb}}$ was constrained to stay in the current circle used for propulsion while $I_{q_{rb}}$ was constrained by the regenerative braking current

circle. ($I_{q_{rb}} = sqrt((1.5I_s)^2 - (1.5I_{d_{rb}})^2)$). Same braking time was obtained with an overall lower stator current magnitude. This theoretically validates the applicability of this technique for braking EVs during emergencies and handling the surge current. However, in practice, each machine has its overload capability, which can be the most significant limitation of this braking approach. The associated power electronics, as well, have to be able to handle the overloading current.

5.4. Summary

This chapter presented a description of the test bench used to obtain the experimental results throughout the thesis. A short comparison of commonly used test benches is provided, followed by the details on the commissioned test bench. The main components of the test bench are described. Also, a regenerative braking analysis of high-speed PMSMs during emergency conditions is presented. It has been concluded that overloading the electrical machine during regenerative braking in emergency conditions using FOC is a feasible approach that can reduce the braking time of EVs. However, the rating of the individual drivetrain components should not be exceeded.

Chapter 6. Conclusion and Future Works

6.1. Conclusion

The following can be stated based on the work presented in this thesis.

Chapter 1 reviewed the state-of-the-art technology used for transportation electrification. This showed that the BEVs, PHEVs, and FCEVs are the future of electrified transportation. Drivetrains of EVs available in the market are described and compared. The main advantages and limitations of each drivetrain configuration are provided to guide EV selection. Regarding the PEIs, it is concluded that IPEIs can offer onboard charging with grid support capabilities. The trend in the main components of EV drivetrains revealed that EMs are replacing some ICEs, and PMSMs are the preferred candidates. Hence, the need for EMs that can provide similar or better performance compared to ICEs over a wide range of speed and torque became evident. Also, the requirement of a matching PEI is established for better drivetrain performance. It is found that the available design steps that synchronize the drivetrain design are not adequately investigated in the literature. This resulted in a trial-and-error approach between the motor designers and the drive specialists on how to select the ratings of the drivetrain components.

To solve this issue of lack of common ground in the EV drivetrain design, Chapter 2 proposed a new step-by-step design method for EV drivetrain design and testing, considering the PMSM and its drive inverter specifications. Using the torque-speed and battery nominal voltage information, feasible parameters are obtained analytically. A new set of equations have been developed for calculating IPMSM parameters from feasible SPMSM parameters. This way of estimating the parameters beforehand is found to be crucial. It provides both drive and machine designers the ability to foresee the feasibility of the specifications and their effects on the rating of the drive system. Also, this step provides feasible machine terminal parameters, current, and voltage which are the input to FEA software and the emulating setups. Many case studies have been performed through this thesis to test and validate the proposed method. A theoretical case study based on a 2010 Prius validated this method for its ability to estimate feasible parameters that can be matched using FEA software. Experimental validation has been performed on twin PMSMs where the IPMSM parameters are calculated as a known SPMSM. Based on FEA, simulations, and experimental results, it has been concluded that the proposed method can speed

up the EV drivetrain design, emulation, and testing by providing initial guidelines allowing machines and drive specialists to work in parallel on the drivetrain components design.

To take advantage of the V2G opportunity, which allows for grid support during emergencies or revenue generation by selling energy, Chapter 3 proposed an integrated multipurpose power electronics interface designed for PHEVs and EVs. This novel IPEI has been analyzed and compared to several other IPEIs and the CPEI. Analyses and measurements have revealed that the IMPEI has the highest flexibility in modes of operation and can be reconfigured to interface with various grid systems in vehicle-to-grid (V2G) and grid-to-vehicle (G2V) modes. This is accomplished using the flexible IPEI topology and its associated control strategies. The IMPEI and other topologies are compared in terms of configuration, device count, cost, and efficiency, with the BMW i3 as the benchmark application. The design requirements are presented and discussed including modes of operation, switch and passive element sizing, and ratings. According to the findings of this study, the IMPEI, among other IPEIs, has a low switch count, more flexibility in operating modes (propulsion, regenerative braking, single-phase and three-phase V2G and G2V), and high efficiencies. It has also been demonstrated that the IMPEI is cost-effective and easy to implement. The results of experiments in propulsion, regenerative braking, and single-phase and three-phase V2G and G2V are presented. The experimental efficiency analysis is also carried out in the propulsion, V2G, and G2V modes. The difference in efficiency between the IMPEI and the CPEI is quantified. This chapter validates the IMPEI concept and demonstrates that IMPEI's reconfigurability offers an acceptable trade-off in terms of charging capability, grid flexibility, efficiency, and cost.

In Chapter 4, the potential fuel economy of the drivetrain of the Twizy EV, based on experimental and simulation data, is investigated. The drivetrain components in this chapter, mainly the PMSM, and the drive inverter, are designed based on the proposed steps in Chapter 2 and Chapter 3. The drivetrain specifications include the battery nominal voltage, base speed, maximum speed, and rated torque. The proposed IMPEI, in Chapter 3, has been sized and simulated in PSIM software to obtain its efficiency map throughout the operating envelope. The designed PMSM efficiency map is obtained from JMAG software. The mechanical system efficiency map is obtained practically throughout a drive cycle in Aachen city in Germany. The fuel economy analysis provided results that are close to reality.

Chapter 5 focussed on describing the test bench used to obtain the experimental results throughout this thesis. A short comparison of commonly used test benches is provided, followed by the details on the commissioned test bench. This chapter analyzes the regenerative braking of high-speed PMSMs during emergency conditions. It is concluded that overloading the electrical machine during regenerative braking in emergency conditions is a safe and feasible approach that can reduce the EV braking time by using FOC. However, the rating of individual drivetrain components should not be exceeded.

6.2. Future Works

Based on the acquired experience, this section proposes improvements and future research works as follows:

- The IMPEI has been designed, tested, and compared throughout this work. However, this work focussed on the IMPEI as an individual component of the drivetrain. Analyzing the efficiency of the IMPEI along with the other powertrain components will provide a complete picture with more insight into the effect of the IMPEI switches that are turned ON continuously.

- The designed drivetrain in Chapter 4 can perform fuel economy analysis using the worldwide harmonized light vehicles test procedure (WLTP) on a practical Renault Twizy. This will provide fuel economy data that can be used for comparison.

- Throughout this work, the IMPEI has been designed and tested for 96 V and 400 V DC buses. Since the new trend in EVs is to use 800 V drivetrains for their fast charging capabilities, the IMPEI can be designed and tested for its modes of operation at 800 V.

- Test the prototyped motor and validate its parameters and operating envelopes.

References

[1] A. Negi and M. Mathew, "Study on Sustainable Transportation Fuels Based on Green House Gas Emission Potential," in *Int. Conf. Power Energy, Environ. and Intell. Cont. (PEEIC)*, Greater Noida, India, 2018.

[2] D. Kurczyński, P. Łagowski and M. Warianek, "The impact of natural gas on the ecological safety of using Diesel engine," in *XI Int. Sci.-Tech. Conf. Automot. Saf.*, Casta, Slovakia, 2018.

[3] S. Majumder, K. De and P. Kumar, "Zero emission transportation system," in *Int. Conf. Power Electron., Drives and Energy Syst. (PEDES)*, Trivandrum, India, 2016.

[4] X. Lu, K. Ota, M. Dong, C. Yu and H. Jin, "Predicting Transportation Carbon Emission with Urban Big Data," *Trans. Sustain. Comput.,* vol. 2, no. 4, pp. 333-344, 2017.

[5] R. Xiong et al, "Lithium-Ion Battery Health Prognosis Based on a Real Battery Management System Used in Electric Vehicles," *Trans. Veh. Technol.,* vol. 68, no. 5, pp. 4110-4121, 2019.

[6] M. S. A. Chowdhury, K. A. A. Mamun and A. M. Rahman, "Modelling and simulation of power system of battery, solar and fuel cell powered Hybrid Electric vehicle," in *3rd Int. Conf. Elect. Eng. Inf. Commun. Technol. (ICEEICT)*, Dhaka, Bangladesh, 2016.

[7] Z. Lei, F. Wentao, W. Zhenpo, L. Weihan and S. Dirk Uwe, "Battery heating for lithium-ion batteries based on multi-stage alternative currents," *J. Energy Storage,* vol. 32, 2020.

[8] C. Bilaţiu et al, "Identification and Evaluation of Electric and Hybrid Vehicles Propulsion Systems," in *2019 Elect. Veh. Int. Conf. (EV)*, Bucharest, Romania, Romania, 2019.

[9] C. C. Chan, "The State of the Art of Electric Hybrid, and Fuel Cell Vehicles," *IEEE Proc.,* vol. 95, no. 4, pp. 704-718, April 2007.

[10] C. C. Chan, "Electric, Hybrid, and Fuel-Cell Vehicles: Architectures and Modeling," *IEEE Trans. Veh. Tech.,* vol. 59, no. 2, pp. 589-598, 2010.

[11] US Department of Energy, 20 07 2022. [Online]. Available: https://www.fueleconomy.gov/feg/evtech.shtml.

[12] K. H. Nam, AC Motor Control and Electrical Vehicle Applications, 2nd ed., CRC Press, December 18.

[13] M. Ehsani et al, "State of the Art and Trends in Electric and Hybrid Electric Vehicles," *IEEE Proc.,* vol. 109, no. 6, pp. 967-984, June 2021.

[14] A. S. Theodoros et al, "Electrical Vehicles: Current State of the Art, Future Challenges, and Perspectives," *J. Clean Technol.,* vol. 2, pp. 1-16, 2020.

[15] X. Hu, J. Han, X. Tang and X. Lin, "Powertrain Design and Control in Electrified Vehicles: A Critical Review," *IEEE Trans. Transp. Electrific.,* vol. 7, no. 3, pp. 1990 - 2009, 2021.

[16] V. M. Joeri et al, "Beyond the State of the Art of Electric Vehicles: A Fact-Based Paper of the Current and Prospective Electric Vehicle Technologies," *J. World Electr. Veh.,* vol. 1, no. 20, 2021.

[17] EMADI et al., "Power Electronics and Motor Drives in Electric, Hybrid Electric, and Plug-In Hybrid Electric Vehicles," *EEE Trans. Ind. Electron.,* vol. 55, no. 6, pp. 2237-2245, 2008.

[18] M. Yilmaz and P. T. Krein, "Review of battery charger topologies charging power levels, and infrastructure for plug-in electric and hybrid vehicles," *IEEE Trans. Power Electron.,* vol. 28, no. 5, pp. 2151-2169, 2013.

[19] A. M. Lulhe and T. N. Date, "A technology review paper for drives used in electrical vehicle (EV) & hybrid electrical vehicles (HEV)," in *2015 Int. Conf. Control, Instrum. Commun. Comput. Technol. (ICCICCT)*, Kumaracoil, India, Dec. 2015.

[20] M. A. H. Rafi and J. Bauman, "A Comprehensive Review of DC Fast-Charging Stations With Energy Storage: Architectures, Power Converters, and Analysis," *IEEE Trans. Transp. Electrific.,* vol. 7, no. 2, pp. 345 - 368, 2021.

[21] A. Salem and M. Narimani, "A Review on Multiphase Drives for Automotive Traction Applications," *IEEE Trans. Transp. Electrific.,* vol. 5, no. 4, pp. 1329 - 1348, 2019.

[22] W. Sanjaka G and E. Ali, "Classification and review of control strategies for plug-in hybrid electric vehicles," in *Veh. Power and Propulsion Conf.*, Dearborn, MI, USA, 2009.

[23] X. Ding, Z. Wang and L. Zhang, "Hybrid Control-Based Acceleration Slip Regulation for Four-Wheel-Independent-Actuated Electric Vehicles," *IEEE Trans. Transp. Electrific.,* vol. 7, no. 3, pp. 1976 - 1989, 2021.

[24] I. A. Tasiu, Z. Liu, S. Wu, W. Yu, M. Al-Barashi and J. O. Ojo, "Review of Recent Control Strategies for the Traction Converters in High-Speed Train," *IEEE Trans. Transp. Electrific.,* vol. 8, no. 2, pp. 2311 - 2333, 2022.

[25] A. Stippich et al, "Key Components of Modular Propulsion Systems for Next Generation Electric Vehicles," *Trans. Power Electron. Appl.,* vol. 2, no. 4, pp. 249-258, 2017.

[26] S. Rothgang, B. Lunz and et al, "HV Traction Battery: From Layout to Realization," *J. World Elec. Veh. ,* vol. 5, no. 2, pp. 350-359, 2012.

[27] A. Sewergin et al, "Modular bidirectional full-sic dc-dc converter for automotive application," in *12th Int. Conf. Power Electron. Drive Syst. (PEDS)*, Hawaii, 2017.

[28] Porshe, "Porshe," 14 03 2022. [Online]. Available: https://www.porsche.com/canada/en/models/taycan/taycan-models/?gclid=Cj0KCQjwz7uRBhDRARIsAFqjulmbWj48qsQ_60NX6zF44WvpPHpTTE7GrA9iMuN41I-NEUMs6w4G9kIaAgT9EALw_wcB&gclsrc=aw.ds.

[29] I. Aghabali et al, "800-V Electric Vehicle Powertrains: Review and Analysis of Benefits, Challenges, and Future Trends," *IEEE Trans. Transp. Electrific.,* vol. 7, no. 3, pp. 927 - 948, 2021.

[30] J. Christian, "Power Up with 800-V Systems: The benefits of upgrading voltage power for battery-electric passenger vehicles," *Electrific. Mag.,* vol. 5, no. 1, pp. 53-58, 2017.

[31] J. O. Estima and A. J. M. Cardoso, "Efficiency Analysis of Drive Train Topologies Applied to Electric/Hybrid Vehicles," *IEEE Trans. Veh. Technol,* vol. 61, no. 3, pp. 1021-1031, 2012.

[32] M. Eull, L. Zhou, M. Jahnes and M. Preindl, "Bidirectional Nonisolated Fast Charger Integrated in the Electric Vehicle Traction Drivetrain," *IEEE Trans. Transp. Electrific.,* vol. 8, no. 1, pp. 180 - 195, 2022.

[33] C. Shi, Y. Tang and A. Khaligh, "A Single-Phase Integrated Onboard Battery Charger Using Propulsion System for Plug-in Electric Vehicles," *IEEE Trans. Veh. Technol.,* vol. 66, no. 12, pp. 10899 - 10910, 2017.

[34] G. Jinhao, W. Hui, W. Tengxin and W. Yubin, "An integrated topology for on-board charger and driven of electric vehicle," in *IEEE Int. Conf. Ind. Technol. (ICIT)*, Toronto, ON, 2017.

[35] C. Shi and A. Khaligh, "A Two-Stage Three-Phase Integrated Charger for Electric Vehicles With Dual Cascaded Control Strategy," *IEEE J. Emerg. Sel. Topics in Power Electron.,* vol. 6, no. 2, pp. 898 - 909, 2018.

[36] U. Anwar et al, "A high power density drivetrain-integrated electric vehicle charger," in *IEEE Energy Convers, Congr. Expo. (ECCE)*, Milwaukee, WI, 2016.

[37] M. Tong et al, "An Integrated On-board Battery Charger for EVs With Voltage Matching Ability Based on a Six-Phase HEFS Machine," in *12th IEEE PES Asia-Pacific Power and Energy Eng. Conf. (APPEEC)*, Nanjing, China, 2020.

[38] D.-G. Woo, D.-M. Joo and B.-K. Lee, "On the Feasibility of Integrated Battery Charger Utilizing Traction Motor and Inverter in Plug-In Hybrid Electric Vehicles," *IEEE Trans. Power Electron.,* vol. 30, no. 12, pp. 7270 - 7281, 2015.

[39] S. You et al, "An Integrated Electrolytic Capacitorless Onboard Charger for Electric Vehicles," in *IEEE Energy Convers. Cong. Expo. (ECCE)*, Portland, OR, USA, 2018.

[40] I. Subotic, N. Bodo and E. Levi, "An EV Drive-Train With Integrated Fast Charging Capability," *IEEE Trans. Power Electron.,* vol. 31, no. 2, pp. 1461 - 1471, 2016.

[41] S. Semsar, T. Soong and P. W. Lehn, "On-Board Single-Phase Integrated Electric Vehicle Charger With V2G Functionality," *IEEE Trans. Power Electron.,* vol. 35, no. 11, pp. 12072 - 12084, 2020.

[42] V. F. Pires, A. Cordeiro, D. Foito and J. F. Silva, "A Three-Phase On-Board Integrated Battery Charger for EVs with Six-Phase Machine and Nine Switch Converter," in *IEEE 13th Int. Conf. Compat. Power Electron. Power Eng. (CPE-POWERENG)*, Sonderborg, Denmark, 2019.

[43] C. Shi, Y. Tang and A. Khaligh, "A Three-Phase Integrated Onboard Charger for Plug-In Electric Vehicles," *IEEE Trans. Power Electron.,* vol. 33, no. 6, pp. 4716 - 4725, 2018.

[44] D.-H. Kim, M.-J. Kim and B.-K. Lee, "An Integrated Battery Charger With High Power Density and Efficiency for Electric Vehicles," *IEEE Trans. Power Electron.,* vol. 32, no. 6, pp. 4553 - 4565, 2016.

[45] K. A. Chinmaya and G. K. Singh, "A Multifunctional Integrated Onboard Battery Charger for Plug-in Electric Vehicles (PEVs)," in *IEEE 18th Int. Power Electron. Motion Control Conf. (PEMC)*, Budapest, Hungary, 2018.

[46] R. Razi, B. Asaei and M. R. Nikzad, "A new battery charger for plug-in hybrid electric vehicle application using back to back converter in a utility connected micro-grid," in *8th Power Electron. Drive Syst. & Technol. Conf. (PEDSTC)*, Mashhad, 2017.

[47] U. Singh, Y. Pal, S. Nagpal and G. Sarkar, "Single-Phase On-Board Integrated Bi-Directional Charger with Power Factor Correction for an EV," in *6th Int. Conf. Signal Process. Integr. Networks (SPIN)*, Noida, India, 2019.

[48] K. Fahem, D. E. Chariag and L. Sbita, "On-board bidirectional battery chargers topologies for plug-in hybrid electric vehicles," in *Int. Conf.on Green Energy Convers. Syst. (GECS)*, Hammamet, 2017.

[49] C. Viana and P. W. Lehn, "A Drivetrain Integrated DC Fast Charger With Buck and Boost Functionality and Simultaneous Drive/Charge Capability," *IEEE Trans. Transp. Electrific.,* vol. 5, no. 4, pp. 903 - 911, 2019.

[50] A. K. Singh and M. K. Pathak, "A Comprehensive Review of Integrated Charger for on-Board Battery Charging Applications of Electric Vehicles," in *IEEE 8th Power India Int.Conf. (PIICON)*, Kurukshetra, India, 2018.

[51] T. Na, X. Yuan, J. Tang and Q. Zhang, "A review of on-board integrated electric vehicles charger and a new single-phase integrated charger," *CPSS Trans. Power Electron. Appl.,* vol. 4, no. 4, pp. 288 - 298, 2019.

[52] N. Uzhegov et al, "Multidisciplinary design process of a 6-slot 2-pole high-speed permanent-magnet synchronous machine," *IEEE Trans. Ind. Electron.,* vol. 63, no. 2, pp. 784-795, 2016.

[53] K. H. Nam, AC motor control and electric vehicles applications, CRC Press, 2010.

[54] C. Lu, S. Ferrari and G. Pellegrino, "Two Design Procedures for PM Synchronous Machines for Electric Powertrains," *IEEE Trans. Transp. Electrific.,* vol. 3, no. 1, pp. 98 - 107, 2017.

[55] T. Burress and C. S, "Benchmarking EV and HEV power electronics and electric machines," in *IEEE Transp. Electrific. Conf. Expo. (ITEC)*, Detroit, MI, USA, 2013.

[56] Kai C. et al, "Analysis and Design of Current Regulators for PMSM Drives Based on DRGA," *IEEE Trans. Transp. Electrific.,* vol. 6, no. 2, pp. 659 - 667, 2020.

[57] Nicorici A, "Design and Analysis of a Surface Permanent Magnet Synchronous Machine for Automotive Applications," in *15th Int. Conf. Eng. Modern Electr. Syst. (EMES)*, Oradea, Romania, 2019.

[58] C. He and T. Wu, "Analysis and design of surface permanent magnet synchronous motor and generator," *CES Trans. Electr. Mach. Syst.,* vol. 3, no. 1, pp. 94-100, March 2019.

[59] Xie P. et al, "Simplified Analytical Machine Sizing for Surface Mounted Permanent Magnet Machines," in *IEEE Int. Electr. Mach. Drives Conf. (IEMDC)*, San Diego, CA, USA, 2019.

[60] Fernández D. et al, "Impact of Machine Magnetization State on Permanent Magnet Losses in Permanent Magnet Synchronous Machines," *IEEE Trans. Ind. Appl.,* vol. 55, no. 1, pp. 344-353, Jan.-Feb. 2019.

[61] Zhang C. et al, "Loss Calculation and Thermal Analysis for High-Speed Permanent Magnet Synchronous Machines," *IEEE Access,* vol. 8, pp. 92627-92636, 2020.

[62] Lee S. et al, "Design of the High Efficiency IPMSM Considering the Operating Point with Different Characteristic," in *Int. Electr. Mach. Drives Conf. (IEMDC),*, San Diego, CA, USA, 2019.

[63] A. Krings and C. Monissen, "Review and Trends in Electric Traction Motors for Battery Electric and Hybrid Vehicles," in *Int. Conf. Electr. Mach. (ICEM), 2020, pp. 1807-1813*, Gothenburg, Sweden, 2020.

[64] K. S. Amitkumar, R. S. Kaarthik and P. Pillay, "A Versatile Power-Hardware-in-the-Loop-Based Emulator for Rapid Testing of Transportation Electric Drives," *IEEE Trans. Transp. Electrific.,* vol. 4, no. 4, pp. 901 - 911, 2018.

[65] *JMAG-Designer, (2018-2019), [Offline], Available: https://www.jmag-international.com/products/jmag-designer/.*

[66] "Decoupled Speed and Torque Control of IPMSM Drives Using a Novel Load Torque Estimator," *J. Advances Elect. Comput. Eng.,* vol. 17, no. 3, pp. 19-28, 2017.

[67] K. Dambrauskas et al, "A Method for Efficiency Determination of Permanent Magnet Synchronous Motor," *J.*

Energies, vol. 13, no. 1004, 2020.

[68] M. Zaky, E. Elattar and M. METWALY, "Decoupled Speed and Torque Control of IPMSM Drives Using a Novel Load Torque Estimator," *J. Advances Elect. Comput. Eng.,* vol. 17, no. 3, pp. 19-28, 2017.

[69] K. T. Chau, Electric Vehicle Machines and Drives: Design, Analysis and Application, © 2015 John Wiley & Sons Singapore Pte. Ltd., 2015 (first edition).

[70] F. Blaabjerg, Control of Power Electronic Converters and Systems, F. Blaabjerg, Ed., 1st Edition - January 24, 2018.

[71] J. F. Sultani, "Modelling, Design and Implementation Of D-Q Control in Single-Phase Grid-Connected Inverters for Photovoltaic Systems Used in Domestic," De Montfort University, Leicester, UK, 2013.

[72] S. Kumar and A. Usman, "A Review of Converter Topologies for Battery Charging Applications in Plug-in Hybrid Electric Vehicles," in *IEEE Industry Appl. Soc. Annu. Meeting (IAS)*, Portland, OR, USA, Sept. 2018.

[73] H. Tu, H. Feng, S. Srdic and S. Lukic, "Extreme Fast Charging of Electric Vehicles: A Technology Overview," *IEEE Trans. Transp. Electrific.,* vol. 5, no. 4, pp. 861 - 878, 2019.

[74] M. Moradpour and G. Gatto, "A New SiC-GaN-Based Two-Phase Interleaved Bidirectional DC-DC Converter for Plug-In Electric Vehicles," in *Int. Symp. Power Electron. Elect. Drives, Automat. Motion (SPEEDAM)*, Amalfi, Italy, June 2018.

[75] D. Ravi et al, "An Overview of Various DC-DC Converter Techniques used for Fuel Cell based Applications," in *Int. Conf. Power Energy, Environ. Intell. Control (PEEIC)*, Greater Noida, India, India, April 2018.

[76] K. Fahem, D. E. Chariag and L. Sbita, "On-board bidirectional battery chargers topologies for plug-in hybrid electric vehicles," in *2017 Int. Conf. Green Energy Convers. Syst. (GECS)*, Hammamet, Tunisia , March 2017, 2017.

[77] G. N. Goyal and M. V. Aware, "A comparative performance of six-phase nine switch inverter operation with SPWM and SVPWM," in *IEEE Int. Conf. Power Electron. Drives and Energy Syst. (PEDES)*, Bengaluru, India, 2012.

[78] Z. B. and Q. D, "6-Mode SVPWM for Nine-Switch Dual-Output Inverter," in *M-Mode SVPWM Technique for Power Converters*, Singapore, CPSS Power Electronics Series. Springer, 2019.

[79] X. Li, B. Zhang, D. Qiu and D. Wang, "New PWM strategy for nine-switch inverters with minimum number of semiconductor switching," in *Int. Power Electron. Appl. Conf. Expo.*, Shanghai, China, 2014.

[80] S. Angshuman and S. Santanu, "Review of power electronics in vehicle-to-grid systems," *J. Energy Storage,* vol. 21, no. https://doi.org/10.1016/j.est.2018.11.022, pp. 337-361, 2019.

[81] R. Peña-Alzola et al, "LCL-Filter Design for Robust Active Damping in Grid-Connected Converters," *IEEE Trans. Ind. Inform.,* vol. 10, no. 4, pp. 2192 - 2203, 2014.

[82] A. K. Morya et al, "Wide Bandgap Devices in AC Electric Drives: Opportunities and Challenges," *IEEE Trans. Transp. Electrific.,* vol. 5, no. 1, pp. 3-20, 2019.

[83] O. Hegazy et al, "An Advanced Power Electronics Interface for Electric Vehicles Applications," *IEEE Trans. Power Electron.,* vol. 28, no. 12, pp. 5508-5520, 2013.

[84] T. Burress, S. A. Rogers and Burak Ozpineci, "FY 2016 Annual Progress Report for Electric Drive Technologies Program," U.S. Department of Energy, Office of Energy Efficiency and Renewable Energy, July 2017.

[85] S. Jayalath and M. Hanif, "An LCL-Filter Design With Optimum Total Inductance and Capacitance," *IEEE Trans. Power Electron.,* vol. 33, no. 8, pp. 6687 - 6698, 2018.

[86] T. Payarou, S. Singh, M. Muthusamy and P. Pillay, "Design Criteria for EV Drivetrain," in *47th Annu. Conf. of the IEEE Ind. Electron. Soc. (IECON)*, Toronto, ON, Canada, 2021.

[87] Wakefield-Vette, "Heat Sink Design Facts & Guidelines for Thermal Analysis," [Online]. Available: www.wakefield-vette.com. [Accessed 18 Aug. 2022].

[88] Government of Canada. [Online]. Available: https://www.nrcan.gc.ca/energy-efficiency/transportation-alternative-fuels/personal-vehicles/choosing-right-vehicle/buying-electric-vehicle/understanding-the-tables/21383. [Accessed 01 09 2022].

[89] "The car Guide," [Online]. Available: https://www.guideautoweb.com/en/makes/renault/twizy/2017/specifications/40/. [Accessed 02 09 2022].

[90] Yoong M. K. et al, "Studies of regenerative braking in electric vehicle," in *IEEE Conf. Sustain. Utilization and Develop. Eng. Technol. (STUDENT)*, Petaling Jaya, Malaysia, 2010.

[91] Ji Yang M. et al, "A Cost-Effective Method of Electric Brake With Energy Regeneration for Electric Vehicles" Ming-Ji Yang, Hong-Lin Jhou, Bin-Yen Ma, and Kuo-Kai Shyu, Member, IEEE Trans. Ind. Electronics, 56(6), 2203 -," *IEEE Trans. Ind. Electron.,* vol. 56, no. 6, pp. 2203 - 2212, June 2009.

[92] D. Lu et al, "Instantaneous optimal regenerative braking control for a permanent-magnet synchronous motor in a four-wheel-drive electric vehicle," *J. Automobile Eng.,* vol. 228, no. 8, pp. 894-908, July 2014.

[93] C.-H. Chen, W.-C. Chi and M.-Y. Cheng, "Regenerative braking control for light electric vehicles," in *IEEE 9th Int.l Conf. Power Electron. Drive Syst. (PEDS)*, Singapore, 2011.

[94] F. Naseri, E. Farjah and T. Ghanbari, "An Efficient Regenerative Braking System Based on Battery/Ultracapacitor for Electric, Hybrid and Plug-In Hybrid Electric Vehicles with BLDC Motor," *IEEE Trans. Veh. Technol.,* vol. 66, no. 5, p. 3724–3738, 2017.

[95] Y. Bian et al, "Regenerative Braking Strategy for Motor Hoist by Ultracapacitor," *J. Mech. Eng.,* vol. 25, no. 2, p. 377–384, March 2012.

[96] Z. Zhang et al, "A high-efficiency energy regenerative shock absorber using supercapacitors for renewable energy applications in range extended electric vehicle," *J. Appl. Energy,* vol. 178, p. 177–188, 2016.

[97] J. F. Gieras and M. Wing, Permanent Magnet Motor Technology (Design and Application), Marcel Dekker Inc, second edition, revised and expanded, 2002.

[98] O. Sinchuk and I. Kozakevich, "Research of regenerative braking of traction permanent magnet synchronous motors," in *Int. Conf. Modern Elect. Energy Syst. (MEES)*, Kremenchuk, 2017.

[99] T. M. Jahns, "Flux-Weakening Regime Operation of an Interior Permanent-Magnet Synchronous Motor Drive," *IEEE Trans. Ind. Appl.,* Vols. IA-23, no. 4, 1987.

[100] P.L. Rongmei et al, "A Novel Fast Braking System for Induction Motor," *Int. J. Eng. Innovative Technol.*

(IJEIT), vol. 1, no. 6, June 2012.

[101] M. Darko P. and M. Petar R., "Nonregenerative Braking of Permanent Magnet Synchronous Motor," *IEEE Trans. Ind. Electron.,* vol. 67, no. 10, pp. 8186 - 8196, 2020.

[102] 2. Adel A. O. et al., "Plugging Braking of Two-PMSM Drive in Subway Applications with Fault -Tolerant Operation," *Iraq J. Electrical and Electronic Engineering,* vol. 12, no. 1, pp. 1-11, 2016.

[103] A. A. Mahapatra, "Improved Braking Performance of an Electric Vehicle by Integrating Plug Braking With Regenerative Braking," Department of Electrical Engineering National Institute of Technology, Rourkela - 769008, 2015.

[104] Aravind S. M. et al, "Comparison of regenerative braking controllers for permanent magnet synchronous machines," in *IEEE Int. Elect. Mach. Drives Conf. (IEMDC)*, Coeur d'Alene, ID, USA, 2015.

[105] Lu et al., "Instantaneous optimal regenerative braking control for a permanent-magnet synchronous motor in a four-wheel-drive electric vehicle," *J. Automotive Eng.,* vol. 228, no. 8, pp. 894-908, 2014.

[106] A. Adib and R. Dhaouadi, "Performance Analysis of Regenerative Braking in Permanent Magnet Synchronous Motor Drives," *J. Adv. Sc. Technol. Eng. Syst.,* vol. 3, no. 1, pp. 460-466, 2018.

[107] Renault, 11 Aug. 2022. [Online]. Available: https://www.renault.ro/vehicule-electrice/twizy.html.

[108] The State of Queensland, "Queensland Government," 21 April 2021. [Online]. Available: https://www.qld.gov.au/__data/assets/image/0020/44561/stoppingdistancesinfographic.jpg. [Accessed 21 April 2021].

Appendix A: More Details of the Prototyped IMPEI
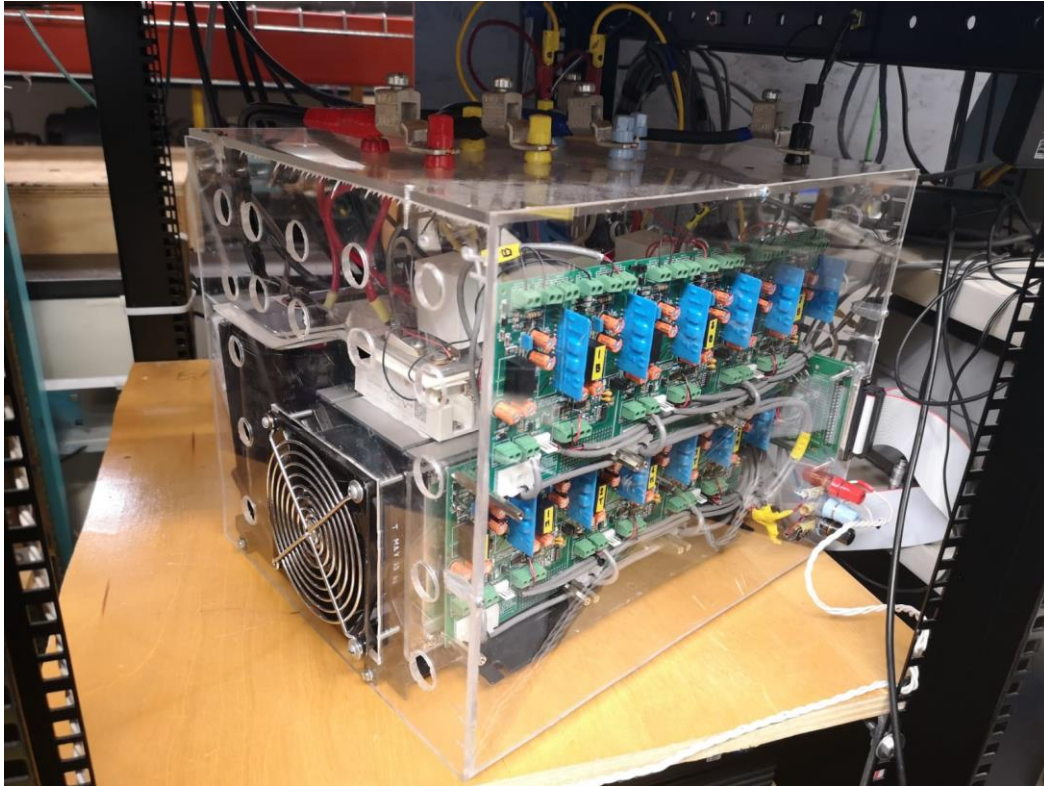
(a)
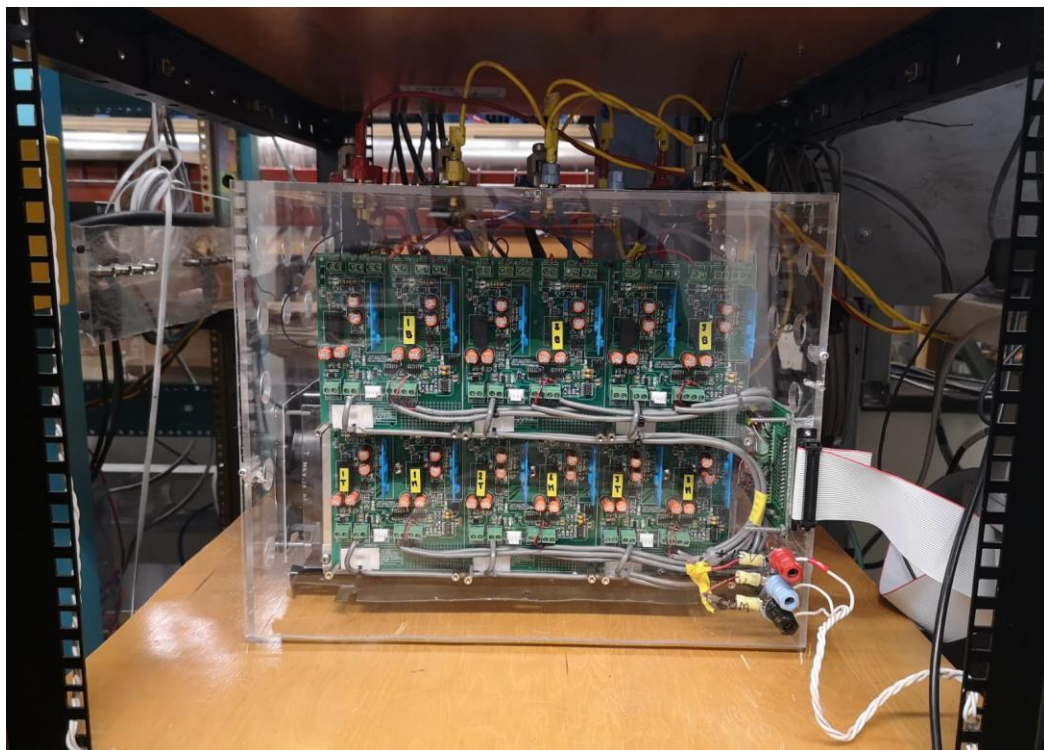
(b)

Fig. A-1. IMPEI views: (a) side view and (b) front view.
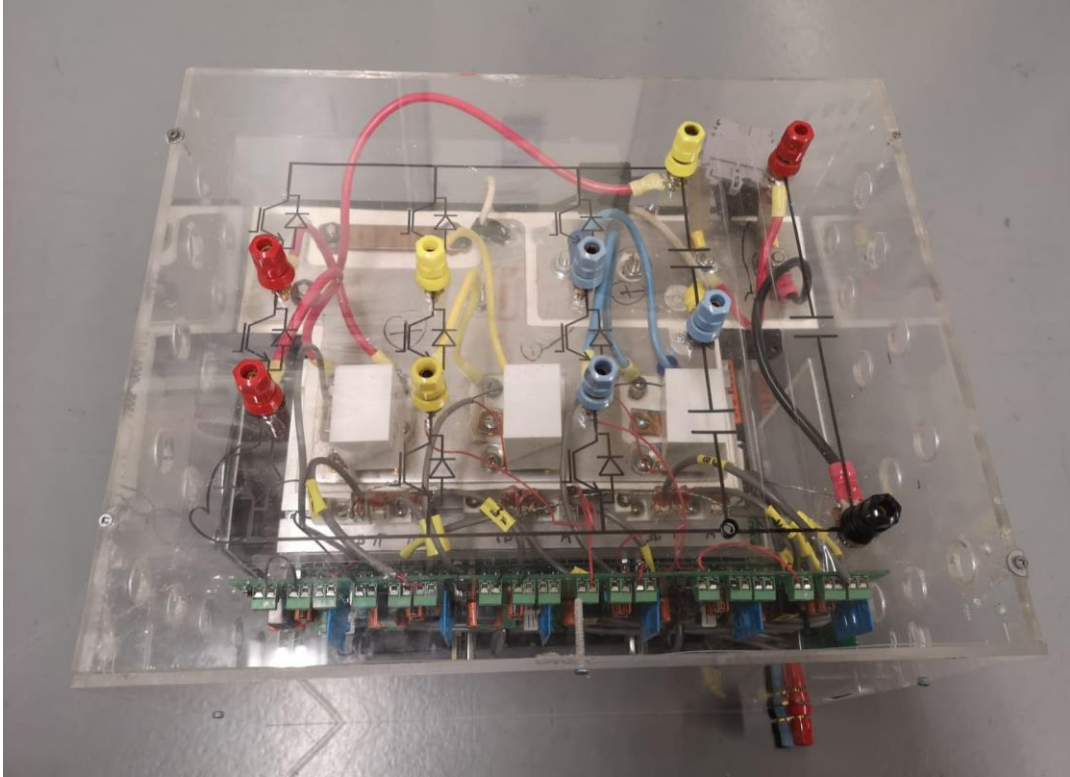
(a)
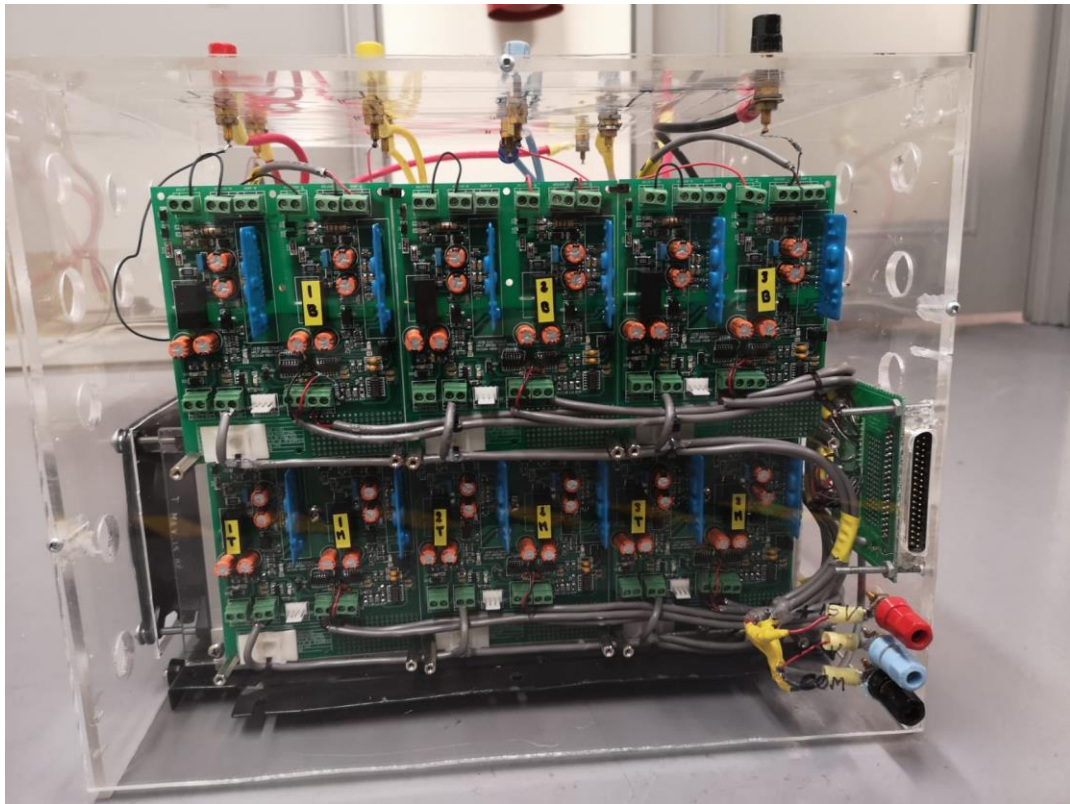
(b)
Fig. A-2. IMPEI views: (a) top and (b) front view (custom gate drivers based on MORNSUN QC962-8A).
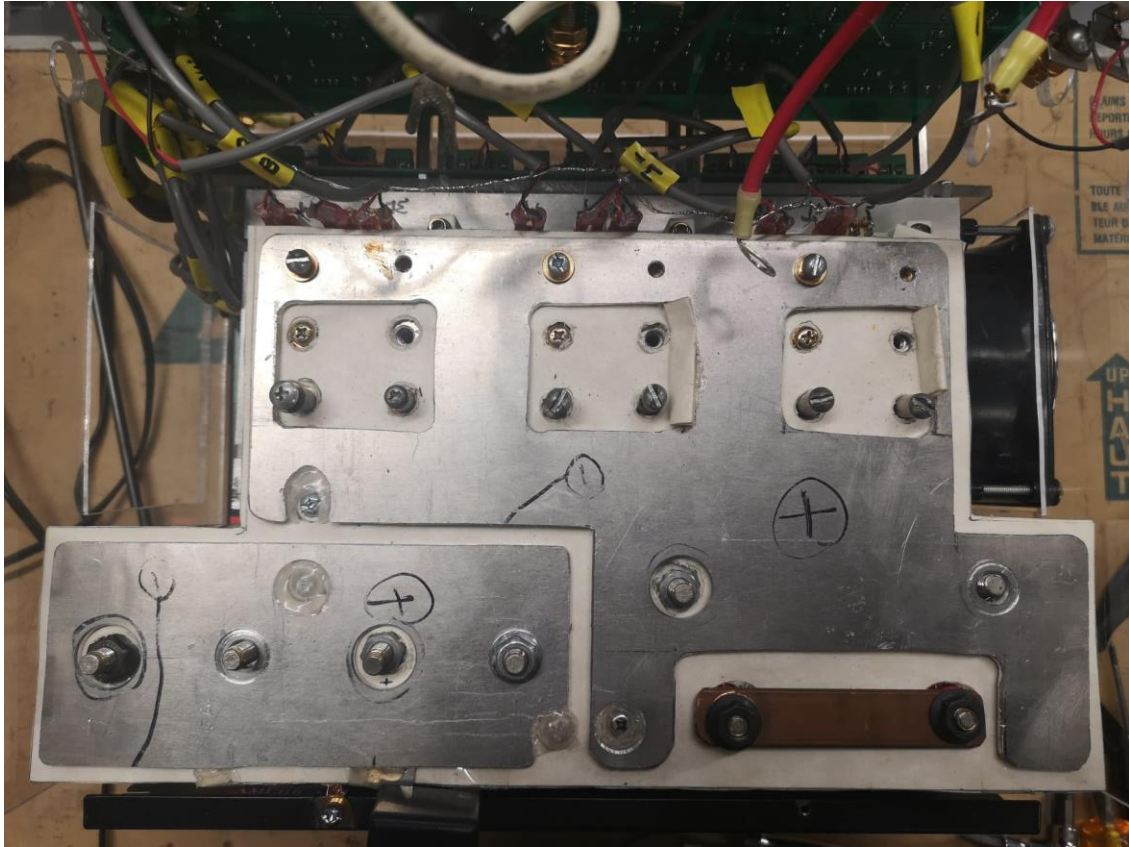
(a)
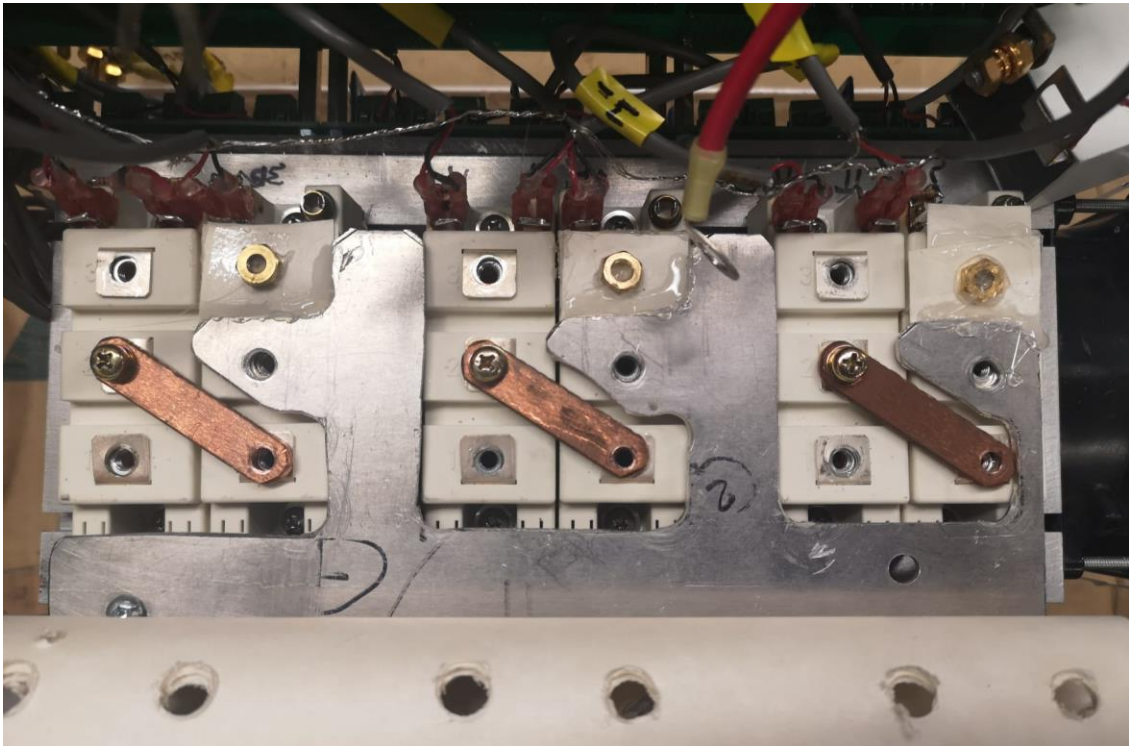
(b)

Fig. A-3. IMPEI busbar layout: (a) negative polarity and (b) positive polarity.
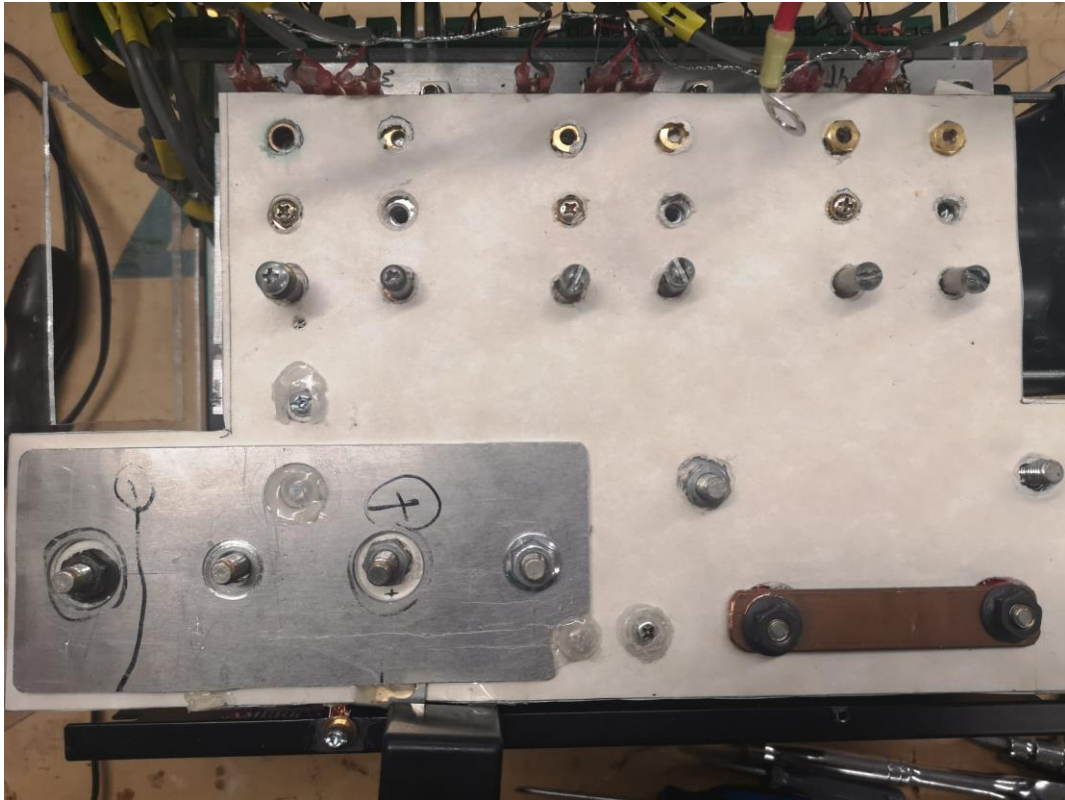
(a)
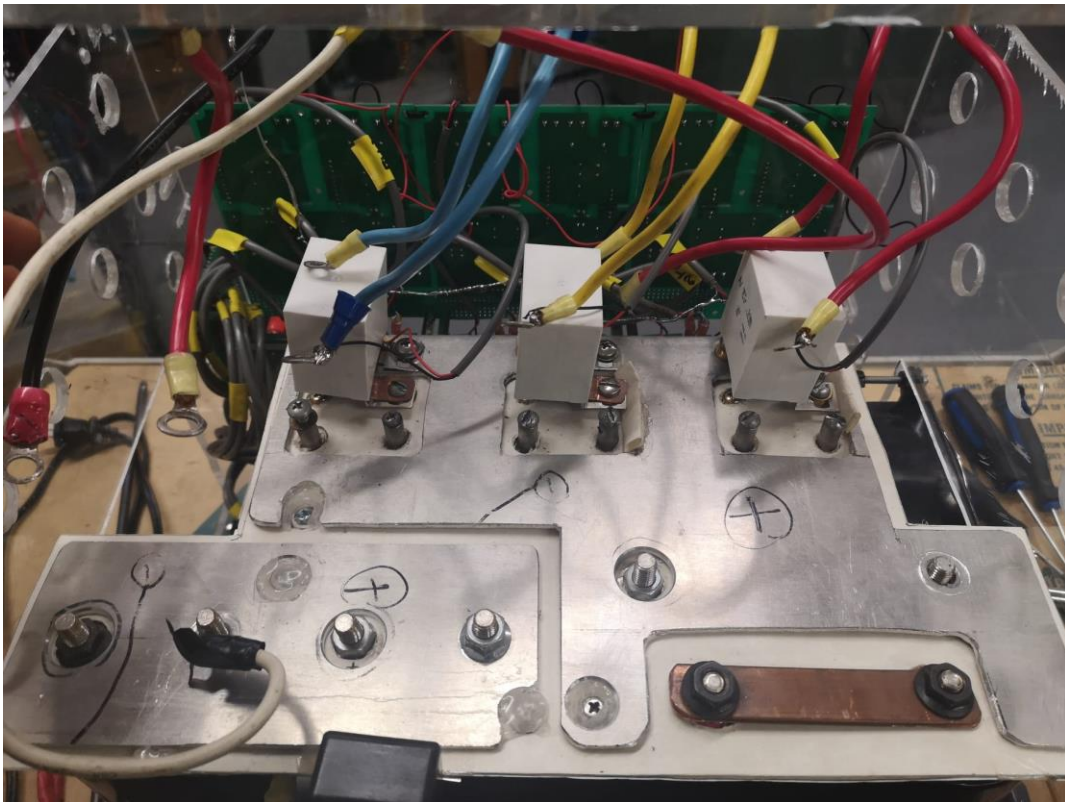
(b)

Fig. A-4. IMPEI: (a) insulation sheets, (b) snubber capacitors.
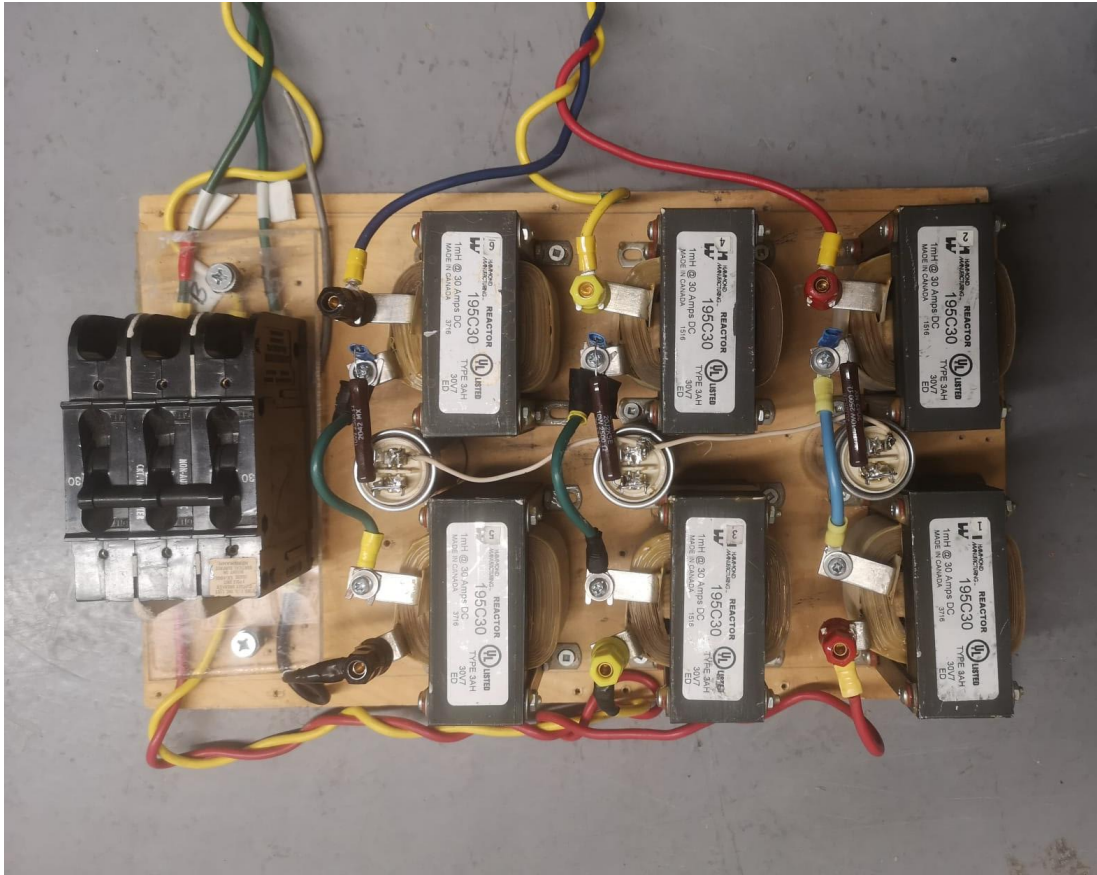
(a)
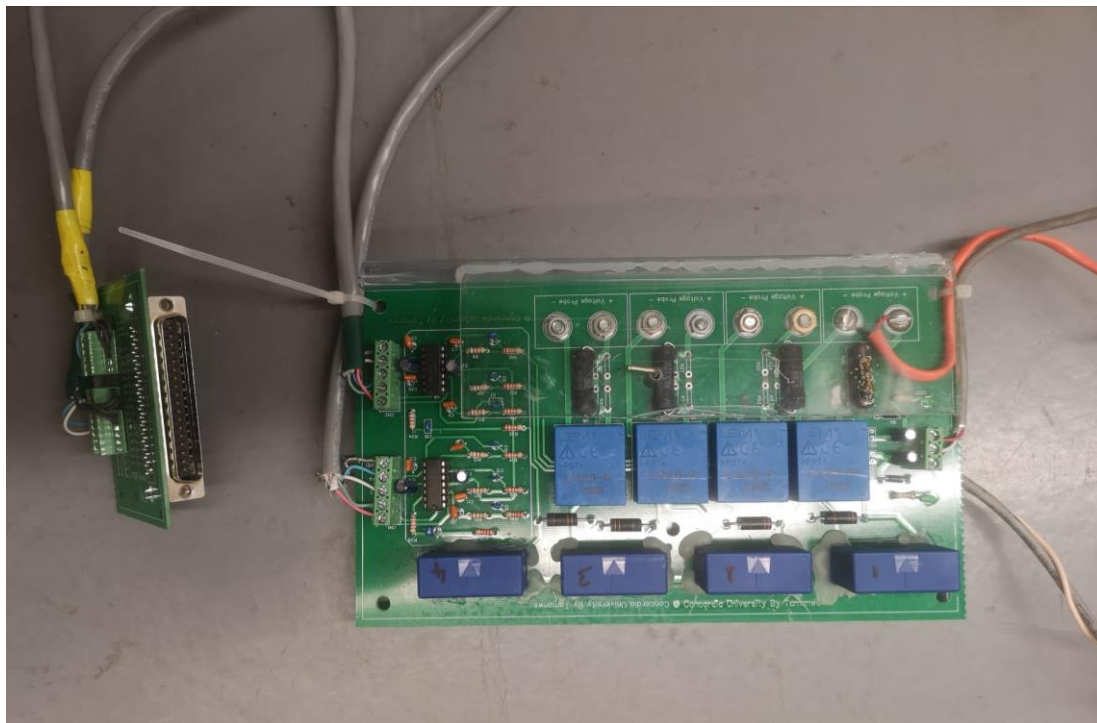
(b)

Fig. A-5. Prototyped (a) LCL filter and (b) current (LA55P) and voltage (LV20-P) sensors.
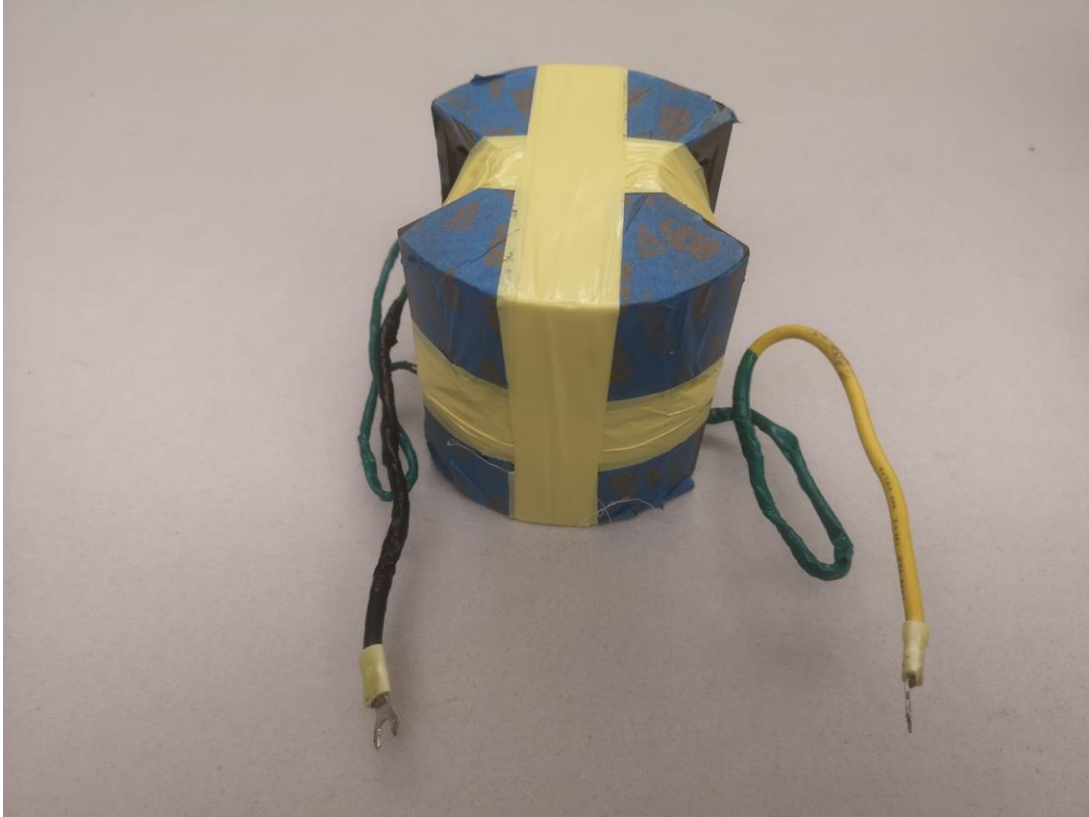
Fig. A-6. 10 mH inductor for the DC-DC operation.

Appendix B: PMSM Control Diagram without the Feed Forward Terms
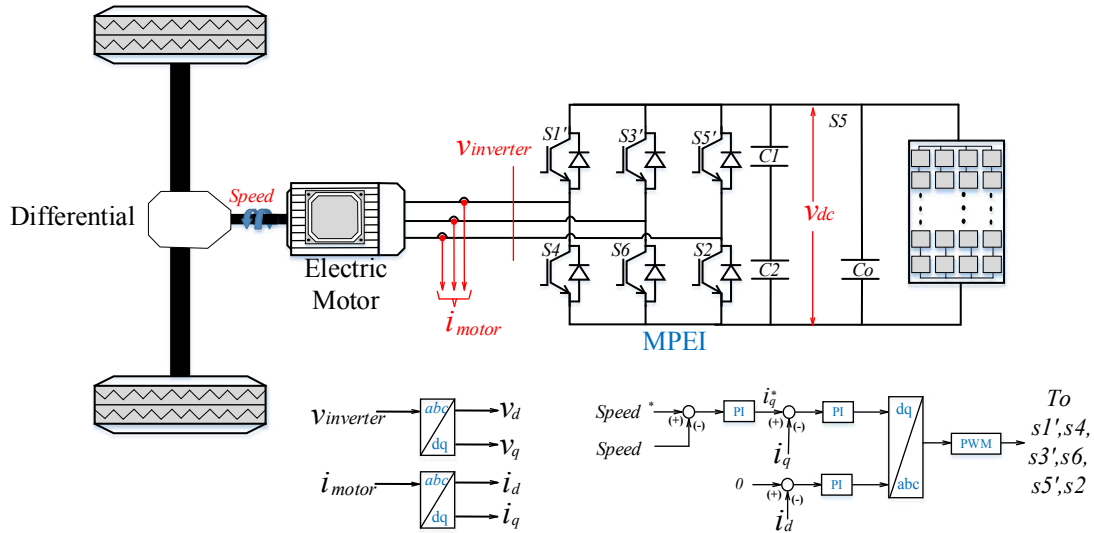
Fig. B-1. FOC control scheme of PMSM
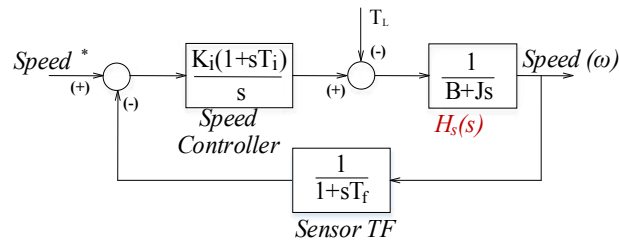
Fig. B-2. Block diagram of the PMSM speed loop
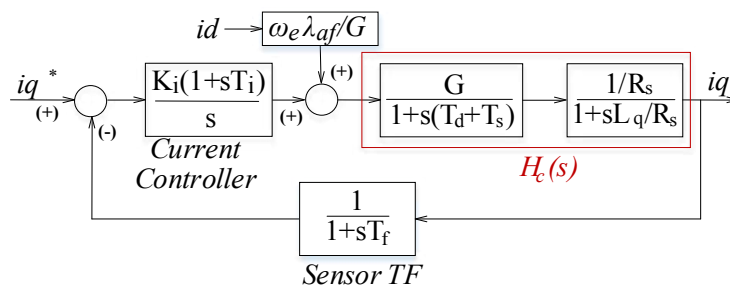
Fig. B-3. Block diagram of the PMSM q-axis current loop
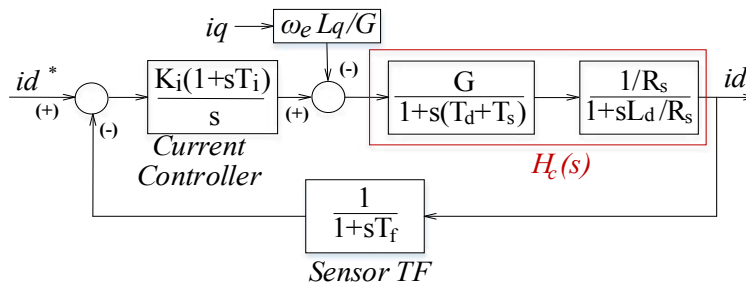
Fig. B-4. Block diagram of the PMSM d-axis current loop

Appendix C: Real-time FOC for Propulsion and Regenerative Braking.

In this section, the blocks used for implementing the FOC control as well as the protection circuit have been expanded sequentially.
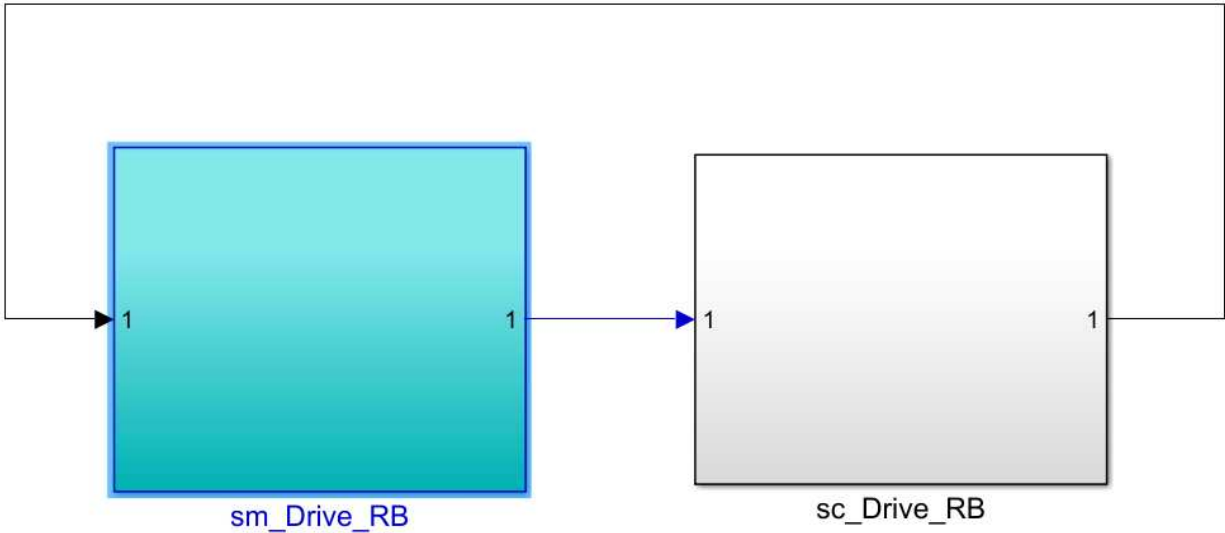
(a)
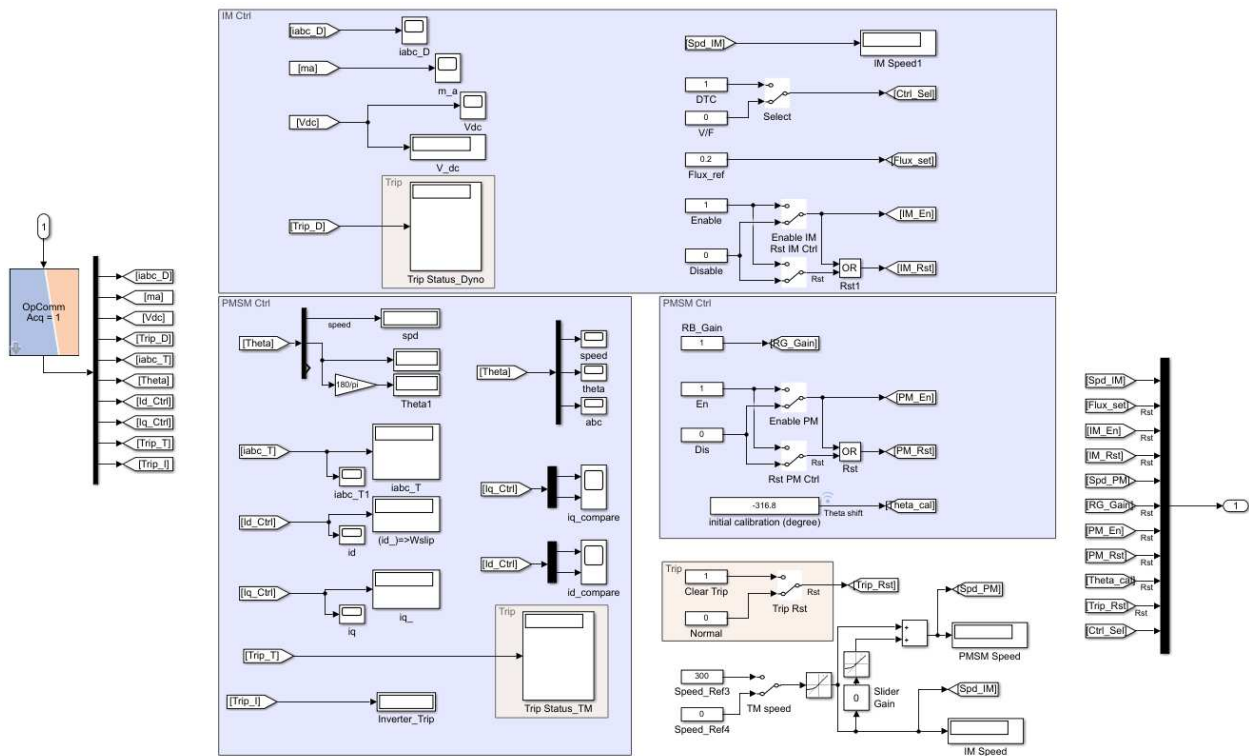
(b)

Fig. C-1. FOC control: (a) real-time model, (b) inside the "sc_Drive_RB" block (this block represents the command panel).
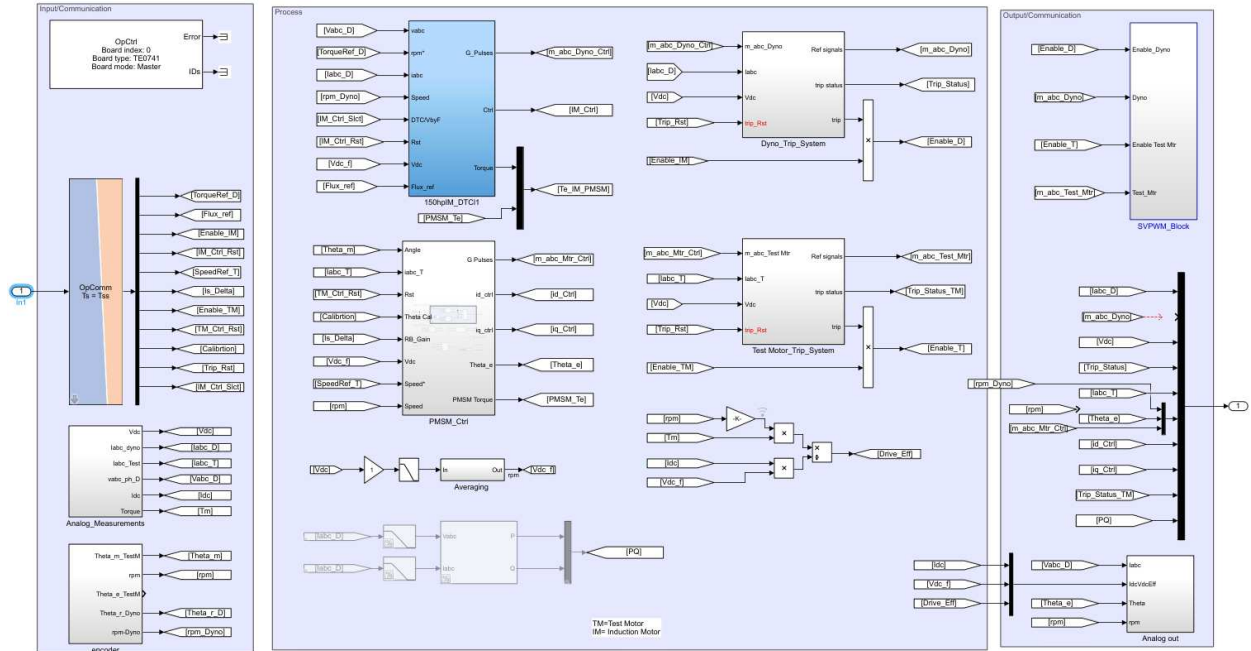
(a)
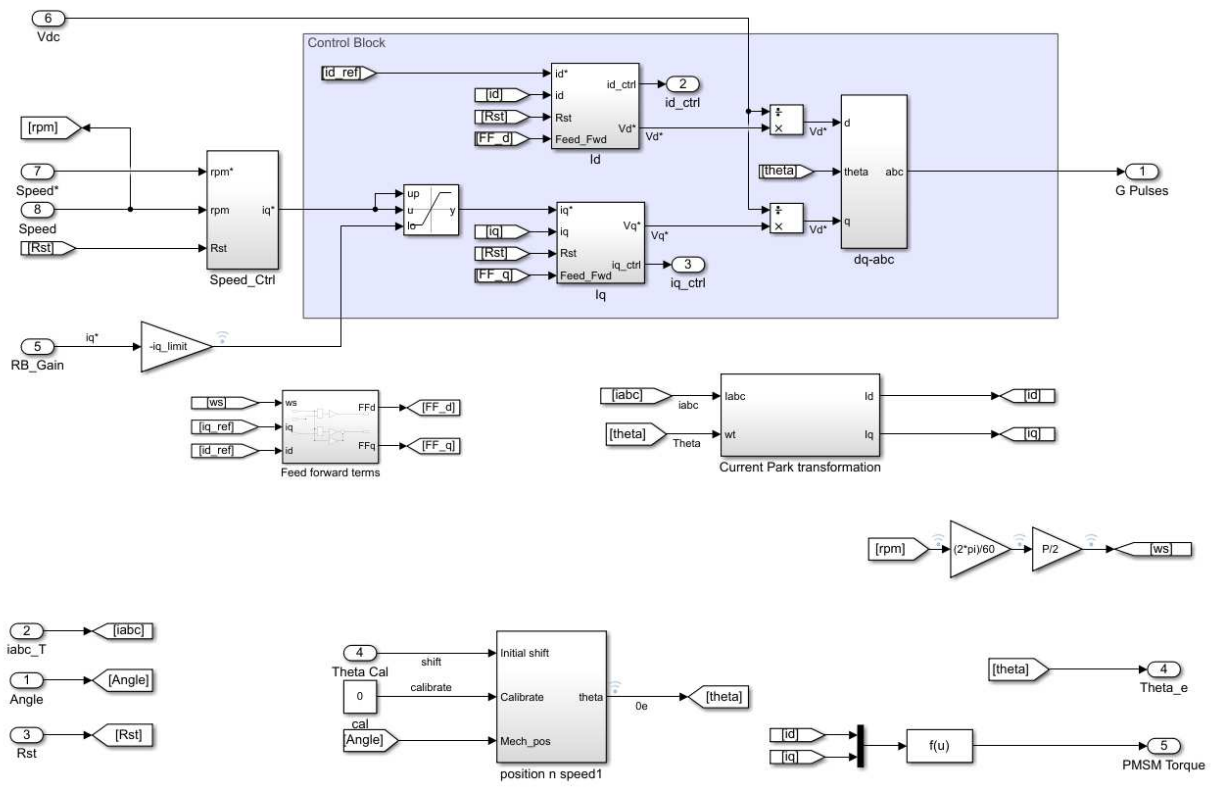
(b)

Fig. C-2. FOC control: (a) inside the "sm_Drive_RB" block (This block represents the process loaded on the FPGA. The systems in this block run in real-time), (b) inside the "PMSM_Ctrl" block.
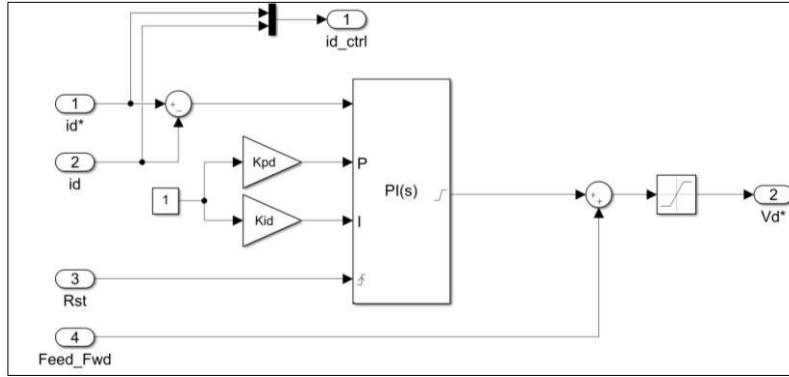
(a)
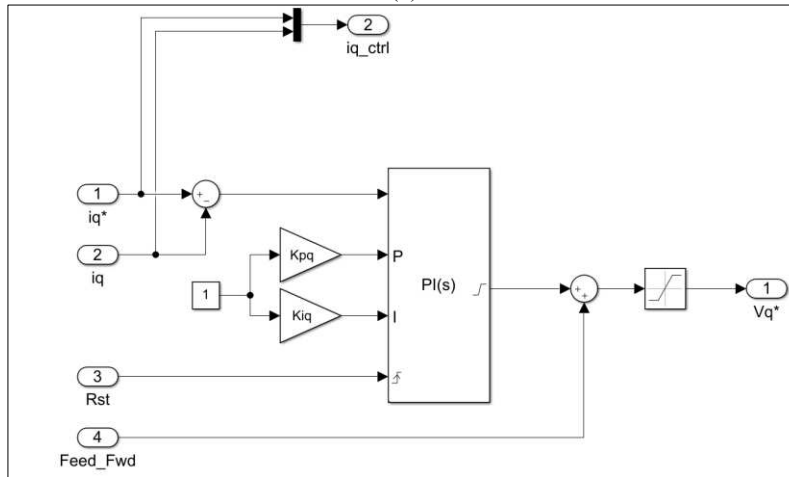
(b)
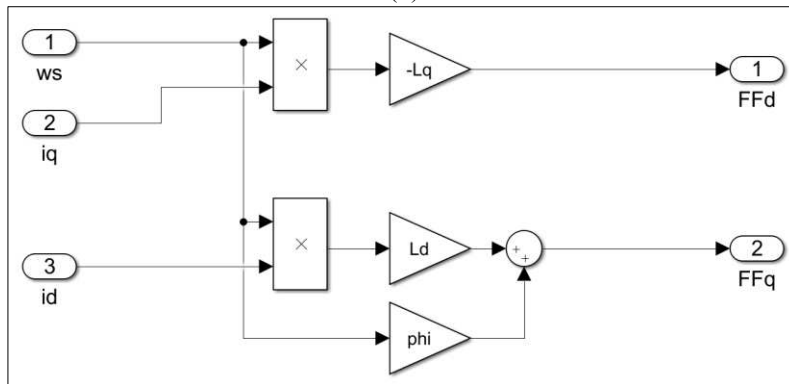
(c)
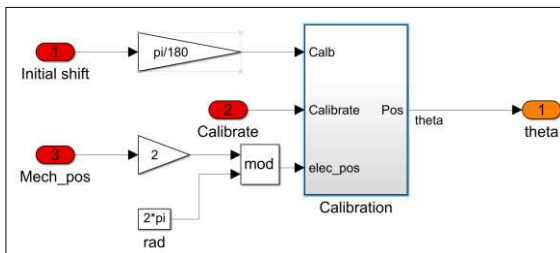
(d)
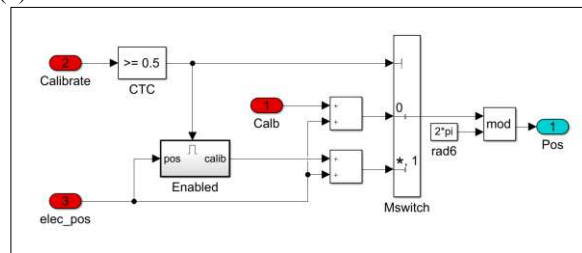
(e)

Fig. C-3. FOC control: (a) inside the "Id" block, (b) inside the "Iq" block, (c) inside the "Feedforward terms" block, (d) inside "position n speed1" block (this block is used for initial position calibration of the PMSM), and (e) inside "calibration" block.

131
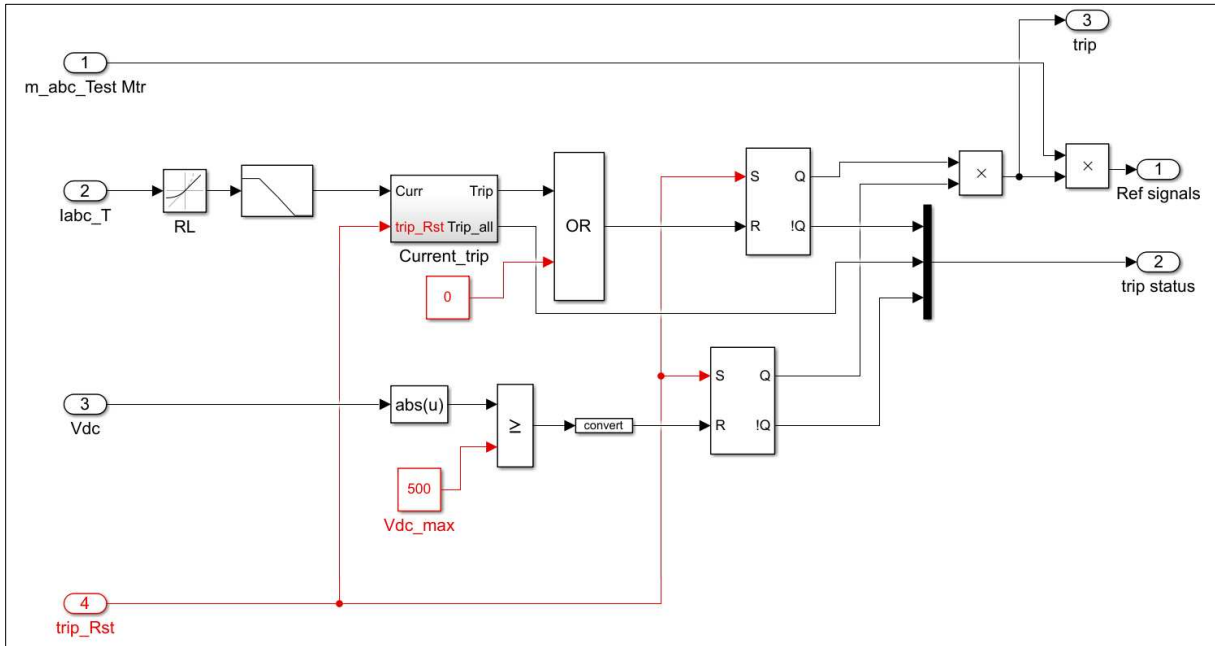
(a)
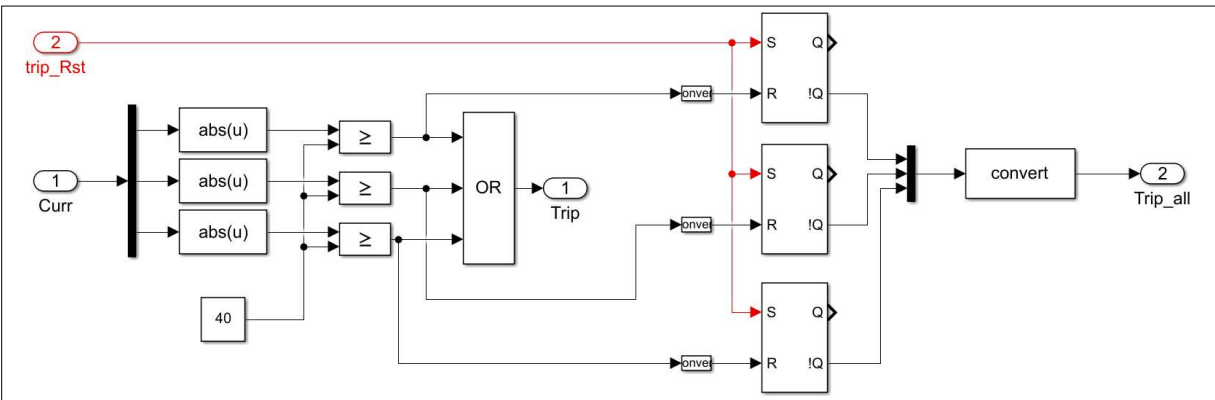
(b)
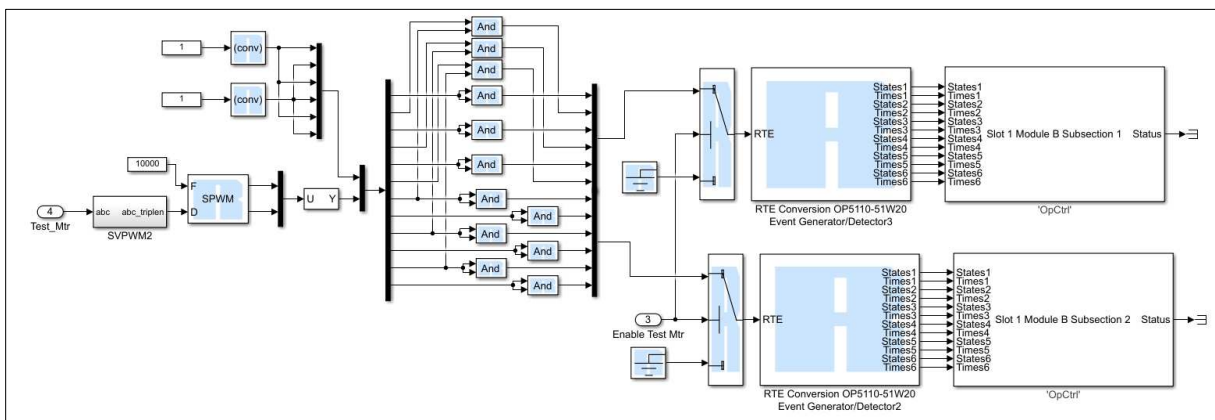
(c)

Fig. C-4. FOC control: (a) inside the "Test Motor_Trip_System" block (this block turns OFF the gating pulses once the preset safe operating ranges of voltage and current are exceeded), (b) inside the "Current_trip" block, and (c) inside the "SVPWM_Block" block.
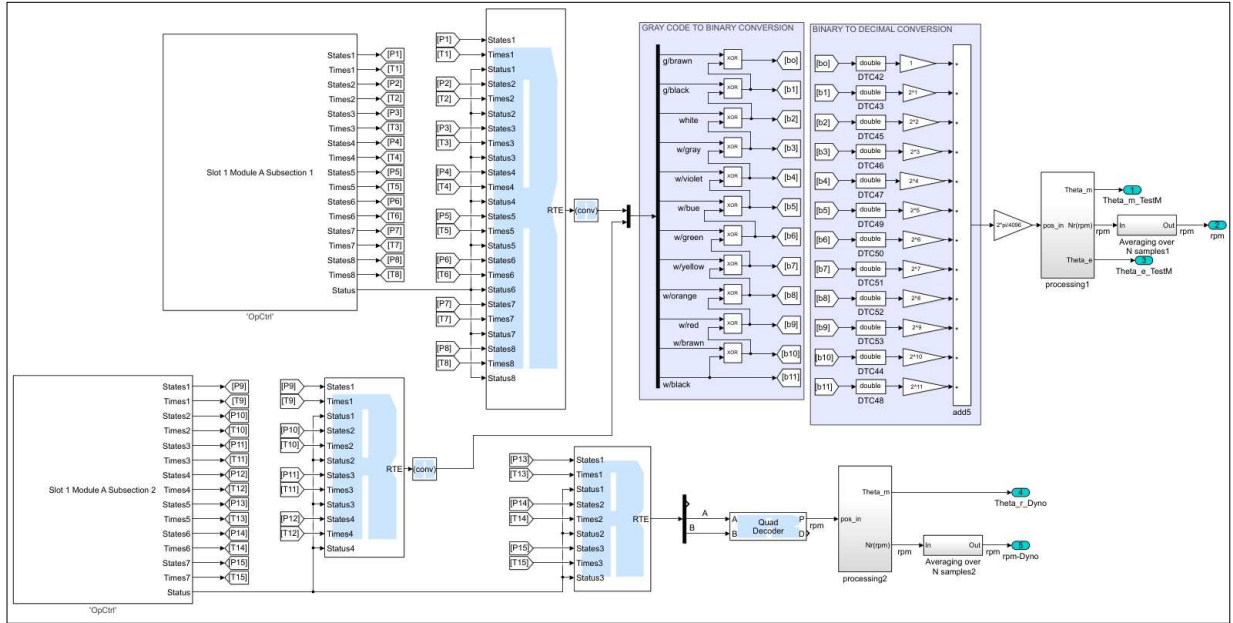
(a)
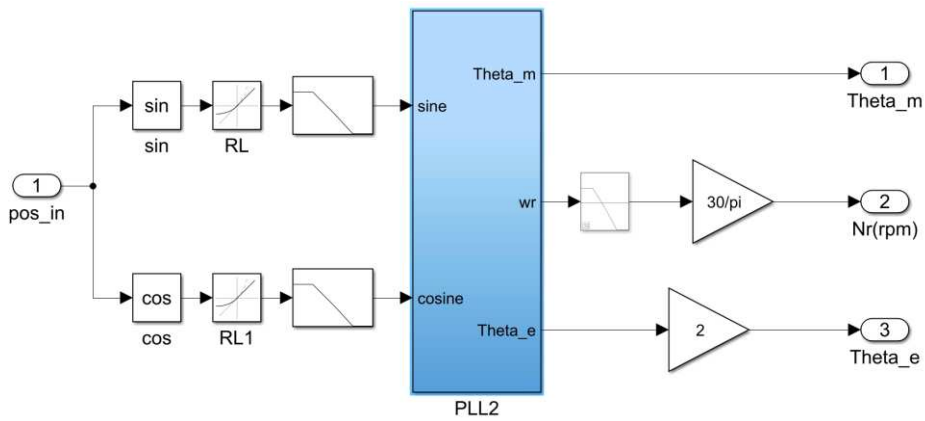
(b)
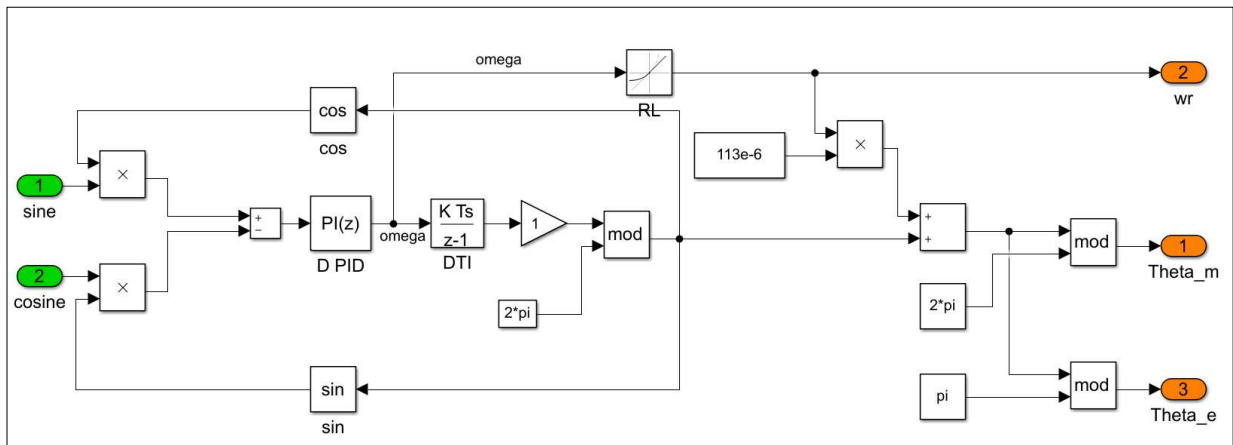
(c)

Fig. C-5. FOC control: (a) inside the "encoder" block (the encoder is a grey coded absolute encoder), (b) inside the "Processing1" block, and (c) inside the "PLL2" block.

133

Appendix D: Real-time Controller for Three-phase V2G and G2V

In this section, the blocks used for implementing the three-phase V2G and G2V real-time control as well as the protection circuit have been expanded sequentially.
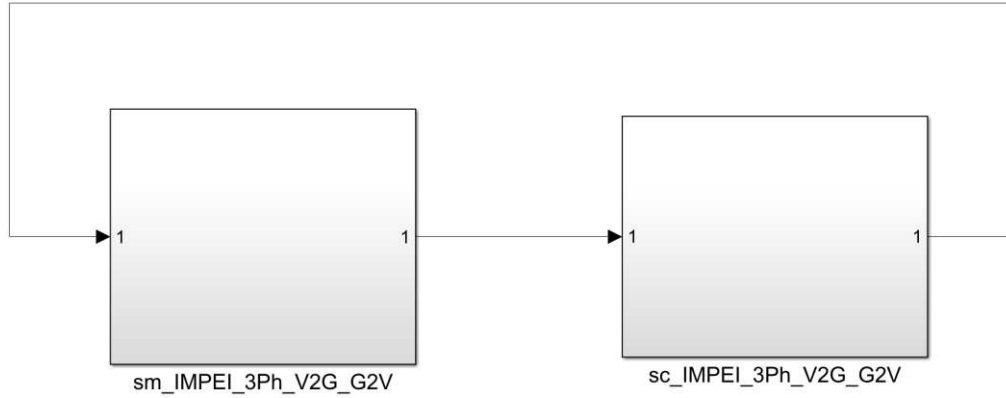
(a)
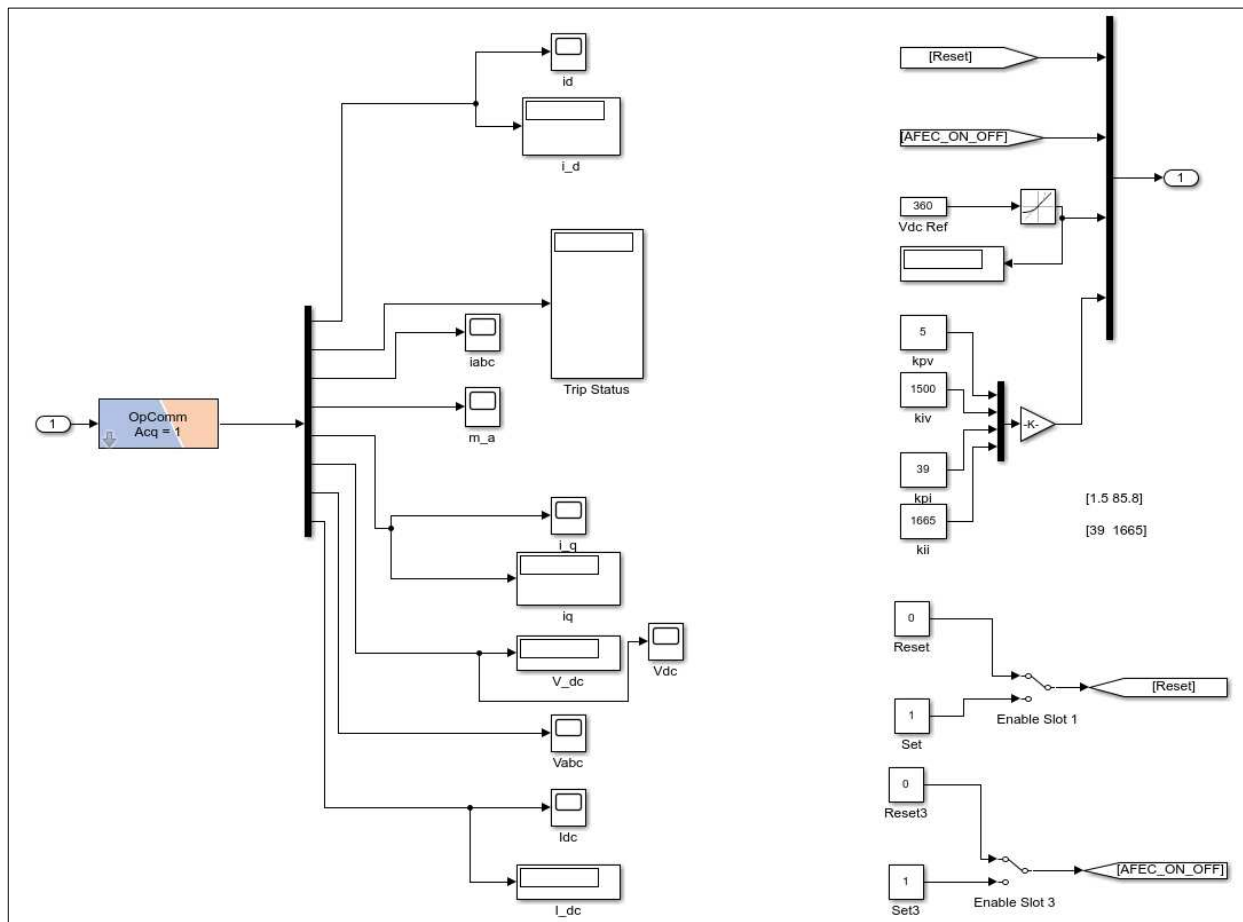
(b)

Fig. D-1. Three-phase V2G and G2V control: (a) real-time model, (b) inside the "sc_IMPEI_3Ph_V2G_G2V" block (this block represents the command panel).
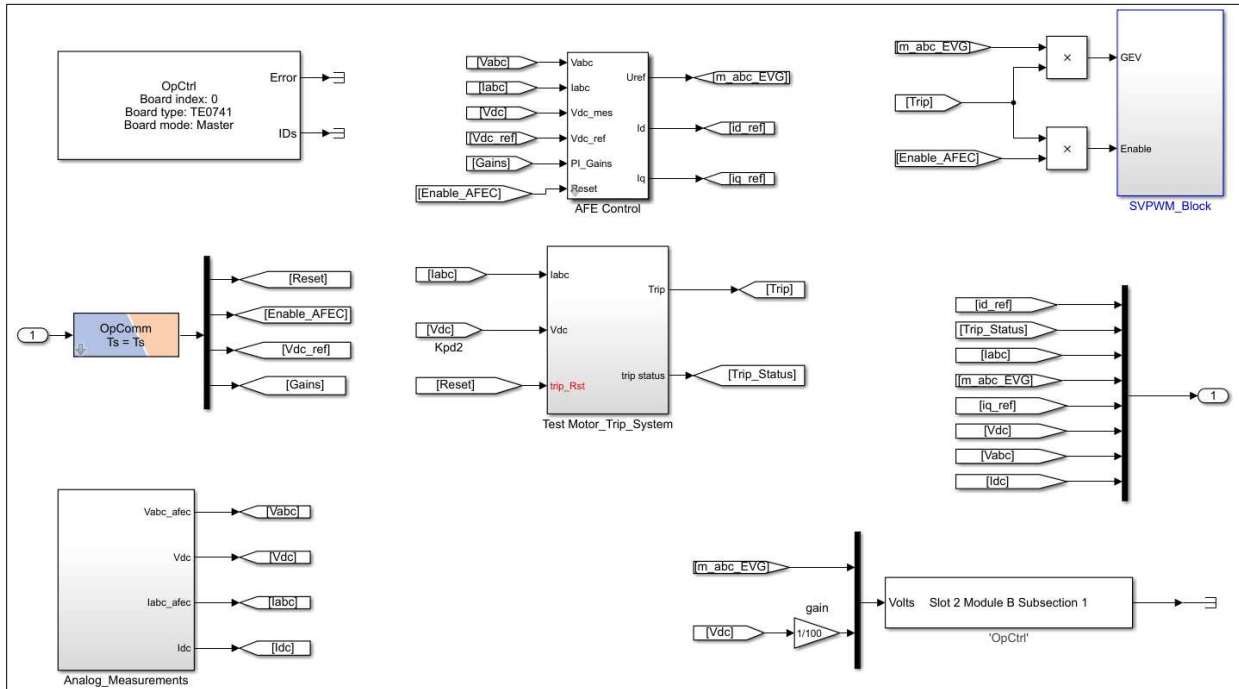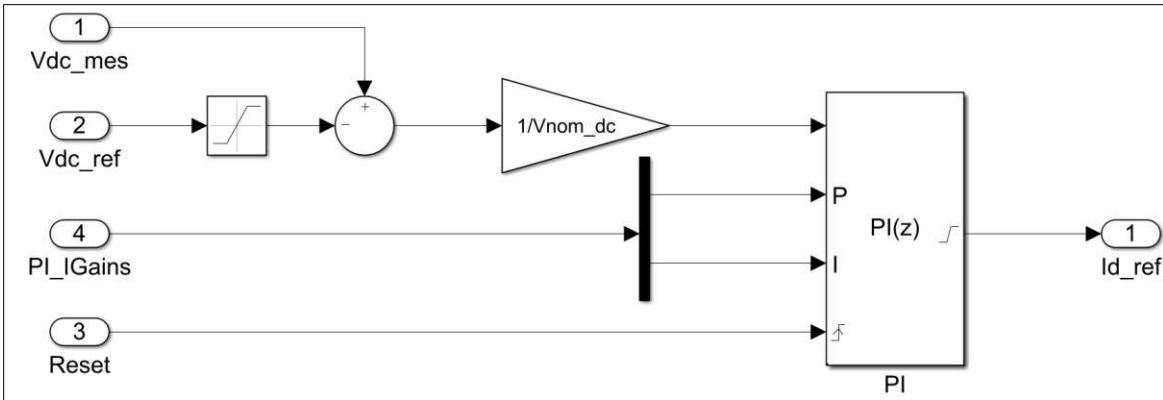
(a)
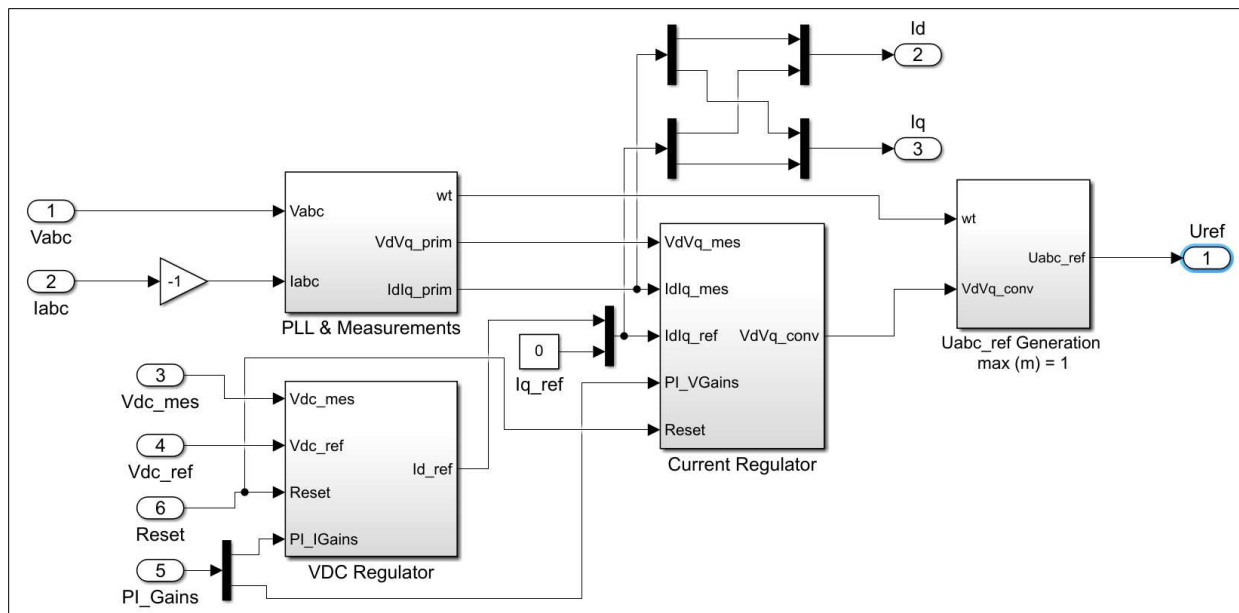
(b)

Fig. D-2. Three-phase V2G and G2V control: (a) inside the "sm_ IMPEI_3Ph_V2G_G2V" block (this block represents the process loaded on the FPGA. The systems in this block run in real-time), (b) inside the "AFE_Control" block.
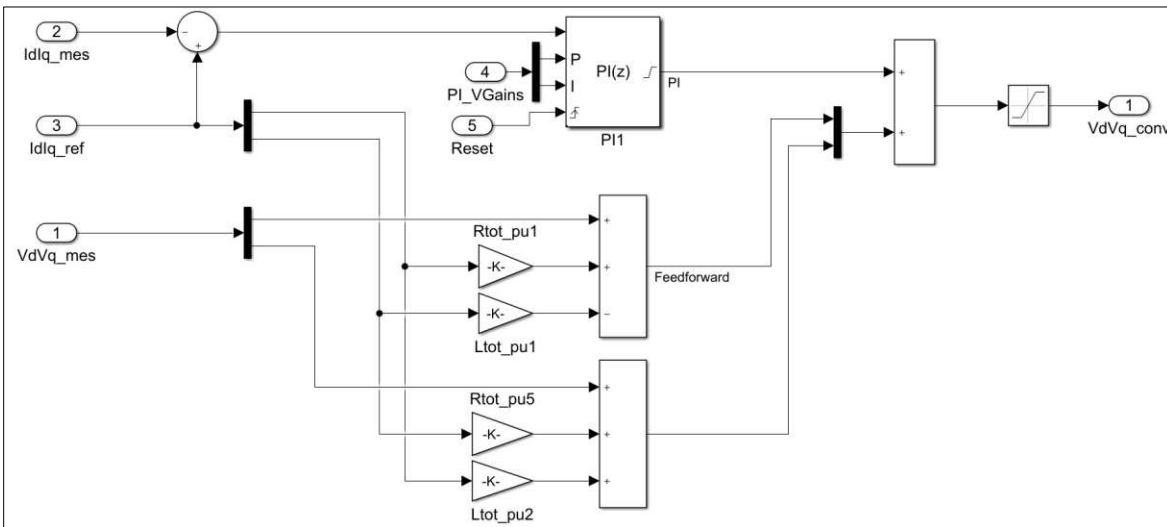
The "Test Motor_Trip_System" block is similar to the one discussed in Appendix B in Fig. C-4.(a) and Fig. C-4.(b).
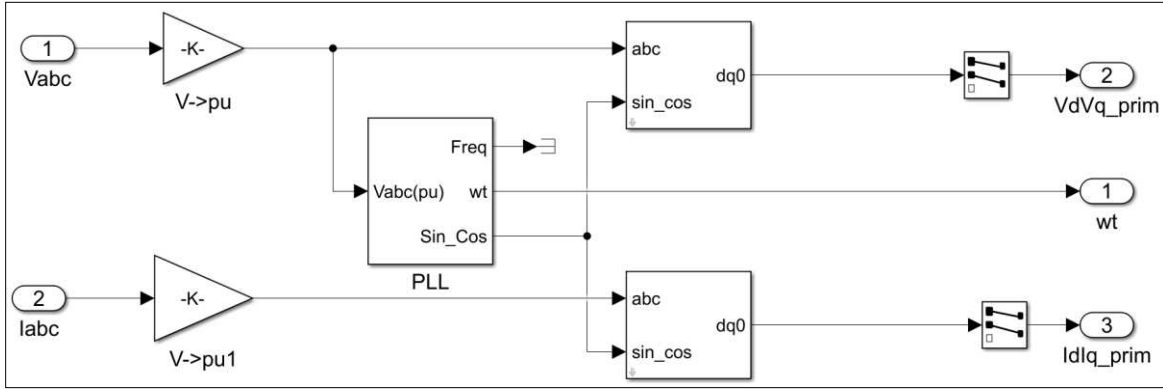
(a)

(b)

(c)

Fig. D-3. Three-phase V2G and G2V control: (a) inside the "PLL & Measurements" block, (b) inside the "VDC Regulator" block, and (c) inside the "Current Regulator" block.

These control blocks have been inspired by the work in presented by Patrice Brunelle (2021).

Three-Phase AC-DC-AC PWM Converter, MATLAB Central File Exchange. Retrieved June 2,

2022. (https://www.mathworks.com/matlabcentral/fileexchange/34272-three-phase-ac-dc-ac-pwm-converter).

Appendix E : Modeling and Control of the IMPEI in Single-phase V2G and G2V

The following discussion is based on the "Control of Power Electronic Converters and Systems" Edited by Frede Blaabjerg in [70].

1. Diagram of the IMPEI in level 1 and 2 V2G and G2V
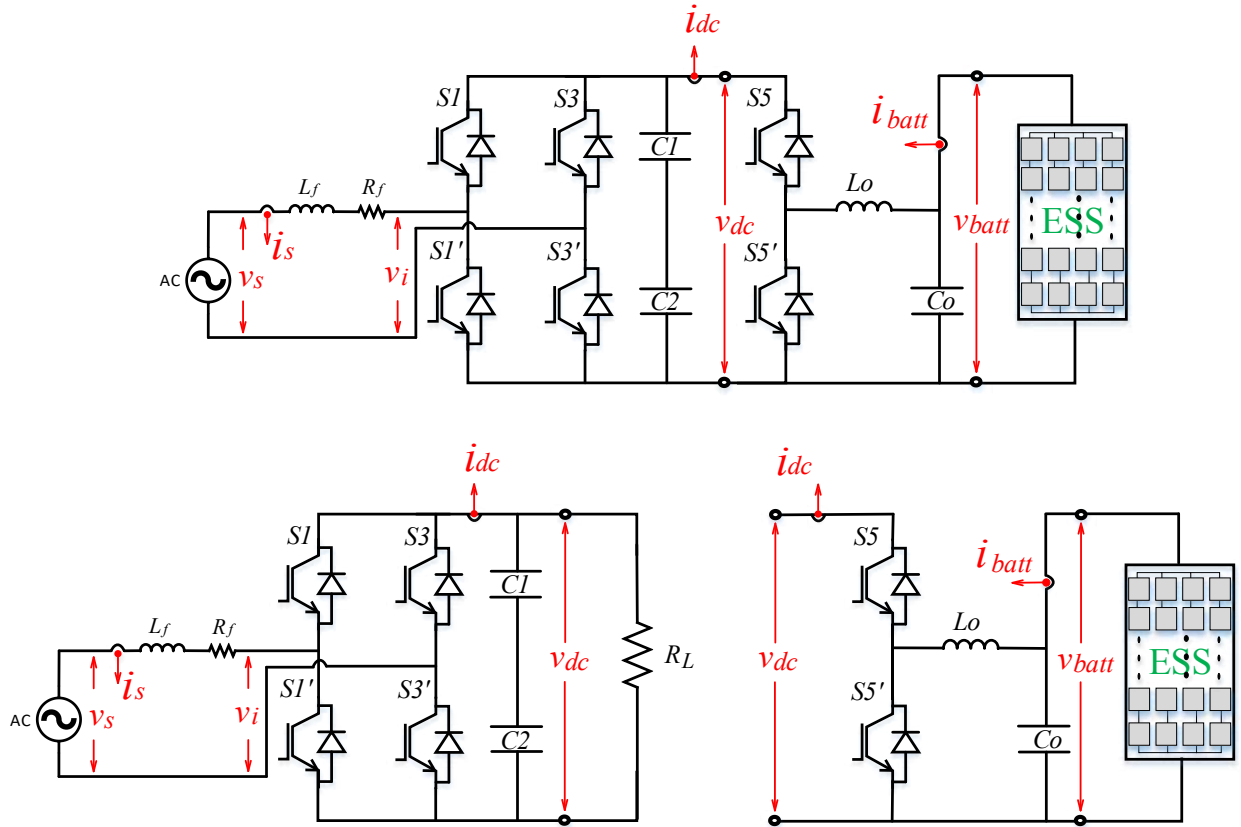
2. AC-DC control using DQ frame

The condition to ensure power transfer: $v_{dc}^* > \sqrt{2}v_s$

The mathematical model of the AC-DC converter is as follows.

$$\frac{di_s}{dt} = -\frac{R_f}{L_f}i_s + \frac{1}{L_f}v_s - \frac{1}{L_f}v_i \, ,$$

$$\frac{dv_{dc}}{dt} = -\frac{1}{(C_1 + C_2)R_L}V_{dc} + \frac{1}{(C_1 + C_2)}i_{dc} \, .$$

Assuming a PWM modulation technique and that $(C_1 + C_2)$ can maintain V_{dc} constant,

$$v_i = mv_{dc},$$

$$i_{dc} = mi_{ac},$$

where m is the modulation index. We have

$$\begin{bmatrix} \dfrac{di_s}{dt} \\ \dfrac{dv_{dc}}{dt} \end{bmatrix} = \begin{bmatrix} -\dfrac{R_f}{L_f} & -\dfrac{m}{L_f} \\ \dfrac{m}{(C_1 + C_2)} & -\dfrac{1}{(C_1 + C_2)R_L} \end{bmatrix} \begin{bmatrix} i_s \\ v_{dc} \end{bmatrix} + \begin{bmatrix} \dfrac{1}{L_f} \\ 0 \end{bmatrix} v_s.$$

3. Transformation stationary reference frame to rotating frame

$$\begin{bmatrix} X_d \\ X_q \end{bmatrix} = T \begin{bmatrix} X_\alpha \\ X_\beta \end{bmatrix}, \text{ with } T = \begin{bmatrix} cos\omega t & sin\omega t \\ -sin\omega t & cos\omega t \end{bmatrix} \text{ where } TT^{-1} = I,$$

$$T^{-1} = \begin{bmatrix} cos\omega t & -sin\omega t \\ sin\omega t & cos\omega t \end{bmatrix},$$

$$X_\alpha = Xsin\omega t,$$
$$X_\beta = Xsin(\omega t - 90),$$

$$\frac{di_s}{dt} = -\frac{R_f}{L_f}i_s - \frac{m}{L_f}v_{dc} + \frac{1}{L_f}v_s,$$

$$\frac{d}{dt}\begin{bmatrix} i_\alpha \\ i_\beta \end{bmatrix} = -\frac{R_f}{L_f}\begin{bmatrix} i_\alpha \\ i_\beta \end{bmatrix} - \frac{1}{L_f}\begin{bmatrix} m_\alpha \\ m_\beta \end{bmatrix}v_{dc} + \frac{1}{L_f}\begin{bmatrix} v_{s\alpha} \\ v_{s\beta} \end{bmatrix},$$

$$\begin{bmatrix} i_\alpha \\ i_\beta \end{bmatrix} = T^{-1}\begin{bmatrix} i_d \\ i_q \end{bmatrix}, \begin{bmatrix} v_\alpha \\ v_\beta \end{bmatrix} = T^{-1}\begin{bmatrix} v_d \\ v_q \end{bmatrix}, \begin{bmatrix} m_\alpha \\ m_\beta \end{bmatrix} = T^{-1}\begin{bmatrix} m_d \\ m_q \end{bmatrix},$$

$$\frac{d}{dt}\left(T^{-1}\begin{bmatrix} i_d \\ i_q \end{bmatrix}\right) = -\frac{R_f}{L_f}T^{-1}\begin{bmatrix} i_d \\ i_q \end{bmatrix} - \frac{1}{L_f}T^{-1}\begin{bmatrix} m_d \\ m_q \end{bmatrix}v_{dc} + \frac{1}{L_f}T^{-1}\begin{bmatrix} v_d \\ v_q \end{bmatrix}.$$

Using the chain rule

$$\frac{d}{dt}\left(T^{-1}\begin{bmatrix} i_d \\ i_q \end{bmatrix}\right) = \frac{d}{dt}T^{-1}\begin{bmatrix} i_d \\ i_q \end{bmatrix} + T^{-1}\frac{d}{dt}\begin{bmatrix} i_d \\ i_q \end{bmatrix},$$

$$T\frac{d}{dt}\left(T^{-1}\begin{bmatrix} i_d \\ i_q \end{bmatrix}\right) = T\frac{d}{dt}T^{-1}\begin{bmatrix} i_d \\ i_q \end{bmatrix} + TT^{-1}\frac{d}{dt}\begin{bmatrix} i_d \\ i_q \end{bmatrix},$$

$$T\frac{d}{dt}T^{-1} = \omega \begin{bmatrix} cos\omega t & sin\omega t \\ -sin\omega t & cos\omega t \end{bmatrix} \begin{bmatrix} -sin\omega t & -cos\omega t \\ cos\omega t & -sin\omega t \end{bmatrix} = \begin{bmatrix} 0 & -\omega \\ \omega & 0 \end{bmatrix},$$

$$\frac{d}{dt}\begin{bmatrix} i_d \\ i_q \end{bmatrix} = -\begin{bmatrix} 0 & -\omega \\ \omega & 0 \end{bmatrix}\begin{bmatrix} i_d \\ i_q \end{bmatrix} - \frac{R_f}{L_f}TT^{-1}\begin{bmatrix} i_d \\ i_q \end{bmatrix} - \frac{1}{L_f}TT^{-1}\begin{bmatrix} m_d \\ m_q \end{bmatrix}v_{dc} + \frac{1}{L_f}TT^{-1}\begin{bmatrix} v_d \\ v_q \end{bmatrix},$$

$$\begin{bmatrix} \dfrac{di_d}{dt} \\ \dfrac{di_q}{dt} \end{bmatrix} = \begin{bmatrix} -\dfrac{R_f}{L_f} & \omega \\ -\omega & -\dfrac{R_f}{L_f} \end{bmatrix}\begin{bmatrix} i_d \\ i_q \end{bmatrix} + \frac{1}{L_f}\begin{bmatrix} v_d \\ v_q \end{bmatrix} - \frac{1}{L_f}\begin{bmatrix} m_d \\ m_q \end{bmatrix}v_{dc}.$$

4. Laplace Transform

$$\begin{cases} si_d = -\dfrac{R_f}{L_f}i_d + \omega i_q + \dfrac{1}{L_f}v_d - \dfrac{1}{L_f}m_d v_{dc}. \\[4mm] si_q = -\omega i_d - \dfrac{R_f}{L_f}i_q + \dfrac{1}{L_f}v_q - \dfrac{1}{L_f}m_q v_{dc}. \end{cases}$$

$$\begin{cases} (L_f s + R_f)i_d = \omega L_f i_q + v_d - m_d v_{dc}. \\ (L_f s + R_f)i_q = -\omega L_f i_d + v_q - m_q v_{dc}. \end{cases}$$

$$\begin{cases} i_d = \dfrac{\omega L_f i_q}{(L_f s + R_f)} + \dfrac{v_d}{(L_f s + R_f)} - \dfrac{m_d v_{dc}}{(L_f s + R_f)}. \\[4mm] i_q = -\dfrac{\omega L_f i_d}{(L_f s + R_f)} + \dfrac{v_q}{(L_f s + R_f)} - \dfrac{m_q v_{dc}}{(L_f s + R_f)}. \end{cases}$$

5. Decoupling equations

$$\begin{cases} m_d = -m_d^* + \dfrac{1}{v_{dc}}\omega L_f i_q. \\[4mm] m_q = -m_q^* - \dfrac{1}{v_{dc}}\omega L_f i_d. \end{cases}$$
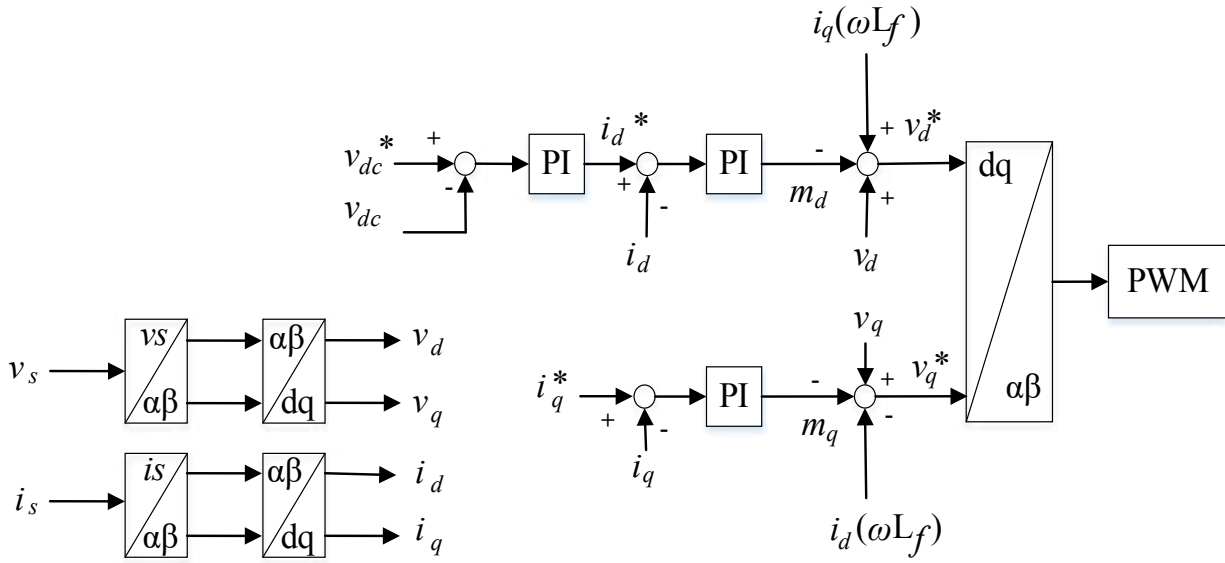
We have

$$\begin{cases} i_d = \dfrac{\omega L_f i_q}{(L_f s + R_f)} + \dfrac{v_d}{(L_f s + R_f)} - \dfrac{v_{dc}}{(L_f s + R_f)}\left(-m_d^* + \dfrac{1}{v_{dc}}\omega L_f i_q\right). \\[4mm] i_q = -\dfrac{\omega L_f i_d}{(L_f s + R_f)} + \dfrac{v_q}{(L_f s + R_f)} - \dfrac{v_{dc}}{(L_f s + R_f)}\left(-m_q^* - \dfrac{1}{v_{dc}}\omega L_f i_d\right). \end{cases}$$

$$
\begin{cases}
i_d = \dfrac{\omega L_f i_q}{\left(L_f s + R_f\right)} + \dfrac{v_d}{\left(L_f s + R_f\right)} + \dfrac{m_d^* v_{dc}}{\left(L_f s + R_f\right)} - \dfrac{\omega L_f i_q}{\left(L_f s + R_f\right)} \;. \\[3mm]
i_q = -\dfrac{\omega L_f i_d}{\left(L_f s + R_f\right)} + \dfrac{v_q}{\left(L_f s + R_f\right)} + \dfrac{m_q^* v_{dc}}{\left(L_f s + R_f\right)} + \dfrac{\omega L_f i_d}{\left(L_f s + R_f\right)} \;.
\end{cases}
$$

$$
\begin{cases}
i_d = \dfrac{v_d}{\left(L_f s + R_f\right)} + \dfrac{m_d^* v_{dc}}{\left(L_f s + R_f\right)} \;. \\[3mm]
i_q = +\dfrac{v_q}{\left(L_f s + R_f\right)} + \dfrac{m_q^* v_{dc}}{\left(L_f s + R_f\right)} \;.
\end{cases}
$$

6. Control Diagram

7. Current Loop

Both currents loops have the same dynamics. V_d and V_q are treated as disturbances.

$$
H_i(s) = \frac{i_d^*}{m_d^*}\Big|_{v_d=0} = \frac{i_q^*}{m_q^*}\Big|_{v_q=0} = \frac{1}{sL_f + R_f}\, v_{dc} = \frac{1/R_f}{1 + sL_f/R_f}\, v_{dc} \;.
$$
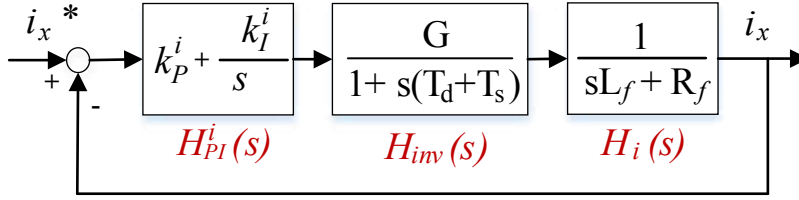
G is the inverter gain, Td and Ts are dead time delay and the sampling time.

$$K_P^i + \frac{K_I^i}{s} = \frac{sK_P^i + K_I^i}{s} = \frac{K_I^i(1 + sT_i)}{s}, T_i = \frac{K_P^i}{K_I^i}.$$

The close loop TF of the current loops is as follows,

$$T_{i_x}(s) = \frac{H_{PI}^i(s)H_{inv}(s)H_i(s)}{1 + H_{PI}^i(s)H_{inv}(s)H_i(s)}.$$

For design, $T_i = \frac{L_f}{R_f}$, $G = \frac{1}{v_{dc}}$.

$$T_{i_x}(s) = \frac{\dfrac{K_I^i/R_f}{s(1 + s(T_d + T_s))}}{1 + \dfrac{K_I^i/R_f}{s(1 + s(T_d + T_s))}} = \frac{K_I^i/R_f}{s(1 + s(T_d + T_s)) + K_I^i/R_f},$$

$$T_{i_x}(s) = \frac{\dfrac{K_I^i}{R_f}}{s + s^2(T_d + T_s) + K_I^i} = \frac{\dfrac{K_I^i}{(T_d + T_s)R_f}}{s^2 + s\dfrac{1}{(T_d + T_s)} + \dfrac{K_I^i}{(T_d + T_s)R_f}}.$$

For a second order system,

$$\begin{cases} \omega_n = \sqrt{\dfrac{K_I^i}{(T_d + T_s)R_f}}, \\[4mm] \zeta = \sqrt{\dfrac{R_f}{4(T_d + T_s)K_I^i}}. \end{cases}$$

The damping coefficient can be calculated as follows,

$$\zeta = \frac{\sqrt{2}}{2}.$$

The controller gains can be calculated using the following equations.

$$K_I^i = \frac{R_f}{4(T_d + T_s)\zeta^2},$$

$$K_P^i = T_i K_I^i = \frac{L_f}{4(T_d + T_s)\zeta^2},$$

The bandwidth of the system can be calculated as follows,

$$2\zeta\omega_n = \frac{1}{T_d + T_s} = \tau.$$

8. Voltage Loop

For the voltage loop, the transfer function is obtained as follows,

$$\begin{bmatrix} \dfrac{di_s}{dt} \\ \dfrac{dv_{dc}}{dt} \end{bmatrix} = \begin{bmatrix} -\dfrac{R_f}{L_f} & -\dfrac{m}{L_f} \\ \dfrac{m}{(C_1 + C_2)} & -\dfrac{1}{(C_1 + C_2)R_L} \end{bmatrix} \begin{bmatrix} i_s \\ v_{dc} \end{bmatrix} + \begin{bmatrix} \dfrac{1}{L_f} \\ 0 \end{bmatrix} v_s,$$

$$\frac{dv_{dc}}{dt} = \frac{m}{(C_1 + C_2)} i_s - \frac{1}{(C_1 + C_2)R_L} v_{dc}.$$

For the small signal representation, $v_{dc} \geq \sqrt{2}V_s$, and $M = \dfrac{V_s}{v_{dc}} = \dfrac{1}{\sqrt{2}}$.

By introducing the perturbation, we have,

$$v_{dc} = V_{dc} + \hat{v}_{dc},$$

$$i_s = I_s + \hat{i}_s,$$

$$m = M + \hat{m},$$

$$\frac{d(V_{dc} + \hat{v}_{dc})}{dt} = \frac{(M + \hat{m})}{(C_1 + C_2)}(I_s + \hat{i}_s) - \frac{1}{(C_1 + C_2)R_L}(V_{dc} + \hat{v}_{dc}),$$

$$\frac{dV_{dc}}{dt} = 0,$$

$$\frac{d\hat{v}_{dc}}{dt} = \frac{1}{(C_1 + C_2)}(I_s + \hat{i}_s)(M + \hat{m}) - \frac{1}{(C_1 + C_2)R_L}(V_{dc} + \hat{v}_{dc}),$$

$$\frac{d\hat{v}_{dc}}{dt} = \frac{1}{(C_1 + C_2)}(I_s M + \hat{i}_s M + I_s \hat{m} + \hat{i}_s \hat{m}) - \frac{1}{(C_1 + C_2)R_L}V_{dc} - \frac{1}{(C_1 + C_2)R_L}\hat{v}_{dc}.$$

The DC and AC quantities can be separated as follows by ignoring the second order quantities.

$$\begin{cases} \dfrac{d\hat{v}_{dc}}{dt} = \dfrac{\hat{i}_s M + I_s \hat{m}}{C_1 + C_2} - \dfrac{1}{(C_1 + C_2)R_L}\hat{v}_{dc}, \\[3mm] 0 = \dfrac{I_s M}{C_1 + C_2} - \dfrac{1}{(C_1 + C_2)R_L}V_{dc}. \end{cases}$$

By proceeding with ac quantities, we have,

$$\frac{d\hat{v}_{dc}}{dt} = \frac{\hat{i}_s M + I_s \hat{m}}{C_1 + C_2} - \frac{1}{(C_1 + C_2)R_L}\hat{v}_{dc}.$$

Using the Laplace transformation,

$$s\hat{v}_{dc} + \frac{1}{(C_1 + C_2)R_L}\hat{v}_{dc} - \frac{\hat{i}_s M + I_s \hat{m}}{C_1 + C_2} = 0,$$

$$\left(s + \frac{1}{(C_1 + C_2)R_L}\right)\hat{v}_{dc} - \frac{\hat{i}_s M}{C_1 + C_2} - \frac{I_s \hat{m}}{C_1 + C_2} = 0.$$

The transfer function can be obtained as below,

$$\frac{\hat{v}_{dc}}{\hat{i}_s} = \frac{\dfrac{M}{C_1 + C_2}}{s + \dfrac{1}{(C_1 + C_2)R_L}} = \frac{MR_L}{s(C_1 + C_2)R_L + 1},$$

$$T_{v_{dc}}(s) = \frac{\hat{v}_{dc}}{\hat{i}_d} = \frac{1}{\sqrt{2}}\frac{MR_L}{s(C_1 + C_2)R_L + 1} = \frac{1}{2}\frac{R_L}{s(C_1 + C_2)R_L + 1}.$$

The block diagram of the system can be obtained as shown in the Fig. bolow.
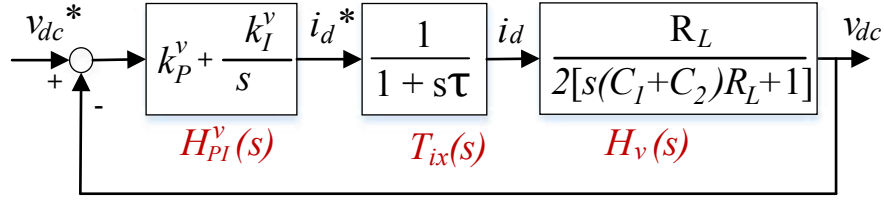
$$K_P^v + \frac{K_I^v}{s} = \frac{sK_P^v + K_I^v}{s} = \frac{K_I^v(1 + sT_v)}{s}, T_v = \frac{K_P^v}{K_I^v}$$

The closed loop transfer function is obtained as follows,

$$T_{i_x}(s) = \frac{H_{PI}^v(s)T_{ix}(s)H_v(s)}{1 + H_{PI}^i(s)H_{inv}(s)H_i(s)}.$$

By designing the controller to cancel the dominant pole,

$$T_v = (C_1 + C_2)R_L,$$

$$T_{i_x}(s) = \frac{\dfrac{K_I^v}{s}\dfrac{R_L}{2}}{1 + s\tau}}{1 + \dfrac{\dfrac{K_I^v}{s}\dfrac{R_L}{2}}{1 + s\tau}} = \frac{K_I^v R_L}{2s(1 + s\tau) + K_I^v R_L} = \frac{K_I^v R_L}{s^2\tau + 2s + K_I^v R_L},$$

$$T_{i_x}(s) = \frac{\dfrac{K_I^v R_L}{\tau}}{s^2 + s\dfrac{2}{\tau} + \dfrac{K_I^v R_L}{\tau}},$$

$$\begin{cases} \omega_n = \sqrt{\dfrac{K_I^v R_L}{\tau}}, \\ \zeta = \sqrt{\tau K_I^v R_L} \end{cases}$$

$$K_I^v = \frac{\zeta^2}{\tau R_L},$$

$$K_P^v = T_v K_I^v = \frac{(C_1 + C_2)\zeta^2}{\tau}.$$

144

Appendix F : Real-time Controller for Single-phase V2G and G2V

In this section the blocks used for implementing the single-phase V2G and G2V real-time control as well as the protection circuit have been expanded sequentially.
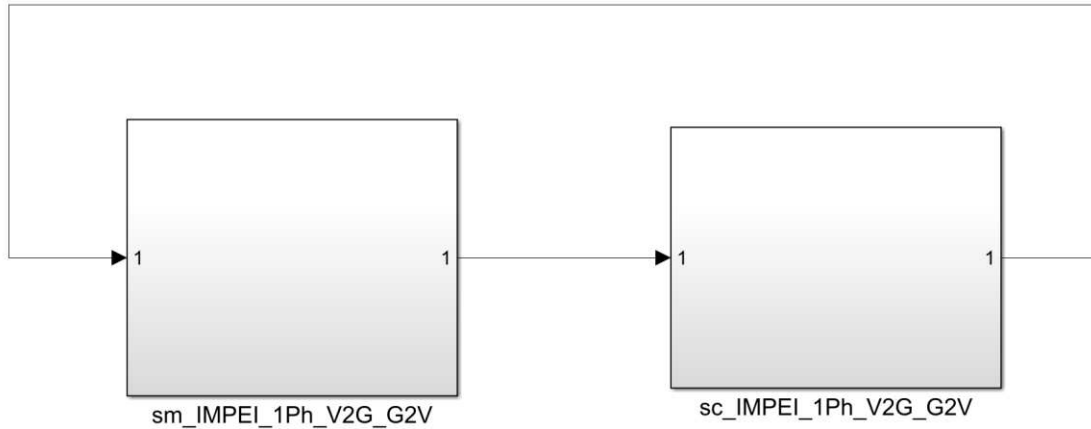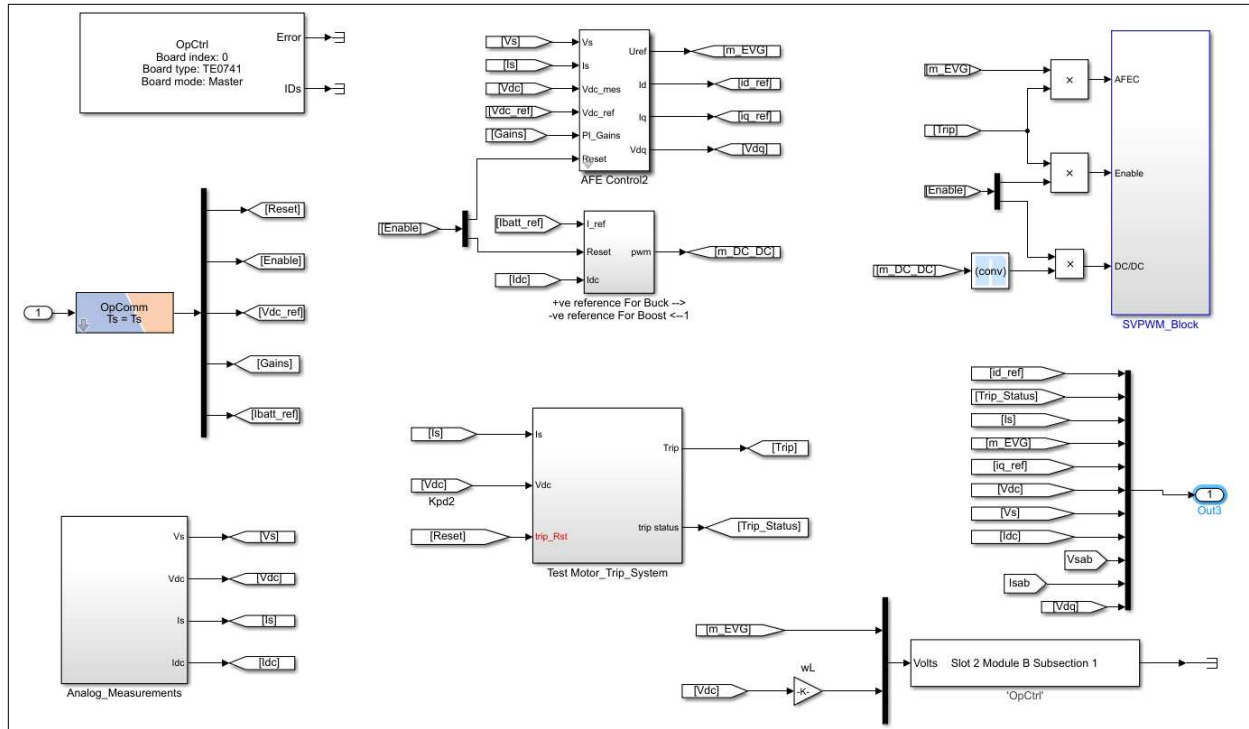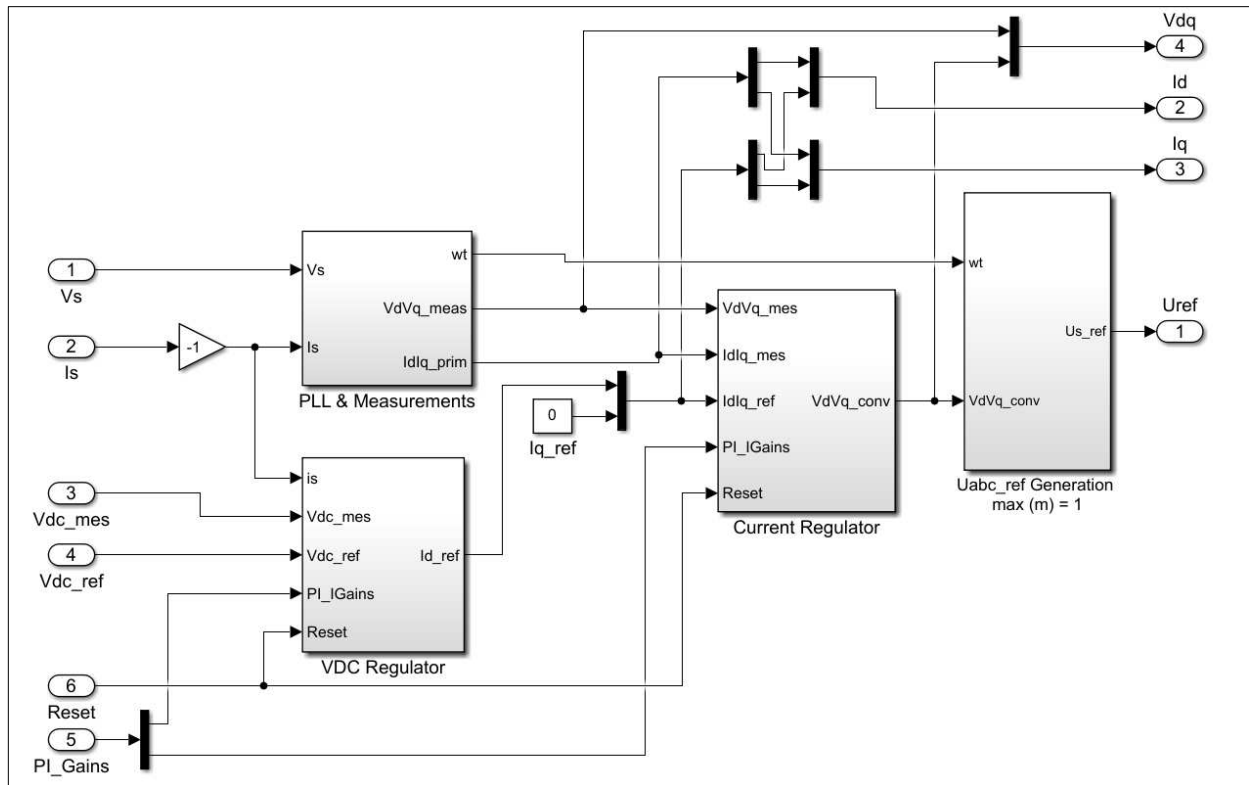

(a)
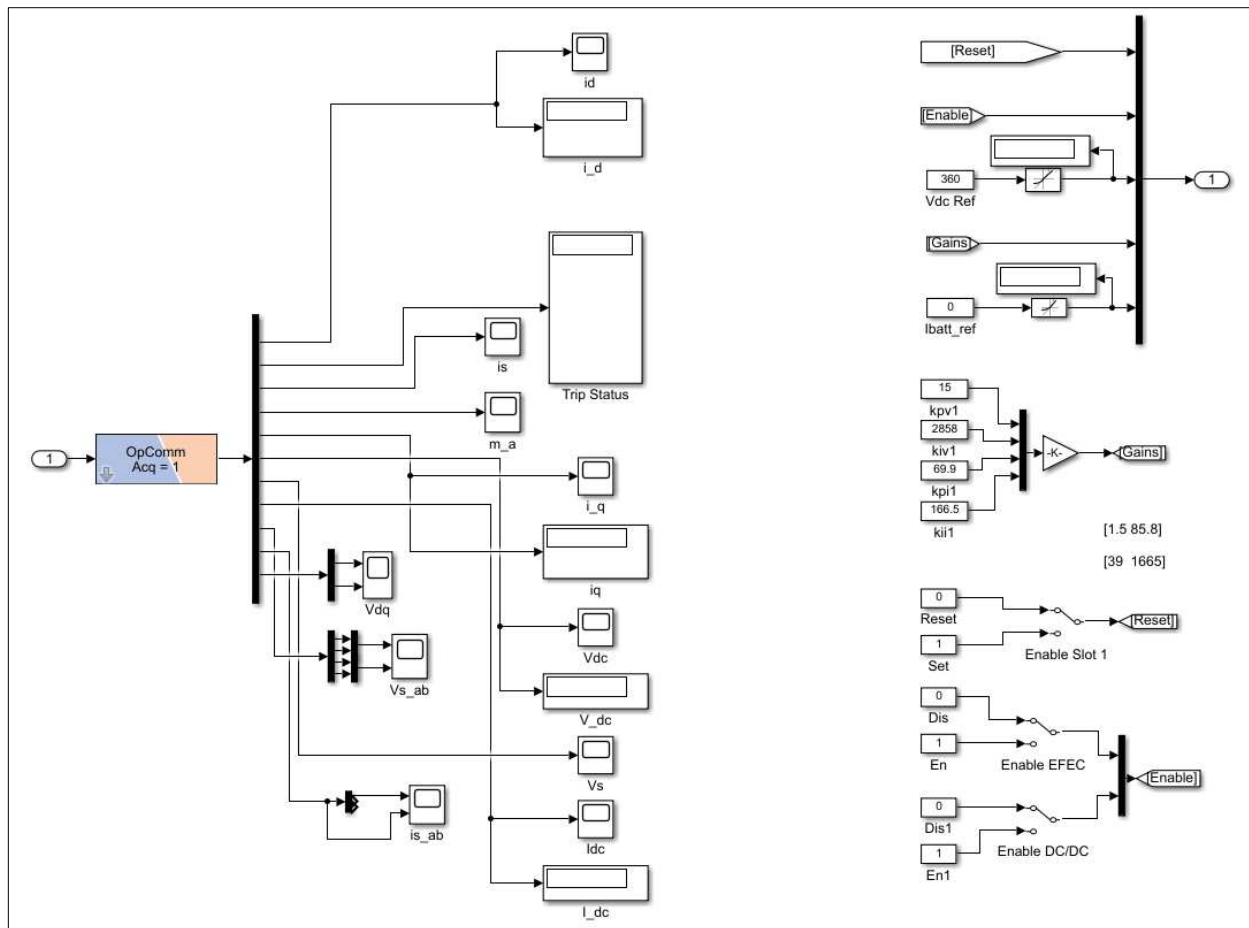
(b)

Fig. F-1. Single-phase V2G and G2V control: (a) real-time model, (b) inside the "sc_IMPEI_1Ph_V2G_G2V" block (this block represents the command panel).

(a)

(b)

Fig. F-2. Single-phase V2G and G2V control for full-bridge AFEC configuration at 120 V: (a) inside the "sm_ IMPEI_1Ph_V2G_G2V" block (this block represents the process loaded on the FPGA. The systems in this block run in real-time), (b) inside the "AFE_Control2" block (this block implements the control for the full-bridge AFEC).
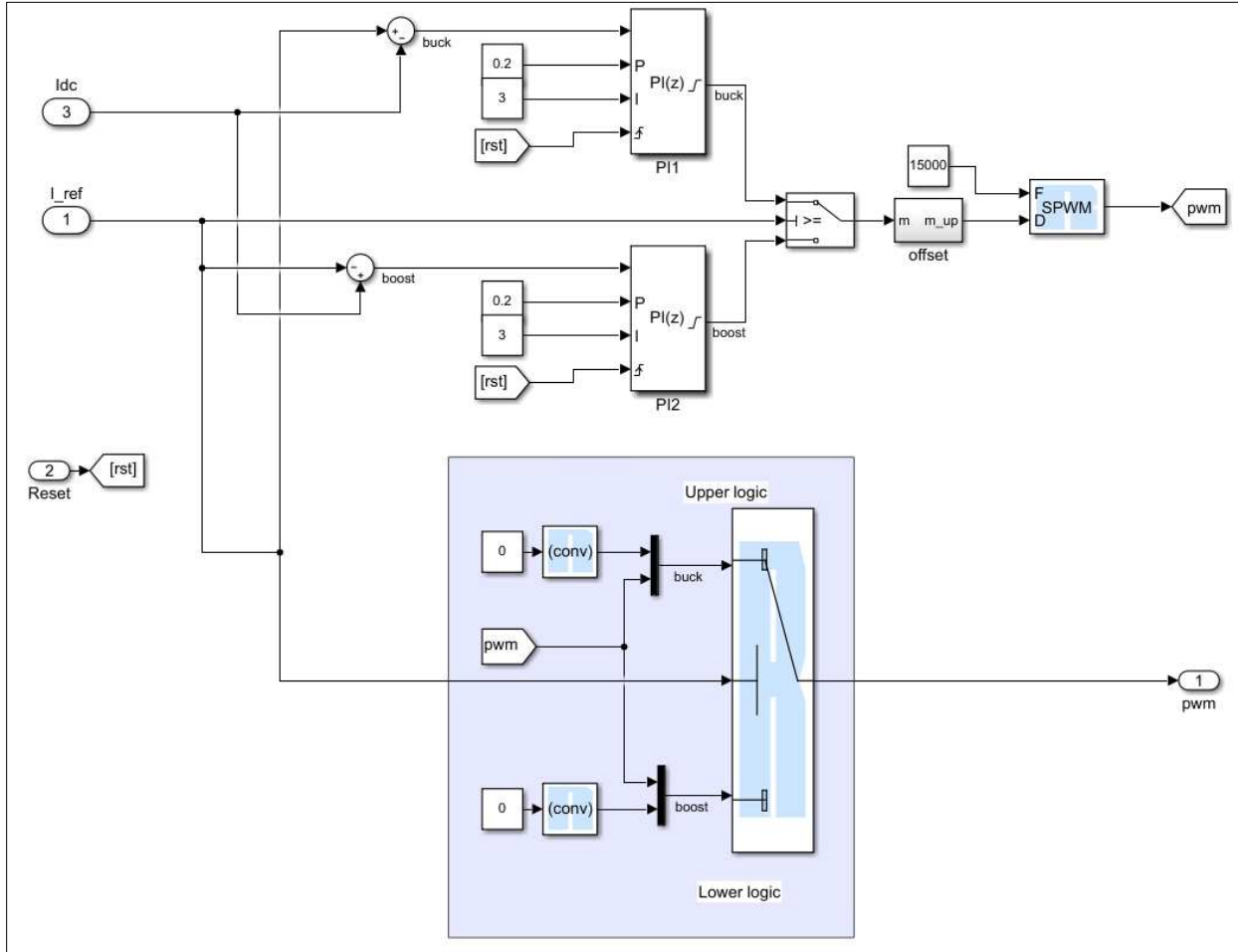
Fig. F-3. Single-phase V2G and G2V control for full-bridge AFEC configuration at 120 V: inside the "+ve reference For Buck -->-ve reference For Boost <--1" block (this block implements the DC-DC stage control of the IMPEI).
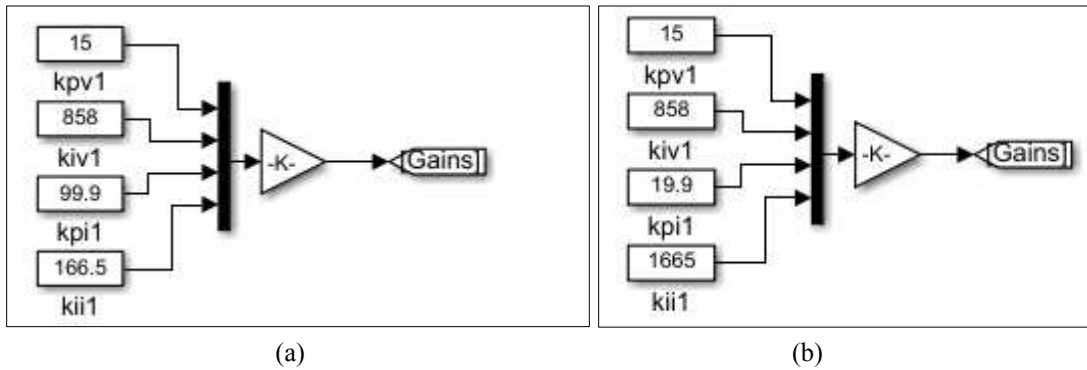

|	(a)		(b)

Fig. F-4. Single-phase V2G and G2V control: (a) controller gains for half-bridge AFEC configuration at 120 V, (b) controller gains for full-bridge AFEC configuration at 240 V.

The blocks presented here are used for both half-bridge and full-bridge AFEC configurations. The trip levels as well as the PI gains have been adjusted for each mode.
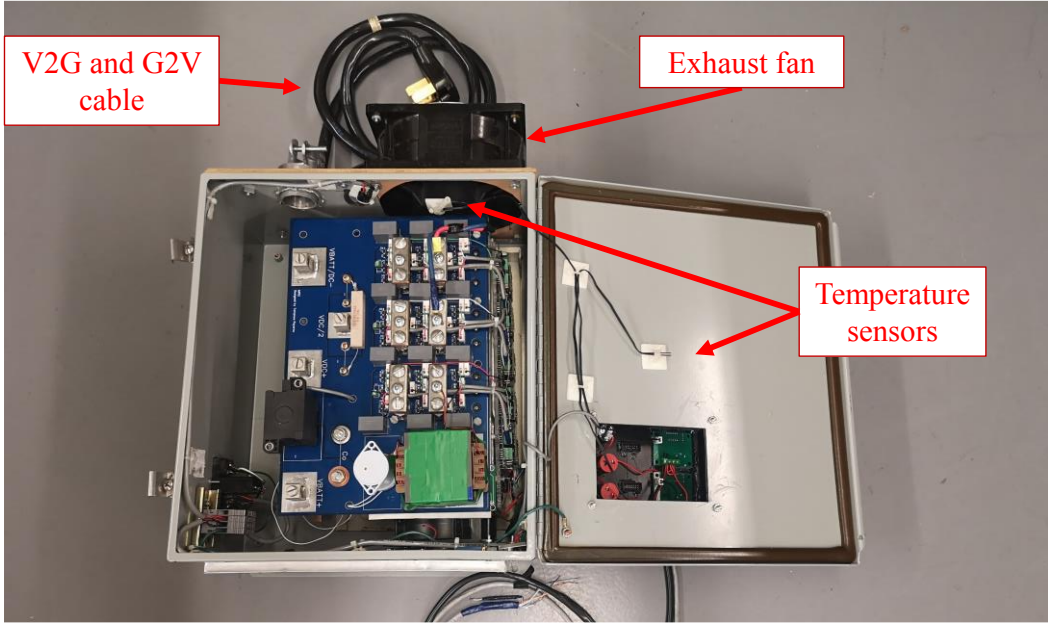
147

Appendix G : MOSFET-Based IMPEI
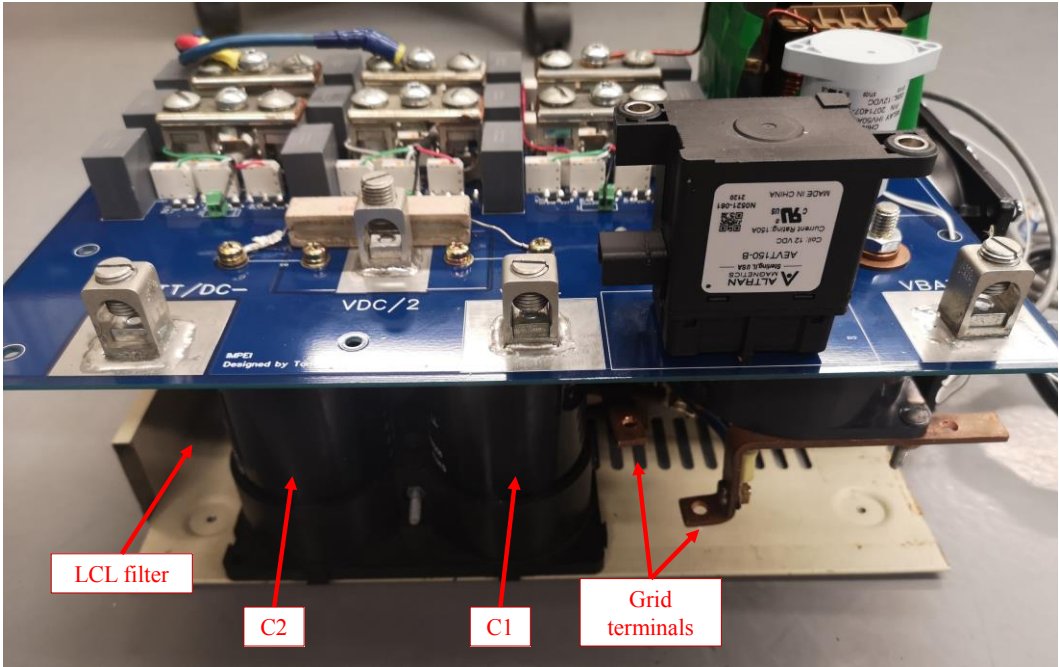
(a)
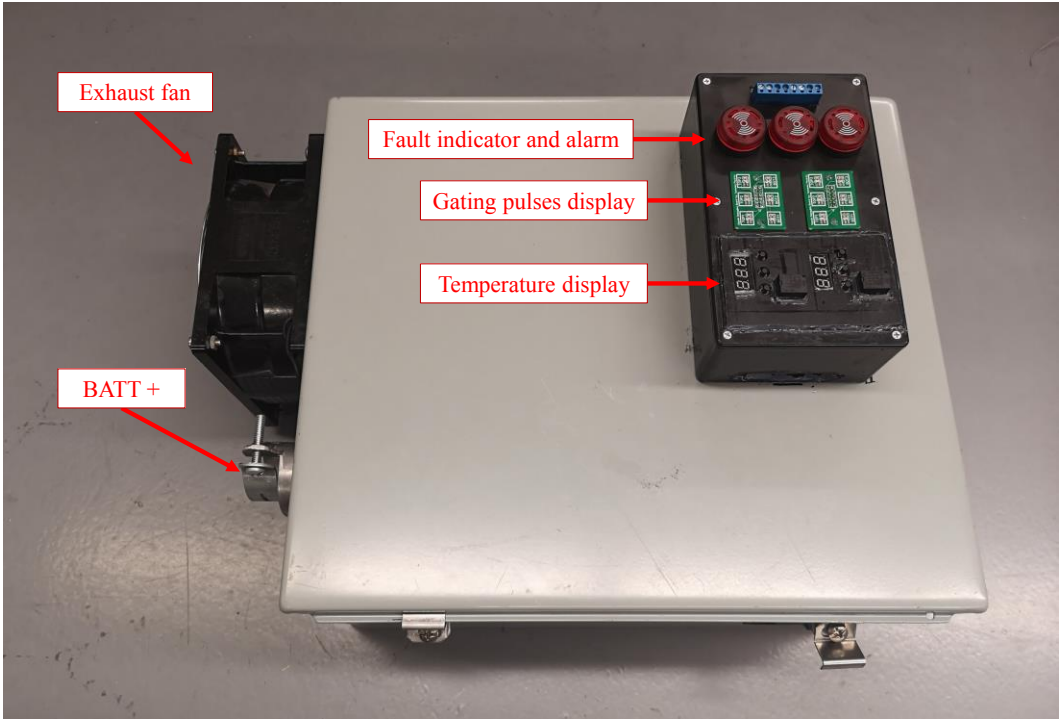
(b)

Fig. G-1. MOSFET-Based IMPEI: (a) back side of the IMPEI and (b) IMPEI enclosure.

(a)

(b)

Fig. G-2. MOSFET-Based IMPEI: (a) inside view, IMPEI during test.